UNIVERSIDAD NACIONAL AUTÓNOMA DE MÉXICO
PROGRAMA DE MAESTRÍA Y DOCTORADO EN INGENIERÍA
INGENIERÍA CIVÍL – ESTRUCTURAS

COCIENTE ESPECTRAL H/V BAJO LA TEORÍA DE CAMPOS DIFUSOS

TESIS
QUE PARA OPTAR POR EL GRADO DE:
DOCTOR EN INGENIERÍA

PRESENTA:
JOSÉ PIÑA FLORES

TUTOR PRINCIPAL
FRANCISCO JOSÉ SANCHEZ SESMA,
INSTITUTO DE INGENIERÍA

CIUDAD UNIVERSITARIA, CD. MX., SEPTIEMBRE, 2020

JURADO ASIGNADO:

Presidente:	Dr. Juan José Pérez Gavilán Escalante
Secretario:	Dr. Martín Cárdenas Soto
1 er. Vocal:	Dr. Francisco José Sánchez Sesma
2 do. Vocal:	Dra. Úrsula Xiomara Iturrarán Viveros.
3 er. Vocal:	Dr. Antonio García Jerez

Lugar o lugares donde se realizó la tesis:
Cd. Mx., México, Ciudad Universitaria UNAM,
Septiembre 2020

TUTOR DE TESIS:

Francisco José Sánchez Sesma

FIRMA

Para Cintia y Alexis

Agradecimientos

Agradezco a la Universidad Nacional Autónoma de México (UNAM) por darme la gran oportunidad de realizar mí Posgrado, en particular, al Posgrado de Ingeniería, al Instituto de Ingeniería y a la Facultad de Ingeniería por otorgarme todas las facilidades durante el desarrollo de este trabajo.

A las instituciones que me apoyaron económicamente: CONACYT (Beca Nacional 449268), la Facultad de Ingeniería y al Instituto de Ingeniería, y a los proyectos UNAM-DGAPA-PAPIIT :IN100917, IN117119.

Agradezco infinitamente a mi asesor, el Dr. Francisco José Sánchez Sesma por haberme ayudado en todo momento, por sus enseñanzas, orientación y paciencia. Al Dr. Martín Cárdenas Soto y al MC. David Escobedo Zenil por la oportunidad de desarrollarme profesionalmente en la Facultad de Ingeniería. Al Dr. Antonio García Jerez y al Dr. Francisco Luzón del Research Group on Applied Geophysics de la Universidad de Almería, por otorgarme sus códigos y datos para la realización de esta tesis.

A mis sinodales: Dra. Úrsula Iturrarán Viveros, al Dr. Juan José Pérez Gavilán Escalante, al Dr. Antonio García Jerez, Al Dr. Martin Cárdenas Soto y al Dr. Francisco José Sánchez Sesma. Muchas gracias por el tiempo dedicado durante los cuatro años que duro mi formación, así como a la revisión y comentarios de este trabajo.

Al Arqueólogo Alejandro Sarabia González, a su hermano Fernando Sarabia González y al Consejo de la Zona Arqueológica Teotihuacán por todas las facilidades para poder llevar a cabo este trabajo.

Agradezco al Dr. Jorge Aguirre-González, al Ing. Horacio Mijares, a los estudiantes de la carrera de ingeniería geofísica de la Facultad de Ingeniería y a los becarios de la Coordinación de Ingeniería Sismológica del Instituto de Ingeniería por su apoyo en las campañas de medición de ruido sísmico ambiental en la Pirámide del Sol.

Al Dr. César A. Sierra-Álvarez y al Dr. Mario A. Sáenz-Castillo por sus valiosas contribuciones de modelado mediante el método BEM.

También quiero agradecer al Ing. Jesús Sánchez-González, al Dr. Mauricio Nava Flores y al equipo de trabajo de la División de Ciencias de la Tierra de la Facultad de Ingeniería de la UNAM quienes ayudaron en las mediciones GPS y de Gravimetría en la Pirámide del Sol.

Finalmente, agradezco a todas aquellas personas que hicieron posible este trabajo y al Grupo de Facebook *“BCSC”* por los momentos divertidos que motivaron la realización de esta tesis.

Índice General

Resumen

La utilidad del ruido sísmico ambiental (RSA), en distintos métodos geofísicos, ha sido muy popular en los últimos años a partir del surgimiento de la teoría de campos difusos. Bajo la hipótesis de que el RSA es un campo de ondas de carácter difuso, se han aplicado algunas técnicas de sísmica pasiva para obtener las propiedades dinámicas del subsuelo, en particular, las técnicas del cociente espectral H/V (HVSR) y de correlaciones cruzadas (CC). A pesar de que no se ha podido comprobar por completo que el RSA es de carácter difusivo, las técnicas de sísmica pasiva han tenido un enorme éxito en su aplicación y en sus resultados. Sin embargo, aún existe varias interrogantes acerca de las características y propiedades del RSA; de la aplicación en: a) La técnica de HVSR y su relación con otras técnicas de prospección sísmica, b) Las técnicas de sísmica pasiva en distintos escenarios (por ejemplo, medios elásticos con topografía), c) La inversión de la curva del HVSR de onda completa, etc. En este trabajo, se busca dar una respuesta a estas interrogantes, de modo que esta tesis está dividida en cinco secciones. En la primera sección, analizo datos de RSA obtenidos en diferentes lugares en México con el fin de explorar posibles indicadores en la estabilización de la relación de la energía sísmica que señalen que el RSA es de carácter difusivo. En la segunda sección, exploro la relación entre las formas de onda de las curvas de dispersión de las ondas de Rayleigh y el HVSR calculado bajo el enfoque de campos difusos. En la tercera sección, utilizo datos de RSA obtenido en un medio elástico con geometría irregular, la Pirámide del Sol en Teotihuacán, con el objetivo de estimar un modelo 3D de velocidades de onda de corte (Vs) aplicando las técnicas del HVSR y de CC entre pares de estaciones. En la cuarta sección muestro los avances y continuación del proyecto HV-Inv (2016-2020) con el objetivo de crear una herramienta de interfaz gráfica para obtener el cálculo directo e inverso del cociente HVSR para un medio estratificado bajo la teoría de campos difusos. Finalmente, en la quinta sección, analizo y explico el trabajo a futuro para el procesamiento de datos de RSA para obtener el HVSR. Además, en esa última sección doy las pautas para el estudio de la distribución de la energía sísmica asociada a cada tipo de ondas para un medio estratificado y su relación con el HVSR; todo esto con el enfoque de la teoría de campos difusos.

Abstrac

The utility of ambient seismic noise (ASN), in different geophysical methods, has been very popular in recent years since the emergence of the diffuse field theory. Under the hypothesis that the ASN is a diffuse wave field, some passive seismic techniques have been applied to obtain the dynamic properties of the subsoil, the H/V spectral ratio (HVSR) and cross-correlation techniques. (CC). Although it has not been possible to fully verify that ASN is diffusive in nature, passive seismic techniques have been enormously successful in its application and in its results. However, there are still several questions about the characteristics and properties of ASN; the application of the HVSR technique and its relationship with other seismic prospecting techniques; of the applications of passive seismic techniques in different scenarios (for example, elastic media with topography), of the inversion of the full-wave HVSR curve, etc. In this work, we seek to answer these questions, so that this thesis is divided into five sections. In the first section, a search and analysis of possible indicators is carried out that indicate that the ASN is diffusive in nature from the stabilization of the seismic energy relationship with ASN data obtained in different places in Mexico. In the second section, the relationship between the waveforms of the dispersion curves of Rayleigh waves and the HVSR calculated under the diffuse field approach is explored. In the third section, the ASN obtained in an elastic medium with irregular geometry, the Pyramid of the Sun in Teotihuacán, is used with the objective of estimating a 3D model of shear wave velocities (Vs) applying the HVSR and CC techniques. between pairs of stations. The fourth section shows the creation and continuation of the HV-Inv project (2016-2020) with the aim of creating a graphical interface tool to obtain the direct and inverse calculation of the HVSR for a stratified medium under the theory of diffuse fields. Finally, in the fifth section, the future work is mentioned where a way of processing the ASN data to obtain the HVSR is being developed. In addition, the distribution of seismic energy associated with each type of wave for a stratified medium and its relationship with the HVSR is studied; all this with the approach of difusse field theory.

Introducción

El ruido sísmico ambiental (RSA) están compuestas de vibraciones que se producen en el subsuelo y son generadas por eventos naturales (por ejemplo, erupción de un volcán, mareas, etc.) y artificiales (llamado microtremores) producto de la actividad humana tales como el paso de vehículos, maquinaria industrial etc. Antes del siglo XXI, no se había establecido una teoría solida acerca del tipo de ondas que conforman el RSA. Hoy en día, se ha postulado la teoría de que el RSA es un campo de ondas de carácter difusivo. Si bien, el concepto de campo difuso es de gran utilidad en la acústica, recientemente se ha comenzado a emplear en el campo de las ondas elásticas en sólidos. El concepto de un campo difuso corresponde a una descripción estadística de la respuesta elástica de los cuerpos finitos. Extendiendo este concepto a los sólidos, tenemos que las múltiples heterogeneidades de la litosfera terrestre provocan que los desplazamientos inducidos por un sismo o por fuentes antropogénicas no sean sencillos, pues esas heterogeneidades producen ondas reflejadas, refractadas y difractadas en diversas direcciones. Un campo difuso es una aproximación estadística para ondas acústicas y elásticas con base en tres hipótesis básicas (Murray, 1996): 1.- El campo de ondas aleatorias; las fases de las ondas son aleatorias, no llegan al mismo tiempo. 2.- Las ondas inciden de todas direcciones con igual intensidad, en otras palabras, el campo es acimutalmente isótropo. 3.-En un espacio abierto, la amplitud de las ondas es la misma en cualquier punto del dominio espacial; el campo es espacialmente homogéneo en escala local.

Weaver (1982), ha establecido dos definiciones de campo difuso. La primera señala que el estado mecánico de un medio en vibración es descrito en función de sus modos normales. En el caso de un campo difuso, se acepta que la energía está equitativamente distribuida en todos los modos y estados (diferentes tipos de ondas elásticas). Es decir, que cumplen el Principio de Equipartición de la energía. La segunda definición establece que, en cada punto del medio en vibración, el campo difuso puede ser representado como una superposición isótropa con distribución espacial aleatoria de ondas planas. El principio de Equipartición significa que la energía sísmica se distribuye en proporciones fijas entre todos los “estados” posibles (modos y/o tipos de ondas elásticas) en el campo de ondas. Una proporción de energía sísmica constante implica que la contribución relativa de ondas P y S se estabilice a un valor aproximado al cociente de energías sísmicas independiente de los detalles particulares de la difracción. Por lo tanto; La equipartición de energía sísmica es una condición necesaria para recuperar la Función de Green, que es la propiedad intrínseca de los sistemas elásticos, mediante correlaciones del campo elástico. En caso contrario; al no existir un régimen equiparticionado, la Función de Green no se recupera, pero las correlaciones pueden proporcionar resultados valiosos de significado físico, así como permitir la reconstrucción de arribos específicos (Shapiro *et al.,* 2000). Los estudios anteriores señalan que la definición de un campo difuso se basa en la equipartición de la energía, la cual se describe usualmente en términos de la polarización y dirección de las ondas. Sin embargo, existe otro punto de vista alternativo, el cual asocia igualdad de energías con los modos o estados de vibración.

La reconstrucción de la Función de Green (FG) se basa en dos descripciones diferentes. La primera consiste en promediar las correlaciones de señales generadas por un gran número de fuentes, las cuales son independientes entre sí, pero las fuentes deben estar distribuidas de manera homogénea a lo largo de un contorno cerrado. En este caso no se requiere que exista difracción; pero la existencia de difracción no le quita al campo de ondas su carácter difusivo. En la segunda descripción, la reconstrucción se realiza a partir de señales que son representativas de un campo difuso, donde aparece la difracción múltiple. Bajo esta hipótesis se supone que el campo de ondas resultante es equiparticionado, condición necesaria para la recuperación de la FG. La recuperación de la FG a partir del RSA considera que, el cociente espectral H/V (HVSR), es una propiedad intrínseca del medio y se relaciona con el cociente de los componentes del tensor de Green. Esta consideración puede proporcionar una visión física del fenómeno y explicar el éxito de estas técnicas y otras, por ejemplo, la técnica de Correlación Espacial (Spatial Autocorrelation, SPAC por sus siglas en ingles) y de la técnica de Correlación Cruzada (CC) entre par de estaciones.

El objetivo de este trabajo es determinar que el RSA es de carácter difusivo partiendo de la definición del Principio de Equipartición de energía para diferentes escenarios. Esto se lleva a cabo mediante experimentos controlados de mediciones de RSA en arreglos de sensores en una disposición geométrica en forma de “L”. El principal enfoque de determinar que el RSA es de carácter difusivo es el de validar y sustentar la aplicación de la técnica HVSR y otras técnicas de prospección de sísmica pasiva; incluso en escenarios con irregularidad geométrica como es el caso de la Pirámide del Sol en Teotihuacán; donde se utilizaron las técnicas de HVSR y CC para poder estimar un modelo 3D de velocidades de onda de corte (Vs) del interior de la estructura. Además, se relaciona el HVSR con otro tipo de observaciones como son las curvas de dispersión de las ondas superficiales de Rayleigh bajo el enfoque de difusividad.

Los resultados obtenidos durante mis estudios de doctorado son los siguientes: i) La elaboración de esta tesis. ii) Cinco artículos científicos; tres artículos como primer autor, uno como tercer autor y otro como quinto autor); iii) El desarrollo de una herramienta informática HV-Inv v2.5, el cual ha sido propuesto al Millennium Technology Prize of the Technology Academy Finland 2020 por parte del Instituto de Ingeniería, UNAM y iv) Dos nuevas líneas de investigación acerca del HVSR y del Principio de equipartición de la energía sísmica. El primer artículo trata sobre la generación local de ondas superficiales de Love en el borde de un valle aluvial que está formado por una capa blanda con interfaz de inmersión y fue publicado en el *Bulletin of the Seismological Society of America el* 19 de junio de 2018. El segundo artículo es sobre la caracterización de respuesta sísmica de la localidad de El Ejido en España obteniendo modelos de velocidad de ondas S a partir de la inversión conjunta de las curvas de dispersión de ondas de Rayleigh y el HVSR bajo el supuesto de campo difuso (DFA) y fue publicado en *Soil Dynamics and Earthquake Engineering* el 16 de marzo de 2019. El tercer artículo es sobre la identificación de las curvas de dispersión utilizando la curva HVSR bajo el enfoque de campos difusos y fue publicado en el *Journal of Applied Geophysics* el 14 de abril del 2020. El cuarto artículo es sobre la búsqueda de las propiedades difusivas del ruido sísmico ambiental, sometido en el

Bulletin of the Seismological Society of America el cual se ha realizado las correcciones propuestas por los revisores. El quinto artículo es sobre la obtención de las propiedades dinámicas de la estructura de la Pirámide del Sol (Teotihuacan, México) aplicando métodos de sísmica pasiva. El texto es sometido en la revista científica *Engineering Geology* el cual se ha realizado las correcciones propuestas por los revisores. Además, se concluyó la fase 1 del Proyecto HV-Inv, dando como resultado la herramienta informática HV-Inv® v2.5 (Registrado en INDAUTOR) y ha sido utilizado ampliamente alrededor del mundo con fines de investigación científicas e industriales. Por el momento, el proyecto HV-Inv está la fase 2 de soporte y mantenimiento. Además, el proyecto HV-Inv ha sido propuesto al Millennium Technology Prize of the Technology Academy Finland 2020. Por otro lado, la primera línea de investigación, resultado de este trabajo, es acerca del desarrollo y la aplicación de una nueva forma de procesar el RSA para obtener el HVSR. Actualmente, se ha desarrollado software *HVprocess* en su versión beta. La segunda línea de investigación es sobre la partición de la energía sísmica para los distintos tipos de onda en medios estratificados y su relación con las técnicas geofísicas de sísmica pasiva (SPAC, F-K, CC y HVSR) con el enfoque de que el RSA es de carácter difusivo.

Sección 1

Evidencia de la Equipartición de energía en el ruido sísmico ambiental

1.1.- Introducción

En los últimos años, el ruido sísmico ambiental (RSA) se ha utilizado ampliamente en la exploración geofísica. EL RSA es una combinación de contribuciones oceánicas, atmosféricas, sísmicas y humanas (ver, por ejemplo, Asten, 1978; Asten y Henstridge, 1984; Ardhuin *et al.*, 2011). Aunque las fuentes de ruido asociadas con diferentes bandas de frecuencia no se conocen con precisión, se ha encontrado que para baja frecuencia ($f < 0.3$ Hz), el RSA puede estar dominado por las interacciones del océano con la tierra sólida (Friederich *et al.*, 1998; Rhie y Romanowicz, 2004; Ardhuin *et al.*, 2011). Por otro lado, a una frecuencia más alta ($f > 0.3$ Hz), el RSA es producido localmente por la actividad humana y el viento. Debido a la atenuación en los materiales del subsuelo, este ruido de alta frecuencia no se puede propagar a grandes distancias. En cualquier caso, el RSA proviene de fuentes poco profundas que generan en gran medida ondas superficiales (Campillo, 2006).

Los primeros trabajos sistemáticos con el RSA a principios del siglo pasado se deben a Kanai (ver Kanai *et al.*, 1954). Más tarde, en un estudio pionero, Aki (1957) calculó la autocorrelación espacial (SPAC, por sus siglas en inglés) utilizando datos de RSA. Para la técnica de SPAC, el promedio azimutal del coeficiente de correlación del movimiento vertical permite evaluar la velocidad de fase de las ondas de superficie de Rayleigh y el tratamiento de componentes horizontales permite la recuperación de ondas de Love. En este enfoque, el autor aprovecha la iluminación natural del RSA. Además, se ha demostrado que con datos de RSA es posible obtener la parte más visible de la Función de Green (que es una propiedad intrínseca de los sistemas elásticos estratificados) mediante la correlación cruzada entre dos receptores. Algunos autores utilizaron la técnica de correlaciones cruzadas de largo alcance para aplicaciones prácticas en sismología (por ejemplo; Shapiro y Campillo 2004, Sabra *et al.,* 2005 y Shapiro *et al.,* 2005).

A partir de lo anterior, numerosos estudios en todo el mundo han usado esta técnica para recuperar las Funciones de Green Empíricas y extraer las curvas de dispersión de las ondas de superficie de Rayleigh y Love, que son ondas con velocidad de propagación en función de la frecuencia. Por ejemplo, existen varios mapas tomográficos regionales y locales de las velocidades de fase y grupo para diferentes partes del mundo. En estos mapas se correlacionan bien con la geología y la tectónica de la región y, en algunos casos, revelaron nuevas características. Mencionemos el trabajo de Shapiro y Campillo (2004); Shapiro *et al.* (2005) y Ritzwoller *et al.* (2011) para América del Norte, la investigación de Ward *et al.* (2013) en América del Sur, de Yang *et al.* (2007) para Europa, el estudio de Zheng *et al.* (2008) para Asia, Saygin y Kennett (2010) consideraron Nueva Zelanda y Australia, y Gudmundsson *et al.* (2007) trató con Nueva Zelanda y Australia.

Por otro lado, Sánchez-Sesma *et al.* (2011) establecieron la relación entre la relación espectral horizontal a vertical HVSR, propuesta por Nakamura (1989, 2000), y las partes imaginarias de la función de Green, varios estudios (Kawase *et al.*, 2011; 2015; Lontsi *et al.*, 2015, Spica *et al.*, 2015; 2017; García-Jerez *et al.*, 2016; Piña-Flores *et al.*, 2017; y Wu *et al.*, 2017) se han llevado a cabo para obtener velocidad perfiles en función de la profundidad a través de la inversión, incluso considerando la irregularidad lateral en profundidad (Matsushima *et al.,* 2014, 2017 y Perton *et al.,* 2018) consideraron la irregularidad lateral. La relevancia que tienen estos estudios puede explicarse la relación entre el HVSR observada con las partes imaginarias de la Funciones de Green. Esta relación implica la teoría de que el RSA es un campo difuso y, por lo tanto, puede considerarse como el subproducto de la iluminación isotrópica de ondas aleatorias.

Desde la perspectiva que el RSA es un campo de ondas difusivo, las fuentes del RSA son aleatorias y las ondas sísmicas generadas sufren difracciones múltiples debido a las heterogeneidades (Campillo, 2006). De acuerdo con Shapiro *et al.* (2000), el campo de ondas alcanza un régimen difusivo cuando la distribución de energía sísmica (fuentes primarias y secundarias) es casi isotrópica y la fase es aleatoria como resultado de la dispersión múltiple. Si el medio no tiene una irregularidad lateral significativa, las condiciones ideales de iluminación se pueden verificar en la realidad y, en presencia de irregularidades, esta isotropía del campo no es verificable; pero el campo de ondas aún puede ser difusivo. Un ejemplo de lo anterior lo podemos encontrar en los trabajos de Sánchez-Sesma *et al.* (2006) y Pérez-Ruiz *et al.* (2008) donde muestran que la iluminación uniforme en la frontera del sistema produce un campo difuso.

Según Weaver (1982, 1985), se pueden concebir dos definiciones simples de un régimen difusivo para comprender las características del RSA. La primera definición considera que un campo de ondas difusivo, a una frecuencia dada, es un estado de vibración para el cual los modos normales del sistema están en equilibrio estadístico. Es decir, la energía sísmica se distribuye entre todos los modos normales de acuerdo con el Principio de Equipartición de energía. Este principio establece que todos los modos, debidamente normalizados, contribuyen con la misma energía para construir la Función de Green. De hecho, algunas conexiones relevantes entre soluciones analíticas y deterministas surgen de la teoría de campo difuso (ver Sánchez-Sesma *et al.*, 2011, Pérez-Ruiz *et al.*, 2008; Perton y Sánchez-Sesma, 2016). La segunda definición afirma que, para cada punto del medio en vibración, un campo difuso se puede representar como una superposición isotrópica y aleatoria de ondas planas las cuales tiene una amplitud variable en función del tiempo y con una fase aleatoria (Shapiro *et al.*, 2000). Esta visión asume implícitamente la isotropía y descuida la irregularidad.

La Equipartición de energía es una propiedad física del campo de ondas que define el carácter difusivo. En los trabajos de Shapiro *et al.*, (2000) y Hennino *et al.*, (2001) se muestra la primera observación de la Equipartición de energía en registros sísmicos como el resultado de un experimento, cuidadosamente planificado, en el que se analizaron las codas de 13 terremotos registrados en un arreglo cuadrado de sensores muy pequeña (aproximadamente 50 m) en Guerrero (México). Estos autores determinaron que las energías sísmicas pueden separarse en términos del módulo del rotacional y la divergencia de campo obtenida numéricamente de las derivadas espaciales y concluyen que la estabilidad de la relación de la energía sísmica es un fuerte indicador de que el campo de onda tiene un régimen difusivo, en este caso para la coda sísmica. Además, Shapiro *et al.*, (2000) y Hennino *et al.*, (2001) señalaron la difracción múltiple en la coda de sismogramas registrados en Guerrero, México y, siguiendo a Aki y Chouet (1975), excluyeron la dispersión única como una explicación alternativa de la coda. En otro experimento para la observación de la Equipartición de energía, Margerin *et al.* (2009) estudian las energías potencial y cinética de las ondas de corte en las codas de diez terremotos registradas en el Observatorio Pinyon Flats, California. Estos autores demostraron una clara estabilización de la relación entre las energías de onda P y onda S en la coda sísmica con valores similares para los diez terremotos estudiados. Estos autores interpretaron estas observaciones como una clara firma de Equipartición de Energía. Por otro lado, las simulaciones de onda completas tanto en acústica (Wegler *et al.*, 2006) como en elasticidad dinámica (Papanicolaou *et al.*, 1996; Przybilla *et al.*, 2006) demostraron que, en un régimen difusivo, la relación de la energía de las ondas P y S se estabilizan a una constante.

Por otro lado, Mulargia (2012) desarrolló un procedimiento para establecer la aplicabilidad del paradigma de campo difuso al RSA. Su método se basa en la isotropía azimutal y la homogeneidad espacial y se aplicó a RSA registrado en 65 sitios que cubren una amplia variedad de condiciones ambientales. Con base en sus resultados, Mulargia afirma que el ruido sísmico no es difuso y que los argumentos físicos básicos sugieren que la teoría de campo difuso puede no ser aplicable al RSA. Sin embargo, señala que tal conclusión no tiene ningún efecto inhibidor práctico sobre la imagen pasiva pasando por alto los roles de la dispersión múltiple y la estabilización del campo hacia un estado que no necesariamente isotrópico.

Con el objetivo de observar la Equipartición de energía en el RSA, en este trabajo, muestro la estabilización de la relación de energía sísmica (EPS) $\frac{W_p}{W_s}$ del RSA registrado en diferentes sitios en México mediante arreglos de sensores, siguiendo los enfoques de Shapiro *et al.*, (2000), Hennino *et al.* (2001) y Margerin (2009). Estudie tres sitios: 1) En las instalaciones de la Facultad de Ingeniería de la UNAM (UNAM-SE) en el campus principal de la Universidad, al sur de la Ciudad de México, registrando datos de RSA durante dos horas en un arreglo de tres sensores en forma de "L". Para este sitio, la relación de energía en los registros de RSA es estable (con un valor promedio de 7.28 ± 0.88) para un tiempo de grabación prolongado. 2) En Zapopan, Jalisco, México, se registró datos de RSA durante tres horas en una serie de tres sensores en forma de L en el parque La Primavera. Además, se registró el terremoto M 7.1 del 19 de septiembre de 2017 (SSN, 2017). Para este sitio, se encontró que son estables las EPS para el pre-evento, el post-evento y el RSA (con un valor promedio de 7.1±0.5). Para este sitio en particular, se analizó la estabilidad del HVSR para tres estaciones en conjunto con la estabilización de la EPS en función del tiempo. 3) Se analizo la estabilización de la EPS de RSA en el pre-evento y la coda sísmica de uno de los registros de terremotos en Chilpancingo, Guerrero, México, estudiados por Shapiro *et al.* (2000) y Hennino *et al.* (2001). La comparación entre estos dos tipos de registros muestra que la EPS es estable, tanto en la RSA como en la coda sísmica. Con base en estos resultados, los sitios de estudio muestran una clara evidencia de que la Equipartición de energía sísmica está presente en los registros de RSA y, por definición, el RSA exhibe el carácter difuso.

1.2.- Teoría de la Equipartición de energía sísmica

Siguiendo a Shapiro *et al.* (2000), las energías de deformación por compresión y de corte son:

$$W_P = \frac{1}{2}\rho\alpha^2(\nabla\cdot\vec{u})^2 \tag{1.1}$$

$$W_S = \frac{1}{2}\rho\beta^2|\nabla\times\vec{u}|^2 \tag{1.2}$$

donde α, β y ρ denotan las velocidades de onda de compresión y de corte y la densidad de masa en el receptor y $\vec{u}$ es el vector de desplazamiento. La relación de las densidades de energía, W_p y W_s asociadas con la deformación en un medio sólido en la superficie está dada por:

$$\frac{W_s}{W_p} = \frac{\left(\frac{\mu}{2}\right)|\nabla\times\vec{u}|^2}{\left(\frac{\lambda}{2}+\mu\right)(\nabla\cdot\vec{u})^2} \tag{1.3}$$

donde λ and μ son las constantes de Lamé.

Para una serie de sismómetros instalados en la superficie libre de un semiespacio, esta relación de energía es una función de las derivadas con respecto al sistema de coordenadas cartesianas como:

$$\frac{W_s}{W_p} = \frac{1}{4}\left(\frac{\alpha}{\beta}\right)^2 \frac{4\left(\frac{\partial u_z}{\partial x}\right)^2 + 4\left(\frac{\partial u_z}{\partial y}\right)^2 + \left(\frac{\partial u_x}{\partial y} - \frac{\partial u_y}{\partial x}\right)^2}{\left(\frac{\partial u_x}{\partial x} + \frac{\partial u_y}{\partial y}\right)^2} \tag{1.4}$$

La ecuación (1.4) permite evaluar la EPS en la coda sísmica y en los registros de RSA. El RSA para un espacio completo en 3D, compuesto solo por ondas de cuerpo, Weaver (1982) obtuvo que la estabilización de energía de ondas sísmicas es proporcional a $2\left(\frac{\alpha}{\beta}\right)^3$; donde, para un sólido de Poisson, el valor de la estabilización de energía es de 10.4. Por otro lado, si el campo de ondas consiste solo de ondas superficiales, el valor de la estabilización de energía es cercana a 6.5 (Hennino *et al.*, 2001).

1.3.- Arreglo de sensores sísmicos en la facultad de ingeniería, en los campos deportivos (UNAM) y en "La primavera"

Para estimar las energías de deformación W_p y W_s en los datos de RSA, se desplegaron dos conjuntos de tres sensores Guralp 6TD en el patio de la Facultad de Ingeniería y en el Campo Deportivo (UNAM). En cada sitio, los sensores se instalaron en una matriz en forma de L con un espacio de 12 y 15m, respectivamente, medido desde la estación de vértice. La figura 1.1 muestra la configuración de los arreglos. La duración de los registros fue de aproximadamente dos horas y el tiempo absoluto se sincronizo con los GPS. Con este tipo de arreglo de sensores, podemos estimar las derivadas espaciales del campo de desplazamiento en dos direcciones horizontales linealmente independientes.

Los datos de RSA utilizados en el experimento La Primavera se obtuvieron de una disposición espacial con sensores Guralp 6TD ubicados en La Primavera en Zapopan, Jalisco, México. Los sensores se instalaron en un arreglo en forma de L con un espacio de 1,5 km. desde la estación de vértice (Ver figura 1.1). Durante el experimento, se registró el sísmo ocurrido del 19 de septiembre de 2017 con una magnitud de 7.1 con el epicentro ubicado en la frontera estatal entre los estados de Puebla y Morelos, a 12 km al sureste de Axochiapan, Morelos (SSN, 2017) teniendo una distancia epicentral de aproximadamente 500 km.

Antes de aplicar la ecuación (1.4) en los datos de RSA, se corrigió las señales por respuesta instrumental e integrando los registros de velocidad para obtener los desplazamientos. La orientación de los sensores en el arreglo se verificó en el momento de la instalación, por lo que no se requirió ningún procedimiento de rotación. Posteriormente, estimamos las derivadas espaciales de los desplazamientos en cada instante de tiempo a través de las siguientes ecuaciones:

$$\frac{\partial u_i}{\partial x} = \frac{u_i^2 - u_i^1}{d}; \frac{\partial u_i}{\partial y} = \frac{u_i^3 - u_i^2}{d}; \;\; i = x, y, z \tag{1.5}$$

Donde u_i^n son los desplazamientos en la dirección i en la estación n.

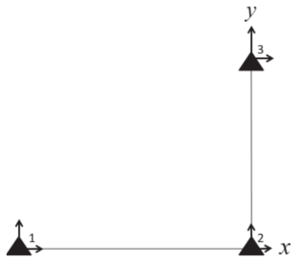

Figura 1.1.- Configuración de sensores en arreglo de L. Las flechas de los triángulos indican la orientación de cada sensor.

Shapiro *et al.* (2000) indican que la derivada estimada con el método de diferencias finitas difiere del valor exacto según la siguiente ecuación (Bodin *et al.*, 1997; Lomnitz, 1997):

$$\frac{\left[\frac{\partial u_i}{\partial x_j}\right]_{Arreglo}}{\left[\frac{\partial u_i}{\partial x_j}\right]_{exacto}} = \frac{\sin\left(\frac{\pi L}{\lambda}\right)}{\frac{\pi L}{\lambda}} \qquad (1.6)$$

donde L es la distancia entre los receptores y λ es la longitud de onda. Sí $\frac{L}{\lambda} \leq 0.1$ el error de cálculo de las derivadas es menor al 2%.

El rango de frecuencias de interés para estimar las derivadas de los desplazamientos, de acuerdo con la separación de las estaciones, está entre 2 y 4 Hz para el arreglo de la Facultad de Ingeniería y para el campo deportivo de 2.5 a 4.5 Hz. Mientras que para el arreglo La Primavera el rango de frecuencias se encuentra entre 0.25 a 0.45. Estos valores de frecuencias se obtuvieron aplicando la relación $f = \frac{Vs}{\lambda}$, donde *f* es el valor de la frecuencia, Vs es la velocidad de propagación de las ondas S y λ es la longitud de onda. Para obtener los valores de Vs y λ, usamos la misma disposición "L" (ver figura 1.1) para obtener la velocidad de fase de las ondas de Rayleigh usando la técnica de SPAC (Aki, 1957). Por ejemplo, suponiendo que el material tiene un coeficiente de Poisson de 0.25, podemos estimar la velocidad de las ondas S en función de la velocidad de fase Vs=VR/0.92=600 m/s. Para esta longitud de onda, consideramos de la ecuación (1.6) que L/λ debe ser menor que 0.1. En nuestro caso, elegimos un valor máximo de L/λ=0.07 y un valor mínimo de L/λ=0.05.

1.4.- Experimento Chilpancingo

Los datos de RSA utilizados en este estudio se recopilaron en un arreglo de sensores temporales ubicado en las cercanías de Chilpancingo, Guerrero (México) durante junio - agosto de 1997. El arreglo consta de cuatro estaciones instaladas en los vértices de un cuadrado con lados de 50 m. Durante el experimento, 13 eventos sísmicos fueron registrados y analizados por Shapiro *et al.*, 2000 y Hennino *et al.*, 2001. A partir de estos 13 eventos, solo el evento #12 tiene datos previos al evento principal con tiempo suficiente (es decir, RSA). Por esta razón solo se estudia este evento. Para el evento #12 se estimó las energías de deformación W_p y W_s siguiendo el mismo preprocesamiento y métodos descritos en Shapiro *et al.*, (2000).

1.5.- Resultados experimentales

Después de realizar el procesamiento de datos, se evalúo la EPS usando la ecuación (1.4). El cálculo de los valores promedios de la EPS para cada registro, se utilizaron diferentes ventanas de promedio móvil; estos anchos de ventana han sido seleccionados con base a valores cercanos del "*Mean Free Time*" (Margerin, 2001; Shapiro *et al.*, 2000). El Mean Free Time es un parámetro muy difícil de estimar con técnicas tradicionales basadas en estudios de atenuación porque los efectos de la absorción de energía y los de dispersión múltiple están relacionados entre sí (Larose *et al.*, 2004). En la práctica, se considera que el ancho de tiempo de la ventana promedio móvil, donde se alcanza la estabilización, es un estimador del parámetro Mean Free Time.

La figura 1.2 se muestran los resultados de la relación de EPS para los datos de RSA de Chilpancingo. La relación de EPS en los datos de la coda sísmica se estabiliza a niveles muy diferentes del RSA en el pre-evento. Sin embargo, la EPS del RSA en algunos instantes de tiempo (por ejemplo, 0 a 200s), muestra una estabilidad de energía con valores promedio de 7.47 ± 0.83, mientras que la coda se muestra estable con valores promedio de 7,29 ± 0,42. Las fluctuaciones presentes en los resultados, probablemente se deban al fenómeno de dispersión múltiple de las ondas en un medio aleatorio. Nótese que la EPS de RSA se estabiliza durante 55 segundos de ventana de promedio móvil y la EPS de la coda solo necesita 16 segundos. Además, se observa que la relación de energía Ws/Wp de RSA no exhibe fluctuaciones superiores al diez por ciento del valor promedio en la coda sísmica.

Los resultados de la EPS del arreglo de la Facultad de Ingeniería, exhibe una estabilización en algunos intervalos de tiempo con un valor promedio de 7.28 (por ejemplo, véase en el intervalo de 2,000-5,000s) con una ventana de promedio móvil de 35s. El valor de EPS en todos los datos de RSA muestra fluctuaciones de estabilización con valores entre 5 a 10 para diferentes tiempos en el evento. Los resultados para el arreglo de la Facultad de Ingeniería se muestran en la figura 1.3. La tabla 1.1 muestra los valores teóricos y observados de estabilización de las energías y valor de la ventana promedio móvil utilizado para la superficie libre de un semiespacio con $\lambda = \mu$.

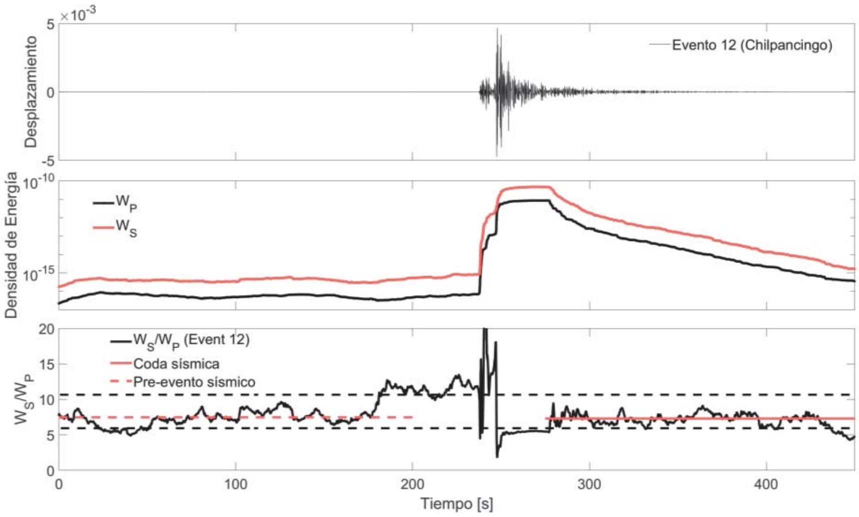

Figura 1.2.- Mediciones de la EPS para el arreglo de Chilpancingo. El panel superior muestra el registro del componente vertical filtrado entre 1 y 3 Hz. En el panel central, las energías *Wp* y *Ws* corresponden a una ventana de media móvil de 16 s para coda y de 55 s para ruido previo al evento. El panel inferior muestra la EPS

Los resultados de la relación de EPS del campo deportivo de la UNAM (figura 1.3) se estabilizan en un promedio de 2.9 ± 0.47 con una ventana promedio móvil de 45s. Este valor de estabilización está muy lejos del valor teórico esperado, que es de 7.19 para las ondas elásticas equiparticionadas en la superficie para un medio homogéneo Poissoniano. Sin embargo, Margerin *et al.* (2009) encontraron valores de EPS similares (EPS= 2.8) para 10 terremotos registrados en un arreglo denso de sensores, ubicada en el Observatorio Pinyon Flats (PFO), California. Para explicar estos valores de estabilización de la EPS, los autores desarrollaron la teoría de Equipartición de energía aplicado a un medio elástico estratificado sobre un semiespacio y utilizan una descomposición espectral rigurosa de la ecuación de onda elástica. Esta teoría extendida de la Equipartición predice que, cerca de la frecuencia de resonancia de una capa de baja velocidad, la relación de EPS disminuirá.

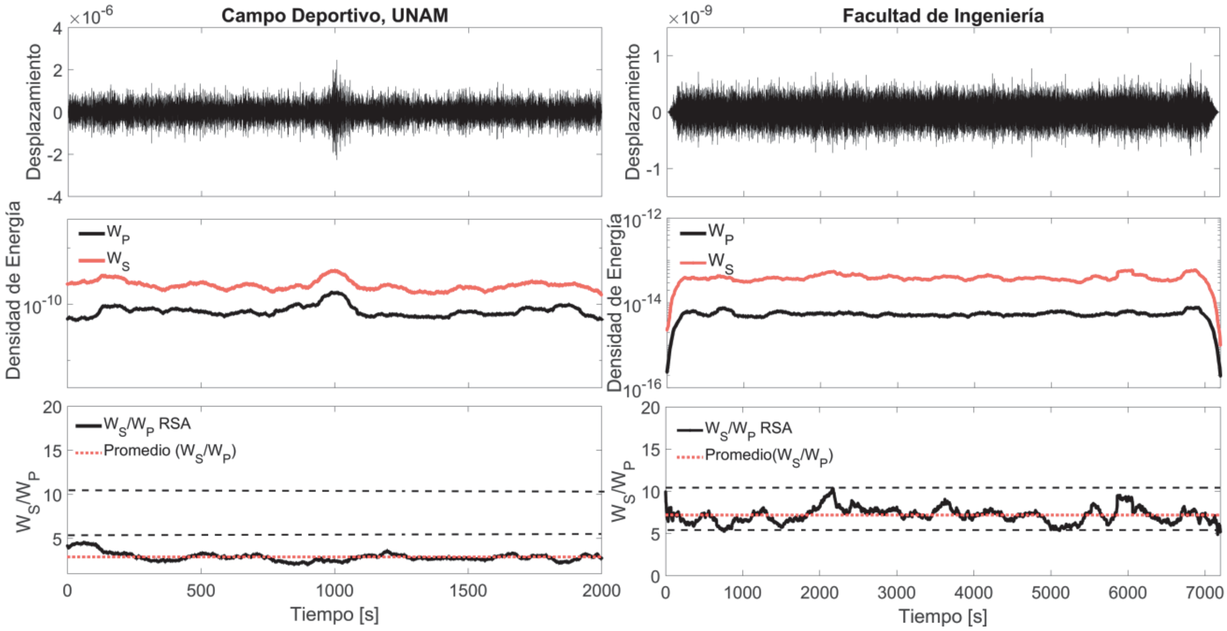

Figura 1.3.- Mediciones de la relación de energía Ws/Wp en el Campo Deportivo y de la Facultad de Ingeniería (UNAM). El panel superior izquierdo muestra el componente vertical, filtrado entre 2 y 4 Hz, registrado en la Facultad de Ingeniería. El panel izquierdo-medio muestra las energías Wp y Ws con una ventana de promedio móvil de 35s y el panel izquierdo-inferior muestra la relación de energía Ws/Wp. El panel superior derecho muestra el componente vertical, filtrado entre 2.5 y 4.5 Hz, registrado en el Campo Deportivo. En el panel intermedio-derecho, las energías Wp y Ws se muestran con una ventana de promedio móvil de 45s y en el panel izquierdo-inferior muestra la relación de energía Ws/Wp.

El experimento de La Primavera muestra que la relación de EPS para el RSA se estabiliza en un intervalo de tiempo prolongado con un valor promedio de 7.1 ± 0.5 (por ejemplo, vea el intervalo de 1.5 a 3 horas. Ver la figura 1.4 panel c), con una ventana promedio móvil de 150 seg. logrando alcanzar el régimen de partición (durante largos tiempos). Una ventana promedio móvil de larga duración indica la dimensión típica de la heterogeneidad está en el orden de su longitud de onda (Shapiro et al 2000). El valor de EPS en todo instante de tiempo del RSA muestra fluctuaciones en el rango de 6.5 a 10 diferente del RSA en el post-evento. El valor de EPS esperado para un campo de ondas puramente de Rayleigh es de 6.5 y el esperado para un campo de onda de cuerpo es de 10. En la figura 1.4 encontramos que, después del evento sísmico (0.3 a 0.5 hrs.), el valor de EPS no es estable y está por debajo del valor teórico esperado (<6.5). Posteriormente, el valor de EPS oscila entre los valores de 6 y 10 y, a medida que pasa el tiempo, tiende a estabilizarse en el valor de 7.1 ± 0.5.

Para explorar algunas consecuencias que genera la estabilización de la relación de energía EPS en la técnica de los cocientes espectrales H/V (HVSR, por sus siglas en ingles), se calculó la curva HVSR para los tres sensores utilizando una ventana de 150 segundos (en orden de la ventana promedio móvil) con una superposición del 99% para obtener los HVSR en función del tiempo. En la figura 1.4 (paneles d, e, f) los HVSR en función del tiempo se observan que las curvas promedio se encuentran en un rango de frecuencia entre 0.2-20 Hz. Con estos resultados, se observa que, durante el pre-evento sísmico, los HVSR son estables en su forma y amplitud (0-0.1 h). Cuando comienza el evento sísmico, los HVSR son inestables y no alcanzan la amplitud promedio para los primeros arribos. Después de los primeros arribos, hay un intervalo de tiempo (ondas superficiales) donde las amplitudes se estabilizan. Por otro lado, en el intervalo de tiempo de 0.2-0.4 hrs encontramos que los HVSR no son estables y su forma no emerge con respecto al pre-evento y el tiempo de las mediciones de RSA. Por el contrario, cuando se presentan la coda sísmica y el RSA, las relaciones espectrales HVSR emergen gradualmente tanto en forma como en amplitud hasta que alcanza su estabilización promedio.

Tabla 1.1 Comparación entre los valores de estabilización de la EPS de los datos y los valores teóricos en la superficie libre Z = 0.

	Relación de energía $\frac{W_s}{W_p}$	**Teoría(Z=0)**	**Mean Free Time**
Coda Sísmica	7.29±0.42	7.19	16 seg
Ruido Pre-evento	7.47±0.83	7.19	55 seg
Facultad de Ingeniería	7.28±0.88	7.19	32 seg
Campo deportivo	2.9±0.47	7.19	45 seg
La Primavera	7.1±0.5	7.19	150 seg

Con base en los resultados de la relación de EPS, se demuestra que existe una relación entre la estabilización de la relación de EPS con el HVSR. Es decir, que si la energía EPS no se estabiliza en los valores teóricos esperados (entre valores de 6 y 10), el HVSR no recupera su amplitud y forma promedio, este comportamiento se observa en la figura 1.4 para el intervalo de tiempo entre 0.2 a 0.4 hrs. Por otro lado, cuando la EPS muestra oscilaciones de estabilización, esta oscilación se refleja en la amplitud del HVSR, es decir, mientras que la EPS excede el valor promedio, la amplitud del HVSR aumenta y viceversa. Un ejemplo de este comportamiento se observa para los intervalos de tiempo de 0.8-1 hrs y 1.3-1.4 hrs (Ver figura 1.4). Así, los resultados del experimento de La Primavera indican que, si no se obtiene la Equipartición de energía en los datos de RSA o de un evento sísmico, no es posible recuperar la forma y amplitud de la relación espectral HVSR y, en consecuencia, la función de Green no se puede recuperar.

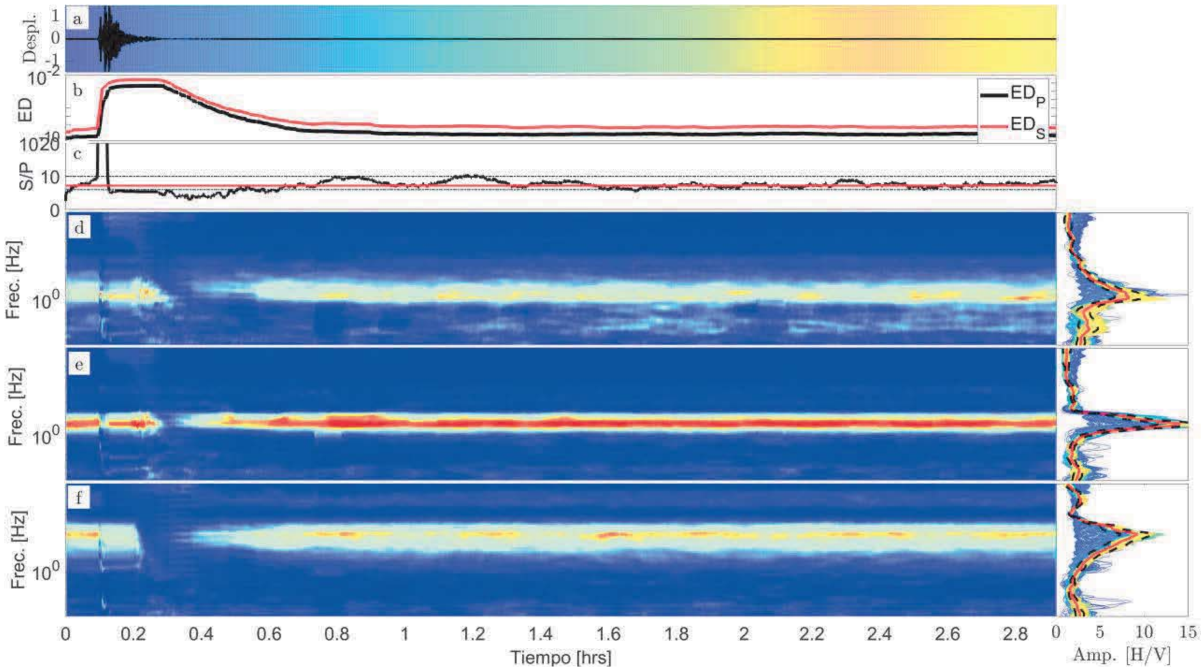

Figura 1.4.- Mediciones de la relación de EPS en La Primavera. El panel a) muestra los datos del componente vertical filtrado entre 0.2 y 0.4 Hz. El panel b) muestra las energías Wp y Ws con una ventana de media móvil de 150s y el panel c) muestra la relación de EPS. Los paneles d, e y f muestran la evolución del HVSR en función del tiempo.

Además, en las observaciones de la estabilización de energía, se considera que las fluctuaciones presentes en la relación de energía Ws/Wp, para los datos de La Primavera, se deben al hecho de que el RSA contiene todo tipo de ondas (ondas superficiales y de cuerpo) con fase aleatoria y amplitud diferente en contraste con la interpretación de la estabilización energética de la coda sísmica, el cual es un proceso genuino de dispersión múltiple y difracción (Hennino *et al.*, 2001). Por lo tanto, el RSA puede interpretarse, basándose en la clara estabilización de la EPS, como un régimen difusivo. En resumen, las observaciones de la relación de energía de cizallamiento y dilatación para el RSA son estables durante un largo intervalo de tiempo. El equilibrio entre los diferentes modos de vibración ocurre más rápido en la coda sísmica en comparación con el RSA, por lo que se necesita un tiempo más corto para que la coda sísmica se estabilice mientras que el RSA le toma 3.5 veces más de tiempo. La estabilización de la energía en el pre-evento y en el RSA es un fuerte indicador de que el campo de ondas ha alcanzado el régimen de difusión. Además, Margerin y Campillo (2000) señalaron que la evolución temporal de la relación de energía Ws/Wp podría usarse como un indicador de los diferentes mecanismos de dispersión. La figura 1.5 muestra la estabilización de la relación de energía Ws/Wp para los diferentes arreglos frente a τ (Mean Free Time).

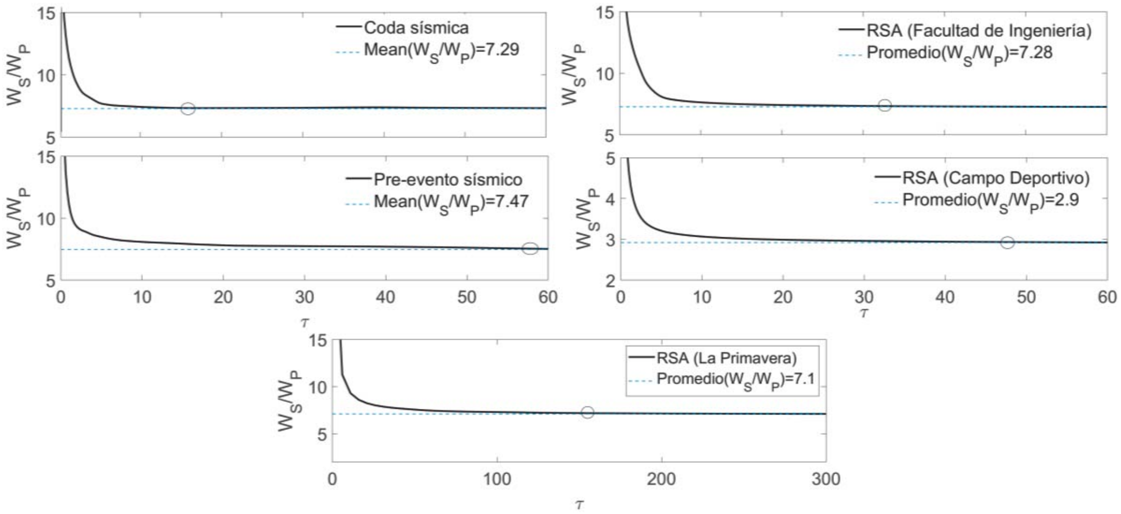

Figura 1.5.- Mediciones de la relación de energía Ws/Wp versus Mean Free Time. Las líneas continuas representan la relación media de EPS. La línea discontinua representa la estabilización asintótica de la relación de EPS. Los círculos abiertos marcan dónde se alcanza el nivel asintótico de EPS. El panel superior muestra la relación de EPS para la onda coda, que requiere 16s de Mean Free Time. El segundo panel muestra que la estabilización de la EPS para el ruido previo al evento necesitaba 55s. El tercer panel muestra la estabilización de EPS para RSA en la Facultad de Ingeniería con 32s de Mean Free Time. El cuarto panel muestra la relación de energía de estabilización EPS para RSA en el campo deportivo con 45s de Mean Free Time. El panel inferior muestra la relación de energía de estabilización EPS para RSA en los 150s Mena Free Time requeridos por el campo La Primavera.

1.6.- Conclusiones

A partir de la definición de la Equipartición de energía y de la relación de EPS, estudiamos la estabilización de las energías transportadas por el ruido sísmico ambiental (RSA) en diferentes ambientes geológicos:

Tabla 1.2 Descripción de ambientes geológicos para los diferentes experimentos

Experimento	**Ambiente geológico**
Chilpancingo (Guerrero, México)	Suelo firme caracterizado por rocas intrusivas de composición granitica-granodioritica.
Facultad de Ingeniería de la UNAM	Suelo firme que se caracteriza por la presencia de basalto meteorizado con un grado alto de fracturamiento
Campo deportivo de la UNAM	Suelo blando que se caracteriza por la presencia de material blando sobre basalto degradado a unos cuantos metros de profundidad (~3m).
La Primavera	Suelo firme que se caracteriza por intercalaciones de lava y material piroclástico de composición andesítica-basáltica dentro del Cinturón NeoVolcánico Transverso Mexicano.

En los cuatro experimentos de RSA, aplicamos el procedimiento descrito por Shapiro *et al.* (2000) con el objetivo de separar las energías sísmicas del RSA y seguir su evolución temporal. Los experimentos de la Facultad de Ingeniería de la UNAM y La Primavera muestran que la relación de EPS se mantiene estable durante largos lapsos de tiempo. Sin embargo, ocasionalmente exhibe fluctuaciones entre los valores teóricos esperados para las ondas de cuerpo (Ws/Wp=10) y para las ondas de Rayleigh (Ws/Wp=6.4). Los resultados para el campo deportivo de la UNAM muestran que la relación de energía Ws/Wp se estabiliza en un promedio de 2.9 ± 0.47. Este promedio está muy lejos del valor teórico esperado que es alrededor de 7.19 para ondas elásticas equiparticionadas en la superficie para un semiespacio Poissoniano y homogéneo.

Los resultados del arreglo de Chilpancingo, exhibe que el pre-evento sísmico se estabiliza para valores de ventanas diferentes a los de la coda sísmica mientras que la relación de energía EPS, para la coda sísmica, es 7.29±0.42 y para el RSA del pre-evento se estabiliza en valores de 7.47±0.83. Además, la EPS en la coda se alcanza rápidamente la estabilización, después de una ventana promedio móvil de pocos segundos. Es decir, el RSA necesita ventanas 3.5 veces más grandes que la coda sísmica para alcanzar su estabilización de energías. Todas estas observaciones permiten definir que: La estabilización de las energías en el pre-evento y en el RSA es un fuerte indicador de que el campo de onda ha alcanzado el régimen de difusión. Esto significa que el RSA es difuso en función de la ventana promedio móvil que se utilice para exhibir el equilibrio y propiedades difusas. Finalmente, en contraste con lo mencionado con Mulargia (2012) de que el RSA no es difuso, en este trabajo se concluye que RSA, generalmente, exhibe propiedades difusas mediante la observación de la estabilización de energía sísmica.

Sección 2

Diagramas de dispersión y el cociente espectral HVSR para un medio estratificado

2.1.- Introducción

En las últimas dos décadas, el ruido sísmico ambiental se ha utilizado ampliamente en trabajos de geofísica para obtener diagramas de dispersión de onda de Rayleigh. El objetivo principal de estos trabajos es obtener perfiles de velocidad de onda S y evaluar los efectos del sitio (ver Xia *et al.*, 1999; Bonnefoy-Claudet *et al.*, 2006; Foti *et al.*, 2011). Existen diferentes métodos geofísicos que permiten la recuperación de curvas de dispersión utilizando señales de ruido sísmico ambiental, entre los cuales los más importantes son: 1.- Autocorrelación espacial (SPAC, por sus siglas en inglés) (Aki, 1957; Köhler *et al.*, 2007; García-Jerez *et al.*, 2008;). 2.- Análisis de Frecuencia-Número de onda (F-K, por sus siglas en inglés) (Capón 1969; Ohori *et al.*, 2002). 3. Análisis multicanal de ondas superficiales (MASW, por sus siglas en inglés) (Dai *et al.* 2019, Coelho *et al.* 2018, Mi *et al.* 2017) 3.- Refracción de Microtremores (ReMi, por sus siglas en inglés) (Louie, 2001).

La selección de curvas de dispersión en las imágenes de frecuencia-velocidad o diagramas equivalentes generalmente se realiza manualmente, identificando bandas de alta energía con segmentos de curvas de dispersión de un modo particular. Por lo tanto, se pueden cometer errores de interpretación con probabilidad considerable. En métodos como el SPAC o en configuraciones de arreglos de sensores limitados, se puede seleccionar una curva de dispersión de velocidad llamado *curva de dispersión efectiva*, el cual es una combinación del modo fundamental con modos superiores de onda de Rayleigh (Tokimatsu *et al.*, 1992; Shuangxi, 2009). La transición entre diferentes modos puede incluso contener ondas de superficie con fugas que no pueden interpretarse en términos de modos de onda normal de Rayleigh (Gao *et al.*, 2014, García-Jerez y Sánchez-Sesma, 2015). Cuando el medio de propagación tiene un contraste de alta impedancia o zonas de baja velocidad, la curva de dispersión de velocidad de fase a menudo muestra protuberancias debidas a *efectos de osculación,* el cual consiste en que el modo fundamental está demasiado cerca de los modos superiores*,* y/o contribuciones significativas de modos superiores llamado *efecto multimodo* (Tokimatsu *et al.*, 1992; Ikeda *et al.*, 2012; Pan *et al.*, 2013; Gao *et al.*, 2016). Estos efectos multimodales pueden incluso deberse a la contribución direccional de las fuentes de ruido (Ma *et al.*, 2016) o a la presencia de topografía de la superficie que puede influir fuertemente en la distribución de energía en una imagen de dispersión a alta frecuencia (Zeng *et al.*, 2012, Ning *et al.*, 2018).

Cuando se trabaja con un número limitado de estaciones, la falta de resolución en el diagrama de dispersión puede dificultar la separación de los diferentes modos (por ejemplo, Lin *et al.*, 2017), particularmente cuando hay efectos de osculación. La identificación incorrecta de los modos generalmente conducirá a una sobreestimación de las velocidades de la onda S y errores en las profundidades durante la inversión (Zhang y Chang 2009; Gao *et al.*, 2016). La separación de los modos de las curvas de dispersión que funcionan en velocidades de grupo se vuelve aún más complicada debido a la existencia de cruces de modo a diferentes frecuencias (ver Baena-Rivera *et al.*, 2016). Sin embargo, cuando se realiza una identificación correcta de los modos, la contribución de los modos superiores permite explotar más información, la profundidad del levantamiento aumenta y la resolución del modelo mejora (Maraschini *et al.*, 2010).

Diferentes estudios han tratado de mitigar el problema de la identificación del modo predominante en un diagrama de dispersión. Tokimatsu *et al.* (1992) discutieron los efectos del efecto multimodo en las curvas de dispersión de onda de Rayleigh para reducir la no unicidad de los perfiles de velocidad de onda de corte (Vs), proponiendo la definición de curvas de dispersión efectivas que aparecen como una combinación de curvas modales. Lunedei y Albarello (2009) encontraron una relación entre las curvas de dispersión efectivas en función de las curvas de dispersión de velocidad de fase modal. La ecuación que proponen estos autores ha sido utilizada para obtener perfiles de velocidad con curvas de dispersión efectivas por Farrugia *et al.*, (2016). Además, Lai *et al.* (2014) y Astaneh & Guddati (2016) presentaron derivaciones matemáticas explícitas para diferentes definiciones de la velocidad de fase efectiva de las ondas de Rayleigh en un medio isotrópico elástico horizontalmente en capas basado en derivados analíticos. Estas fórmulas pueden conducir al desarrollo de una nueva clase de algoritmos de inversión capaces de tener en cuenta la influencia de todos los modos de propagación de ondas de superficie.

Las relaciones de amplitud y el análisis del movimiento de partículas pueden ayudar en la separación de modos. Rivet *et al.* (2015) propusieron utilizar el cociente espectral Horizontal y Vertical (HVSR, por sus siglas en ingles) para la identificación de modos superiores. Estos autores invirtieron independientemente las curvas de dispersión suponiendo que correspondían a: (1) el modo fundamental y (2) el primer modo superior. Posteriormente calcularon el HVSR teórico para los modelos obtenidos y los compararon con HVSR observada, lo que permitió la identificación del modo de excitación. Ma *et al.* (2016) utilizaron el enfoque propuesto por Tokimatsu *et al.* (1996) para distinguir la excitación del modo fundamental de los modos superiores, observando el movimiento de partículas para las ondas de Rayleigh en un rango de período de 1-10 seg. La frecuencia de corte del primer modo está controlada por la profundidad del basamento y coincide con la rápida disminución de la relación espectral HVSR del modo fundamental (elipticidad).

Recientemente, Maranò *et al.* (2017) lograron recuperar la elipticidad de las ondas de Rayleigh a partir de registros de ruido sísmico ambiental. Indicaron que el ángulo de fase de la elipticidad puede ser información valiosa para la separación de modos. El ángulo de elipticidad permite encontrar con precisión la frecuencia de sus singularidades, que a su vez corresponden a un cambio en la dirección del movimiento de las partículas del medio de retrógrado a retrógrado o viceversa. Boué *et al.* (2016) también utilizaron el análisis del movimiento de partículas en la correlación cruzada entre pares de estaciones para distinguir entre curvas de dispersión fundamentales y de modo más alto considerando estas diferencias en las direcciones de movimiento. Finalmente, Maraschini *et al.* (2010) propusieron un método para invertir los datos de las ondas superficiales en el que la función de desajuste es una norma del determinante de la matriz de Thomson-Haskell evaluada en los puntos de datos de dispersión experimental. La principal ventaja del método está dada por la posibilidad de tener en cuenta varios modos simultáneamente, sin especificar a qué modos pertenecen.

Por otro lado, HVSR es el método más simple y frecuente para obtener la frecuencia dominante del sitio a partir del procesamiento del ruido sísmico ambiental (RSA) registrado por una sola estación (Nakamura 1989; Lermo y Chávez-García 1993) los cuales han realizado estudios para descubrir la conexión entre esta curva observable y la distribución vertical de las propiedades elásticas (Arai y Tokimatsu 2004; Kawase *et al.*, 2011). Recientemente, la hipótesis que propone que el RSA es de carácter difusivo, ha sido abordado con buenos resultados al obtener las propiedades dinámicas del subsuelo invirtiendo el HVSR (Sánchez-Sesma *et al.*, 2011; Spica *et al.*, 2015; Lontsi *et al.*, 2015). Además, se ha extendido la inversión del HVSR bajo el esquema de inversión conjunta del HVSR y las curvas de dispersión de modos fundamentales y/o superiores. Este esquema ha resultado ser robusto y relativamente simple y mitiga los problemas de no unicidad del modelo obtenido (por ejemplo, Piña-Flores *et al.*, 2017; Sivaram *et al.*, 2018; García-Jerez *et al.*, 2019).

En este trabajo, exploro la relación entre las formas de las curvas de dispersión de las ondas de Rayleigh y el HVSR calculado bajo el enfoque de campos difusos (DFA). Utilizando dos modelos simples con parámetros variables, muestro que la forma del HVSR observada permite identificar las curvas de dispersión de las ondas de Rayleigh en modo fundamental evitando la contaminación de modos superiores. Además, presento una aplicación para mediciones de un arreglo de estaciones en el delta del río Andarax (Almería, España). Los datos de RSA registrados por arreglos pentagonales se analizaron utilizando el método de SPAC, el método F-K y las correlaciones cruzadas entre pares de receptores (CC). Además, Se puede aprovechar las características de la forma del HVSR para elegir curvas confiables de dispersión de fase y grupo de ondas de Rayleigh en modo fundamental. Una inversión conjunta de estas curvas, bajo el supuesto de campo difuso, condujo a perfiles de velocidades de Vs y Vp mejorados para este sitio. Finalmente, los cálculos directos muestran que parte de la información en los diagramas de dispersión de correlación cruzada y SPAC, F-K corresponde a modos superiores.

2.2.- Cociente espectral HVSR bajo la teoría de campos difusos

Se ha establecido que el HVSR está definido como la raíz cuadrada del cociente entre las densidades espectrales de potencia horizontal y vertical bajo la teoría de campos difusos (DFA por sus siglas en ingles). El HVSR puede expresarse en términos de las partes imaginarias de las funciones de Green en el dominio de la frecuencia cuando fuente y receptor son coincidentes (Sánchez-Sesma *et al.*, 2011). En particular, el HVSR puede expresarse en términos de la parte imaginaria de los componentes de la función de Green como:

$$\mathrm{HVSR}(x,\omega) = \sqrt{\frac{\mathrm{Im}[G_{11}(x,x;\omega)] + \mathrm{Im}[G_{22}(x,x;\omega)]}{\mathrm{Im}[G_{33}(x,x;\omega)]}}. \tag{2.1}$$

La ecuación (2.1) muestra la forma de calcular la HVSR con la hipótesis de que el RSA es un campo difuso. En esta expresión, los componentes de la función de Green están asociados con la geometría y las propiedades elastodinámicas del suelo. Para fines de este trabajo, se considera un medio estratificado con interfaces horizontales ilimitadas sobre un semiespacio. La superficie superior es una superficie libre y se supone que los medios son homogéneos, isotrópicos y elásticos, con velocidades de ondas P y S, densidades de masa ρ y espesores h. En García-Jerez *et al.*, (2016) se describen más detalles sobre el cálculo eficiente de HVSR.

2.3.- Relación entre la curva de dispersión y la relación espectral HVSR

Para mostrar la relación entre el comportamiento de las curvas de dispersión de onda de Rayleigh y el HVSR, se han examinado dos modelos de ejemplo enumerados en la tabla 2.1. El modelo 1 consiste en una capa sobre un semiespacio más rígido, mientras que dos capas con dos contrastes de impedancia significativos se consideran para el modelo 2. Las velocidades aumentan en profundidad y los contrastes de impedancia entre las capas son suficientes para ejemplificar el efecto de osculación entre el modo fundamental y el primero modo superior.

Tabla 2.1. Modelos de ejemplo utilizados en este trabajo.

h (m)	Vp(m/s)	Vs(m/s)	Densidad(kg/m^3)
Modelo 1			
25	663	200	1700
∞	866	500	2200
Modelo 2			
15	2000	380	1600
350	2300	850	1800
∞	3500	2000	2500

En la figura 2.1 se muestran las curvas de dispersión de ondas de Rayleigh para el modelo 1 del modo fundamental y los primeros dos modos superiores para las velocidades de fase y de grupo en conjunto con el HVSR teórico calculado a partir del concepto de DFA. Se pueden identificar dos frecuencias características en los HVSR. La primera frecuencia corresponde al pico principal (aproximadamente coincidente con la frecuencia de resonancia fundamental de las ondas S) y la segunda corresponde al mínimo absoluto (cercano a la frecuencia de resonancia fundamental de las ondas P, ver Piña-Flores *et al.*, 2017). Estas dos frecuencias y, en particular, la frecuencia del máximo es de interés en estudios geotécnicos. Por otro lado, podemos identificar las frecuencias de los puntos de inflexión en las curvas de dispersión de velocidad de fase, f_{Inf}, y las frecuencias f_{crit} de los puntos críticos para las curvas de velocidad de grupo, es decir:

$$\frac{d^2c(f_{Inf})}{df^2} = 0\,; \frac{dU(f_{crit})}{df} = 0. \qquad (2.2)$$

Se puede establecer una primera relación entre las curvas de dispersión de velocidad de fase y la forma de la del HVSR teniendo en cuenta la frecuencia del primer mínimo espectral del HVSR. La frecuencia del primer mínimo del HVSR es cercana a la frecuencia del punto de inflexión de la curva de dispersión de modo fundamental. Este mismo patrón se puede observar para el primer modo superior, donde la frecuencia del punto de inflexión está cerca de la frecuencia de amplitud mínima de la primera oscilación del HVSR. Otra característica de las curvas de dispersión de velocidad de fase son las zonas de osculación entre modos. Este efecto de osculación, entre el modo fundamental y el primer modo superior, está presente entre las frecuencias del pico principal y el primer mínimo del HVSR.

Por otro lado, la relación entre el HVSR y la curva de dispersión de velocidad del grupo es evidente. La frecuencia del mínimo en la relación espectral HVSR es coincidente a la frecuencia del punto crítico de la curva de dispersión, incluso con un mayor grado de proximidad en comparación con el punto de inflexión. Además, la frecuencia del primer cruce entre el modo fundamental y el primer modo más alto en la velocidad del grupo está entre el pico principal y el primer mínimo del HVSR. Nótese, que existe también un punto crítico de la curva de dispersión para el 1er modo superior en el rango de frecuencia analizada.

La figura 2.2 muestra el cálculo del modo fundamental y el primer modo superior para la velocidad de fase y grupo de las ondas de Rayleigh junto con el HVSR para el modelo 2. Para este modelo, el HVSR muestra dos picos prominentes y dos valles. De la misma manera que en el ejemplo anterior, podemos observar el comportamiento mencionado de las curvas de dispersión entre las frecuencias del máximo y el mínimo para los dos pares de pico. Es decir, las frecuencias donde el HVSR presenta estos mínimos corresponden aproximadamente a las ubicaciones de los puntos de inflexión en la curva de velocidad de fase y de los puntos críticos en la curva de velocidad de grupo correspondientes al modo fundamental.

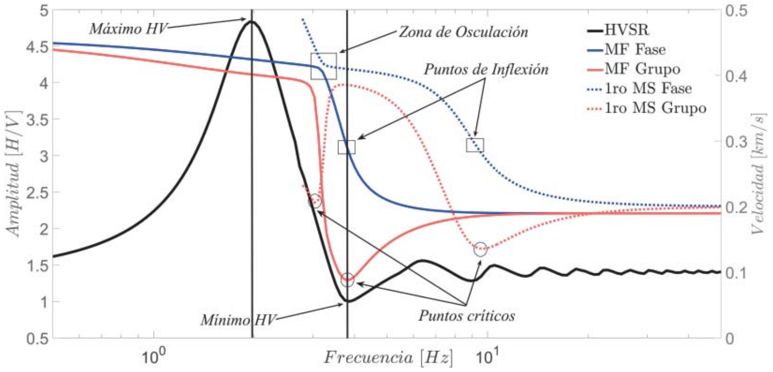

Figura 2.1: Relación espectral HVSR (línea negra continua) y curvas de dispersión de las ondas de Rayleigh para la velocidad del grupo (líneas rojas) y la velocidad de fase (líneas azules) calculadas para el modelo 1. Los círculos pequeños apuntan a los puntos críticos de las curvas de velocidad del grupo mientras que los cuadrados pequeños muestran los puntos de inflexión de las curvas de velocidad de fase. La frecuencia del punto de inflexión en c (f) y el punto crítico en U (f), para el modo fundamental, están muy cerca del mínimo de la relación HVSR. Las frecuencias donde existen posibles efectos de osculación están entre el primer máximo y mínimo de la relación HVSR.

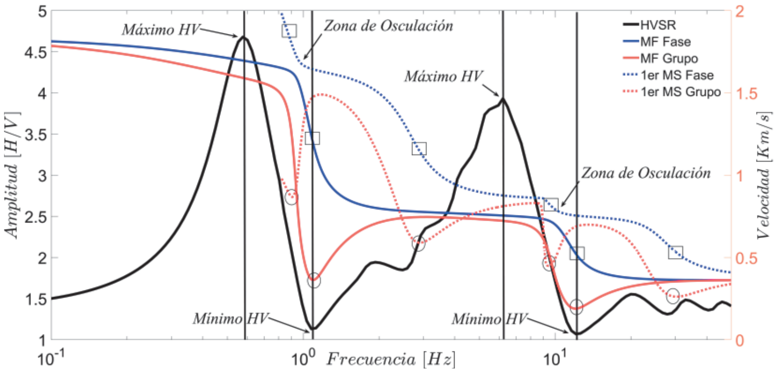

Figura 2.2: Relación espectral HVSR (línea negra) y curvas de dispersión de las ondas de Rayleigh para velocidad de grupo (líneas rojas) y velocidad de fase (líneas azules) calculadas para el modelo 2. Los círculos apuntan a los puntos críticos de las curvas de velocidad de grupo mientras los cuadrados muestran los puntos de inflexión para las curvas de velocidad de fase. Las frecuencias de los puntos de inflexión y los puntos críticos del modo fundamental están al lado de los canales de la relación HVSR. Los posibles efectos de osculación aparecen entre las frecuencias del máximo y el mínimo de la relación HVSR.

Los efectos de osculación para las curvas de dispersión de velocidad de fase están presentes entre las frecuencias del máximo y el mínimo del HVSR. Con respecto a las curvas de dispersión de velocidad de grupo, el efecto de osculación pasa a ser un efecto de cruces de multimodos. Es decir, que hay varios cruces de los modos superiores con el modo fundamental a diferentes frecuencias, lo que dificulta ver una relación visual de la curva de dispersión del modo fundamental con la forma del HVSR. Sin embargo, podemos identificar que estos cruces entre los modos fundamentales y los primeros modos superiores de velocidad de grupo aparecen entre el máximo y el mínimo de la relación HVSR.

2.4.- Aplicación a datos experimentales en la desembocadura del río Andarax (Almería, España)

La identificación de la curva de dispersión del modo fundamental de las ondas de Rayleigh (velocidades de fase y grupo) y la obtención de un perfil de velocidad representativo se llevó a cabo para el delta del río Andarax (SE España). Se registraron datos de ruido sísmico ambiental utilizando cinco sensores en cinco arreglos pentagonales concéntricos Las configuraciones de los arreglos cuentan con radios de 12, 25, 50, 94 y 420 m en los sitios indicados en la figura 2.3. Los diagramas de dispersión de velocidad de fase de onda de Rayleigh son obtenidos mediante las técnicas SPAC y F-K utilizando el software Geopsy (http: // www. geopsy.org/, último acceso en febrero de 2017). Las ventanas de tiempo utilizadas para el procesamiento variaron de 40 a 120 seg de largo con una superposición del 50% entre ventanas consecutivas. Los diagramas de dispersión de velocidad de grupo de onda de Rayleigh son obtenidos a partir de las correlaciones cruzadas entre pares de receptores haciendo uso del análisis de frecuencia-tiempo FTAN (Benzen *et al.,* 2007). El cálculo del HVSR se realizó el procesamiento estándar (Geopsy) utilizando 2 horas de registros de RSA.

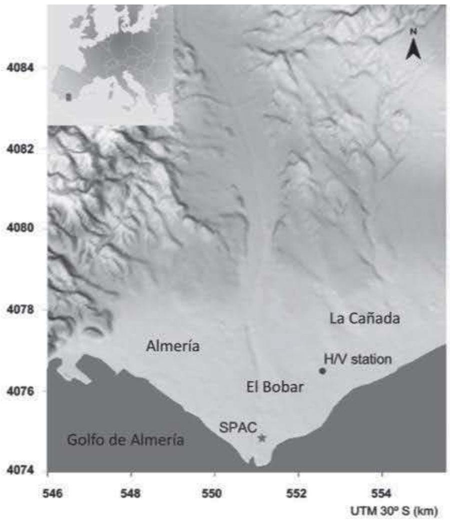

Figura 2.3: Ubicación de las mediciones de RSA para obtener el HVSR (circulo) y la curva de dispersión utilizando la técnica de SPAC (estrella) (coordenadas UTM).

La figura 2.4 muestra los diagramas de dispersión obtenidos y el HVSR para el área de estudio. A partir del diagrama de dispersión derivado de la técnica SPAC (figura 2.4a) es posible observar una discontinuidad o un salto de energía del modo fundamental al modo superior en el rango de 0.6 a 0.8 Hz. En el rango entre 0,8 y 2 Hz, la curva de dispersión del modo fundamental emerge claramente. En la banda de frecuencia entre 1,72 y 4 Hz, la velocidad de fase parece aumentar a medida que aumenta la frecuencia. Este tipo de fenómeno puede ocurrir en casos donde: a) El medio tiene una zona de baja velocidad (LVZ). b) Los modos superiores están presentes (Tokimatsu *et al.*, 2009). Sin embargo, la existencia de un LVZ puede descartarse porque la amplitud del HVSR no es menor que la unidad en todo el rango de frecuencias de observación (Castellaro y Mulargia, 2006) y, por lo tanto, asociamos este efecto a el efecto multimodal. Finalmente, en el rango de 4 a 8 Hz, el diagrama de dispersión muestra una parte de la curva de dispersión de modo fundamental con una contaminación severa por modos superiores que dificulta la identificación y selección del modo fundamental.

Desde otra perspectiva, el diagrama de dispersión obtenido de la técnica FK (figura 2.4b) muestra claramente la curva de dispersión en modo fundamental en el rango de frecuencia de 4 a 10 Hz (donde su identificación con la técnica SPAC no es clara). En la banda de frecuencia de 2.7 a 4 Hz, un crecimiento continuo de las velocidades de fase para frecuencias decrecientes puede asociarse a la presencia de modos superiores, como es el caso del diagrama de dispersión derivado de SPAC. En la banda entre 0,5 y 1 Hz, este método proporcionó una resolución pobre y la tendencia de la curva de dispersión no está clara.

En el diagrama de dispersión, obtenido de la técnica de correlación cruzada, es posible observar la curva de dispersión de velocidad de grupo en el rango de frecuencia entre 0.7 y 7 Hz. (figura 2.4c). En este caso, el amplio rango de frecuencias de observación para la curva de dispersión puede estar asociado a una transición más suave entre los diferentes modos, lo que puede mostrar velocidades de grupo muy cercanas. Hay que considerar que las curvas de velocidad de grupo de modos superiores pueden cruzarse entre sí, incluso el modo fundamental. Finalmente, el HVSR (figura 2.4d) presenta dos picos principales a 0.38 y 2.5 Hz y dos mínimos a 0.79 y 5 Hz, respectivamente. Se observan pequeñas oscilaciones que no representan picos principales (ver Piña-Flores *et al.*, 2017) en el rango de frecuencia entre 0,8 y 2,5 Hz.

Como se mencionó en la sección anterior, la observación de la forma de la curva del HVSR es útil para identificar el modo fundamental y aquellas bandas con posible osculación y efectos multimodo en los diagramas de dispersión, que corresponden a las frecuencias entre y alrededor del principal máximos y mínimos del HVSR. Las frecuencias de los valles del HVSR (0,8 y 5 Hz en este caso) indican la proximidad de los puntos de inflexión en la curva de dispersión de fase. Los diagramas de dispersión, derivados de las técnicas SPAC y F-K, exhiben velocidades bien definidas en el rango de 1.7 a 2.5 Hz y de 4 a 10 Hz, respectivamente. Sin embargo, en un rango de 2 a 5 Hz se observa que la energía corresponde a modos superiores teniendo el efecto multimodal. En muchos casos, este efecto provoca una identificación errónea de la curva de dispersión. Incluso, el HVSR indica la presencia del efecto multimodo u osculación en el rango de frecuencia entre 0,38 (primer pico) y 0,8 Hz (primer canal) y entre 2,5 (segundo pico) y 5 Hz (segundo canal). En el diagrama de dispersión calculado a partir de la técnica de correlación cruzada, se observan dos puntos críticos a 0.8 y 5 Hz, correspondientes a los mínimos del HVSR.

La amplitud de los picos del HVSR es un indicador de los contrastes de impedancia entre las capas correspondientes del medio y, por lo tanto, de la tendencia esperada de las curvas de dispersión. Es decir, la amplitud de los picos en el HVSR aumenta a medida que aumenta la pendiente en la velocidad de fase del modo fundamental. Como se muestra en la figura 2.4d, el pico principal en altas frecuencias (5 Hz) tiene una amplitud de 3.5 mientras que el pico principal en bajas frecuencias (0.79 Hz) exhibe una amplitud de 5.5. Por lo tanto, podemos esperar una variación más aguda en la velocidad de fase alrededor de t0.79 Hz.

Una vez identificadas las curvas de dispersión del modo fundamental para la velocidad de fase y de grupo, se realizó una inversión conjunta del HVSR y de las curvas de dispersión utilizando el software gratuito HV-Inv (https://w3.ual.es/GruposInv/hv-inv/, último acceso en junio de 2018) para obtener una estimación del perfil de velocidad de la zona de estudio. La figura 2.5 muestra el resultado de la inversión que exhibe una excelente concordancia entre el HVSR, las curvas de dispersión de velocidad de fase y de velocidad de grupo observados con las contrapartidas teóricas en todo el rango de frecuencias. Los resultados de inversión de la curva de dispersión y del HVSR permitieron estimar la estructura de velocidad para un sitio de prueba en la desembocadura del río Andarax en términos de un modelo de tres capas en un medio espacio, definido por las estructuras de velocidad Vp, Vs y de densidad. La Tabla 2.2 enumera los parámetros del modelo que mejor se ajustan a las observaciones, que muestra una profundidad de roca de fondo estimada de aproximadamente 0,43 km con una velocidad Vs de 1810 m/s. Las curvas de dispersión teóricas para las velocidades de fase y grupo de modos superiores se calcularon para el modelo invertido y se incorporaron en los diagramas de dispersión experimentales (ver figura 2.6). La figura 2.6 pone en evidencia de que algunas zonas de alta energía en diagramas de dispersión corresponden a modos superiores.

Tabla 2.2. Modelo obtenido a partir de la inversión de datos para el sitio de prueba del río Andarax.

h **(m)**	***Vp*****(m/s)**	***Vs*****(m/s)**	***Densidad*****(kg/m^3)**
Perfil de velocidades Propuesto			
12	828	270	1749
26	1269	420	1538
395	2705	662	2165
∞	3538	1810	2500

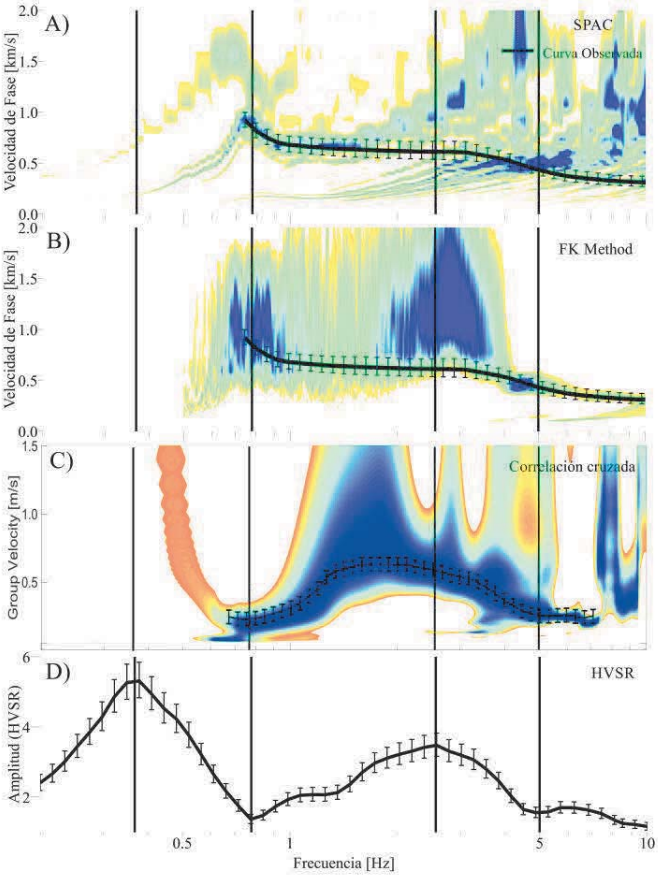

Figura 2.4: Diagramas de dispersión y HVSR obtenida en el delta del río Andarax. A) Diagrama de dispersión (velocidad de fase) aplicando el método SPAC. B) Diagrama de dispersión (velocidad de fase) aplicando el método F-K. C) Diagrama de dispersión (velocidad de grupo) aplicando el método de correlación cruzada y C) Curva HVSR. La línea negra continua muestra la curva de dispersión en modo fundamental elegida utilizando información del HVSR. Las líneas negras verticales representan las frecuencias de los máximos y mínimos del HVSR.

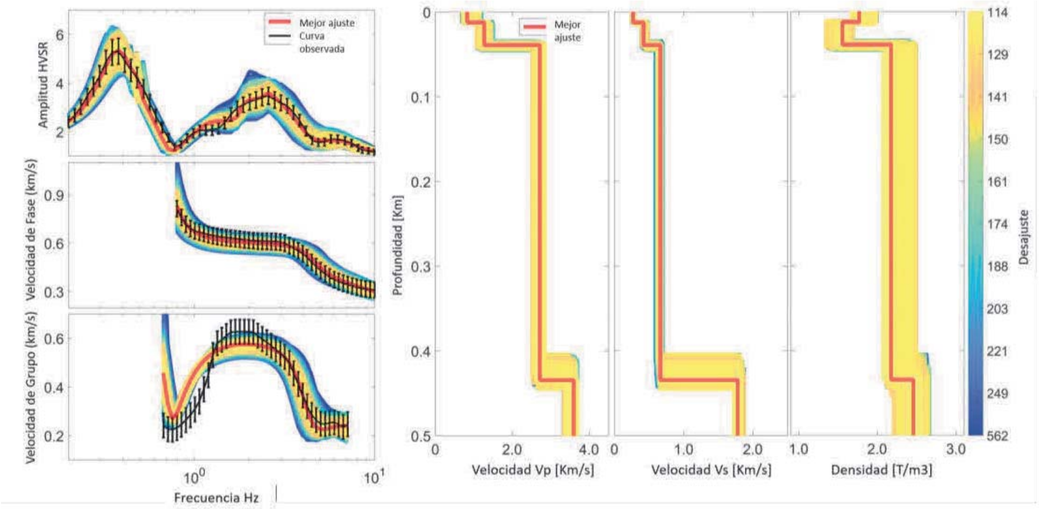

Figura 2.5: Resultados de la inversión conjunta en un sitio de prueba en la desembocadura del río Andarax. A) Objetivo HVSR (línea negra) y HVSR teórico para el modelo que mejor se ajusta (línea roja). B) Objetivo de curva de dispersión de velocidad de fase (línea negra) y curva de dispersión teórica para el mejor modelo de ajuste (línea roja). C) Objetivo de curva de dispersión de velocidad de grupo (línea negra) y curva de dispersión teórica para el mejor modelo de ajuste (línea roja). D) Los perfiles de velocidad y densidad resultan de la inversión simultánea. Las curvas de colores están asociadas con el modelo de prueba generado por el método de inversión iterativa. La profundidad del lecho de roca se estima mediante el modelo que mejor se ajusta a 0,43 km.

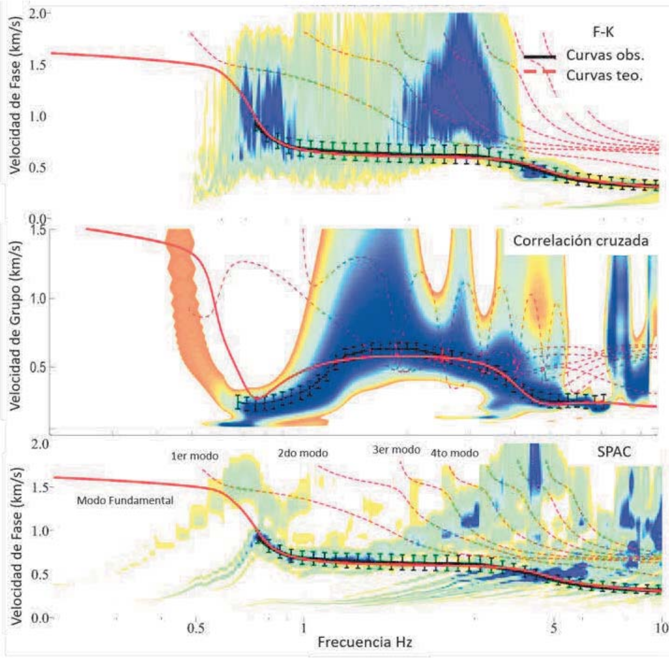

Figura 2.6: Diagramas de dispersión que se muestran en la figura 2.4, incluyendo curvas de dispersión teórica de varios modos (líneas rojas discontinuas) calculadas a partir del perfil de velocidad resultante de la inversión conjunta de las curvas observadas (líneas negras continuas).

2.5.- Conclusiones

En este trabajo, se exploró la relación entre el comportamiento de las curvas de dispersión de velocidad de grupo y fase para el modo fundamental y el primer modo más alto de las ondas de Rayleigh con el HVSR bajo la teoría de campos difusos. La relación entre estas dos curvas se puede resumir en los siguientes cinco puntos.

1.-Las frecuencias donde se encuentran los puntos de inflexión y los puntos críticos, en las curvas de dispersión de velocidad de fase y de grupo, respectivamente, pueden usarse como puntos de control para distinguir el modo fundamental de los modos superiores. Este conocimiento es de gran ayuda para seleccionar adecuadamente las velocidades de Rayleigh en diagramas de dispersión.

2. Las frecuencias de los puntos de inflexión y de los puntos críticos de las curvas de dispersión de velocidad de fase y de grupo, respetivamente, están muy cerca de las frecuencias de los mínimos principales del HVSR.

3. El efecto de osculación y el efecto de cruces modales, entre el modo fundamental y el primer modo superior, para las de velocidad de fase y de grupo, se ubican entre las frecuencias de los picos principales y los mínimos siguientes del HVSR.

4.-La banda de frecuencias de los diagramas de dispersión con posibles efectos multimodos se ubica entre las frecuencias del pico principal y el mínimo subsiguiente del HVSR.

5. La amplitud de los picos principales del HVSR aumenta a medida que aumenta la pendiente (en valor absoluto) de la curva de dispersión de velocidad de fase.

Como ejemplo, se utilizó el HVSR para la identificación de las curvas de dispersión de velocidad de fase y grupo de modo fundamental a partir de diagramas de dispersión en la desembocadura del río Andarax (SE España). El resultado de la inversión permitió estimar un perfil de velocidad confiable para la zona a partir de la inversión conjunta de estas tres curvas. Con este análisis, propongo utilizar la información del HVSR del RSA para identificar las zonas de osculación, el efecto multimodo, el efecto de cruces de modos, los puntos de inflexión y los puntos críticos del modo fundamental a partir de los diagramas de dispersión. Esta forma de proceder puede ser una herramienta complementaria muy útil, junto con las otras formas de identificación de modos, para obtener un perfil de velocidad representativo de la zona de estudio utilizando la inversión conjunta destinada a obtener una evaluación más precisa de los efectos del sitio local en la ocurrencia de un evento sísmico.

Sección 3

Estructura de velocidad de onda de corte en 3D de la Pirámide del Sol en Teotihuacán, México

3.1.- Introducción

La antigua ciudad de Teotihuacán floreció en las tierras altas del centro de México entre 150 a. C. y 550/650 d. C. En su apogeo, la ciudad tenía una población de más de cien mil habitantes y era la más grande del hemisferio occidental, con una extensión de más de 20 kilómetros cuadrados (Cowgill, 2015). El centro de la ciudad tenía un grupo de grandes edificios integrados que mostraban, en un orden muy particular, los vastos espacios y plataformas que formaban los conjuntos arquitectónicos más monumentales de la antigua América. La Pirámide del Sol es uno de los edificios más grandes hechos por el hombre en la antigüedad.

Actualmente, la Pirámide del Sol tiene 64 m de altura con 215 m a cada lado de la base cuadrada. La estructura fue construida en cuatro niveles o cuerpos arquitectónicos, de alguna manera diferente de lo que se ve hoy. Además, en la parte occidental de la Pirámide, hay una plataforma en terrazas que se construyó después de su finalización (Millon y Drewitt, 1961). La Pirámide se construyó en una sola operación, con vertederos y piedras de la región que lograron un volumen sólido de más de un millón de metros cúbicos. Fue construido entre el primer y el segundo siglo de nuestra era durante la Primera Etapa de la ciudad de Teotihuacán (Sarabia y Núñez, 2017).

El sitio arqueológico de Teotihuacán, y especialmente la Pirámide del Sol, es uno de los centros ceremoniales más visitados del centro de México. El número de personas que visitan la Pirámide puede alcanzar hasta 20,000 en el equinoccio de primavera. Para fines de conservación y restauración, es necesario conocer las propiedades mecánicas de los materiales y el subsuelo debajo de la Pirámide. Más allá de los procesos de restauración y entre otras prioridades, es necesario establecer la respuesta sísmica de la estructura para futuros terremotos. De hecho, el centro de México se localiza aproximadamente a unos 300 km de la zona donde mayormente ocurren los sismos y es afectado regularmente por sismos de subducción, por sacudidas de intraplacas de fallas normales (M> 6) y, aunque menos frecuentes, por sismos corticales poco profundos. Los estudios geotécnicos y la evaluación de la respuesta sísmica en estas estructuras son escasos. Por ejemplo, en lo que puede considerarse un caso de éxito, la Pirámide de Zoser en Egipto no colapsó durante algunos terremotos locales porque fue restaurada previamente (Khalil *et al.*, 2016). En este trabajo utilizamos una metodología no invasiva para estimar las propiedades físicas y geotécnicas de este legado único y monumental de nuestros antepasados teotihuacanos.

El trabajo pionero de Aki (1957) tenía como objetivo recuperar las propiedades de propagación de ondas sísmicas del tratamiento del ruido ambiental sísmico (RSA). Desde entonces, se han desarrollado varias técnicas de procesamiento. Por ejemplo, algunos estudios demostraron que las llegadas de ondas Rayleigh de las Funciones de Green, entre pares de estaciones, se pueden recuperar mediante las correlaciones cruzadas de los registros de coda sísmica y/o registros de RSA (Shapiro y Campillo, 2004, Shapiro *et al.*, 2005), dado que este método puede extenderse al corto período (Chávez-García y Luzón, 2005), es útil para estudios geotécnicos. Por ejemplo, varios autores han utilizado largas secuencias de registros de RSA en varias estaciones con el objetivo de extraer las funciones de Green y las imágenes de velocidad de onda sísmica dentro de cuerpos 3D complejos como cámaras magmáticas dentro de volcanes (Brenguier *et al.*, 2007, Spica *et al.*, 2017).

Las tomografías de ondas superficiales, utilizando datos de RSA, se han aplicado con éxito en diferentes regiones del mundo para obtener tomografías de velocidad de fase y de grupo. Estas imágenes generalmente se correlacionan bien con la geología y la tectónica de la región y pueden revelar características nuevas y desconocidas. Se han realizado estudios de este tipo para Norteamérica (Ritzwoller *et al.*, 2011), Sudamérica (Ward *et al.*, 2013), Europa (Yang *et al.*, 2008), Asia (Zheng *et al.*, 2008), Nueva Zelanda y Australia (Saygin y Kennett, 2010) o Islandia (Gudmundsson *et al.*, 2007), entre otros.

En este trabajo, estimamos un modelo 3D de velocidades de onda de corte (Vs) dentro de la Pirámide del Sol en Teotihuacán. Se calculó las correlaciones cruzadas entre pares de estaciones para recuperar e identificar las velocidades de grupo de Rayleigh de paquetes de ondas prominentes obteniendo las curvas de dispersión. Utilizando las formas de onda recuperadas y las curvas de dispersión, se realizó una tomografía de ondas de superficie 2D para diferentes frecuencias. Finalmente, utilizamos la información de la tomografía, junto con las relaciones espectrales horizontal a vertical (HVSR) de RSA, para obtener un modelo 3D de velocidades de ondas de corte para la estructura, mediante un procedimiento de inversión.

3.2.- Procesamiento de datos de ruido sísmico ambiental

Para la evaluación del modelo de velocidad de onda de corte (Vs) de la Pirámide del Sol, utilizamos 15 sensores triaxiales de banda ancha sísmica (30s) 6TD, fabricados por Guralp Systems. La distribución del sensor se realizó en distintos niveles de la Pirámide del Sol para cubrir aproximadamente toda la superficie de la estructura (ver figura 3.1a). Las mediciones de RSA se tomaron durante ~ 4 horas en modo continuo, utilizando el GPS para la sincronización del tiempo absoluto. Los datos de RSA se corrigieron mediante la respuesta instrumental, la línea base y la tendencia lineal. Posteriormente, la correlación cruzada del desplazamiento vertical entre pares de estaciones (ver figura 3.1b) se llevó a cabo siguiendo la propuesta de Bensen *et al.*, (2007). Ejemplos de estas correlaciones cruzadas se representan en las figuras 3.2a y 3.2b.

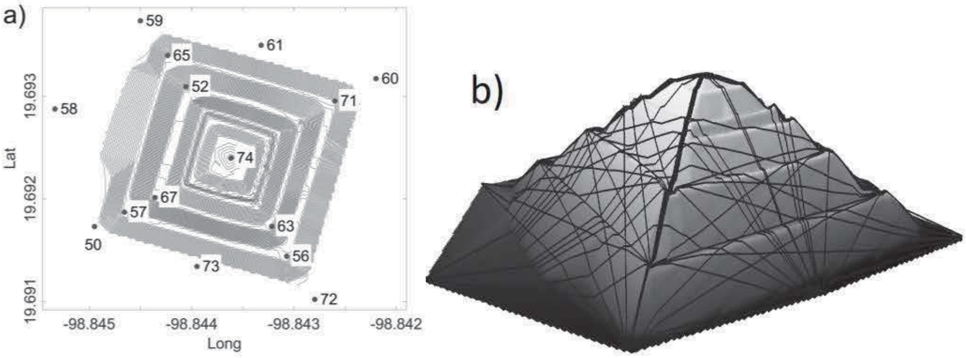

Figura 3.1. (a) Diagrama de la distribución de sensores en la superficie de la Pirámide del Sol. (b) Esquema de las rutas de superficie más cortas entre pares de estaciones para las cuales se calcularon las distancias a lo largo de las pendientes.

El análisis de las funciones de Green se llevó a cabo mediante el método de Análisis de Tiempo-Frecuencia (FTAN, por sus siglas en ingles) para extraer las velocidades de grupo de cada correlación cruzada, una para cada par de estaciones (por ejemplo, Ritzwoller y Levshin, 1998, Bensen et al, 2007). Se obtuvieron 105 diagramas de dispersión confiables para extraer las curvas de dispersión de velocidad de grupo en un rango de frecuencia entre 3 y 10 Hz. Para una frecuencia de 3 Hz, encontramos velocidades de alrededor de 750 m / s, mientras que a frecuencias más altas (10 Hz) la velocidad es de ~ 100 m / s en promedio para todas las curvas de dispersión (ver figura 3.2e). La selección de curvas de dispersión se realizó manualmente y asumimos que corresponden al modo fundamental de las ondas de Rayleigh. Las figuras 3.2 c-d muestran los diagramas de dispersión, para diferentes trayectorias, obtenidos mediante la correlación cruzada de RSA entre la estación de la cima (# 74) y las estaciones de base (# 73) y de primer nivel (# 57) de la estructura (ver figuras 3.2 a-b).

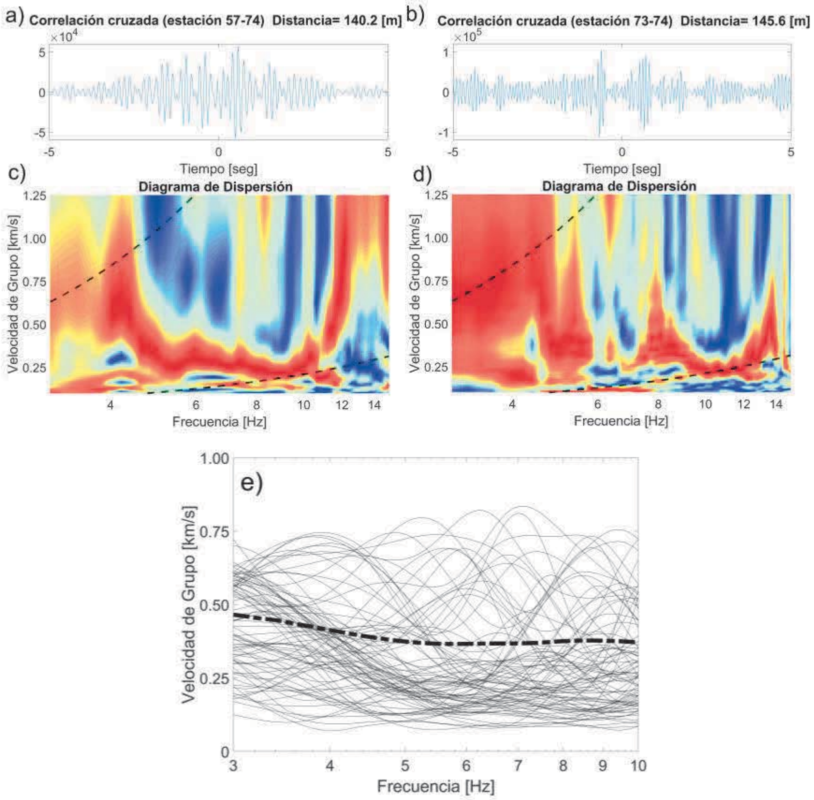

Figura 3.2. (a) y (b) Correlación cruzada para el ruido sísmico (partes causales y anti causal) entre las estaciones 57-74 y 73-74, respectivamente. (c) y (d) diagramas de dispersión de onda de Rayleigh para 57-74 y 73-74 pares, respectivamente. Las líneas discontinuas representan los límites de longitud de onda superior e inferior en función de la distancia entre los receptores. (e) Curvas de dispersión para los 105 pares de estaciones (líneas negras) y curva promedio (línea discontinua).

Tomando en cuenta que la Pirámide del Sol es una estructura construida principalmente de arcillas y rocas de los alrededores, se llevó a cabo la simulación de la propagación de ondas elásticas en 2D con el objetivo de observar la propagación de las ondas considerando un modelo semejante a la gemetria de la Piramide del Sol bajo el esquema de del Elemento de Frontera (BEM, por sus siglas en inglés) (Manolis y Beskos, 1988). Los desplazamientos verticales son generados mediante una fuente vertical puntual. De la simulación, se observa que las ondas de superficie viajan sobre la superficie del modelo. Además, se calculó las correlaciones cruzadas de los sismogramas sintéticos y se verificó que las curvas de dispersión, de velocidad del grupo, se puedan obtener mediante las correlaciones cruzadas de los desplazamientos verticales. A partir del diagrama de dispersión, observamos que el fragmento de la curva de dispersión, que se puede recuperar, está limitado por las longitudes de onda máximas y mínimas del orden de 1,2 y 0,2 veces la distancia entre los receptores, respectivamente (véase el apéndice A). Con base en estas observaciones, incluimos la información de la topografía de la Pirámide del Sol y se calcularon las distancias entre las estaciones sobre las caras de la estructura para obtener distancias de propagación correctas y así evitar una subestimación de las velocidades de grupo de Rayleigh. Para modelar la estructura de la Pirámide del Sol, se obtuvieron 657 puntos diferenciales de GPS en diferentes niveles. La figura 3.1b muestra un diagrama de las trayectorias en la superficie de la Pirámide a partir de las cuales se calcularon las distancias entre estaciones.

3.3.- Tomografía de ondas superficiales

La tomografía de onda de Rayleigh se realizó a partir de los tiempos de viaje, extraídos de las curvas de dispersión de velocidad de grupo para cada frecuencia, utilizando el método de Fast Marching Metod (FMM) para el esquema de inversión. El FMM es un solucionador de la ecuación eikonal basada en mallas bidimensionales, actualmente utilizado en sismología para resolver el problema directo de la predicción de los tiempos de viaje entre la fuente y el receptor. Se pueden encontrar descripciones detalladas de FMM en Rawlinson y Sambridge (2004, 2005).

Dado que el método de FMM funciona en 2-D y la estructura es en 3-D, realizamos una corrección aplicando un esquema de proyección adecuado a la estructura que minimiza la distorsión en distancias y acimut para los pares de estaciones que evita sobreestimar los valores de velocidad (Gómez-Moreno, 2004). Para llevar a cabo esta proyección, se resolvió un sistema indeterminado de ecuaciones no lineales (ver ecuación 3.1 y 3.2) mediante un proceso iterativo para encontrar las nuevas coordenadas de la matriz de receptores 2D que conserva, lo mejor posible, las distancias originales (calculado a lo largo de las pendientes) y acimuts. Esto es:

$$D_m^n = \sqrt{(X_n - X_m)^2 + (Y_n - Y_m)^2} \tag{3.1}$$

$$\alpha_m^n = \tan^{-1}\left[\frac{Y_n - Y_m}{X_n - X_m}\right] \tag{3.2}$$

donde D_m^n se definen como distancias reales (calculadas a partir de las coordenadas 3D), α_m^n es el acimut verdadero, n y m son los números de las estaciones, X e Y son las nuevas coordenadas proyectadas. Se arreglaron las coordenadas (X, Y) de la estación central (ubicada en la parte superior de la estructura). Sin embargo, este tipo de proyecciones tiene el problema de que algunas propiedades no se cumplen para todos los puntos en el plano. Cuanto más lejos están los puntos del centro, que en nuestro caso es el vértice de la pirámide, el error de la distancia y acimut aumenta (Gómez- Moreno, 2004). La figura 3.3c muestra el error de cálculo para nuevas distancias entre pares de estaciones que dependen de las distancias medidas en las caras de la estructura. El error máximo que se reporta es del 16%. Si solo se considera las distancias en el plano horizontal (es decir, ignorando la altura z), el error de las distancias es de hasta el 110%. Por lo tanto, se considera que las nuevas coordenadas son apropiadas para realizar una tomografía con el esquema FMM. Este procedimiento también se aplicó para los puntos GPS de la Pirámide del Sol.

Utilizando las coordenadas transformadas para los receptores, se realizó una prueba de tablero de ajedrez para determinar la resolución óptima de la cuadrícula y verificar que los rayos entre pares de estaciones sean suficientes. Después de algunas pruebas, se seleccionó una resolución espacial de ~ 40 m (celda cuadrada) para usar en el modelo de la Pirámide del Sol. Las figuras 3.3a y 3.3b muestran la prueba del tablero de ajedrez y su reconstrucción mediante el procedimiento de inversión para un tamaño de celda de 40 m. El modelo de velocidad inicial para la inversión tomográfica fue el promedio de las mediciones de velocidad de grupo para cada frecuencia (ver figura 3.2e). Debido a la buena cobertura de los rayos entre pares de estaciones y la resolución espacial moderada, elegimos aplicar suavizado durante la inversión. Los valores teóricos del tiempo de viaje para el modelo resultante muestran desviaciones RMS de los datos observados que oscilan entre 140 ms y 280 ms, dependiendo de la frecuencia analizada.

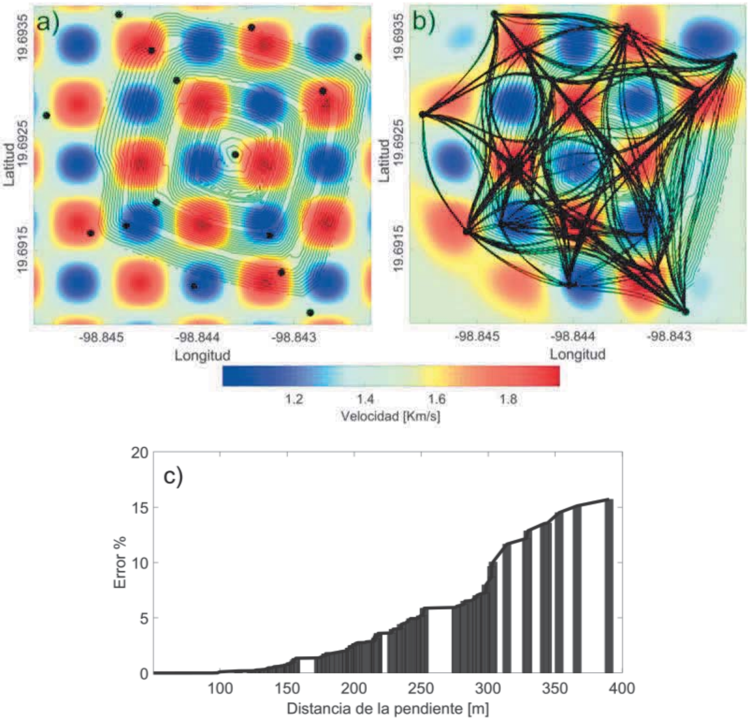

Figura 3.3: Tablero de ajedrez y pruebas del esquema de proyección. (a) Modelo de velocidad sintético para la prueba de tablero de ajedrez, con velocidades de celda entre 1 y 2 km / s. Las líneas negras representan las curvas de nivel de la estructura, y los puntos representan las estaciones. (b) Resultado de la inversión utilizando datos sintéticos. Las gruesas líneas negras representan las rutas de rayos entre las estaciones. (c) Error (expresado como un porcentaje) entre las distancias de la estación real (medidas en las caras laterales) y las distancias entre los puntos proyectados (es decir, después de aplicar la transformación explicada en el texto).

La distribución espacial de las velocidades de grupo de las ondas de Rayleigh para diferentes frecuencias (3.5, 7 y 9 Hz) se muestran en las figuras 3.4 a-d, respectivamente. La tomografía a 3 Hz muestra dos anomalías de baja velocidad (con valores de ~0.5 km/s), una en el noroeste y la otra en la parte sureste de la Pirámide. La imagen a 5 Hz muestra claramente que la anomalía del noroeste disminuye su velocidad a ~0.1 km/s, mientras que la anomalía del sureste se extiende hacia el suroeste. A 7 Hz, las anomalías de baja velocidad permanecen en la parte sur de la Pirámide del Sol, así como en la parte noroeste. Sin embargo, emerge una nueva anomalía aislada de baja velocidad en la parte noreste. Finalmente, la distribución a 9 Hz muestra que las anomalías de baja velocidad predominan en las partes central y sureste de la Pirámide del Sol. Estos patrones probablemente estén relacionados con el flujo natural del agua de lluvia, que tiene una dirección preferencial noroeste-sureste (Ibáñez 2012). Las posibles causas de estas características se discutirán en la siguiente sección.

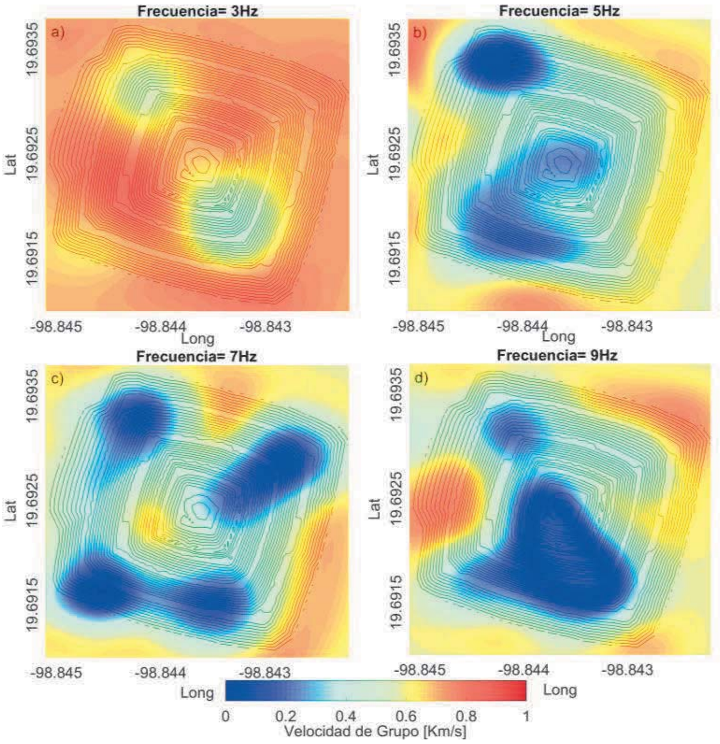

Figura 3.4: (a-d) tomografía sísmica 2D para frecuencias de 3, 5, 7 y 9 Hz, respectivamente. Las líneas negras representan las curvas de nivel de la estructura.

3.4.- Inversión de la estructura de velocidad de onda S

A partir de los mapas de tomografía sísmica correspondientes a cada frecuencia analizada (3-10 Hz), construimos una curva de dispersión para cada celda y se invirtieron utilizando el software HV-Inv (García-Jerez *et al.*, 2016). Para mitigar el problema de no unicidad en las inversiones de curva de dispersión (por ejemplo, Piña-Flores *et al.*, 2017), se calculó el HVSR para cada estación en los diferentes niveles de la estructura y se realizó una inversión conjunta del HVSR y de las curvas de dispersión puntual. El HVSR, calculado en la cima de la estructura, muestra un único pico con amplitud ~2.8 ubicado a 1.75 Hz. Para frecuencias de 5 a 10 Hz, la amplitud es menor que la unidad (ver figura 3.5a). Podemos interpretar este resultado debido a la presencia de una inversión en la velocidad a medida que aumenta la profundidad (Castellaro y Mulargia, 2009). En este trabajo, se asume que el HVSR, se ha modelado bajo la teoría de los campos difusos (Sánchez-Sesma *et al.*, 2011) y se considera una medida puntual no muy sensible a la irregularidad lateral (Perton *et al.*, 2018). Las figuras 3.5 a-c muestran los resultados de la inversión conjunta del HVSR y la curva de dispersión de velocidad de grupo asignada a la parte superior de la Pirámide.

El perfil de velocidad de Vs resultante de la inversión conjunta (figura 3.5c) muestra una inversión de velocidad, con una capa superficial rígida de ~10 m de espesor con una velocidad de Vs de ~1800 m/s que corresponde al recubrimiento de la Pirámide del Sol que está compuesta de fragmentos de hormigón y basalto (Batres, 1993). La segunda capa tiene un grosor de 15 m y una velocidad de Vs =250 m/s y la tercera capa tiene un grosor de 25 m y una velocidad de Vs ~450 m/s. Finalmente, el perfil de velocidad de Vs invertido se utilizó como modelo inicial para las inversiones de curva de dispersión en las celdas vecinas. Este procedimiento se repitió hasta que se invirtieron todas las curvas. Para explorar la profundidad de investigación alcanzada desde las curvas de dispersión en la banda 3-10 Hz, se realizó un análisis de sensibilidad de la velocidad del grupo, en términos de frecuencia, bajo variaciones en Vs a diferentes profundidades alrededor de los valores obtenidos para el modelo de la cima de la Pirámide. En particular, se calculó la matriz de sensibilidad (f, h) definida como:

$$S(f,h) = \frac{dU(f)}{d\,Vs(h)} \tag{3.3}$$

donde $U\,(f)$ es la velocidad del grupo a la frecuencia f y Vs (h) es la velocidad de la onda de corte en función de la profundidad h. En este análisis (figura 3.5 d-f), mostramos que los fragmentos de las curvas de dispersión son sensibles ($S\,(f,\ h)> 0.01$) a las variaciones en el perfil Vs en el rango de 7m a 100m de profundidad.

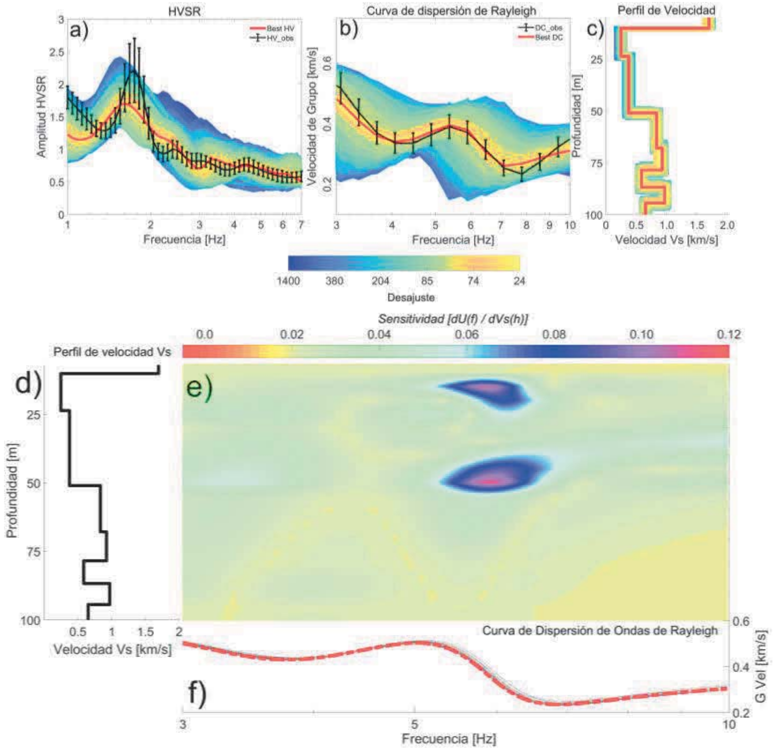

Figura 3.5: La inversión conjunta resulta de (a) la relación espectral HVSR y (b) la curva de dispersión de velocidad del grupo para las ondas de Rayleigh. Las líneas negras representan las curvas observadas con su desviación estándar, y las líneas rojas representan el mejor ajuste. (c) Perfil de Vs obtenido de la inversión conjunta. La línea roja representa el mejor perfil. Los paneles d-f muestran los resultados del análisis de sensibilidad de la curva de dispersión. (d) Perfil de velocidad obtenido de la curva de dispersión (línea de trazos en el panel f). (e) Sensibilidad S a las variaciones en Vs en función de la profundidad de la capa y la frecuencia.

Una vez que se invirtieron los perfiles de velocidad Vs para cada celda, se realizó una interpolación de los perfiles con un suavizado moderado. Posteriormente, a cada perfil de velocidad se asignó de regreso al espacio 3D sobre la base de las coordenadas (proyectadas) del centro. Para realizar esta transformación, se llevó a cabo la transformación inversa descrita anteriormente (es decir, desde coordenadas de estación 2D a 3D) y asignamos la elevación local de la superficie de la pirámide a la superficie libre del modelo. El modelo 3D de velocidad de Vs, presentado en la figura 3.6a, muestra dos anomalías de baja velocidad (~150 m/s), una de ellas se encuentra en el área noroeste y la segunda en la parte sureste de la pirámide. Estas anomalías de baja velocidad (que ya eran detectables en los mapas de velocidad de grupo para las ondas de Rayleigh) se pueden asociar a la saturación del material y/o la meteorización diferencial debido al agua de lluvia que se captura dentro de la Pirámide en áreas específicas. Esto sería congruente con el flujo de agua natural en la zona, con dirección predominante noroeste-sureste (Ibáñez 2012). Estos resultados también se pueden comparar con las características fisicas superficiales de la Pirámide.

En las figuras 3.6a y 3.6b, se muestra que las áreas de baja velocidad corresponden a la posición física de algunos muros escalonados, las cuales proporcionan estabilidad a la estructura (Batres, 1993). En contraste, las zonas de alta velocidad (~1800 m/s) carecen de estos muros. Cabe señalar que los muros escalonados son parte de una serie de estructuras que se unieron a las pendientes de los dos primeros niveles para ampliar la base de la pirámide. Inicialmente, se construyeron muchos más como parte del sistema constructivo para estabilizar la ampliación de poco más de 6 m de ancho de la Pirámide del Sol. A diferencia de la construcción original, que está compuesta de arcillas, las paredes escalonadas consisten en tezontle (roca volcánica ligera y porosa) y rocas de basalto cementadas con barro. La mayoría de estos muros escalonados desaparecieron y solo 64 se conservan actualmente (Ibáñez 2012).

En la figura 3.6c, se presenta una sección vertical del modelo 3D de velocidad de Vs, que pasa por el centro de la Pirámide en dirección este-oeste, que muestra que su interior de la estructura está constituido por diferentes capas de suelo que forman una estructura en forma de cúpula, con un material en la superficie más suave (~450 m/s) que rodea un núcleo de alta velocidad (~1200 m/s). Esta estructura es consistente con los datos recopilados por Millon *et al.* (1965) de las excavaciones de los túneles de Gamio y de Noguera (Gamio, 1922; Noguera, 1935) que cruzan toda la pirámide (ver figura 3.7).

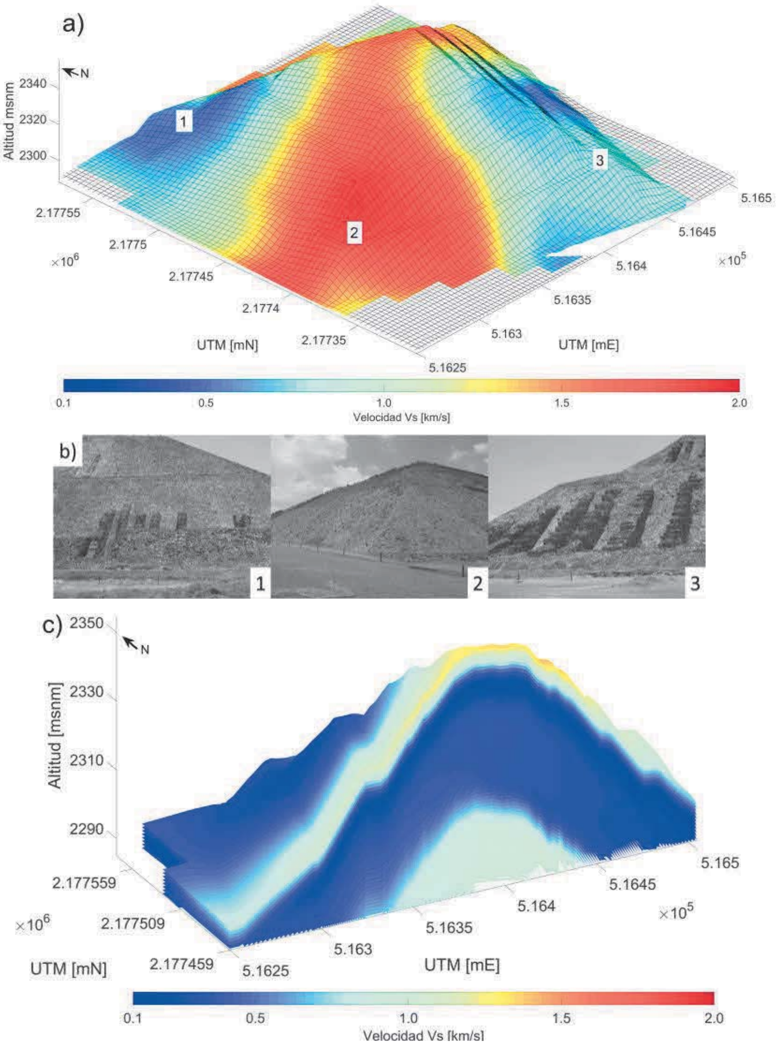

Figura 3.6: (a) Modelo 3D Vs de la Pirámide del Sol. Para las zonas de baja velocidad (zonas 1 y 3) existen paredes escalonadas altas, mientras que la zona de alta velocidad (zona 2) no tiene estas estructuras, (b) Fotografías de las características estructurales de la Pirámide del Sol (tomadas en julio de 2016), correspondiente a zonas de baja (1,3) y alta velocidad (2), (c) Sección transversal del modelo de velocidad en dirección este-oeste.

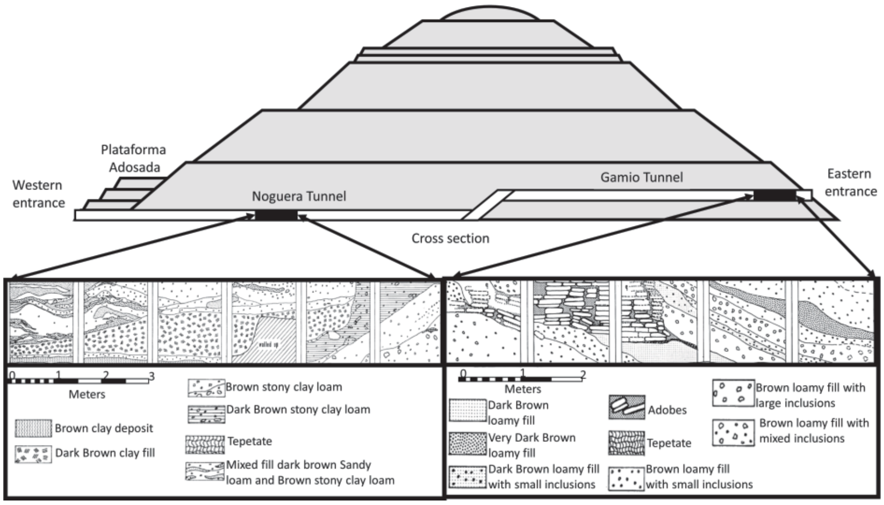

Figura 3.7: Descripción litológica del interior de la Pirámide del Sol a partir de las excavaciones realizadas por Gamio y Noguera. Modificado de Millon *et al.* (1965) págs. 86, 88 y 90.

3.5.- Discusión y conclusiones

Las propiedades mecánicas de los materiales que componen la Pirámide del Sol en Teotihuacán, México, se llevó a cabo mediante la implementación 15 sensores triaxiales distribuidos en la superficie de la Pirámide para registrar ~4 horas de RSA. De este conjunto de datos, obtuvimos las correlaciones cruzadas promedio del RSA registrado entre pares de estaciones. El análisis de las correlaciones cruzadas entre pares de estaciones permitió obtener información estructural valiosa. A partir de estas formas de onda, se obtuvieron curvas de dispersión de onda de Rayleigh y la inversión conjunta de las curvas, en conjunto con los HVSR, permitió obtener un modelo 3D de velocidad de Vs en la Pirámide del Sol. Además, se llevó a cabo una simulación de propagación de ondas elásticas en 2D mediante el método del elemento límite (BEM). Con base en los resultados de la simulación, se verificó que las curvas de dispersión, de velocidad de grupo para las ondas de Rayleigh, pueden recuperarse mediante las correlaciones cruzadas en un medio elástico con geometría irregular.

En este trabajo se realizó con un estricto control de calidad de los datos y de la selección de curvas de dispersión. Como la Pirámide del Sol es una estructura con topografía irregular, hemos aplicado con éxito un método de proyección de coordenadas para evaluar correctamente las velocidades de propagación de las ondas de Rayleigh. Además, aplicamos una inversión simultánea de las curvas de dispersión, obtenida de los mapas de velocidad del grupo y de los HVSR para mitigar los problemas de no unicidad en el modelo Vs recuperado. Esta combinación nos permitió mejorar la resolución del modelo, revelando algunas características como el revestimiento rígido de la pirámide (que estaba fuera del rango de profundidades a las que nuestras curvas de dispersión son sensibles) y la profundidad y magnitud precisas de los principales contrastes de velocidad.

Con base en los resultados, se observa tres características principales de la Pirámide del Sol. En primer lugar, el modelo describe anomalías de baja velocidad que son relacionadas con el flujo natural de agua de lluvia teniendo una dirección preferencial al noroeste-sureste. La segunda característica es de tipo estructural: las anomalías de baja velocidad (~150 m/s) se correlacionan con la posición física de los muros escalonados o estribos de piedra y barro en la superficie (Batres, 1993). En zonas de alta velocidad (~1800 m / s), la estructura carece de estos muros escalonados. Sin duda, estas estructuras fueron parte del proceso constructivo para extender la estructura y brindar apoyo a las partes débiles de la Pirámide del Sol. La última característica es que los materiales dentro de la Pirámide forman una estructura tipo cúpula. El núcleo de la Pirámide consta de varias capas de tierra y tepetate (una roca de color amarillo blanquecino con un conglomerado poroso, que, cuando se corta en bloques, se usa en la construcción) mezclada con piedras y una gran cantidad de cerámica, líticos y fragmentos de carbón. No se utilizaron rocas grandes o adobes (Sugiyama *et al.*, 2014). La estructura de la Pirámide del Sol implica que las paredes son susceptibles a deslizamientos de tierra. Estas características son consistentes con las observaciones realizadas por Millon *et al.* (1965) basadas en las excavaciones de Túneles de Gamio y Noguera (Gamio, 1922; Noguera, 1935) que cruzan toda la Pirámide y describen que los materiales del interior parte de una estructura tipo cúpula. Finalmente, consideramos que los datos proporcionados por nuestro trabajo serán útiles para el diagnóstico estructural de la Pirámide del Sol en Teotihuacán con el objetivo de preservar este monumento, declarado Patrimonio de la Humanidad por la UNESCO.

3.6.- Anexo: Método de elementos de frontera (BEM)

El método del elemento límite (BEM) es un método numérico que ha producido resultados satisfactorios en muchos problemas de elasticidad dinámica. De los teoremas de la representación integral recíproca; y mediante la discretización de los límites entre subdominios homogéneos, los desplazamientos y las tracciones pueden resolverse mediante un proceso iterativo. Entre las ventajas del método, debe enfatizarse que solo requiere la discretización de los límites y satisface automáticamente la condición de radiación sin usar límites especiales sin reflejos, como lo requieren otros métodos (métodos de diferencia finita). El uso de BEM en elastodinámica se pueden encontrar una descripción más detallada en Manolis y Beskos (1988).

La observación de la propagación de las ondas superficiales en un medio 2D con superficie topográfica irregular (es decir, una sección transversal de la Pirámide del Sol) se realizó mediante una simulación numérica basada en el BEM. El modelo utilizado consistió en un cuerpo casi triangular parcialmente enterrado sobre un semiespacio, homogéneo e isotrópico. La figura A1 muestra las dimensiones del modelo y las propiedades asignadas a cada región. En esta primera simulación, se aplicó una fuerza concentrada en la dirección vertical en la parte superior del modelo para obtener el desplazamiento en una matriz densa de receptores verticales colocados en la superficie y dentro del modelo.

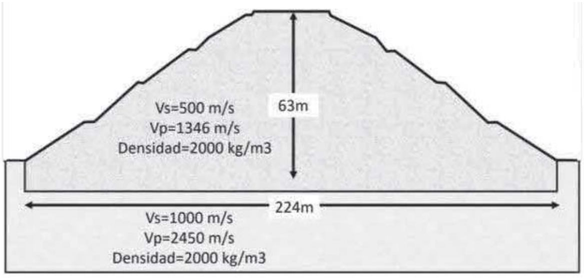

Figura A1: Esquema del modelo de la Pirámide del Sol utilizada en la prueba BEM. El modelo consta de dos medios con diferentes propiedades dinámicas.

La figura A2 muestra algunas capturas de pantalla de los resultados de la simulación. Primero, se observa la propagación de las ondas de compresión con velocidad Vp. Posteriormente (0.2 s), podemos observar la propagación de las ondas de corte y finalmente, emergen las ondas de superficie de Rayleigh. Estas ondas superficiales tienen una energía significativa en profundidad y los desplazamientos son casi perpendiculares a la superficie. Cuando las ondas superficiales alcanzan la mitad de la altura de la pirámide, el movimiento involucra el semiespacio.

Por otro lado, para verificar el cálculo de la curva de dispersión a partir de la correlación cruzada de los registros verticales, se obtuvieron sismogramas sintéticos a lo largo de la superficie del medio irregular (ver figura A3a) para una fuente vertical aplicada fuera de la pirámide. La ubicación de la fuente se basa en la reproducción más cercana a las fuentes de RSA típico. A partir de estos resultados, se estimó la correlación cruzada de dos registros sintéticos (fig. 3Ab) siguiendo la metodología descrita por Bensen *et al.*, (2017).

El análisis de frecuencia de tiempo (FTAN) (por ejemplo, Ritzwoller y Levshin 1998, Bensen et al, 2007) se utilizó para calcular el diagrama de dispersión a partir de la correlación cruzada. En la figura A3c se muestra la curva de dispersión, de velocidad del grupo para las ondas de Rayleigh, en un rango de frecuencia entre 5 y 15 Hz con velocidades entre 250 m/s y 750 m/s. Como referencia, mostramos la curva de dispersión teórica para un modelo 1D que consiste en una capa plana de 30 m de espesor, que corresponde al valor medio de la altura de los receptores, utilizando las mismas propiedades dinámicas de los materiales de nuestro modelo 2D. Esta curva de dispersión teórica se asemeja al diagrama de dispersión.

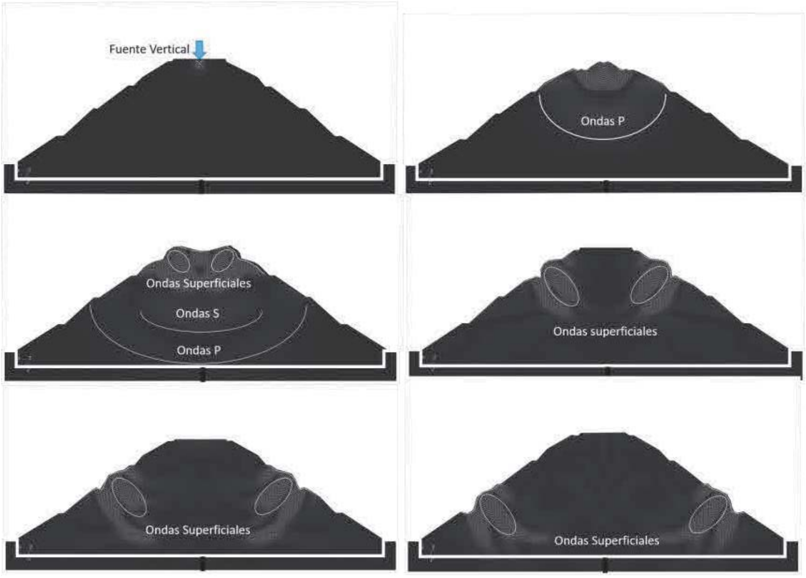

Figura A2.- Instantáneas de desplazamiento vertical debido a una fuente vertical utilizando el método BEM.

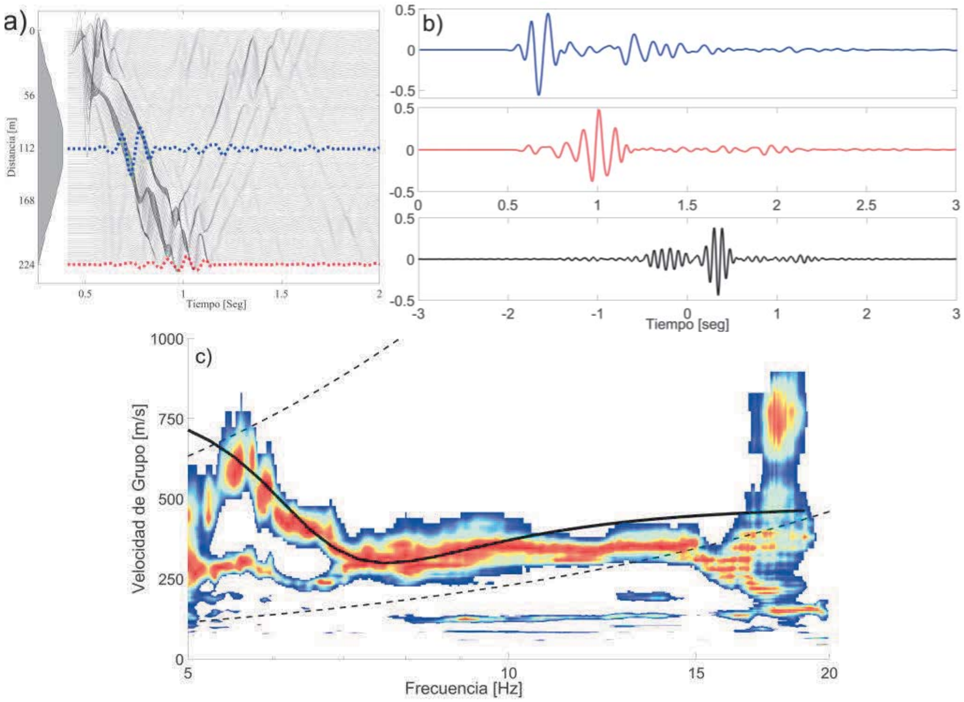

Figura A3.-(a) sismogramas sintéticos obtenidos de la simulación numérica con BEM. (b) Correlación cruzada (línea negra) obtenida de los sismogramas sintéticos de la base (línea roja) y del ápice (línea azul). (c) Curva de dispersión obtenida de la correlación cruzada. La línea continua representa la curva de dispersión teórica para una capa horizontal de 30 m de espesor con las propiedades dadas a la pirámide que recubre un medio espacio con las propiedades del terreno. Las líneas discontinuas corresponden a los límites de longitud de onda de 1.2 y 0.2 veces la distancia de la interestatal.

Sección 4

Proyecto *HV-Inv* (2016-2020)

4.1.- Software HV-Inv® v2.5

El Proyecto HV-Inv es parte de una colaboración de investigadores de la Universidad Nacional Autónoma de México; de las Universidades Españolas de Almería, de Granada y de Barcelona; y de la Universidad de Kyoto, Japón, El proyecto HV-Inv empezó a mediados del año 2016 con el objetivo de crear una herramienta de interfaz gráfica para obtener el cálculo directo del cociente HVSR que se relaciona con la Función de Green para un medio estratificado partir de la teoría de interferometría teniendo como base la hipótesis de que el campo de ruido sísmico ambiental es de carácter difusivo (DFA).El producto del proyecto es el software denominado HV-Inv® v2.5 el cual tiene Registro INDAUTOR México: 03-2018-101011272700-01 (ver anexo) el cual soporta el cálculo directo y la inversión conjunta de HVSR en conjunto con las curvas de dispersión mediante el uso de varios algoritmos locales y globales: Muestreo de Monte Carlo, Simulated Annealing, Downhill Simplex y de Punto Interior.

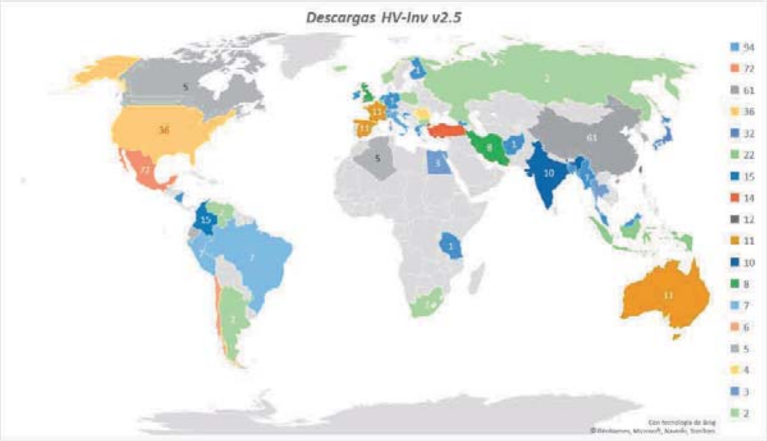

Figura 4.1.-Mapa donde se muestra el número de descargas del software HV-Inv v2.5

A partir del año 2016 y hasta el 2020 se han liberado varias versiones arreglando algunos errores de programación. Actualmente, el software HV-Inv® v2.5 está disponible en los tres principales sistemas operativos (Windows, Linux y MAC) y puede ser descargado en la página de internet http://w3.ual.es/GruposInv/hv-inv/. Hasta la fecha (agosto-2020), el software cuenta con más de 500 descargas en diferentes países distribuidos en los 5 continentes (figura 4.1) y cuenta con ~50 citas en artículos científicos. Si bien, el software ha sido creado para ser utilizado con propósitos académicos, también ha sido utilizado en actividades empresariales. Finalmente, el proyecto HV-Inv ha sido propuesto al Millennium Technology Prize of the Technology Academy Finland 2020 por parte del Instituto de Ingeniería, UNAM.

Sección 5

Trabajo Futuro

5.1.- Procesamiento de datos de ruido sísmico ambiental para obtener el cociente espectral H/V

Actualmente, existen dos procesamientos estándar del ruido sísmico ambiental para obtener el cociente espectral de los desplazamientos horizontales entre los desplazamientos verticales (HVSR). El primer procesamiento para calcular el HVSR es a partir del promedio de la raíz cuadrada del cociente de los espectros de energía para las componentes horizontales con la componente vertical (Wathelet *et al*. 2020):

$$\frac{H(\omega)}{V(\omega)} = \frac{1}{n}\sum_{l=1}^{n}\sqrt{\frac{\left(u_i^l(\omega)\right)^2 + \left(u_j^l(\omega)\right)^2}{\left(u_k^l(\omega)\right)^2}} \tag{5.1}$$

Donde $u_i^l(\omega)$ es el espectro de enegia de los desplazamientos en dirección *i* para cada ventana de tiempo *l* en el dominio de la frecuencia (ω). El segundo procesamiento es a partir de la raíz cuadrada de los promedios de los espectros de energía para las componentes horizontales con la componente vertical. El espectro de densidad de energía, para cada ventana, es normalizado sobre la energía total (Sánchez-Sesma *et al.* 2011):

$$\frac{H(\omega)}{V(\omega)} = \sqrt{\frac{E_i(\omega) + E_j(\omega)}{E_k(\omega)}} \tag{5.2}$$

$$E_i(\omega) = \frac{1}{l}\sum_{l=1}^{n}\left[\frac{\left(u_i^l(\omega)\right)^2}{F_l(\omega)}\right];\, F_l(\omega) = \left(u_i^l(\omega)\right)^2 + \left(u_j^l(\omega)\right)^2 + \left(u_k^l(\omega)\right)^2 \tag{5.3}$$

Donde $u_i^l(\omega)$ es el espectro de enegia de los desplazamientos en dirección *i* para cada ventana de tiempo *l* en el dominio de la frecuencia (ω). $F_l(\omega)$ representa la energía espectral total para cada ventana *l*. $E_i(\omega)$ es el promedio del cociente de la densidad de energía espectral sobre la energía espectral total para cada ventana *l*. Este último procesamiento se basa solo en la segunda hipótesis básica de un campo difuso que menciona que las ondas sísmicas inciden de todas direcciones con igual intensidad, en otras palabras, el campo es acimutalmente isótropo.

A partir de los resultados de la Equipartición del ruido sísmico ambiental en este trabajo, se ha estado estudiado una forma de procesar el ruido sísmico ambiental denominado "Correlación Intemporal "(CI). Este procesamiento se basa en dos de las tres hipótesis de un campo difuso (Murray, 1996): 1.- En un campo de ondas aleatorio; las fases de las ondas son aleatorias y 2.- En un espacio abierto, la amplitud de las ondas es la misma en cualquier punto del dominio espacial y el campo es espacialmente homogéneo. Para aproximarnos a la primera hipótesis, los datos del ruido sísmico ambiental, en un registro continuo, son seccionados en ventanas y correlacionadas en diferente tiempo (intemporal) y para la segunda hipótesis, las ventanas correlacionadas son normalizadas en su espectro de energía y promediadas:

$$E_i^l(\omega) = \frac{1}{n}\sum_{m=1}^{n}\left[\left|u_i^l(\omega) * u_i^m(\omega)\right|\right] \tag{5.4}$$

Donde $E_i^l(\omega)$ es el promedio de la CI para la ventana de tiempo *l* en la componente en dirección *i*; $u_i^l(\omega) * u_i^m(\omega)$ indica la correlación cruzada de los desplazamientos $u_i^l(\omega)$ en la dirección *i* de la ventana de tiempo *l* con los desplazamientos $u_i^m(\omega)$ en la dirección *i* de la ventana de tiempo *m*. | | indica la normalización de energía; ω indica la frecuencia. Para obtener el cociente espectral H/V se realiza el promedio de la raíz cuadrada del cociente de la CI de las componentes horizontales con respecto a la vertical:

$$\frac{H(\omega)}{V(\omega)} = \frac{1}{n}\sum_{l=1}^{n}\sqrt{\frac{E_1^l(\omega) + E_2^l(\omega)}{E_3^l(\omega)}} \tag{5.5}$$

Donde $E_i^l(\omega)$ es el promedio de la CI para la ventana de tiempo *l* en la componente en dirección *i=1,2,3.* En la figura 5.1 se observa una comparación del HVSR obtenida mediante las ecuaciones (5.1) y (5.4). para los datos de un sismo con una longitud de 50 min de duración. Antes de obtener el HVSR, primero se realizó el preprocesamiento de la señal quitando la línea base y la tendencia. Posteriormente, se dividió el registro de RSA en ventanas de 120 seg de longitud. En la figura 5.1 a) se muestra el HVSR obtenido mediante la ecuación (5.1); las líneas de colores representan cada HVSR asociado a cada ventana de tiempo; la línea roja representa el promedio general del HVSR y las líneas negras discontinuas representan la desviación estándar del HVSR. En el panel b) se muestra el HVSR obtenido mediante la ecuación (5.4); las líneas de colores representan cada HVSR asociado a cada ventana de tiempo con una longitud de 120 seg y un traslape al 90%. La línea roja representa el promedio general del HVSR y las líneas negras discontinuas representan la desviación estándar del HVSR. En el panel c) se observa el registro del sismo para la componente vertical; las líneas verticales de colores representan cada una de las ventanas con una longitud de 120 seg. En el panel d) y e) se muestra el HVSR en función del tiempo (HVgrama) obtenido mediante la ecuación (5.1) y (5.4) respectivamente. En general, el HVSR obtenida mediante procesamiento estándar muestra una gran variación de amplitud en la frecuencia característica (1.5 Hz) con valores que oscilan entre 2 y 25. Por el contrario, el HVSR obtenido mediante CI muestra una variación de su amplitud en la frecuencia característica con valores entre 8 y 18 lo cual implica una desviación estándar menor. Además, en los HVgramas se muestra una estabilización de la amplitud de los HVSR a lo largo del tiempo, mientras que el HVSR estándar se observa que no emerge la forma en el tiempo de 1500 seg. Estos resultados se muestran en la sección 1, donde se compara la estabilización de energía S/P con el HVgrama donde se observa que cuando la señal no alcanza la estabilización de energías, el HVSR no se recupera. Es decir, parte de la coda sísmica no es de carácter difusivo y por lo tanto no se puede recuperar la función de Green.

Sin embargo, el HVSR promedio para los dos procedimientos muestra un comportamiento similar con una amplitud de ~12 en la frecuencia característica. A partir de estos resultados se propone en este trabajo la siguiente hipótesis:

"El HVSR de ruido sísmico ambiental con carácter difusivo es un proceso ergódico para tiempos muy largos de tiempo".

Esto implica que el HVSR converge en tiempos muy largos de medición de RSA, independientemente del tipo de procesamiento de los datos. Esta hipótesis abre una nueva línea de investigación donde se pueda llevar a cabo la obtención del HVSR de ruido sísmico ambiental en diferentes ambientes y estudiar sus las características difusivas del mismo, Esto permitiría tener evidencias que validen la hipótesis aquí planteada. Por el momento, en este trabajo se ha desarrollado un software de interfaz gráfica en el cual se puede calcular el HVSR en la forma estándar y con la nueva propuesta de CI. Este software se le ha llamado *HVprocess* y actualmente está en su versión beta (ver figura 5.2).

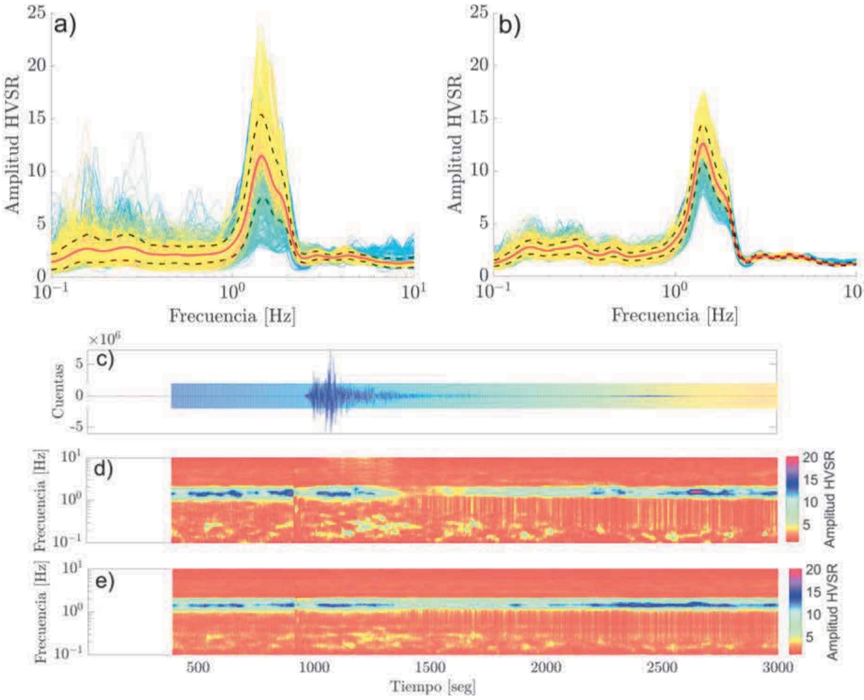

Figura 5.1.-a) HVSR obtenido mediante la ecuación 5.1. b) HVSR obtenido mediante la ecuación 5.4. Las líneas de colores representan cada HVSR asociado a cada ventana de tiempo; la línea roja representa el promedio general del HVSR y las líneas negras discontinuas representan la desviación estándar del HVSR. Panel c) Registro de un sismo para la componente vertical; las líneas verticales de colores representan cada una de las ventanas con una longitud de 120 seg. panel d) y e) se muestra el HVSR en función del tiempo (HVgrama) obtenidos mediante la ecuación 5.1 y 5.4 respectivamente. Los colores representan el valor de la amplitud.

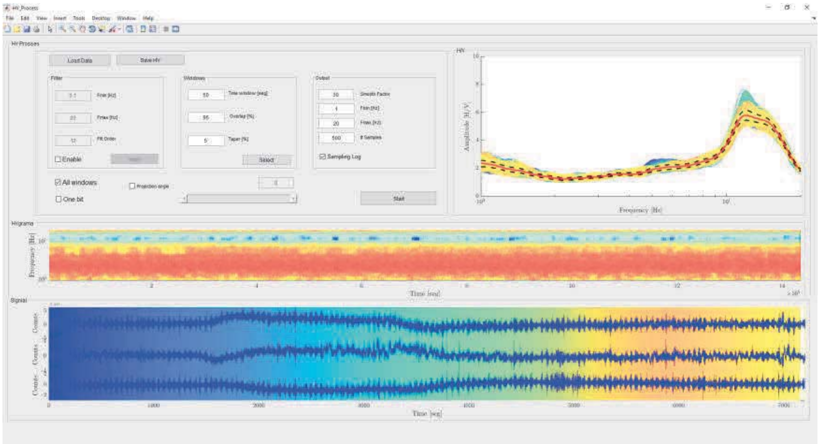

Time window [seg] 50

Taper [%] 5

Smooth Factor 30

Fmin [Hz] 1

Fmax [Hz] 20

Samples 500

☑ Sampling Log

☐ Enable

☑ All windows

☐ One bit

☐ Projection angle

Figura 5.2.- Diseño del software *HVProcess* v-beta para el cálculo del HVSR mediante el procesamiento estándar y el procesamiento de Correlaciones Intemporales

5.2.- Partición de energía sísmica para medios estratificados

Para que un campo de ondas sea de carácter difusivo, Weaver (1982) ha establecido que, para un estado mecánico de un medio en vibración, puede ser descrito en función de sus modos normales; la energía sísmica está equitativamente distribuida en todos los modos y estados (diferentes tipos de ondas elásticas). Es decir, que cumplen el Principio de Equipartición de la energía. Para observar esta distribución de energías, Weaver (1985) obtiene los valores de partición de energía para las ondas P-SV, SH, y Rayleigh para dos casos: 1.- Desplazamientos verticales generados por una fuerza puntual vertical. 2.- Desplazamientos horizontales generados por una fuerza puntual horizontal. Ambos casos son aplicados a un modelo de un semiespacio. Los resultados obtenidos muestran que la energía se distribuye en los distintos tipos de ondas: Para el primer caso, las ondas P se lleva el 8% de energía, las ondas SV les corresponde el 26% y el otro 66% corresponde a las ondas superficiales de Rayleigh. Para el segundo caso, las ondas SH se llevan la mayor parte de la energía sísmica con un 60 %; las ondas superficiales de Rayleigh el 18%; las ondas SV el 16% y las ondas P solo el 6%.

Sin embargo, estos resultados son válidos solamente para un semiespacio. En la naturaleza, el fenómeno es más complejo, por lo que surge la necesidad de extender estas observaciones para medios estratificados. Hoy en día, existe la formulación matemática y física para realizar esta investigación. Para obtener la distribución de la energía de los diferentes tipos de ondas en medios estratificados, este trabajo se apoya en el desarrollo de García-Jerez *et al*. (2013) para calcular las partes imaginarias de la Función de Green (FG) del campo de desplazamientos. García-Jerez *et al.* (2016) desarrolla las expresiones de la parte imaginaria de la FG, en el caso especial cuando la fuente y receptor coinciden, y pueden ser escritos es su forma compacta:

$$
\begin{aligned}
Im[G_{11}^{P-SV}(\omega)] &= \underbrace{-\frac{1}{4}\sum_{m\in Rayleigh}\chi_m^2 A_{Rm}}_{Ondas\quad Superficiales} + \underbrace{\frac{1}{4\pi}\int_0^{\frac{\omega}{\beta_N}} Re[f_{PSV}^{H}(k)]_{4^{th}}\,dk}_{Ondas\ de\ Cuerpo} \\
Im[G_{22}^{SH}(\omega)] &= \underbrace{-\frac{1}{4}\sum_{m\in Love} A_{Lm}}_{Ondas\quad Superficiales} + \underbrace{\frac{1}{4\pi}\int_0^{\frac{\omega}{\beta_N}} Re[f_{SH}(k)]_{4^{th}}\,dk}_{Ondas\ de\ Cuerpo} \qquad (5.6) \\
Im[G_{33}^{P-SV}(\omega)] &= \underbrace{-\frac{1}{2}\sum_{m\in Rayleigh} A_{Rm}}_{Ondas\quad Superficiales} + \underbrace{\frac{1}{2\pi}\int_0^{\frac{\omega}{\beta_N}} Re[f_{PSV}^{V}(k)]_{4^{th}}\,dk}_{Ondas\ de\ Cuerpo}
\end{aligned}
$$

Donde $f_{PSV}^{V}(k)$; $f_{SH}(k)$; $f_{PSV}^{V}(k)$ son los kernels asociados a las ondas de cuerpo, χ_m^2 es la elipticidad del m-ésimo modo de las ondas de Rayleigh, A_{Rm} y A_{Lm} corresponden a la respuesta del medio para el m-ésimos modos de las ondas de Rayleigh and Love, respectivamente (Harkrider, 1964). Con las ecuaciones (5.5) se pueden separar las contribuciones de las ondas de cuerpo P-SV y SH y las ondas superficiales; Rayleigh y Love en sus distintos modos.

Para verificar los valores de la partición de energía para un semiespacio obtenidos por el Dr. Richard Weaver, se realizó el mismo ejemplo utilizando las ecuaciones 5.5. En la figura 5.3 se muestra los valores de partición de energía, en función de la frecuencia, para un semiespacio con valores de Vp= 1732 m/s; Vs=1000 m/s y densidad=2000 kg/m3. Para los desplazamientos horizontales generados por una fuerza puntal horizontal (Im$G_{11}(w)$ y Im$G_{22}(w)$), la partición de energía del modo fundamental de las ondas de Rayleigh es del 18%; para las ondas de cuerpo P-SV, la partición de energía es del 22% (el cual es la suma de la partición de energía de las ondas P=6% y SV=16%) y para las ondas SH el valor es del 60%, mientras que las ondas de Love no existen para este caso. Para los desplazamientos verticales generados por una fuerza puntal vertical (Im$G_{33}(w)$), la partición de energía del modo fundamental de las ondas de Rayleigh es del 66%; Para el caso de las ondas de cuerpo P-SV, la partición de energía es del 34% (el cual es la suma de la partición de energía de las ondas P=8% y SV=26%). Estos resultados son similares a los obtenidos por Weaver (1985).

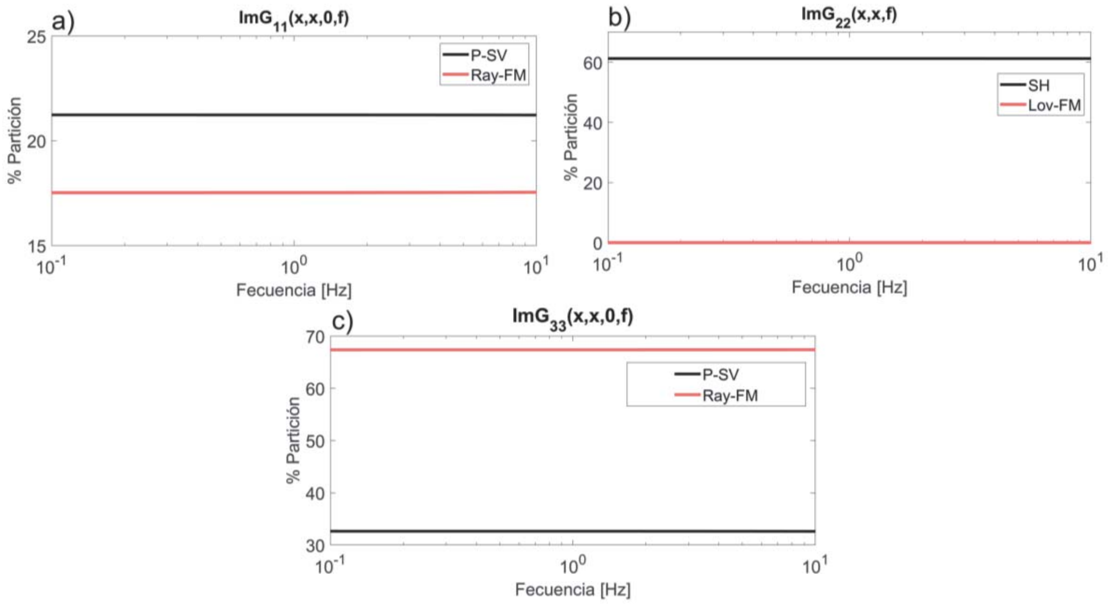

Figura 5.3.- Partición de energía de las ondas elásticas para un semiespacio. a) y b) Partición de energía para los desplazamientos horizontales generados por una fuerza puntal horizontal (ImG11(w) y ImG22(w)). c) Partición de energía para los desplazamientos verticales generados por una fuerza puntal vertical (ImG33(w)). La línea negra representa el valor de la partición de energía para las ondas de cuerpo P-SV y SH. Las líneas rojas representan el valor la partición de energía para las ondas superficiales Rayleigh y Love.

En el ejemplo anterior, la partición de energía es constante para todo el rango de frecuencias. Sin embargo, para un medio estratificado con diferentes valores de parámetros elásticos, esta partición de energía es muy complejo. En la figura 5.3 se muestra la distribución de la partición de energía para un modelo de una capa sobre un semiespacio (ver tabla 5.1). Para la parte imaginaria $G_{11}(w)$ y Im$G_{22}(w)$ (figura 5.3 a-b), se observa que la energía de las ondas de cuerpo y superficiales varían con respecto a la frecuencia. Este comportamiento también se observa para la parte imaginaria $G_{33}(w)$ (figura 5.3 d). Sin embargo, el rango de frecuencias entre 1 y 2 Hz es especial interés; para la parte imaginaria $G_{11}(w)$ se observa que las ondas de cuerpo P-SV y SH tienen valores de partición muy pequeños (~1%) mientras que los modos fundamentales de las ondas de Rayleigh y Love se llevan la mayor parte de la energía; 30% y 60%, respectivamente. Por el contrario, para la parte imaginaria $G_{33}(w)$, se observa que las ondas de cuerpo P-SV aumentan su energía hasta un 70% y después desciende drásticamente hasta 3%. Por otro lado, el comportamiento para el modo fundamental de las ondas de Rayleigh es sorprendente, después de tener el ~80% de la energía, decae rápidamente a valores de %15 y posteriormente sube drásticamente a tener valores cercanos al 95% de la energía. Todo esto sucede en el rango de frecuencias donde el H/V, para el mismo modelo, se presentan las frecuencias de la máxima y la mínima amplitud.

Con base en estos resultados preliminares, el análisis de la partición de energía, con esta metodología, abre la posibilidad de una nueva línea de investigación la cual permitiría sustentar el efecto multimodo y la limitación para identificar el modo fundamental, con respecto a los modos superiores, de las ondas superficiales en los diagramas de dispersión. Además, se puede describir una relación explicita entre las curvas de dispersión y los cocientes espectrales HV bajo la teoría de campos difusos y de realizar experimentos controlados con datos de RSA.

Tabla 5.1. Descripción de modelo 1

H	**Vp m/s**	**Vs m/s**	**Densidad kg/m3**
65	433	250	2000
∝	1732	1000	2000

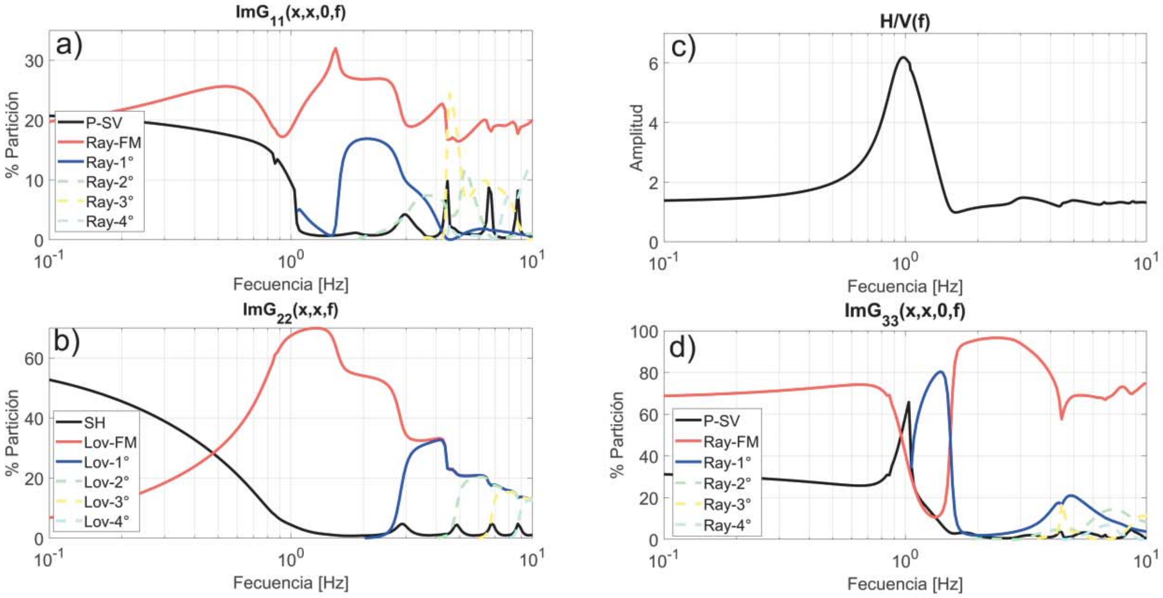

figura 5.3.- Partición de energía de las ondas elásticas para el modelo de la tabla 1. a) y b) Partición de energía para los desplazamientos horizontales generados por una fuerza puntal horizontal (ImG11(w) y ImG22(w)). c) Cociente espectral H/V. d) Partición de energía para los desplazamientos verticales generados por una fuerza puntal vertical (ImG33(w)). La línea negra representa el valor de la partición de energía para las ondas de cuerpo P-SV y SH. Las líneas rojas representan el valor la partición de energía para las ondas superficiales Rayleigh y Love. Las líneas de colores representan los modos superiores

Bibliografía

Aki, K., 1957. Space and time spectra of stationary stochastic waves, with special reference to microtremores, *Bull. Earth. Res. Inst.,* **35,** 415–456.

Aki, K. & Chouet, B., 1975. Origin of coda waves: source, attenuation, and scattering effects, *J. Geophys. Res.,* **80**(23), 3322–3342. doi:10.1029/JB080i023p03322.

Arai, H. & Tokimatsu, K., 2004. S-wave velocity profiling by inversion of microtremor HVSR spectrum, *Bull. Seism. Soc. Am.,* **94**(1), 53–63.

Ardhuin, F., Stutzmann, E., Schimmel, M. & Mangeney, A., 2011, Ocean wave sources of seismic noise, *J. Geophys. Res.- Oceans*, **116**, C09004.

Astaneh, A. V. & Guddati, M. N., 2016. Improved inversion algorithms for near-surface characterization. *Geophys. J. Int.* **206**, 1410–1423 doi: 10.1093/gji/ggw192.

Asten, M.W., 1978. Geological control of the three-component spectra of Rayleigh-wave microseisms, *Bull. Seism. Soc. Am.*, **68**(6), 1623–1636.

Asten, M.W. & Henstridge, J.D., 1984. Arrays estimators and the use of microseisms for reconnaissance of sedimentary basins, *Geophysics* **49**(11), 1828–1837. doi: 10.1071/EG984263.

Baena-Rivera, M., Perton, M. & Sánchez-Sesma, F. J., 2016. Surface-Wave Retrieval from Generalized Diffuse Fields in 2D Synthetic Models of Alluvial Valleys. *Bull. Seism. Soc. Am.,* Vol. **106**, No. 6, pp. doi: 10.1785/0120160084.

Batres, L., 1993. El “descubrimiento” de la Pirámide del Sol, *Arqueología Mexicana*, **1**, 45-48.

Bensen, G.D., Ritzwoller, M. H., Barmin, M. P., Levshin, A. L. Lin, F., Moschetti, M. P., Shapiro N. M. and Yang, Y., 2007. Processing seismic ambient noise data to obtain reliable broad-band surface wave dispersion measurements. *Geophys. J. Int.* **169**, 1239–1260 doi: 10.1111/j.1365-246X.2007.03374.x.

Bonnefoy-Claudet, S., Cotton, F., & Bard, Pierre-Yves., 2006. The nature of noise wavefield and its applications for site effects studies: A literature review. *Earth-Science Reviews* **79** 205–227**.** doi:10.1016/j.earscirev.2006.07.004.

Bodin, P., Gomberg J., Singh S. K., & Santoyo, M., 1997. Dynamic deformations of shallow sediments in the Valley of Mexico, Part I: three dimensional strains and rotations recorded on a seismic array, *Bull. seism. Soc. Am.*, **87,** 528–539.

Boué, P., Denolle, M., Hirata, N., Nakagawa, S., & Beroza, G. C., 2016. Beyond basin resonance: characterizing wave propagation using a dense array and the ambient seismic field. *Geophys. J. Int.* **206**, 1261–1272. doi: 10.1093/gji/ggw205.

Brenguier, F., Shapiro, N. M., Campillo, M., Nercessian, A., & Ferrazzini V., 2007. 3-D surface wave tomography of the Piton de la Fournaise volcano using seismic noise correlations, *Geophys. Res. Lett.*, **34**, L02305, doi:10.1029/2006GL028586.

Campillo, M., 2006. Phase and Correlation in ‘Random’ Seismic Fields and the Reconstruction of the Green Function, *Pure appl. Geophys.,* **163** (2-3), 475-502. doi: 10.1007/s00024-005-0032-8.

Capon, J., 1969. High-resolution frequency-wavenumber spectrum analysis, *Geophysics.* **34,** no. 1, 21–38.

Castellaro, S. & Mulargia, F., 2006. The Effect of Velocity Inversions on HVSR, *Pure Appl. Geophys.* **166**, 567–592. doi: 10.1007/s00024-009-0474-5.

Chávez-García, F. J., & Luzón, F., 2005. On the correlation of seismic microtremors. *Journal of Geophysical Research: Solid Earth,* **110**(B11). doi: 10.1029/2005JB003671.

Coelho, M. J., Santos, J., & Pereira, M., 2018. Stacking of multilayout and multichannel surface-wave data on the f-k domain. *J. Appl. Geophys.*, **159**, 93-107. doi: 10.1016/j.jappgeo.2018.08.006.

Cowgill, George L., 2015. Ancient Teotihuacan. Early Urbanism in Central México. Cambridge University Press.

Dai, K., Liu, K., Li, X., You, Q., Tang, H., & Xu, Q., 2019. Application of passive multichannel analysis of surface waves method at sites close to underground railways-Problems and a case study. *J. Appl. Geophys.*, **164**, 191-199. doi: 10.1016/j.jappgeo.2019.03.009.

Farrugia, D., Paolucci, E., D'Amico, S., & Galea, P., 2016. Inversion of surface wave data for subsurface shear wave velocity profiles characterized by a thick buried low-velocity layer. *Geophys. J. Int.*, **206**(2), 1221-1231. doi: 10.1093/gji/ggw204.

Friederich, A., Kruger F. & Klinge, K., 1998. Ocean-generated microseismic noise located with the GRFO array, *J. Seismol.,* **2**, 47–64. doi: 10.1023/A:1009788904007.

Foti, S., Parolai, S., Albarello, D. & Picozzi, M., 2011. Application of Surface-Wave Methods for Seismic Site Characterization. *Surveys in Geophysics*, **32**(6), 777-825. doi: 10.1007/s10712-011-9134-2.

Gamio, M., 1922. Introducción, síntesis y conclusiones de la obra La población del valle de Teotihuacán. Secretaria de Educación Pública, Dirección de Talleres Gráficos, México.

Gao, L., Xia, J., & Pan, Y., 2014. Misidentification caused by leaky surface wave in high-frequency surface wave method. *Geophys. J. Int.*, **199**(3), 1452-1462. doi: 10.1093/gji/ggu337.

Gao, L., Xia, J., Pan, Y., & Xu, Y., 2016. Reason and Condition for Mode Kissing in MASW Method. *Pure Appl. Geophys*, **173**(5), 1627-1638. doi: 10.1007/s00024-015-1208-5.

García-Jerez, A., Luzón, F., Navarro, M. & Pérez-Ruiz, J. A., 2008. Determination of elastic properties of shallow sedimentary deposits applying a spatial autocorrelation method. *Geomorphology.* **93,** 74–88. doi: 10.1016/j.geomorph.2006.12.018.

García-Jerez A., F. J. Sánchez-Sesma., 2015. Slowly Attenuating P-SV Leaky Waves in a Layered Elastic Halfspace. Effects on the Coherences of Diffuse Wavefields. *Wave Motion*, **54**, 43–57. doi: i.org/10.1016/j.wavemoti.2014.11.010.

García-Jerez, A., Piña-Flores, J., Sánchez-Sesma, F. J., Luzón, F., & Perton, M., 2016. A computer code for forward calculation and inversion of the HVSR spectral ratio under the diffuse field assumption, *Comput. Geosci*., **97**, 67-78. doi:10.1016/j.cageo.2016.06.016.

García-Jerez, A., Seivane, H., Navarro, M., Martínez-Segura, M., & Piña-Flores, J., 2019. Joint analysis of Rayleigh-wave dispersion curves and diffuse-field HVSR for site characterization: The case of El Ejido town (SE Spain). *Soil Dyn. Earthq. Eng*., 121, 102-120. doi: 10.1016/j.soildyn.2019.02.023.

Gómez Moreno, R. A., 2004. Guía de proyecciones cartográficas (No. IN 526.8 G654G.). Instituto Nacional de Estadística, Geografía e Informática (INEGI) México.

Gudmundsson, O., Khan, A., & Voss, P., 2007. Rayleigh-wave group-velocity of the Icelandic crust from correlation of ambient seismic noise, *Geophys. Res. Lett.,* **34**(14), L14314. doi:10.1029/2007GL030215.

Hennino, R., Tregoures, N., Shapiro, N.M., Margerin, L., Campillo, M., Van Tiggelen B.A. & Weaver, R. L., 2001. Observation of equipartition of seismic waves, *Phys. Rev. Lett.,* **86**, 3447–3450. doi: 10.1103/PhysRevLett.86.3447.

Ibáñez Bravo, Silvia 2012 Trabajos de conservación y restauración, Pirámide del Sol. Informe Parcial de los trabajos realizados durante la temporada 2012 Tomo II.: 1-91. Programa de Conservación e Investigación en el Complejo Arquitectónico de la Pirámide del Sol, Teotihuacán, México. Dirección Alejandro Sarabia. Archivo Técnico de la Coordinación Nacional de Arqueología. INAH. México.

Ikeda, T., Matsuoka, T., Tsuji, T. & Hayashi, K., 2012. Multimode inversion with amplitude response of surface waves in the spatial autocorrelation method. *Geophys. J. Int.* **190,** 541–552 doi: 10.1111/j.1365-246X.2012.05496.x.

Kanai, K., Tanaka, T. & Okada, K., 1954. Measurement of the microtremor, *Bull. Earthquake Res. Inst. Tokyo Univ.* **32,** 199–210.

Kawase, H., Sánchez-Sesma, F.J. & Matsushima, S., 2011. The optimal use of horizontal-to-vertical spectral ratios of earthquake motions for velocity inversions based on diffuse-field theory for plane waves, *Bull. Seism. Soc. Am.*, **101**(5), 2001–2014. doi: 10.1785/0120100263.

Kawase, H., Matsushima, S., Satoh, T. & Sánchez-Sesma, F.J., 2015. Applicability of Theoretical Horizontal-to-Vertical Ratio of Microtremors Based on the Diffuse Field Concept to Previously Observed Data, *Bull. Seism. Soc. Am.*, **105**(6), 3092–3103. doi: 10.1785/0120150134.

Khalil, A.E., Abdel Hafi, H.E., Girgis M., & Taha M.A., 2016. Earthquake ground motion simulation at Zoser pyramid using the stochastic method: A step toward the preservation of an ancient Egyptian heritage. NRIAG *Journal of Astronomy and Geophysics*, doi: 10.1016/j.nrjag.2016.11.003.

Köhler, A., Ohrnberger, M., Scherbaum, F., Wathelet, M. & Cornou, C., 2007. Assessing the reliability of the modified three-component spatial autocorrelation technique. *Geophys. J. Int.* **168**, 779–796 doi: 10.1111/j.1365-246X.2006.03253.x.

Lai, C. G., Mangriotis, M-D. & Rix G. J., 2014. An explicit relation for the apparent phase velocity of Rayleigh waves in a vertically heterogeneous elastic half-space. *Geophys. J. Int.* **199**, 673–687 doi: 10.1093/gji/ggu283.

Larose, E., Margerin, L., Campillo, M. & Van Tiggelen, B.A., 2004. Weak localization of seismic waves, *Phys. Rev. Lett*., **93**, 048501. doi: 10.1103/PhysRevLett.93.048501.

Lermo, J. & Chávez-García, F.J., 1993. Site effect evaluation using spectral ratios with only one station, *Bull. Seism. Soc. Am.*, **83**(5), 1574–1594.

Lin, C. P., Lin, C. H., & Chien, C. J., 2017. Dispersion analysis of surface wave testing–SASW vs. MASW. *J. Appl. Geophys.*, **143**, 223-230. doi: /10.1016/j.jappgeo.2017.05.0080926-9851.

Lomnitz, C., 1997. Frequency response of a strainmeter, *Bull. Seism. Soc. Am.*, **87,** 1078–1080.

Lontsi, A. M., Sánchez-Sesma, F. J., Molina-Villegas, J. C., Ohrnberger, M., & Krüger, F., 2015. Full microtremor HVSR (z, f) inversion for shallow subsurface characterization, *Geophys. J. Int.*, **202**(1), 298-312. doi: 10.1093/gji/ggv132.

Louie, J.N., 2001. Faster, Better Shear wave velocity to 100m depth from ReMi arrays. *Bull. Seism. Soc. Am.,* **91**:2, 347-364**.**

Lunedei, E. & Albarello, D., 2009. On the seismic noise wavefield in a weakly dissipative layered Earth. *Geophys. J. Int.* **177**, 1001–1014 doi: 10.1111/j.1365-246X.2008.04062.x.

Ma, Y., Clayton, R. W. & Li, D., 2016. Higher-mode ambient-noise Rayleigh waves in sedimentary basins. *Geophys. J. Int.* 206, 1634–1644 doi: 10.1093/gji/ggw235.

Manolis, G. D. and D. E. Beskos., 1988. Boundary Element Methods in Elastodynamics, Unwin Hyman Ltd., London.

Millon, R., & Drewitt, B., 1961. Earlier Structures within the Pyramid of the Sun at Teotihuacan. *American Antiquity*, **26**(3), 371-380. doi:10.2307/277403.

Millon, R., Drewitt, B. & Bennyhoff, J., 1965. The Pyramid of the Sun at Teotihuacán: 1959 Investigations. *Transactions of the American Philosophical Society*, **55**(6), 1-93. doi:10.2307/1005892.

Maranò, S., Hobiger, M., & Fäh, D., 2017. Retrieval of Rayleigh wave ellipticity from ambient vibration recordings. *Geophys. J. Int.* **209**, 334–352 doi: 10.1093/gji/ggx014.

Margerin, L., Van Tiggelen, B. A. & Campillo, M., 2001. Effect of absorption on energy partition of elastic waves in the seismic coda, *Bull. Seism. Soc. Am.*, **91**(3), 624-627. doi: 10.1785/0120000228.

Margerin, L., Campillo, M., Van Tiggelen, B. A., & Hennino, R., 2009. Energy partition of seismic coda waves in layered media: Theory and application to Pinyon Flats Observatory, *Geophys. J. Int.*, **177**(2), 571-585. doi: 10.1111/j.1365-246X.2008.04068.x.

Matsushima, S., Hirokawa, T., De Martin, F., Kawase, H. & Sánchez-Sesma, F.J., 2014. The effect of lateral heterogeneity on horizontal-to-vertical spectral ratio of microtremors inferred from observation and synthetics, *Bull. Seism. Soc. Am.*, **104**, 381–393. doi: 10.1785/0120120321.

Matsushima, S., Kosaka, H. & Kawase, H., 2017. Directionally dependent horizontal-to-vertical spectral ratios of microtremors at Onahama, Fukushima, Japan, *Earth, Planets and Space*. **69**(1), 96. doi: 10.1186/s40623-017-0680-9.

Maraschini, M., Ernst, F., Foti, S., & Socco, L. V., 2010. A new misfit functions for multimodal inversion of surface waves. *Geophysics*, **75**(4), G31-G43. doi 10.1190/1.3436539.

Mi, B., Xia, J., Shen, C., Wang, L., Hu, Y., & Cheng, F., 2017. Horizontal resolution of multichannel analysis of surface waves. *Geophysics*, **82**(3), EN51-EN66. doi. 10.1190/geo2016-0202.1.

Mulargia, F., 2012. The seismic noise wavefield is not diffuse. *J. Acoust. Soc. Am.*, **131**, 2853–2858. doi: 10.1121/1.3689551.

Murray, H., 1996. When is difuse-field theory applicable? *Applied Acoustics*, **49**(3):197–207.

Nakamura, Y., 1989. A method for dynamic characteristics estimation of subsurface using microtremor on ground surface, *QR of RTRI* **30**(1), 25-33.

Nakamura, Y., 2000, Clear identification of fundamental idea of Nakamura's technique and its applications, *in* 'Proceedings of the 12th World Conference on Earthquake Engineering', Auckland New Zealand.

Ning, L., Dai, T., Wang, L., Yuan, S., & Pang, J., 2018. Numerical investigation of Rayleigh-wave propagation on canyon topography using finite-difference method. *J. Appl. Geophys.*, **159**, 350-361. doi: 10.1016/j.jappgeo.2018.09.0070926-9851.

Noguera, E., 1935. Antecedentes y relaciones de la cultura teotihuacana. *El México Antiguo* Ediciones Mexicanas.

Ohori, M., Mobata, A. & Wakamatsu, K., 2002. A comparison of ESAC and FK methods of estimating phase velocity using arbitrarily shaped microtremor arrays, *Bull. Seism. Soc. Am.,* **92**(6), 2323– 2332**.**

Pan, Y., Xia, J., Gao, L., Shen, C., & Zeng, C., 2013. Calculation of Rayleigh-wave phase velocities due to models with a high-velocity surface layer. *J. Appl. Geophys.*, **96**, 1-6. doi:10.1016/j.jappgeo.2013.06.005.

Papanicolaou, G. C., Ryzhik, L. V. & Keller. J. B., 1996. Stability of the P- to S-energy ratio in the diffusive regime. *Bull. Seism. Soc. Am.*, **86,** 1107–1115.

Pérez-Ruiz, J. A., Luzón, F. & Sánchez-Sesma, F. J., 2008. Retrieval of elastic Green's tensor near a cylindrical inhomogeneity from vector correlations, *Commun. Comput. Phys.*, **3**(1), 250-270. doi:10.1029/. 2006GL026454.

Perton, M. & Sánchez-Sesma, F.J., 2016. Green's function calculation from equipartition theorem, *J. acoust. Soc. Am*., **140**(2), 1309-1318. doi: 10.1121/1.4961208.

Perton, M., Spica, Z., & Caudron, C., 2018. Inversion of the horizontal-to-vertical spectral ratio in presence of strong lateral heterogeneity, *Geophys. J. Int.*, **212**, 930-941. doi: 10.1093/gji/ggx458.

Piña-Flores, J., Perton, M., García-Jerez, A., Carmona, E., Luzón, F., Molina-Villegas, J. C., & Sánchez-Sesma, F. J., 2017. The inversion of spectral ratio HVSR in a layered system using the Diffuse Field Assumption (DFA), *Geophys. J. Int.*, **208**(1), 577-588. doi: 10.1093/gji/ggw416.

Przybilla, J., Korn, M. & Wegler, U., 2006. Radiative transfer of elastic waves versus finite difference simulations in two-dimensional random media, *J. Geophys. Res.*, **111**, B04305. doi: 10.1029/2005JB003952.

Rawlinson, N. & Sambridge, M., 2004. Wave front evolution in strongly heterogeneous layered media using the fast-marching method, *Geophys. J. Int.*, **156**, 631–647, doi: 10.1111/j.1365-246X.2004.02153.x.

Rawlinson, N., & Sambridge, M., 2005. The fast-marching method: an effective tool for tomographic imaging and tracking multiple phases in complex layered media. *Exploration Geophysics*, **36**(4), 341-350. doi: 10.1071/EG05341.

Rhie, J. & Romanowicz, B., 2004. Excitation of Earth's continuous free oscillations by atmosphere–ocean–seafloor coupling. Nature, **431**(7008), p.552. doi: 10.1038/nature02942.

Ritzwoller, M.H. & Levshin, A.L., 1998. Eurasian surface wave tomography: group velocities, *J. geophys. Res.*, **103**, 4839–4878. doi: 10.1029/97JB02622

Ritzwoller, M. H., Lin, F. C., & Shen, W., 2011. Ambient noise tomography with a large seismic array, *C. R. Geosci.*, **343**(8), 558-570. doi: 10.1016/j.crte.2011.03.007.

Rivet, D., Campillo, M., Sanchez-Sesma, F., Shapiro, N. M., & Singh, S. K., 2015. Identification of surface wave higher modes using a methodology based on seismic noise and coda waves. *Geophys. J. Int*., **203**, 856–868. doi: 10.1093/gji/ggv339.

Sabra, K.G., Gerstoft, P., Roux, P., Kuperman, W.A., & Fehler, M.C., 2005. Extracting timedomain Green's function estimates from ambient seismic noise, *Geophys. Res. Lett.,* **32**, L03310, doi: 10.1029/2004GL021862.

Sarabia, A. & Núñez, N., 2017. The Sun Pyramid architectural complex in Teotihuacan: vestiges of worship and veneration. Teotihuacan. *City of Water, City of Fire*. pp 62- 67. Editor Matthew Robb. Fine Arts Museums of San Francisco California.

Sánchez-Sesma, F. J. & Campillo, M., 2006. Retrieval of the Green's Function from Cross Correlation: The Canonical Elastic Problem. *Bull. Seism. Soc. Am.*, **96**(3): 1182–1191. doi: https://doi.org/10.1785/0120050181.

Sánchez-Sesma, F. J., Pérez-Ruiz, J. A., Campillo, M. & Luzón, F., 2006. Elastodynamic 2D Green function retrieval from cross-correlation: Canonical inclusion problem', *Geophys. Res. Lett.,* **33**, L13305. doi:10.1029/2006GL026454.

Sánchez-Sesma, F. J., Rodríguez, M., Iturrarán-Viveros, U., Luzón, F., Campillo, M., Margerin, L., García-Jerez, A., Suárez, M., Santoyo, M. A. & Rodríguez-Castellanos, A., 2011, A theory for microtremor HVSR spectral ratio: application for a layered médium, *Geophys. J. Int*., **186**, 221–225. doi: 10.1111/j.1365-246X.2011.05064.x.

Sánchez-Sesma, F. J., Weaver, R. L., Kawase, H., Matsushima, S., Luzón, F. & Campillo, M., 2011. Energy partitions among elastic waves for dynamic surface loads in a semi-infinite solid, *Bull. Seism. Soc. Am.*, **101**(4), 1704–1709. doi: 10.1785/0120100196.

Saygin, E., & Kennett, B. L., 2010. Ambient seismic noise tomography of Australian continent, *Tectonophysics*, **481**(1), 116-125. doi: 10.1016/j.tecto.2008.11.013.

Shapiro, N.M., Campillo, M., Margerin, L., Singh, S.K., Kostoglodov, V., and Pacheco, J., 2000. The energy partitioning and the diffusive character of the seismic coda, *Bull. Seism. Soc. Am.*, **90**, 655–665. doi: 10.1785/0119990021.

Shapiro, N.M. and Campillo, M., 2004, Emergence of broadband Rayleigh waves from correlations of the ambient seismic noise, *Geophys. Res. Lett.,* **31**, L07614. doi: 10.1029/2004GL019491.

Shapiro, N.M., Campillo, M., Stehly, L., and Ritzwoller, M., 2005. High resolution surface wave tomography from ambient seismic noise, *Science.,* **307**, 1615–1618. doi: 10.1126/science.1108339.

Sivaram, K., Gupta, S., Kumar, S., & Prasad, B. N. V., 2018. Shear velocity structural characterization around the Lonar crater using joint inversion of ambient noise HVSR and Rayleigh wave dispersion. *J. Appl. Geophys.*, **159**, 773-784. doi: 10.1016/j.jappgeo.2019.06.0220926-9851.

Spica, Z., Caudron, C., Perton, M., Lecocq, T., Camelbeeck, T., Legrand, D., Piña-Flores, J., Iglesias, A. & Syahbana, D.K., 2015. Velocity models and site effects at Kawah Ijen volcano and Ijen caldera (Indonesia) determined from ambient noise cross-correlations and directional energy density spectral ratios, *J. Volcanol. Geoth. Res*., **302**, 173–189. doi: 10.1016/j.jvolgeores.2015.06.016.

Spica, Z. J., Perton, M., Nakata, N., Liu, X. & Beroza. G. C., 2017. Site characterization at Groningen gas field area through joint surface-sorehole HVSR analysis, *Geophys. J. Int*., **212 (1)**, 412-421. doi: 10.1093/gji/ggx426.

Shuangxi, Z., 2009. Effective Dispersion Curve and Pseudo Multimode Dispersion Curves for Rayleigh Wave. *Journal of Earth Science*, Vol. **22**, No. 2, p. 226–230. doi: 10.1007/s12583-011-0175-8.

Sugiyama, S., Sugiyama, N., Sarabia-González A., 2014. El interior de la Pirámide del Sol en Teotihuacán. *Arqueología Mexicana*, **125**, 24-29.

Tokimatsu, K., Tamura, S. & Kojima, H., 1992. Effects of multiple modes on Rayleigh wave dispersion characteristics. *J. Geotech. Engrg.*, **118**(10): 1529-1543.

Ward, K. M., Porter, R. C., Zandt, G., Beck, S. L., Wagner, L. S., Minaya, E., & Tavera, H., 2013. Ambient noise tomography across the Central Andes, *Geophys. J. Int.*, **196** (2), 1264-1265. doi: 10.1093/gji/ggt166.

Wathelet, M., Chatelain, J.-L., Cornou, C., Di Giulio, G., Guillier, B., Ohrnberger, M. and Savvaidis, A., 2020. Geopsy: A User-Friendly Open-Source Tool Set for Ambient Vibration Processing. *Seismological Research Letters*, **91**(3), 1878--1889, doi: 10.1785/0220190360.

Weaver, R. L., 1982. On diffuse waves in solid media, *J. Acoust. Soc. Am*., **71**(6), 1608-1609. doi: 10.1121/1.387816.

Weaver, R. L., 1985. Diffuse elastic waves at a free surface, *J. Acoust. Soc. Am*., **78**(1), 131-136. doi: 10.1121/1.392576.

Wegler, U., Korn, M. & Przybilla, J., 2006. Modeling full seismogram envelopes using radiative transfer theory with born scattering coefficients, *Pure appl. Geophys*., **163,** 503–531. doi: 10.1007/s00024-005-0027-5.

Wu, H., Masaki K., Irikura K. & Sánchez-Sesma, F. J., 2017. Application of a simplified calculation for full waves microtremor HVSR based on the diffuse field approximation to identify underground velocity structures, *Earth, Planets and Space* **69**:162. DOI 10.1186/s40623-017-0746-8.

Xia, J., Miller, R.D. & Park C.B., 1999. Estimation of near-surface shear-wave velocity by inversion of Rayleigh waves. *Geophysics*. **64**, 3; 691-700. doi: 10.1190/1.1444578.

Yang, Y., & Ritzwoller, M. H., 2008. Characteristics of ambient seismic noise as a source for surface wave tomography, *Geochem. Geophys. Geosyst.,* **9** (2), Q02008. doi:10.1029/2007GC001814.

Zeng, C., Xia, J., Miller, R. D., Tsoflias, G. P., & Wang, Z., 2012. Numerical investigation of MASW applications in presence of surface topography. *J. Appl. Geophys.*, **84**, 52-60. doi:10.1016/j.jappgeo.2012.06.004.

Zhang, S. X. & Chan, L. S., 2009. Possible effects of misidentified mode number on Rayleigh wave inversion. *J. Appl. Geophys.,* **53**, 17– 29. doi: 10.1016/S0926-9851(03)00014.

Zheng, S., Sun, X., Song, X., Yang, Y., & Ritzwoller, M. H., 2008. Surface wave tomography of China from ambient seismic noise correlation, *Geochem. Geophys. Geosyst.,* **9** (5). doi:10.1029/2008GC001981.

Anexos

CERTIFICADO

Registro Público del Derecho de Autor

Para los efectos de los artículos 13, 162, 163 fracción I, 164 fracción I, 168, 169, 209 fracción III y demás relativos de la Ley Federal del Derecho de Autor, se hace constar que la **OBRA** cuyas especificaciones aparecen a continuación, ha quedado inscrita en el Registro Público del Derecho de Autor, con los siguientes datos:

AUTORES:	GARCIA JEREZ ANTONIO PIÑA FLORES JOSE
TITULO:	HV-INV
RAMA:	PROGRAMAS DE COMPUTACION
TITULARES:	GARCIA JEREZ ANTONIO PIÑA FLORES JOSE

Con fundamento en lo establecido por el artículo 168 de la Ley Federal del Derecho de Autor, las inscripciones en el registro establecen la presunción de ser ciertos los hechos y actos que en ellas consten, salvo prueba en contrario. Toda inscripción deja a salvo los derechos de terceros. Si surge controversia, los efectos de la inscripción quedarán suspendidos en tanto se pronuncie resolución firme por autoridad competente.

Con fundamento en los artículos 2, 208, 209 fracción III y 211 de la Ley Federal del Derecho de Autor; artículos 64, 103 fracción IV y 104 del Reglamento de la Ley Federal del Derecho de Autor; artículos 1, 3 fracción I, 4, 8 fracción I y 9 del Reglamento Interior del Instituto Nacional del Derecho de Autor, se expide el presente certificado.

Número de Registro: **03-2018-101011272700-01**

México D.F., a 10 de octubre de 2018

SUBDIRECTOR DE REGISTRO DE OBRAS Y CONTRATOS

DANIEL RAMOS LOPEZ

SECRETARIA DE CULTURA
INSTITUTO NACIONAL DEL
DERECHO DE AUTOR
DIRECCIÓN DE REGISTRO PÚBLICO
DEL DERECHO DE AUTOR

CULTURA
SECRETARÍA DE CULTURA

INDAUTOR
Instituto Nacional del Derecho de Autor

INSTITUTO
DE INGENIERÍA
UNAM

CONSEJO INTERNO

Oficio: CI/20190611-07

To the Technology Academy Finland,

It is my pleasure to inform you that the Internal Council of the Engineering Institute of the Universidad Nacional Autónoma de México (II-UNAM) has decided to Nominate for the **2020 Millennium Technology Prize** of the Technology Academy Finland, the Innovation:

The Horizontal-to-Vertical Spectral Ratio (HVSR) of Seismic Ambient Noise and Earthquakes: Measurement, Modeling and Inversion using the Diffuse Field Concept

Whose results from a **Collective Endeavor** achieved by a group of noteworthy academics that explicitly have agree to be **Nominees**, joining **Prof Francisco José Sánchez-Sesma**, Emeritus Researcher of this Institute. The members and contributions in alphabetical order of this nomination are:

Marcela Baena-Rivera, for her work on numerical modeling of HVSR in alluvial basins
Pierre-Yves Bard, for his contribution to understand seismic noise within the **SESAME project**
Michel Campillo, for his contributions to diffuse field concept and passive seismology worldwide
Cécile Cornou, for her contribution to promote passive seismology and the **GEOPSY project**
Donat Fäh, for his contribution to theoretical and experimental studies within the **SESAME project**
Antonio García-Jerez for his contribution to **HVSR**, diffuse fields and the **HV-INV project**
Kojiro Irikura, for his contributions to the rigorous applications of **HVSR** and diffuse fields
Ursula Iturrarán-Viveros, for her contribution to the numerical modeling and diffuse field concept
Hiroshi Kawase, for his work on the diffuse field concept for earthquakes (EHVSR) and noise
Javier Lermo-Samaniego, for his contributions to the practice of passive seismology for zonation
Agostiny M Lontsi, for the modeling and inversion of H/V for underground and offshore data
Francisco Luzón, for the theory and applications of diffuse fields and the **HV-INV project**
Ludovic Margerin, for his contributions to the theory and applications of diffuse fields
Kazuaki Masaki, for his contributions to the massive practice of passive seismology in Japan
Shinichi Matsushima, for his contributions to the modeling of HVSR in irregular configurations
Juan Camilo Molina-Villegas, for the modeling of **HVSR** for underground data
Peter Moczo, for his contribution to numerical modeling within the **SESAME** project
Fumiaki Nagashima, for the modeling and inversion of EHVSR of recent earthquakes
Yutaka Nakamura, for proposing the **HVSR idea** starting the worldwide diffusion of its main advantages
Matthias Ohrnberger, for his contribution to numerical modeling and **GEOPSY project**
Mathieu Perton, for his theoretical and practical inputs to the theory of diffuse fields and the **HV-INV project**
José Piña Flores, for his contributions to the practice of passive seismology and **HV-INV pro**ject
Francisco J Sánchez-Sesma, for his work on **HVSR**, diffuse fields and the **HV-INV project**
Zack Jack Spica, for his contributions to the theory and applications of diffuse fields
Richard Weaver, for his groundbreaking contributions to the theory and applications of diffuse field concept
Hao Wu, for his contributions to the fast modeling of HVSR in stratified configurations

Yours faithfully.

"POR MI RAZA HABLARÁ EL ESPÍRITU"
Ciudad Universitaria, Ciudad de México, June 11th, 2019.
THE PRESIDENT OF THE INTERNAL COUNCIL

DR. LUIS A. ÁLVAREZ-ICAZA LONGORIA

RMRZ/crg

Bulletin of the Seismological Society of America, Vol. 108, No. 4, pp. 2090–2103, August 2018, doi: 10.1785/0120170360

Local Generation of Love Surface Waves at the Edge of a 2D Alluvial Valley

by Juan Camilo Molina-Villegas,* Juan Diego Jaramillo-Fernández,
José Piña-Flores, and Francisco José Sánchez-Sesma

Abstract This work deals with the local generation of Love surface waves at the edge of an alluvial valley that is formed by a soft layer with dipping interface. These waves are extracted from the system response due to the incidence of antiplane *SH* plane waves. The indirect boundary-element method (IBEM) is used for computations. Results are given as modal emission spectra of Love waves, as functions of frequency, for the fundamental mode and the first two harmonics for various combinations of incidence angles, interface geometries, and impedance ratios. The structure of these emission spectra is inspired by the analytical solution of the canonical antiplane problem of a semi-infinite layer with a moving base and wall, which allows indication of the 1D response and the locally generated surface waves.

Introduction

Current practice almost neglects the effects of surface waves in their dual role: (1) as incoming waves produced by the earthquake source and modulated by the spatial variability of the site structure and (2) as locally generated by basin edges. This investigation focuses on the second issue, as the first problem is explored in the recent study by Bowden and Tsai (2016). In any event, the explicit consideration of surface waves may help reduce epistemic uncertainty. Novikova and Trifunac (1993, 1994) explore the role of surface waves and even suggest some ground-motion prediction equations (GMPEs). In fact, Bowden and Tsai (2016) noticed that many GMPEs include terms for the presence of basins or long-period signals.

There is significant field evidence of the effects of lateral irregularities in the seismic response of alluvial valleys. It suffices to give a few examples here. During the 1971 San Fernando, California, earthquake, large differences between peak ground motions at close stations were attributed to the presence of lateral irregularities (Hudson, 1972). On the other hand, King and Tucker (1984) analyzed the response of several valleys in Russia to different earthquakes and concluded that such response could not be explained near the edges by 1D models. During the 1995 Kobe earthquake in Japan, extensive damage and strong motions were observed in narrow strips in the vicinity of zones with lateral irregularity (Pitarka *et al.*, 1998). Regarding the 1985 Michoacán earthquake, which caused significant damage in Mexico City, the large duration of recorded ground motion can be partially attributed to the emission of surface waves at the edges of the valley (Campillo *et al.*, 1989) and the ensuing energy trapping in the deep sediments (Cruz-Atienza *et al.*, 2016). In Greece, large ground motions have been documented for the valley of Volvi, and these were attributed to lateral and vertical irregularities (Semblat *et al.*, 2005). Finally, in the Turkish town of Dinar in 1995, serious structural damage was concentrated in a region near the rocky outcrops that form the basin edge (Bakır *et al.*, 2002).

Many authors analyzed the dynamic response of 2D alluvial valleys with lateral irregularity. Bard and Bouchon (1980a) studied the response of closed alluvial valleys to the vertical incidence of *SH* plane waves and examined the generation of Love waves. They performed their analysis in both frequency and time domains. Bard and Gariel (1986) did the same for stratified models. In an attempt to examine the effects of small irregularities in the bottom of a soft layer overlying a half-space, Campillo *et al.* (1990) computed synthetic seismograms and found evidence of the significance of such effects. Meanwhile, Moczo and Bard (1993) used finite differences and studied the response of a semi-infinite alluvial valley including an analysis of differential motion. Somewhat later, Heymsfield (2000) used the boundary-element method (BEM) to study the response of an alluvial valley with a lateral irregularity geometry similar to that proposed in this communication but the layer was assumed viscoelastic. The response was studied in the frequency domain at different locations in the soft sediments and a comparison was made with the response of the 1D model. Additionally, Narayan and coworkers (Narayan and Richharia, 2008; Narayan and Kumar, 2009; Narayan, 2012) studied the response of alluvial valleys with lateral irregularity using either

---

*Also at Facultad de Minas, Universidad Nacional de Colombia – Sede Medellín, Colombia 050041.

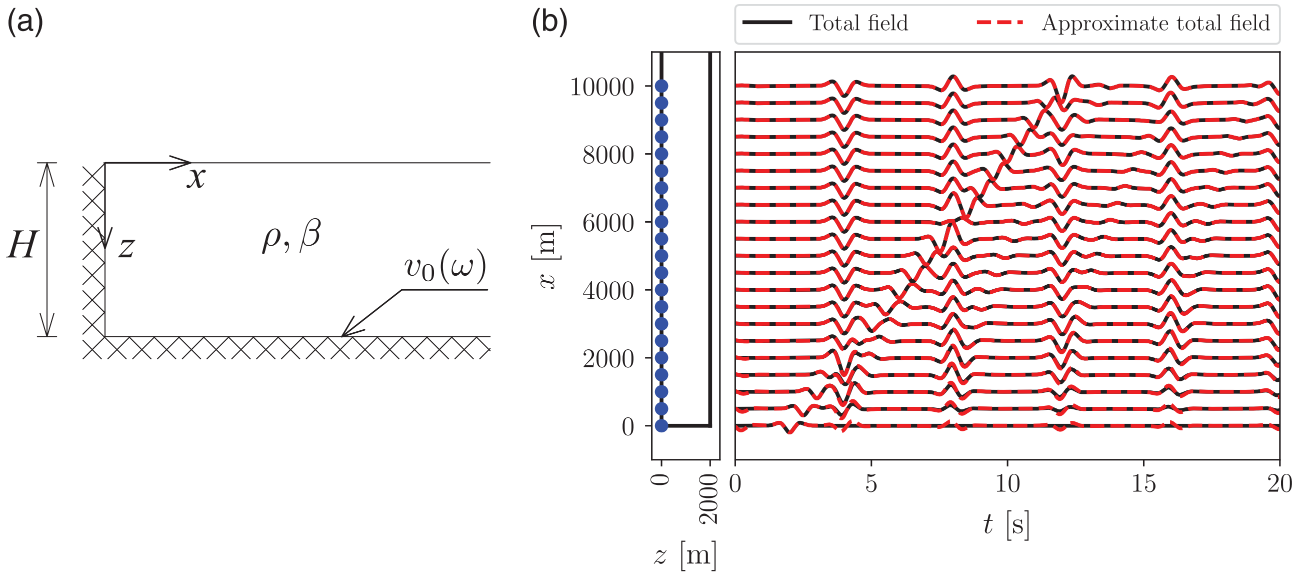

Figure 1. Canonical model and synthetic seismograms at surface: (a) the canonical model: semi-infinite homogeneous layer with synchronous moving rigid base and wall, and (b) comparison of the total displacement field and the approximate total displacement field (total field less inhomogeneous waves) at the surface for a model with $\beta = 1000$ m/s, $H = 2000$ m, and a prescribed displacement defined by Ricker wavelet with $t_s = 2.0$ s and $t_p = 1.0$ s. The color version of this figure is available only in the electronic edition.

homogeneous or stratified models over a homogeneous half-space. They explored various wave types and the effect of incident angle as well. With the goal of reaching the engineering practice, their results are given in terms of the so-called aggravation factor for the nominal 1D model response.

For the inplane case (*P*, *SV*, and Rayleigh waves), there are few studies. In a pioneering work, Bard and Bouchon (1980b) analyzed the inplane time-domain response of three closed 2D valleys under vertical incidence of plane *P* and *SV* waves, documented the generation of Rayleigh waves, and showed the importance of vertical motion as well.

For the 3D case, Volk *et al.* (2017) studied the effect of subsurface canyon on the site amplification on the Israeli coast and Stolte *et al.* (2017) use the ambient noise to measure the topographic amplification due to a soft-rock ridge at Los Alamos, New Mexico.

Despite those contributions, we note that there is not a complete parametric study by means of which the modal emission spectra of Love waves could be extracted and used to compute the approximate response of irregular basins by a denormalization process.

In this work, a parametric study on the generation of Love waves in 2D alluvial valleys due to the incidence of *SH* plane waves is made. Furthermore, the concept of modal emission spectrum for Love waves is established inspired in the canonical solution for the semi-infinite layer with antiplane moving rigid horizontal base with a vertical wall. The extension of these results to 2D and 3D realistic settings is the subject of our current research.

A Canonical Model

Consider the semi-infinite horizontal layer of mass density ρ, shear-wave velocity β, and thickness H shown in Figure 1a. For harmonic antiplane motion of its rigid base and rigid vertical wall given by $v_0(\omega)$, the resulting displacement field can be analytically expressed, with Fourier series, in terms of a modal sum in which both the 1D response and the effect of the wall are explicit (Rodríguez-Zúñiga *et al.*, 1995). The complete displacement field is

$$\begin{aligned} v_C(x,z,\omega) &= v_C^{1D}(x,z,\omega) + v_C^{D}(x,z,\omega) \\ &= v_0(\omega)\frac{4}{\pi}\sum_{n=0}^{+\infty}\frac{(-1)^n}{2n+1}\frac{\Omega_n^2-\omega^2\exp(-ik_nx)}{\Omega_n^2-\omega^2}\cos\left(\frac{\Omega_n z}{\beta}\right), \end{aligned} \tag{1}$$

in which $v_C^{1D}(x,z,\omega) = v_0(\omega)\frac{\cos(\omega z/\beta)}{\cos(\omega H/\beta)} = v_0(\omega)\frac{4}{\pi}\sum_{n=0}^{+\infty}\frac{(-1)^n}{2n+1}\frac{\Omega_n^2}{\Omega_n^2-\omega^2}\cos(\Omega_n z/\beta)$ is the antiplane displacement field of the 1D model (without the vertical wall) due to the motion of its rigid base (the 1D solution was expanded in a Fourier series), $v_C^D(x,z,\omega) = v_0(\omega)\frac{4}{\pi}\sum_{n=0}^{+\infty}\frac{(-1)^n}{2n+1}\frac{\omega^2\exp(-ik_nx)}{\omega^2-\Omega_n^2}\cos(\Omega_n z/\beta)$ is the diffracted field, $\Omega_n = 2\pi(2n+1)f_0 = \frac{(2n+1)\pi\beta}{2H}$ are the circular resonant frequencies of 1D model, $k_n = \sqrt{(\omega^2/\beta^2)-(\Omega_n^2/\beta^2)}(\mathrm{Im}(k_n)\leq 0)$ is the horizontal wave number and $f_0 = \beta/4H$ is the fundamental frequency of the 1D model. For $x = 0$ the right side of equation (1) is

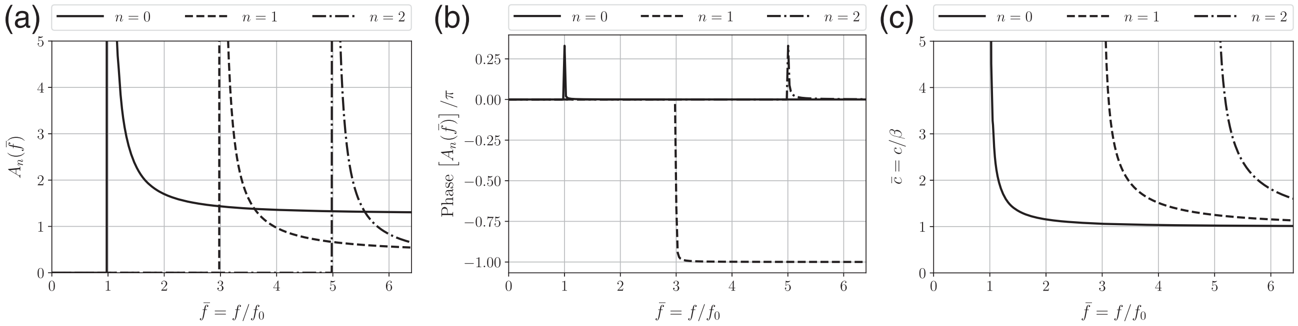

Figure 2. Modal emission spectra of Love waves and phase velocity dispersion curves of the canonical model: (a) amplitude of the Love-wave modal emission spectra, (b) phase of the Love-wave modal emission spectra, and (c) phase velocity dispersion curves.

precisely $v_0(\omega)$, fulfilling the moving rigid wall boundary condition.

Equation (1) can be rewritten in a generalized way as

$$v_C(x,z,\omega) = v_C^{1D}(x,z,\omega) + v_0(\omega)\sum_{n=0}^{+\infty} a_n(\omega)\Phi_n(z)\exp(-ik_n x), \quad (2)$$

in which $a_n = \frac{4}{\pi}\frac{(-1)^n}{2n+1}\frac{\omega^2}{\omega^2-\Omega_n^2}$ are the modal emission spectra of inhomogeneous waves ($\omega < \Omega_n$) and Love waves ($\omega \geq \Omega_n$), whereas $\Phi_n(z) = \cos(\Omega_n z/\beta)$ are the modal shapes of the 1D model.

Considering that not too far from the vertical wall the inhomogeneous waves will vanish, from equation (2), the diffracted field can be approximated as

$$v_C^D(x,z,\omega) \approx v_0(\omega)\sum_{n=0}^{N(\omega)-1} A_n(\omega)\Phi_n(z)\exp(-ik_n x), \quad (3)$$

in which $N(\omega) = \mathrm{floor}(\frac{\omega H}{\pi\beta}+\frac{1}{2})$ are the number of modes of the 1D model for the frequency ω and $A_n(\omega)$ are the modal emission spectra of Love waves:

$$A_n(\omega) = \begin{cases} 0 & \omega < \Omega_n \\ \frac{4}{\pi}\frac{(-1)^n}{2n+1}\frac{\omega^2}{\omega^2-\Omega_n^2} & \omega \geq \Omega_n \end{cases}. \quad (4)$$

A comparison of the total field and the approximate total field (total field minus inhomogeneous waves) for a given model is presented in Figure 1b, in which the close resemblance of those signals makes clear the small influence of inhomogeneous waves for the large range of excitation frequencies. In fact, for low frequencies these are very important. Nonetheless, they are beyond the scope of this work. Therefore, for layered systems over half-space, the evanescent waves are neglected.

From the approximate diffracted field of equation (3), it can be seen that for every frequency the equation is a finite modal sum over all the modes that exist for the 1D model, which includes the product of a nondimensional modal emission spectrum of Love waves $A_n(\omega)$ (Fig. 2a,b), the modal shapes of the 1D model $\cos(\Omega_n z/\beta)$, the propagation term $\exp(-ik_n x)$ that involves the phase velocity dispersion curves of the 1D model (Fig. 2c), and the source or excitation $v_0(\omega)$ term. The latter shows the direct relationship between the diffracted and the 1D model fields.

Some relevant properties of the phase velocity dispersion curves and modal emission spectra of the canonical model (Fig. 2) are (1) they have cutoff frequencies that match the fundamental frequencies of the 1D model ($f_c^n = (2n+1)f_0, n = 0,1,2,\ldots$), (2) they are density independent, and (3) the modal emission spectra for high frequencies have participation factors equal to $\frac{4(-1)^n}{(2n+1)\pi}$, which indicates the small relative importance of higher modes.

Problem Definition

This work stems from some properties of the canonical model presented in the A Canonical Model section. By means of a parametric analysis, the local generation of Love surface waves is characterized. A particular kind of 2D open alluvial valley model with lateral heterogeneity is considered, and the incidence of plane *SH* waves is assumed, as it is depicted in Figure 3. The model is composed of a layer (medium s) of depth H with a dipping linear interface over a horizontal length a, which overlays over a half-space (medium h).

Problem Decomposition

Using the same decomposition as the one employed for the canonical model, the total displacement field is defined as

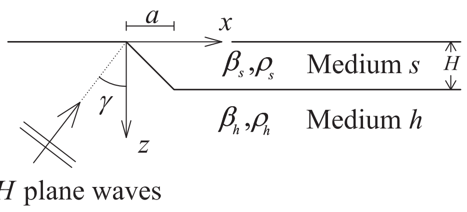

Figure 3. Studied model of a 2D basin with lateral heterogeneity.

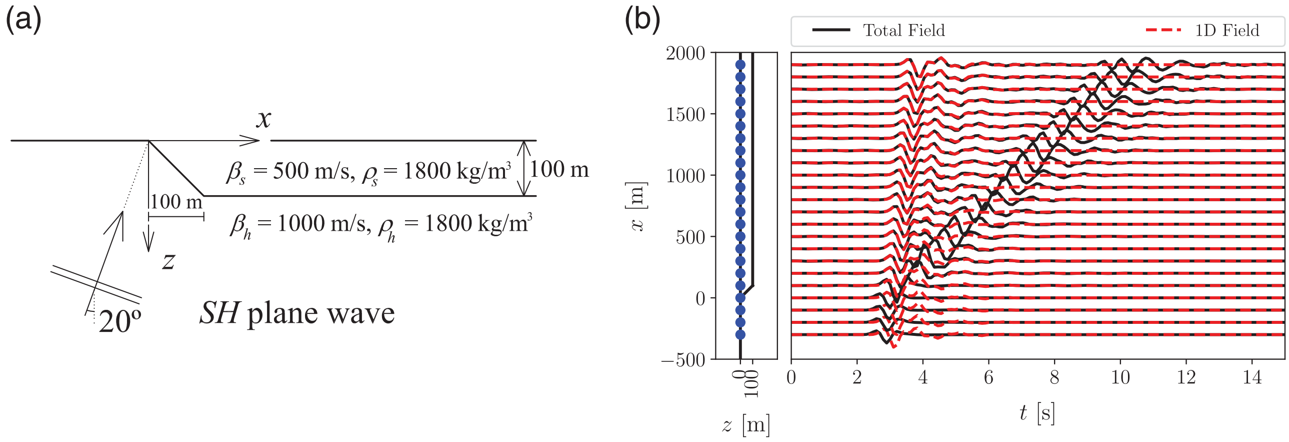

Figure 4. Comparison between the total and 1D field for surface receivers in a particular model: (a) Model used to show the decomposition of the total field as a 1D and a diffracted field; and (b) comparison between the total and 1D field for a time variation of the incoming plane wave defined as a Ricker wavelet with parameters $t_s = 3.0$ s and $t_p = 0.8$ s. The color version of this figure is available only in the electronic edition.

the sum of the 1D field and the diffracted field (Fig. 4 shows an example of this decomposition in the time domain):

$$v(x,z,\omega) = v_{1D}(x,z,\omega) + v_D(x,z,\omega), \quad (5)$$

in which $v(x,z,\omega)$ is the total displacement field (described in the Total Displacement Field section), $v_{1D}(x,z,\omega)$ is the displacement field for the 1D model due to the incidence of the same *SH* plane wave that the model with the lateral heterogeneity (described in the One-Dimensional Model section), and $v_D(x,z,\omega)$ is the diffracted field (described in the Diffracted Field section).

The surface waves generated on the lateral heterogeneity of the model emerges from equation (5). Therefore, the diffracted field can be computed as

$$v_D(x,z,\omega) = v(x,z,\omega) - v_{1D}(x,z,\omega). \quad (6)$$

Once the total field is known using a numerical method and the 1D field from its analytical solution, the diffracted field is computed and from it some properties of the canonical model, such as the modal emission spectra of Love waves, can be obtained.

Total Displacement Field

The total displacement field is computed using a validated implementation of the indirect BEM (IBEM; Sánchez-Sesma *et al.*, 1993). This is a numerical method based on an indirect representation that is a consequence of Somigliana's representation theorem. This approach computes the field from distributed sources at the boundaries of the media and gets an approximate solution of the problem. As a validation example, the comparison of the analytical response of the model presented in Figure 5a for an incoming *SH* plane wave and the one computed using the IBEM is shown in Figure 5b. The diffraction from the edges is negligible.

One-Dimensional Model

The 1D model associated with the studied model is defined as a layer of depth H, mass density ρ_s, and shear-wave velocity β_s over a half-space with mass density ρ_h, shear-wave velocity β_h with a fundamental frequency $f_0 = \beta_s/4H$. The approach presented here requires the use of some characteristics of the 1D model: (1) its response due to the incidence of the same *SH* plane wave that the model with the lateral heterogeneity ($v_{1D}(x,z,\omega)$), (2) its phase dispersion curves or eigenvalues (Fig. 6a), and (3) its modal shapes or eigenvectors (Fig. 6b) that are now functions of depth and frequency and are computed as

$$\Phi_n(z,\omega) = \begin{cases} \cos(\nu_s z) & 0 < z \le H \\ \cos(\nu_s H)\exp[-i\nu_h(z-H)] & z > H \end{cases}, \quad (7)$$

in which $\nu_s = \sqrt{(\omega^2/\beta_s^2) - k_n^2}$ is the layer's vertical wavenumber, $\nu_h = \sqrt{\omega^2/\beta_h^2 - k_n^2}$ is the half-space's vertical wavenumber, $k_n = \omega/c_n(\omega)$ is the horizontal wavenumber for the nth mode, ω is the circular frequency, and $c_n(\omega)$ is the phase velocity of the nth mode as function of frequency (called dispersion curves).

Diffracted Field

The main assumption of this approach is that somehow away from the lateral heterogeneity ($x > 2a$) the diffracted field is composed mainly of the Love waves that can exist on the 1D model. This means that the inhomogeneous waves generated at the basin edge are very inefficient in transport-

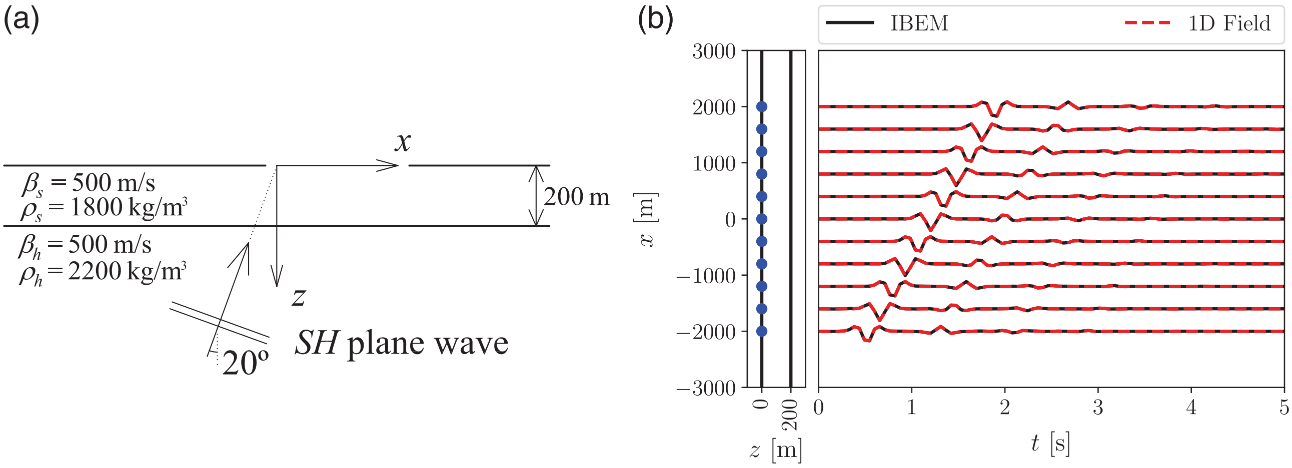

Figure 5. Validation of the indirect boundary-element method (IBEM) for the case of a layer over a half-space under the incidence of a plane *SH* wave: (a) model used to validate the IBEM, the incoming wave has a time variation defined as a Ricker wavelet with parameters $t_s = 1.0$ s and $t_p = 0.3$ s; and (b) comparison of synthetic displacements at surface for the analytical and the IBEM solutions. The lateral size of the IBEM model is 10 times the wavelength within the layer at the fundamental resonance frequency. The color version of this figure is available only in the electronic edition.

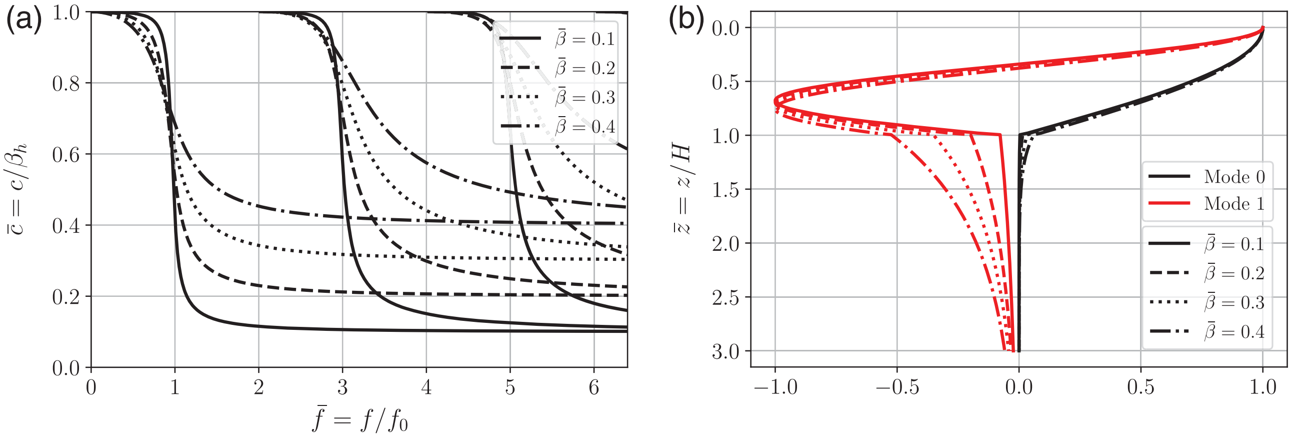

Figure 6. Phase velocity dispersion curves and modal shapes for the 1D model with properties $\bar{\rho} = \rho_s/\rho_h = 1$ and $\bar{\beta} = \beta_s/\beta_h = 0.1$, 0.2, 0.3, and 0.4: (a) phase velocity dispersion curves, and (b) modal shapes for the fundamental mode and first harmonic for $\bar{f} = f/f_0 = 3.0$. The color version of this figure is available only in the electronic edition.

ing energy along the layer. Following equation (3) for the canonical model, the diffracted field can be approximated as

$$v_D(x,z,\omega) \approx \acute{S}_h(\omega) \sum_{n=0}^{N(\omega)-1} A_n(\omega)\Phi_n(z,\omega)\exp[-ik_n(\omega)x], \tag{8}$$

in which $A_n(\omega)$ is the modal emission spectrum of Love waves for the nth mode (unknown), $k_n(\omega) = \omega/c_n(\omega)$ is the horizontal wavenumber for the nth mode of the 1D model (from phase velocity dispersion curves of the 1D model, see Fig. 6a for some examples), $\Phi_n(z,\omega)$ is the modal shape for the nth mode of the 1D model (they are computed from equation 7 and the phase velocity dispersion curves of the 1D model), $N(\omega)$ is the number of modes for frequency ω, and $\acute{S}_h(\omega)$ is the amplitude of the incident wave, which has been defined to have zero phase in the origin of coordinates.

The procedure employed to compute the modal emission spectra of Love waves, which are now complex, is described as follows: (1) compute the diffracted field in some surface points far from the lateral heterogeneity using equation (6), (2) compute equation (8) on the same points from (1) using the phase velocity dispersion curves and modal shapes of the 1D model, and (3) generate a overdetermined system of linear equations that is solved for the modal emission spectra of Love waves using the least-squares method.

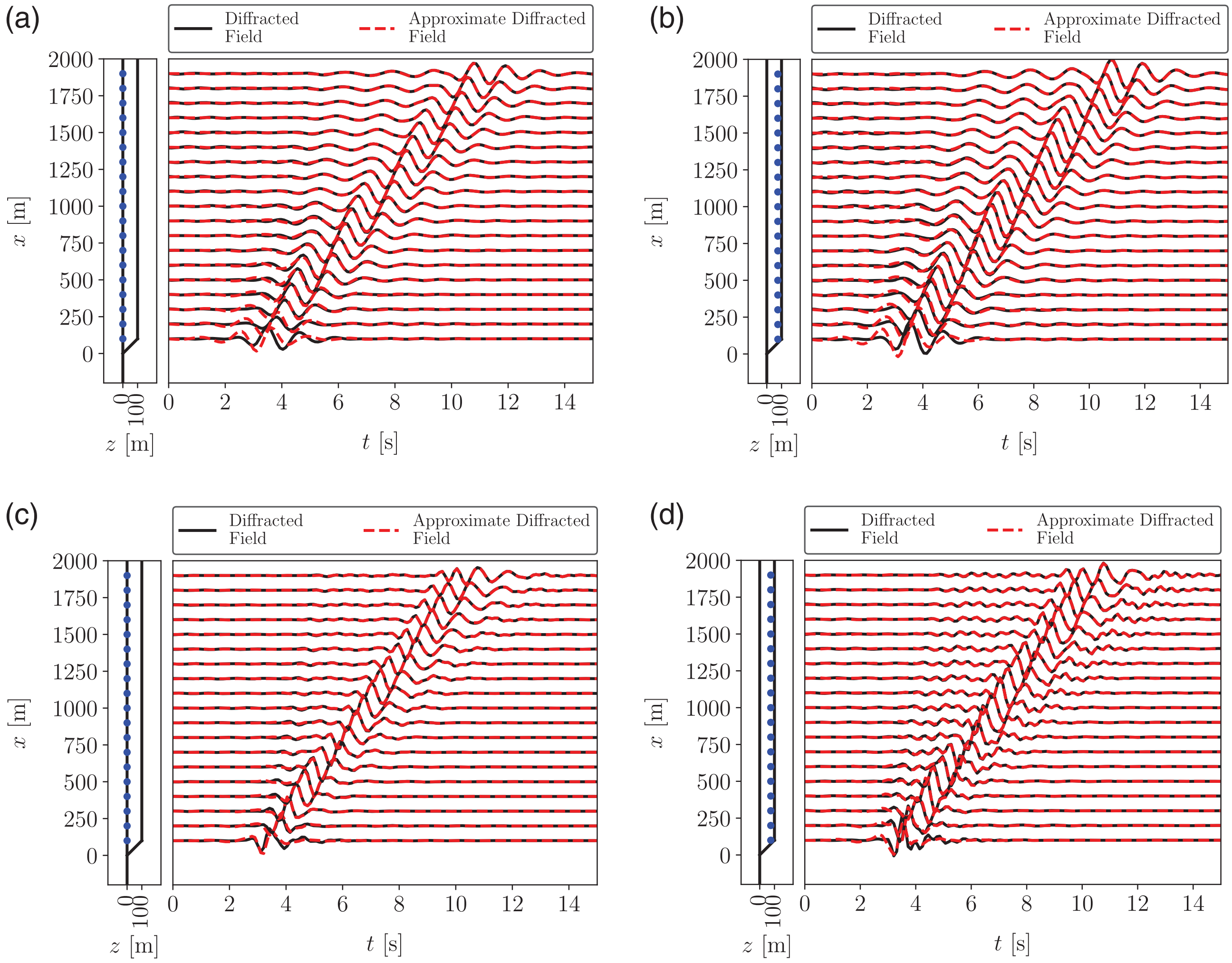

Figure 7. Comparison of the diffracted field and the approximate diffracted field for surface and interior receivers of the model presented in Figure 4a, for low ($t_s = 3$ s and $t_p = 1.5$ s) and high ($t_s = 3$ s and $t_p = 0.8$ s) frequencies, in which Ricker wavelet has been used as temporal variation of the incident *SH* plane wave: (a) surface receivers and low frequencies, (b) interior receivers ($z = 75$ m) and low frequencies, (c) surface receivers and high frequencies, and (d) interior receivers ($z = 75$ m) and high frequencies. The color version of this figure is available only in the electronic edition.

Figure 7 shows the comparison of the diffracted field (obtained from equation 6) and the approximate diffracted field (obtained from equation 8 and using the methodology presented in this section) for the model presented in Figure 4a. The agreement is good even for depth receivers, though only information from surface receivers were employed on the computation of the modal emission spectra of Love waves; for receivers outside the basin the comparison is meaningless because the diffracted field cannot be approximated using equation (8).

To validate the procedure described above, in Figure 8 the amplitudes of the modal emission spectrum of Love waves for the canonical model obtained using only surface receivers (light line) and the analytical ones (dark line) are compared.

Through the use of a parametric analysis, the modal emission spectra of the fundamental mode and the first two harmonics will be presented and analyzed for a wide family of models.

Parametric Analysis

To perform a parametric study, we introduce these normalized quantities: nondimensional horizontal length of the lateral heterogeneity, $\bar{a} = a/H$; nondimensional shear-wave velocity, $\bar{\beta} = \beta_s/\beta_h$; nondimensional density, $\bar{\rho} = \rho_s/\rho_h$; impedance ratio, $\mathrm{IR} = \beta_s\rho_s/\beta_h\beta_h$; and nondimensional frequency, $\bar{f} = f/f_0 = 4Hf/\beta_s$. The analysis includes six geometries ($\bar{a} = 0$, 0.5, 1, 2, 4, and 8), four IRs (0.1, 0.2, 0.3, and 0.4), and three incidence angles ($\gamma = 0°$, 30°, and 60°); nondimensional density $\bar{\rho} = \rho_s/\rho_h = 1$ has been assumed. This amounts to 72 models.

Figures 8–13 show the amplitudes and phases of the modal emission spectra of Love waves for the fundamental

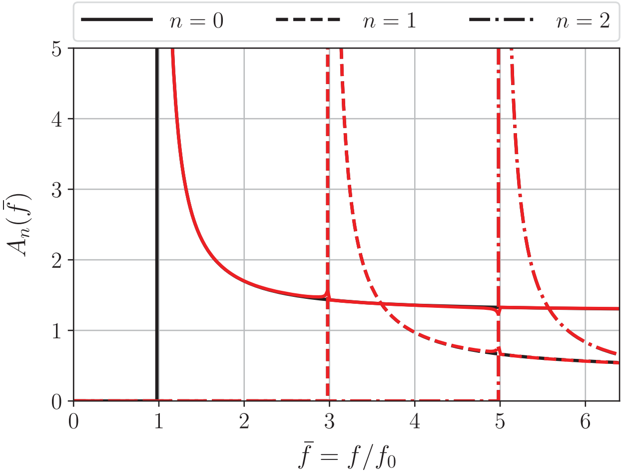

Figure 8. Comparison of the amplitude of the modal emission spectra for the canonical model. Dark line represents the analytic result obtained from equation (4), and light line represents the result obtained using the surface displacement field and the least-squares method described in the Diffracted Field section. The color version of this figure is available only in the electronic edition.

mode and the first two harmonics of the analyzed models, which have been computed using the procedure presented herein.

Figures 8–13 display the salient characteristics of Love-wave emission spectra. We note that the inversion scheme leads to some small effects of other modes that are present in the computed complete response. The bias introduced is very small and can be reduced by adopting explicit analytic templates and performing simultaneous multimode inversion. This is not the main subject of our research and will require further scrutiny. Meanwhile, we highlight the following properties of the modal emission spectra for the studied set of models:

- The most significant parameters that control the modal emission spectra are, in order of importance: IR, the incidence angle (γ), and the geometry of the lateral irregularity ($\bar{a}$); this is shown in Figures 9, 11, and 13.
- The amplitude of the modal emission spectra is null for frequencies smaller than the associated fundamental frequency of the 1D model ($\bar{f} = 2n + 1$), then, with a jump, reaches maximum value. From this, frequency until ($\bar{f} = 2n + 2$) decreases very fast and becomes constant or continues with a very slow decay. This behavior is similar to that of canonical model and is shown in Figures 9, 11, and 13.
- Emission of Love waves appears to be negligible if the IR is greater than 0.4; this is shown in Figures 9, 11, and 13.
- The amplitude of the modal emission spectra increases for small values of the IR; this is shown in Figures 9, 11, and 13.
- The amplitude of modal emission spectra increases with the incidence angle; such effect has been described by Sánchez-Sesma and Esquivel (1979), see Figures 9, 11, and 13.
- The amplitude of modal emission spectrum increases with the horizontal length of the lateral irregularity for frequencies higher than the fundamental, see Figures 9f, 11f, and 13f.
- The lower amplitude of modal emission spectrum for the fundamental mode occurs for the lowest IR, the vertical incidence of the plane waves, and the lower slope of the lateral irregularity ($\bar{a} = 8$). Specifically, in this case, the peak amplitude is about the 6% of the maximum, see Figure 9f.
- The lateral irregularities with small slopes tend to be more efficient at generating Love waves at higher frequencies ($\bar{f} > 2$) than the ones with large slopes, see Figures 9f, 11f, and 13f.
- For higher modes, the amplitude of the modal emission spectrum decreases, as compared to the one of fundamental modes, see Figures 9, 11, and 13.
- The phase of the modal emission spectrum for small values of $\bar{a}$ (large slopes of the lateral heterogeneity) is smoother than for high $\bar{a}$ (lower slopes of the lateral heterogeneity), see Figures 10, 12, and 14.
- For sharp lateral heterogeneity, the phases always have the values of $-\pi$, 0.0, and π, as in the canonical model (see Fig. 2b); this is shown in Figures 10a, 12a, and 14a.

Conclusions

- Starting with the analytical response of a semi-infinite layer with moving rigid base and wall, we introduce the concept of modal emission spectrum of Love waves and propose an inversion scheme to obtain them as functions of frequency and the parameters that define a set of configurations. The inversion scheme provides the salient properties of modal emission spectra. This is being improved to reduce the small bias due to modes different from the studied one.
- These modal emission spectra measure the efficiency of a basin with lateral heterogeneities for the generation of surface waves. This work is focused on Love's waves.
- The modal emission spectrum is a property of the basin edge and the incoming field and does not depend on the location of the receivers used for its computation because the inhomogeneous field is negligible on those points.
- A parametric analysis has been carried out for the computation of the modal emission spectra of Love waves corresponding to the fundamental mode and the first two harmonics for a particular antiplane open valley with lateral heterogeneity. The principal results that emerge from this analysis indicate that: (1) their value is almost zero until a cutoff frequency matches the fundamental frequency of the 1D model $f_c^n = (2n + 1)f_0$. For larger frequencies, their amplitudes continuously decrease and tend to be almost flat for high frequencies, (2) its amplitude increases for small IRs, (3) the amplitude increases with the incidence angle, and (4) small slope irregularities

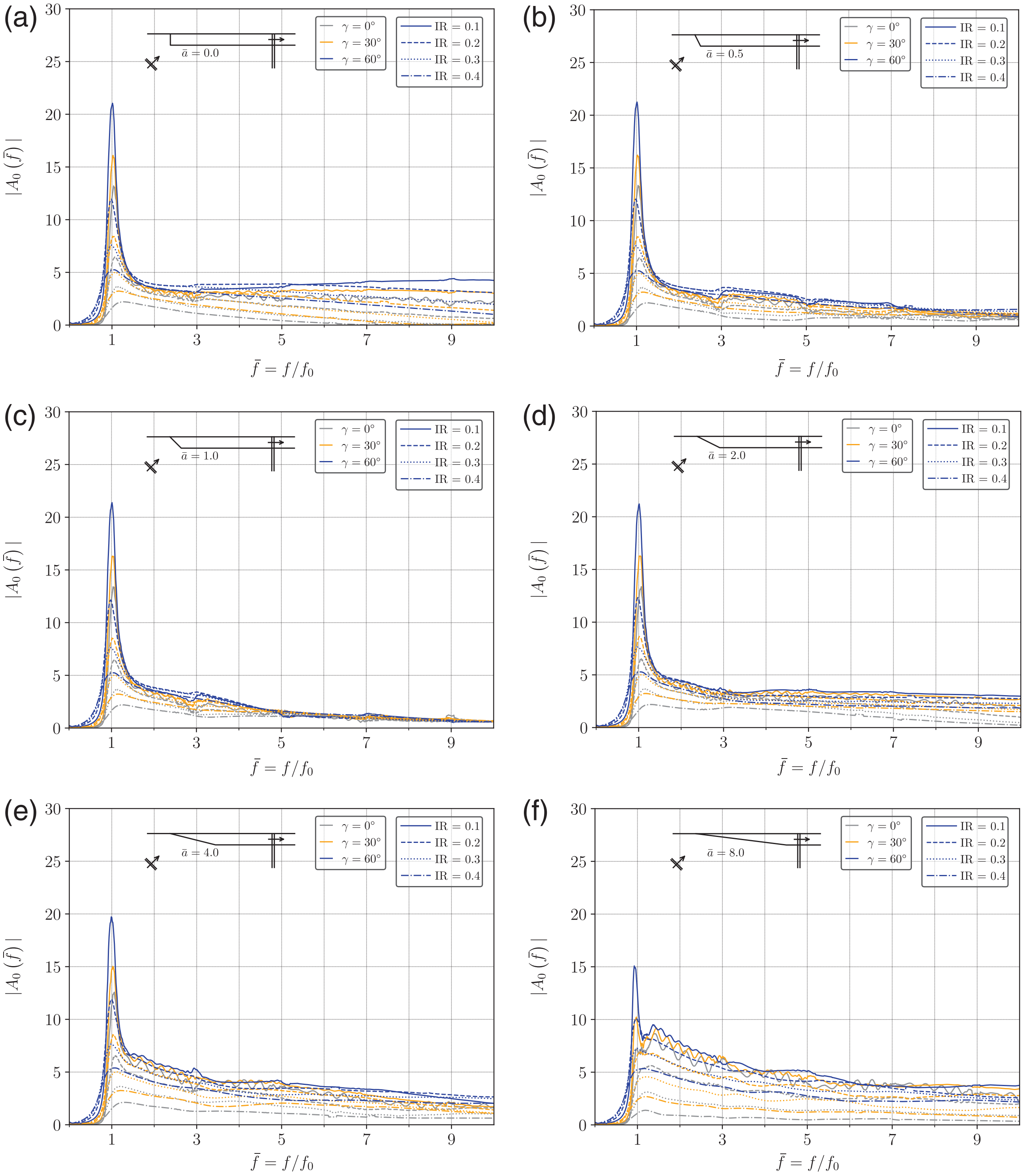

Figure 9. Amplitude of the modal emission spectra for the fundamental mode for different lateral irregularity geometry ($\bar{a}$), impedance ratios (IRs), and incidence angles (γ): (a) $\bar{a} = 0.0$, (b) $\bar{a} = 0.5$, (c) $\bar{a} = 1.0$, (d) $\bar{a} = 2.0$, (e) $\bar{a} = 4.0$, and (f) $\bar{a} = 8.0$. The color version of this figure is available only in the electronic edition.

(large $\bar{a}$) are more efficient in the generation of Love waves than large slope basin edges.

- The results summarized in this communication can be used to approximately assess the response of a particular kind of open alluvial valley with lateral heterogeneity due to the incidence of *SH* plane waves. Besides the Love waves generated at the basin edge, this approach includes the 1D response as well.

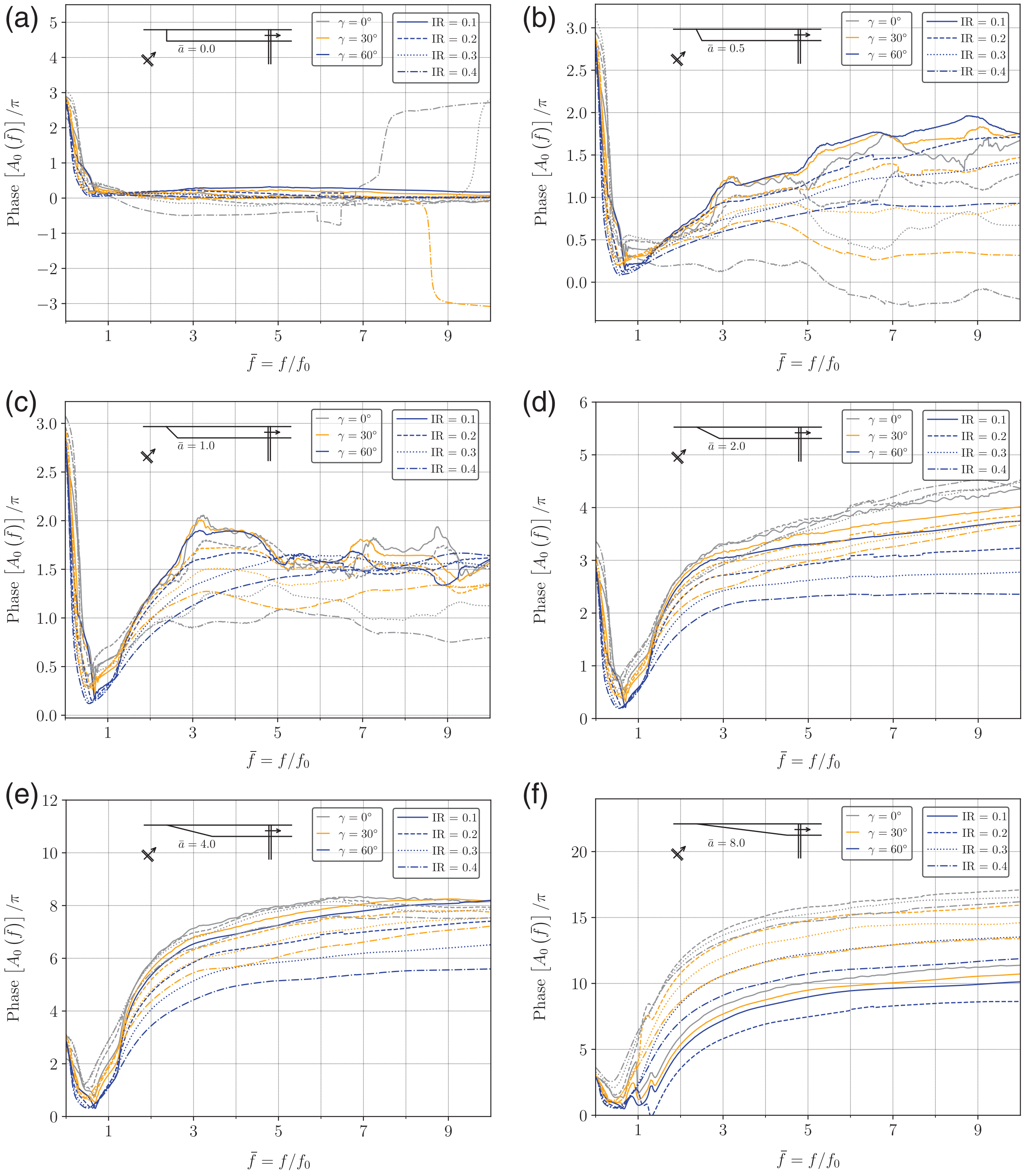

Figure 10. Phase of the modal emission spectra for the fundamental mode for different lateral irregularity geometry ($\bar{a}$), IRs, and incidence angles (γ): (a) $\bar{a} = 0.0$, (b) $\bar{a} = 0.5$, (c) $\bar{a} = 1.0$, (d) $\bar{a} = 2.0$, (e) $\bar{a} = 4.0$, and (f) $\bar{a} = 8.0$. The color version of this figure is available only in the electronic edition.

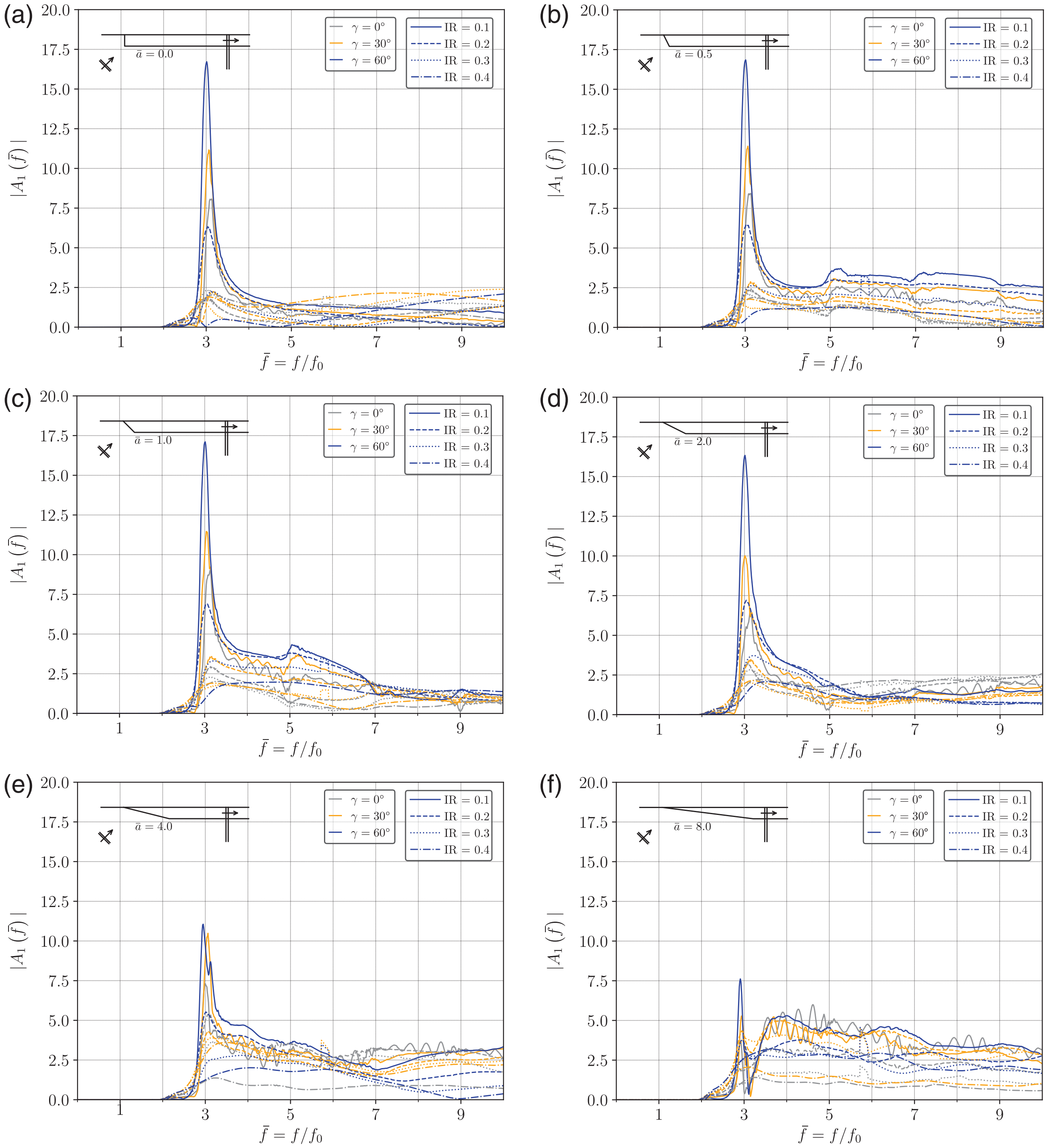

Figure 11. Amplitude of the modal emission spectra for the first harmonic for different lateral irregularity geometry ($\bar{a}$), IRs, and incidence angles (γ): (a) $\bar{a} = 0.0$, (b) $\bar{a} = 0.5$, (c) $\bar{a} = 1.0$, (d) $\bar{a} = 2.0$, (e) $\bar{a} = 4.0$, and (f) $\bar{a} = 8.0$. The color version of this figure is available only in the electronic edition.

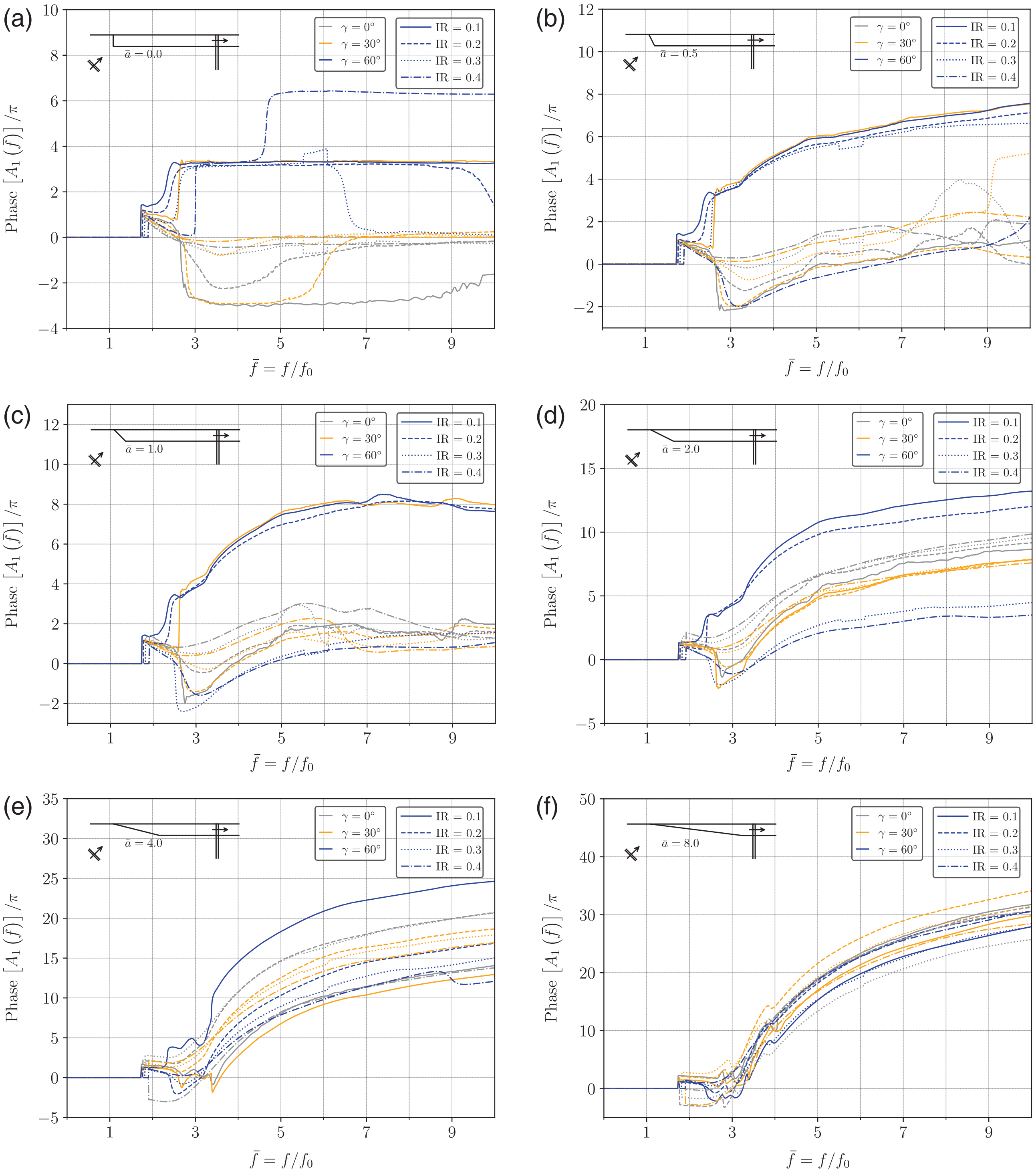

Figure 12. Phase of the modal emission spectra for the first harmonic for different lateral irregularity geometry ($\bar{a}$), IRs, and incidence angles (γ): (a) $\bar{a} = 0.0$, (b) $\bar{a} = 0.5$, (c) $\bar{a} = 1.0$, (d) $\bar{a} = 2.0$, (e) $\bar{a} = 4.0$, and (f) $\bar{a} = 8.0$. The color version of this figure is available only in the electronic edition.

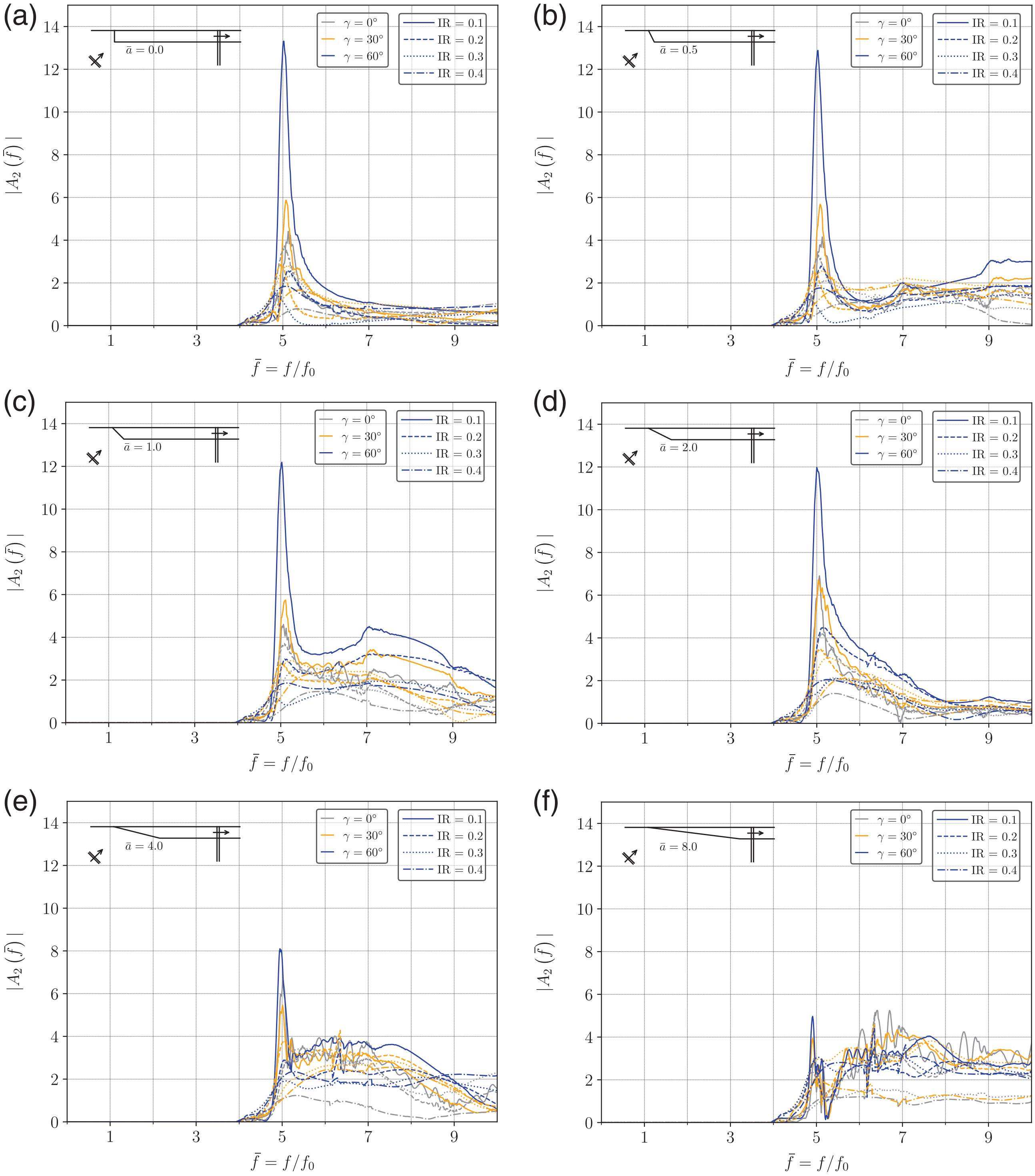

Figure 13. Amplitude of the modal emission spectra for the second harmonic for different lateral irregularity geometry ($\bar{a}$), IRs, and incidence angles (γ): (a) $\bar{a} = 0.0$, (b) $\bar{a} = 0.5$, (c) $\bar{a} = 1.0$, (d) $\bar{a} = 2.0$, (e) $\bar{a} = 4.0$, and (f) $\bar{a} = 8.0$. The color version of this figure is available only in the electronic edition.

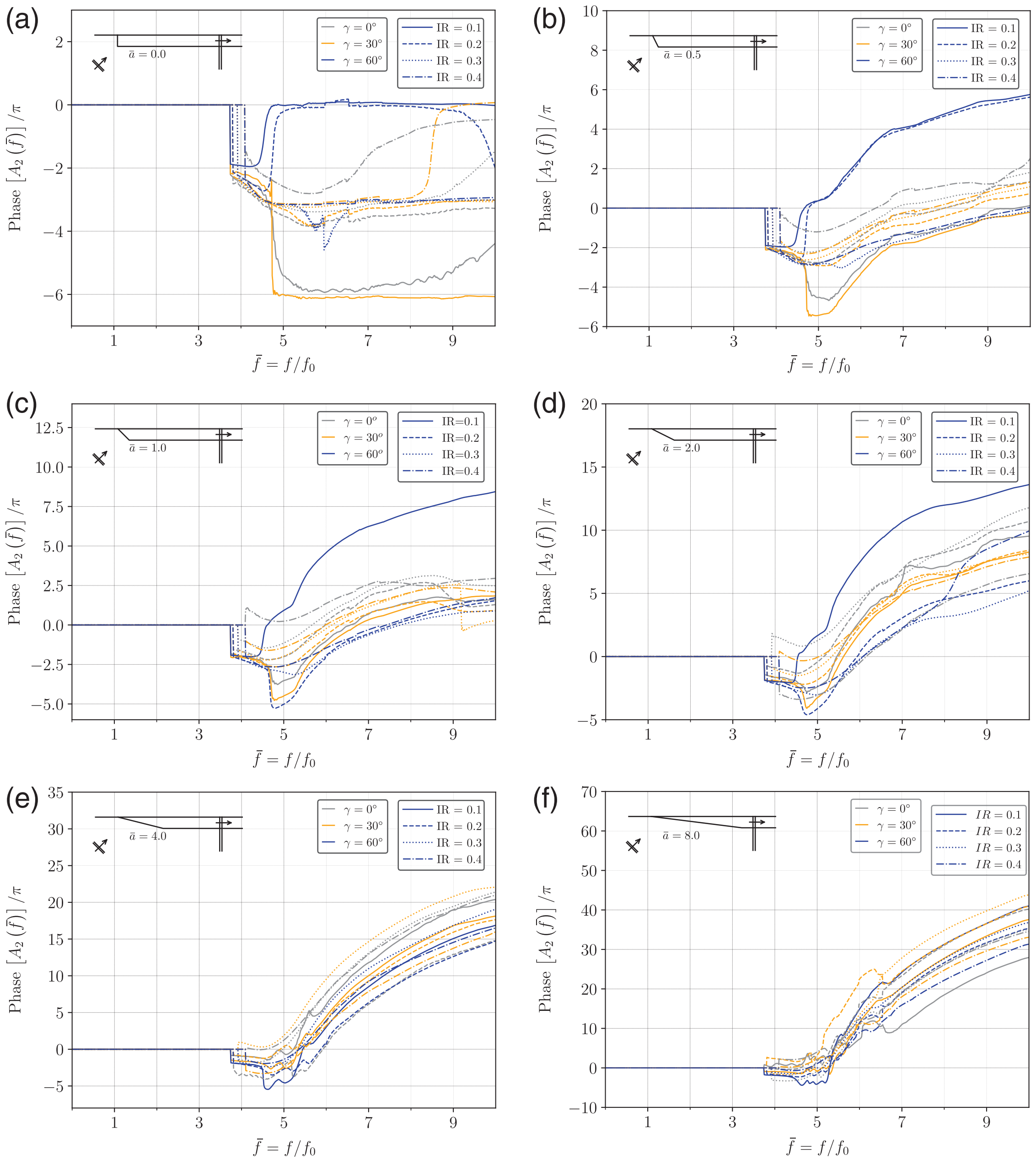

Figure 14. Phase of the modal emission spectra for the second harmonic for different lateral irregularity geometry ($\bar{a}$), IRs, and incidence angles (γ): (a) $\bar{a} = 0.0$, (b) $\bar{a} = 0.5$, (c) $\bar{a} = 1.0$, (d) $\bar{a} = 2.0$, (e) $\bar{a} = 4.0$, and (f) $\bar{a} = 8.0$. The color version of this figure is available only in the electronic edition.

- The extensions of the results presented herein to realistic 2D and 3D settings with the consequent emission of both Love and Rayleigh waves considering near-source effects are all subjects of our current research.

Data and Resources

Synthetic seismograms used in this study were computed by means of our own computer codes that implement the indirect boundary-element method (IBEM). Dispersion curves where computed using our own implementation of Thomson–Haskell method.

Acknowledgments

Thanks are given to Juan Pablo Villada-Rodas for the critical review of the article, to G. Sánchez, E. Plata, and their team of the Unidad de Servicios de Información (USI) of the Institute of Engineering-Universidad Nacional Autónoma de México (UNAM) for locating useful references. This study has been partially supported by AXA Research Fund and by Dirección General de Asuntos del Personal Académico (DGAPA)-UNAM under Project PAPIIT-IN100917.

References

Bakır, B. S., M. Y. Özkan, and S. Cılız (2002). Effects of basin edge on the distribution of damage in 1995 Dinar, Turkey earthquake, *Soil Dynam. Earthq. Eng.* **22,** 335–345.

Bard, P. Y., and M. Bouchon (1980a). The seismic response of sediment-filled valleys. Part 1. The case of incident SH waves, *Bull. Seismol. Soc. Am.* **70,** 1263–1286.

Bard, P. Y., and M. Bouchon (1980b). The seismic response of sediment-filled valleys. Part 2. The case of incident *P* and *SV* waves, *Bull. Seismol. Soc. Am.* **70,** 1921–1941.

Bard, P. Y., and J. C. Gariel (1986). The seismic response of two-dimensional sedimentary deposits with large vertical velocity gradients, *Bull. Seismol. Soc. Am.* **76,** 343–366.

Bowden, D. C., and V. C. Tsai (2016). Earthquake ground motion amplification for surface waves, *Geophys. Res. Lett.* **43,** 121–127.

Campillo, M., J. C. Gariel, K. Aki, and F. J. Sánchez-Sesma (1989). Destructive strong ground motion in Mexico City: Source, path, and site effects during great 1985 Michoacán earthquake, *Bull. Seismol. Soc. Am.* **79,** 1718–1735.

Campillo, M., F. J. Sánchez-Sesma, and K. Aki (1990). Influence of small lateral variations of a soft surficial layer on seismic ground motion, *Soil. Dynam. Earthq. Eng.* **9,** 284–287.

Cruz-Atienza, V. M., J. Tago, J. D. Sanabria-Gómez, E. Chaljub, V. Etienne, J. Virieux, and L. Quintanar (2016). Long duration of ground motion in the paradigmatic valley of Mexico, *Sci. Rep.* **6,** 1–9.

Heymsfield, E. (2000). Two-dimensional scattering of SH waves in a soil layer underlain with a sloping bedrock, *Soil Dynam. Earthq. Eng.* **19,** 489–500.

Hudson, D. E. (1972). Local distribution of strong earthquake ground motions, *Bull. Seismol. Soc. Am.* **62,** 1765–1786.

King, J. L., and B. E. Tucker (1984). Observed variations of earthquake motion across a sediment-filled valley, *Bull. Seismol. Soc. Am.* **74,** 137–151.

Moczo, P., and P. Y Bard (1993). Wave diffraction, amplification and differential motion near strong lateral discontinuities, *Bull. Seismol. Soc. Am.* **83,** 85–106.

Narayan, J. P. (2012). Effects of angle of incidence of *SH*-wave at the basin-edge on the characteristics of basin-edge induced Love wave, *J. Earthq. Tsunami* **6,** no. 1, 1250006.

Narayan, J. P., and S. Kumar (2009). Effects of soil layering on the characteristics of basin-edge induced surface waves, *Acta Geophys.* **57,** 294–310.

Narayan, J. P., and A. A. Richharia (2008). Effects of strong lateral discontinuity on ground motion characteristics and aggravation factor, *J. Seismol.* **12,** 557–573.

Novikova, E. I., and M. D. Trifunac (1993). The modified Mercalli intensity and the geometry of the sedimentary basin as scaling parameters of the frequency dependent duration of strong ground motion, *Soil Dynam. Earthq. Eng.* **12,** 209–225.

Novikova, E. I., and M. D. Trifunac (1994). Duration of strong ground motion in terms of earthquake magnitude, epicentral distance, site conditions and site geometry, *Earthq. Eng. Struct. Dynam.* **23,** 1023–1043.

Pitarka, A., K. Irikura, T. Iwata, and H. Sekiguchi (1998). Three-dimensional simulation of the near-fault ground motion for the 1995 Hyogo-Ken Nanbu (Kobe), Japan, earthquake, *Bull. Seismol. Soc. Am.* **88,** 428–440.

Rodríguez-Zúñiga, J. L., F. J. Sánchez-Sesma, and L. E. Pérez-Rocha (1995). Seismic response of shallow alluvial valleys: The use of simplified models, *Bull. Seismol. Soc. Am.* **85,** 890–899.

Sánchez-Sesma, F. J., and J. A. Esquivel (1979). Ground motion on alluvial valleys under incident plane *SH* waves, *Bull. Seismol. Soc. Am.* **69,** 1107–1120.

Sánchez-Sesma, F. J., J. Ramos-Martínez, and M. Campillo (1993). An indirect boundary element method applied to simulate the seismic response of alluvial valleys for incident *P*, *S* and Rayleigh waves, *Earthq. Eng. Struct. Dynam.* **22,** 279–295.

Semblat, J. F., M. Kham, E. Parara, P. Y. Bard, K. Pitilakis, K. Makra, and D. Raptakis (2005). Seismic wave amplification: Basin geometry vs soil layering, *Soil Dynam. Earthq. Eng.* **25,** 529–538.

Stolte, A. C., B. R. Cox, and R. C. Lee (2017). An experimental topographic amplification study at Los Alamos National Laboratory using ambient vibrations, *Bull. Seismol. Soc. Am.* **107,** 1386–1401.

Volk, O., S. Shani-Kadmiel, Z. Gvirtzman, and M. Tsesarsky (2017). 3D Effects of sedimentary wedges and subsurface canyons: Ground-motion amplification in the Israeli coastal plain, *Bull. Seismol. Soc. Am.* **107,** 1324–1335.

Facultad de Ingenierías
Universidad de Medellín
Carrera 87 Number 30-65
Medellín, Colombia 050026
jcmolina@udem.edu.co
(J.C.M.-V.)

Departamento de Ingeniería Civil
Universidad Eafit
Carrera 49 Number 7 sur – 50
Medellín, Colombia 050022
(J.D.J.-F.)

Instituto de Ingeniería
Universidad Nacional Autónoma de México
Circuito Escolar s/n, Ciudad Universitaria
Coyoacán 04510, CDMX, Mexico
(J.P.-F., F.J.S.-S.)

Manuscript received 5 December 2017;
Published Online 19 June 2018

Soil Dynamics and Earthquake Engineering 121 (2019) 102–120

Contents lists available at ScienceDirect

Soil Dynamics and Earthquake Engineering

journal homepage: www.elsevier.com/locate/soildyn

Joint analysis of Rayleigh-wave dispersion curves and diffuse-field HVSR for site characterization: The case of El Ejido town (SE Spain)

Antonio García-Jerez[a,*], Helena Seivane[a], Manuel Navarro[a], Marcos Martínez-Segura[b], José Piña-Flores[c]

[a] Department of Chemistry and Physics, University of Almeria, 04120 Almeria, Spain
[b] Department of Mining, Geological and Cartographic Engineering, Polytechnic University of Cartagena, 30203 Cartagena, Murcia, Spain
[c] Faculty of Engineering, National Autonomous University of Mexico, Mexico

ARTICLE INFO

Keywords:
Ambient noise analysis
Diffuse wavefields
Site effects
MASW
Spatial autocorrelation method
Joint inversion

ABSTRACT

The location of El Ejido town over a deep sedimentary basin in a zone of high seismicity in the Spanish context has motivated research on its seismic response characterization. To this aim, S-wave velocity models have been obtained from joint inversion of Rayleigh wave dispersion curves and full-wavefield modelling of the horizontal-to-vertical spectral ratio of ambient noise (HVSR) under the diffuse field assumption (DFA). Combination of spatial autocorrelation surveys (SPAC) with array apertures of several hundred metres and HVSRs displaying low-frequency peaks allowed to characterize deep ground features down to the Triassic bedrock. Predominant periods in the town ranged from 0.8 to 2.3 s, growing towards the SE, with few secondary peaks at higher frequencies.

The shallow structure has been explored by means of geotechnical surveys, Multichannel Analysis of Surface Waves (MASW) and SPAC analysis in small-aperture arrays. Resulting models support a general classification of the ground as stiff soil.

1. Introduction

As cities grow up, the number of elements exposed to risk becomes bigger and updated strategies to reduce the seismic risk are required. This is the case of El Ejido, a new town in southeast Spain with a constant growth rate which has trebled its population since the early eighties. It is located 10 km from the Alboran sea coast, the most seismically active region in the country. The significant seismic hazard in this area is supported by historical seismic reports [1] and has been evidenced by recent strong earthquake swarms occurred in Alboran Sea [2]. This perspective made it worthwhile for us to carry out a seismic microzonation in terms of seismic velocities and predominant periods of the ground motion.

Regarding to the local ground conditions of El Ejido, there are two remarkable features which turn this area into a singular framework. It is located atop Campo de Dalías, which is a deep sedimentary basin capable of developing low-frequency resonances of seismic waves, whereas the relatively hard soils found near surface could lead to underestimating the seismic hazard that really exists. European seismic code [3] includes a soil characterization in terms of shear wave velocities. Nevertheless, such classifications of soil based solely on the average shear-wave velocities for the upper 30 m (V_{S30}) ignore velocity contrasts between soil layers below 30 m, especially in cases of deep sites as Campo de Dalías [4–6] which could result in a less accurate determination of elastic response spectra. Moreover, the ratio between the resonant periods and the natural period of the building structures has been demonstrated as an explanatory parameter of damage increment in affected buildings [7].

Modern structural design codes [8,9] begin to include the site period in the definition of soil classes and researchers are proposing new site classifications based on this property [10,11]. It is a well-known fact that unconsolidated deposits amplify seismic waves [12]. Destructive earthquakes as the 1985 Michoacán and 2015 Kathmandu events, as well as moderate ones like the 1993–1994 Adra earthquakes [13] are evidence of this. On the other hand, long-period ground motion is increasingly often considered as an essential point due to its interaction with large-scale structures [14,15] because long predominant periods linked to deep basins might play a role as important as softer sediments in shallower basins.

Geological and geotechnical information gives evidence of the actual landform conditions for shallow and deep layers through a characterization of existing materials, being the shear-wave velocity (Vs)

---

[*] Corresponding author.
E-mail address: agarcia-jerez@ual.es (A. García-Jerez).

https://doi.org/10.1016/j.soildyn.2019.02.023
Received 17 June 2018; Received in revised form 19 February 2019; Accepted 22 February 2019

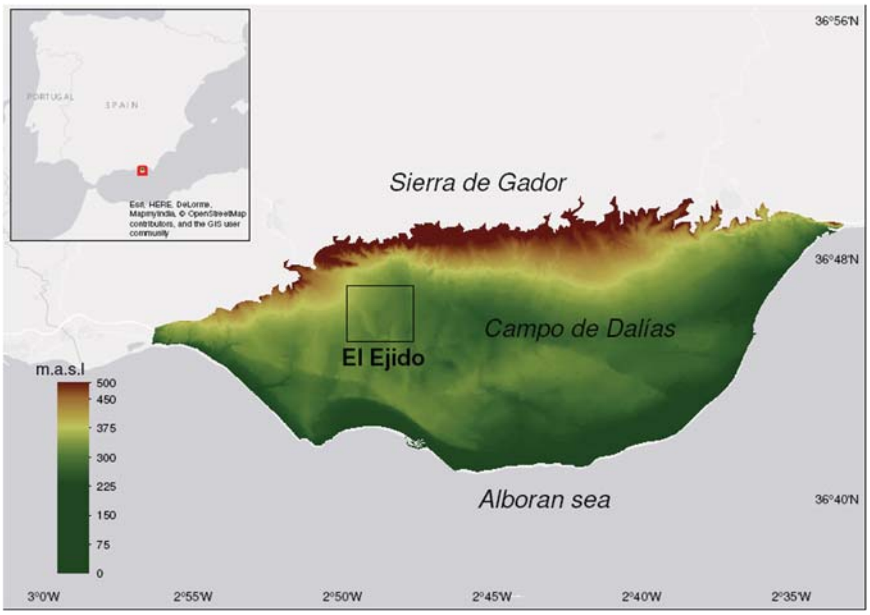

Fig. 1. Location of the study area. Background colour of Campo de Dalías displays the digital elevation model.

structure the most relevant parameter for site effect estimation. A long-established parameter in geotechnical studies, the N_{SPT} value is widely used for estimation of *V*s ground structure where more specific methods are not available (e.g. [16–18]).

The *V*s structure of ground materials can be also obtained by processing short-period Rayleigh waves by means of techniques that take advantage of their dispersive properties when they travel through a layered media. The phase-velocity $c_R(f)$ is mainly determined by the *V*s structure with slight dependence on the P-wave velocity (V_P) and density (ρ). Surface waves provide the highest possible signal-to-noise ratio for shallow seismic exploration. Consequently, the field works for data acquisition and subsequent data analysis become cost-effective in comparison with other classical techniques, ensuring reliable results [19–21].

The spatial autocorrelation method (SPAC, [22]) and the horizontal-to-vertical spectral ratio (HVSR) provide a theoretical basis for ground characterization from analysis of seismic noise signals. The HVSR technique [23] is nowadays used as the standard tool for obtaining the fundamental site period meanwhile array-based techniques provide elastic parameters variations with depth [22]. The combination of these two methods in joint inversion schemes allows resolving lower frequency bands and the effective identification of deeper ground interfaces (e.g. [24–28]). The diffuse wavefield approach (DFA, [29]), based on the seismic interferometry theory, provides a suitable theoretical framework for modelling these observations.

This work is focused on the microzonation of El Ejido through available geological and geotechnical information, active-source surface-wave methods and ambient seismic noise surveys. To this aim, geological and geotechnical data have been compiled and described. Application of the MASW method along six profiles enhanced the resolution in the upper layers. The possibility of estimating V_{S30} from the phase velocity of Rayleigh waves of a particular wavelength, c_λ, has been evaluated using the MASW dataset. Then, a dense seismic microzonation based on the HVSR technique has been carried out. HVSRs have been used for inversion of local 1-D velocity profiles, combined with geological information and/or dispersion curves retrieved from array techniques, and 2D cross-sections have been built from several local models. An algorithm based on the DFA [30] was employed for this task. Instrumental choices and limitations of techniques used for signal analysis were taken into account to interpret the results accurately.

This study is the first stage for future seismic risk mitigation plans which should consider local seismic response effects, based on the whole set of soil dynamic parameters, to assess the seismic hazard level of the populated towns in this coastal plain.

2. Geological and geotechnical settings

The town of El Ejido is located in Campo de Dalías, a basin bordered by the Alboran Sea to the south and by Sierra de Gador mountain range to the north (Fig. 1). From a tectonic point of view, Campo de Dalías basin is located in the Internal Zone of the Alpine Betic Chain, being an emerged portion of the Alboran Sea [31]. It has an extension of around 330 km^2 spanning 33 km long (in E-W direction) and 14 km maximum wide (in N-S direction). El Ejido is over thick sedimentary fillings with ages between Mid-Miocene and Holocene as concluded in previous general studies of Campo de Dalías basin (e.g. [32,33]). These sediments overlay a folded Paleozoic-Triassic metamorphic complex, denoted as Alpujárride complex, which is settled as the bedrock of the coastal plain. Sierra de Gádor is the most representative outcrop of this complex, that remains as the bedrock under the marine sediments in Alboran Sea [34] (Fig. 2).

The basin basement is composed of dolomites and limestones slightly metamorphosed in the upper part, although phyllites and quartzs can be found on the occidental and oriental borders of Sierra de Gádor [33]. Miocene sediments are deposited discordantly over this folded and faulted basement, including rocks of marly, clayey and sandy-silty nature in the study area. The Miocene succession is overlaid, also discordantly, by a Pliocene sequence mainly composed of calcarenites, silts, marls, sands and conglomerates [32,35]. Quaternary deposits lay on top of the upper Pliocene and can be either marine or continental in origin [33]. Those of continental origin are made up of red silts and they are abundantly found on the surface of El Ejido as well as marine terraces (Fig. 2a). Pliocene calcarenites are also found in a small percentage on El Ejido surface, but their bigger outcrop is found in the southwestern sector of Campo Dalías plain. Therefore, Quaternary deposits have a variable lateral continuity while Pliocene unit has a higher continuity on the scale of the study area [35] (Fig. 2b).

Industrial intensive agriculture is the main economic activity in Campo de Dalías using a large percentage of the coastal plain lands. Such activities find on underground aquifers their main water supply, resulting in a huge number of dug wells throughout this area. These

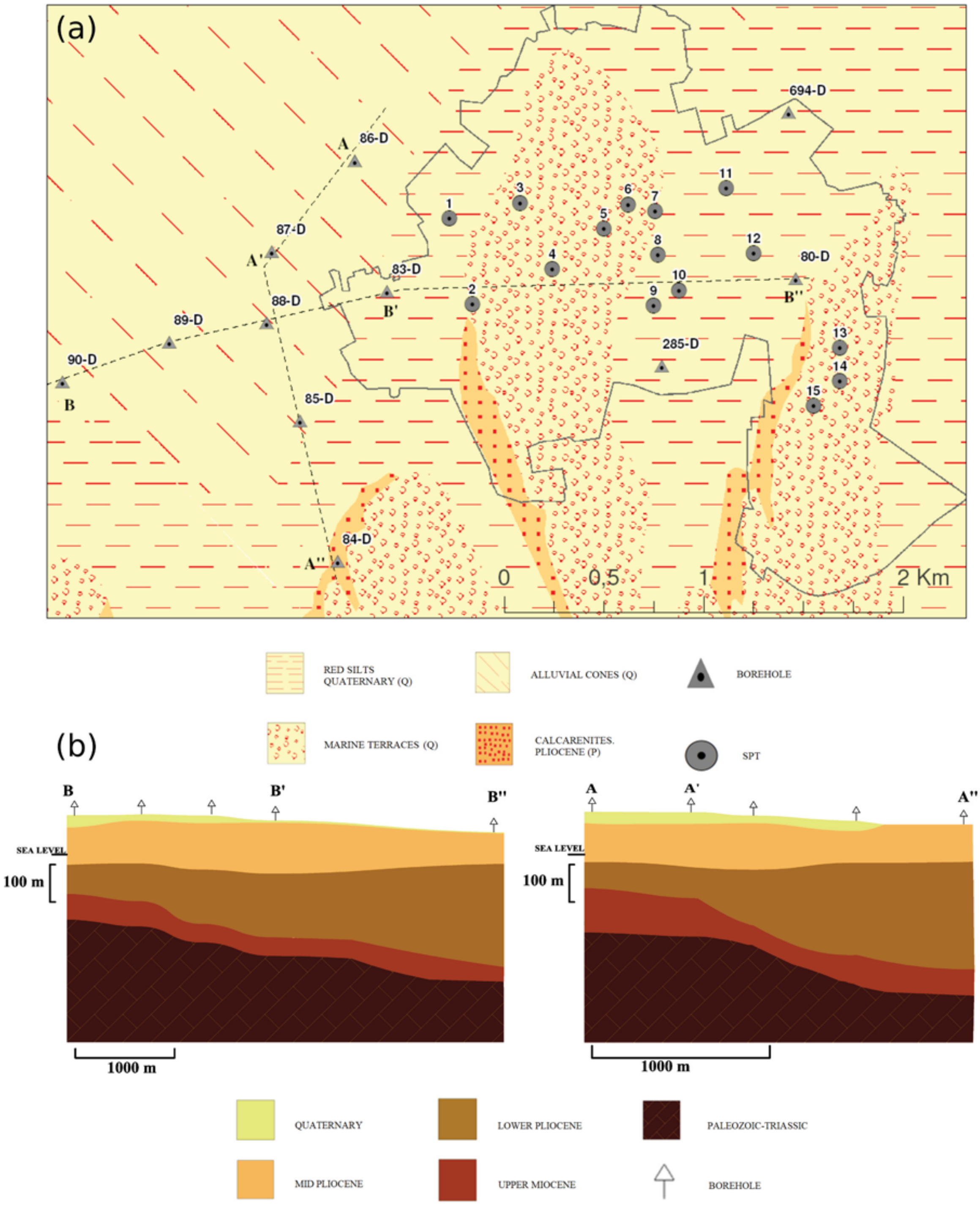

Fig. 2. a) Surface geological map of El Ejido area (modified from MAGNA, Spanish Geological Survey). The urban perimeter is denoted by the black line. Borehole locations are represented by triangles and the Standard Penetration Tests by circles b) Cross-sections along profiles sketched from available boreholes.

resources are useful for interpretation of the passive seismic surveys and they enabled us to draw various preliminary cross sections of the sedimentary cover near El Ejido (Fig. 2b). Borehole data along with some previous studies based on seismic surveys [36] provide us with *a priori* information of average seismic velocities and densities. Materials of the Pliocene unit have been attributed with mean seismic velocities (V_P) around 2.6 km/s [33]. Upper Tortonian calcarenites have estimated seismic velocities (V_P) around 3 km/s. On the other hand, 1-D velocity models in the Alboran Sea obtained by Grevemeyer et al. [37] attribute V_P above 5 km/s to the first crustal layer, which would comprise the Alpujarride complex.

Geotechnical information extracted from 15 standard penetration tests (SPT) made for foundation design (Fig. 3) has been used to investigate the composition and properties of the shallow ground layers. Quaternary red silts and clays cover the central flatland in El Ejido town, which is wedged in between two gently hills with N-S trend enclosed in the marine terraces area (Fig. 2a). The deepest geotechnical surveys show that these Quaternary deposits have thicknesses of up to 25 m in the central-southern zones (surveys 8, 10, 12) increasing up to 40 m in the NE part (694-D). They overlay Pliocene calcarenites which can be effectively considered as the geotechnical basement. Surveys performed on the hills show abundant gravelly levels (1, 5, 6),

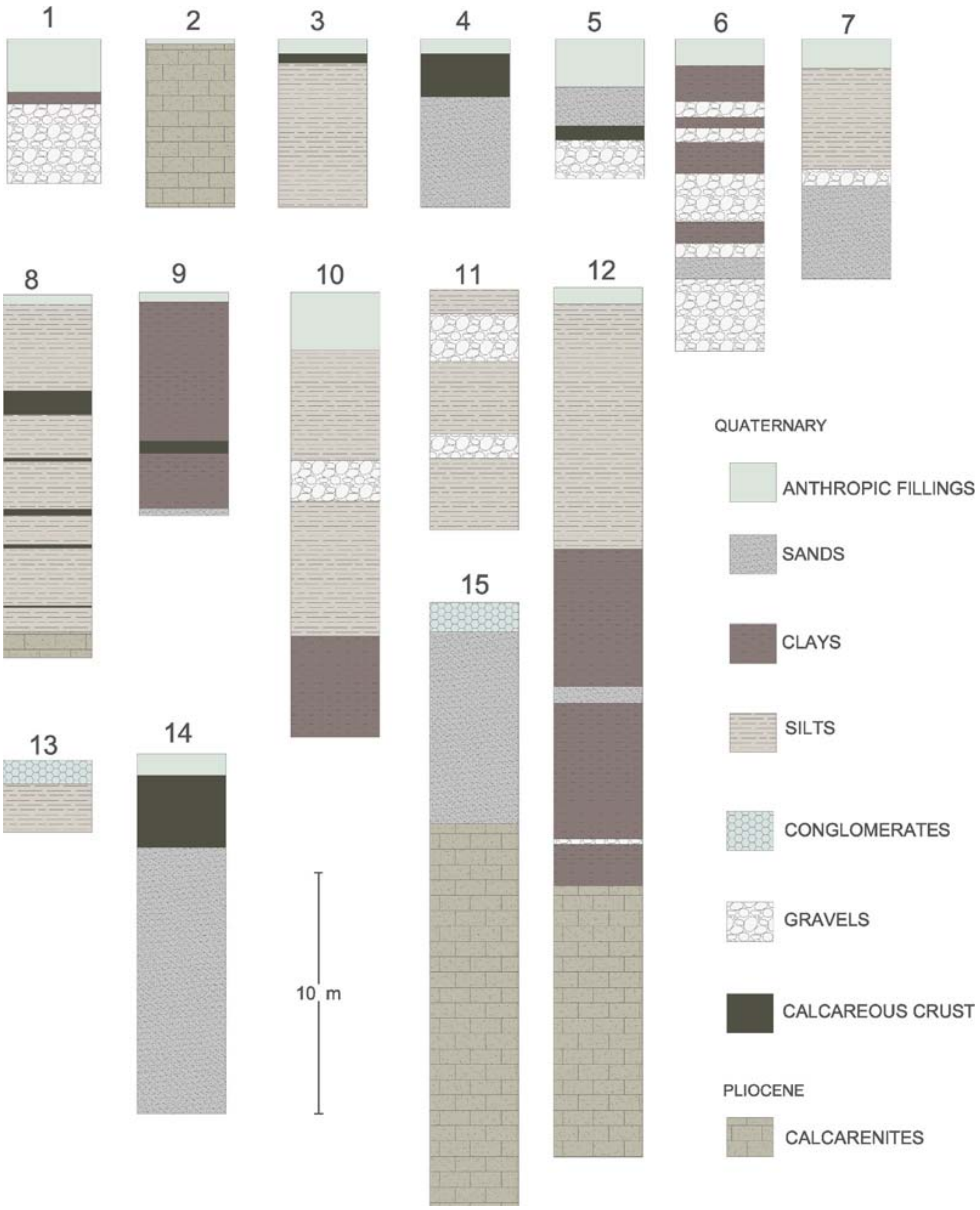

Fig. 3. Lithostratigraphic columns from studied geotechnical loggings. Locations of these logs can be found in Fig. 2a.

Table 1
Empirical correlations based on N_{SPT} vs V_S to process the geotechnical tests.

Author(s)	Soil type	V_S based on N_{SPT}-value (m/s)	r^2
Ohta and Goto [17]	Clays and silts	$85.6\ N^{0.34}$	0.73
	Sand and gravels	$85.6 \cdot 1.048\ N^{0.34}$	0.73
	Gravels	$85.6 \cdot 1.222\ N^{0.34}$	0.73
Akin et al. [16]	All alluvial Soils	$59.44\ N^{0.109}\ z^{0.426}$	0.79
	All Pliocene Soils	$121.85\ N^{0.101}\ z^{0.216}$	0.88
Tan et al. [18]	Soft Soil	$101.34\ N^{0.2364}$	0.83
	Stiff soil	$128.71\ N^{0.2833}$	0.65
	Hard Soil and Soft Rock	$128.05\ N^{0.4081}$	0.73
Yoshida and Motonori [38]	50% Gravel Soil	$60\ N^{0.25}\ \sigma_{\nu0}'^{\,0.14}$	–

z = depth in metres, N = number of blow counts, r^2 = multiple correlation coefficient.
$\sigma'_{\nu0}$ = Vertical pressure in kPa.

calcareous crusts (3, 4, 14) and conglomeratic rocks (13, 15) in the upper metres. Pliocene calcarenites are almost outcropping in surveys 2 and 80-D and at a depth of 9 m in survey 15. The deepest SPTs penetrated 15 m into this calcarenitic layer without reaching its bottom. Deep wells performed in the town (80-D, 285-D, 694-D) reached the bottom of the calcarenitic layer at depths between 60 and 90 m.

3. Analysis and results

A brief description of applied methodologies, data analysis and results obtained for determination of the shallow and deep ground structure in El Ejido town are presented below. The shallow V_S structure has been estimated from geotechnical information and calculated using MASW and SPAC techniques. The deep ground structure is determined by joint inversion of HVSRs and dispersion curves retrieved from ambient noise records.

Table 2
Description of depths (minimum and maximum), N-value, real density (ρ) and V_S computed from the N_{SPT} value by using empirical relationships.

Soil Type	Depth Levels (min.–max.) (m)	N-value			ρ (g/cm^3)			V_S (Ohta and Goto) (m/s)		V_S (Akin et al.) (m/s)		V_S (Tan et al.) (m/s)		V_S (Yoshida and Motonori, 50% gravels) (m/s)	
		n	X	σ	n	X	σ	X	σ	X	σ	X	σ	X	σ
Quaternary															
Sands with gravels	1.0–9.0	1	25	–	2	1.90	0.14	268	–	205	–	320	–		
Silts	1.5–13.6	29	22	16	2	1.84	0.01	256	75	230	125	319	77		
Gravels	2.3–8.7	18	46	8	1	1.72	–	379	43			376	35	287	34
Clays	1.9–24.8	26	33	18	1	1.94	–	282	64	264	86	346	67		
Pliocene															
Calcarenites	3.6–47.4	19	49	22	2	2.15	0.07	–	–	–	–	666	145		

n = number of data, X = mean value, σ = standard deviation.

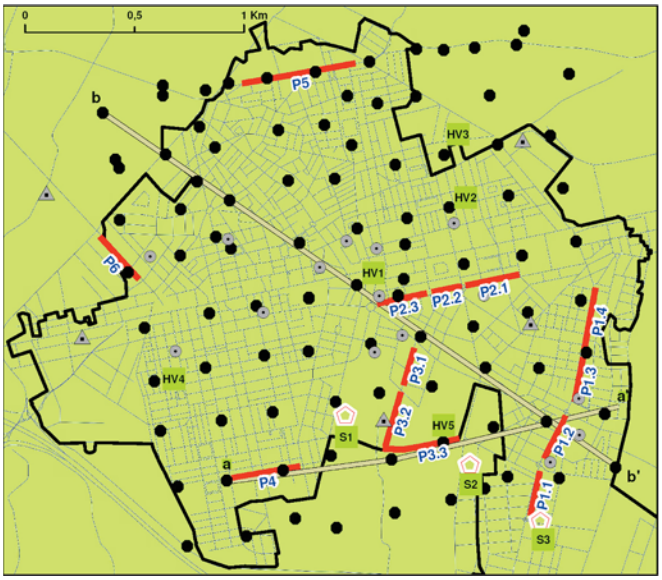

Fig. 4. Distribution of conducted seismic surveys and accessed boreholes in El Ejido urban area. Red lines represent MASW profiles. Black dots are HVSR measurement points (Section 3.3). Red pentagons illustrate the deployment points (S1, S2 and S3) of portable seismic arrays (Section 3.4). Grey circles and triangles show the locations of the analysed SPTs and boreholes (see details in Fig. 2 and 3). Lines a-a′ and b-b′ denote the profiles for which HVSR curves were inverted (Section 3.3.1). (For interpretation of the references to color in this figure legend, the reader is referred to the web version of this article.)

3.1. Geotechnical tests

As a first approach to estimate *Vs* values, empirical relationships between this property and the SPT blow count (N_{SPT}) have been used [16–18,38]. Except for one case of 50 m drilling, all the tests were performed very shallow, between 3 and 30 m deep. The water table was found in the deepest borehole at 34 m in Pliocene calcarenites. Due to the lack of local V_S-N_{SPT} relationships for the soils of the study area, the values obtained with several empirical formulae (Table 1) must be taken as a rough approximation.

Geotechnical data show a Quaternary unit varying widely in composition and interleaved with calcareous and conglomeratic crusts which lead to meet refusal of the in-situ tests even in the top. Stratigraphic sections generally have a first unit of artificial ground with an average thickness of 80 cm. Most of them drilled the Quaternary unit only. The vast majority of empirical relationships between N_{SPT} and V_S found in literature have been calculated for Quaternary soils while older materials are scarcely studied. Therefore, the possibility of comparison of estimated *Vs* values for Pliocene calcarenites is very limited (Table 2).

According to Table 2, materials found on in situ tests were estimated to have average V_S of 263 m/s for sands, 268 m/s for silts, 347 m/s for gravels and 297 m/s for clays. Despite the lack of local and specific correlations for calcarenites a V_S mean value of 511 m/s has been are estimated for these rocks.

3.2. Multichannel analysis of surface waves

In November 2017, 3.4 km of linear transects arranged in six profiles were laid out through several streets of El Ejido (Fig. 4) for an active-source MASW survey. Locations of these transects were chosen to sample the main geological units described in Fig. 2. A Wacker Neuson BS60-4s vibratory rammer was used as seismic source (Fig. 5b). To reach high efficiency in terms of surveyed length per day, a towed land-streamer was built by using a heavy-duty fire hose (Fig. 5a), which enabled collecting data in a roll-along mode. The seismic equipment consisted of 24 geophones of 4.5 Hz natural frequency screwed onto metal plates with 2 m spacing and a SUMMIT II Compact recording unit (Fig. 5a). The offset from the seismic source to the first geophone was 4 m. This linear array of 46 m in length was displaced 10 m between consecutive shots.

The seismic data were processed by using the “SurfSeis” software package from Kansas Geological Survey, USA. Dispersion curves were manually picked from each shot gather after applying the wavefield transformation into the frequency-velocity domain described by Park [39] (see also [20,40]). This processing provided a set of dispersion curve fragments at relatively high frequencies, all of them comprised in the band 7–50 Hz. As an example of data processing, Fig. 5c depicts a dispersion diagram in which the fundamental mode is clearly observed. Since variations in the dispersion curves corresponding to individual profiles remained moderate, the respective average curves are shown for reference (Fig. 6). For each profile, the dense series of dispersion curves were identified as fundamental-mode Rayleigh waves and separately inverted using the gradient-based iterative method described in Xia et al. [41]. The local 1D V_S models were parametrized using 10 layers of variable thicknesses and unbounded seismic velocities V_S and V_P, maintaining a constant Poisson's ratio of 0.25. The models presenting the minimum RMS error between experimental and theoretical dispersion curves were selected, allowing a maximum RMS of 0.5. Then, a 2D (horizontal position versus depth) *Vs* model was built by means of kriging interpolation, assigning every 1D model to the midpoint of each receiver spread [40]. The resulting cross-sections are shown in Fig. 7.

It is usually considered that the maximum reliable Rayleigh wavelength for MASW surveying is of the order of the array length (e.g. [42]). Thus, approximate relationships lead to an effective surveying depth between 15 and 23 m for the here-employed array setup.

Since each MASW line was designed to sample a particular geological unit, the *Vs* structure shows a reasonable lateral uniformity along each cross-section. It allows synthesizing the results in terms of average velocities. Table 3 shows V_{S30} values averaged along the profiles. Since the theoretical maximum penetration of the MASW method for our

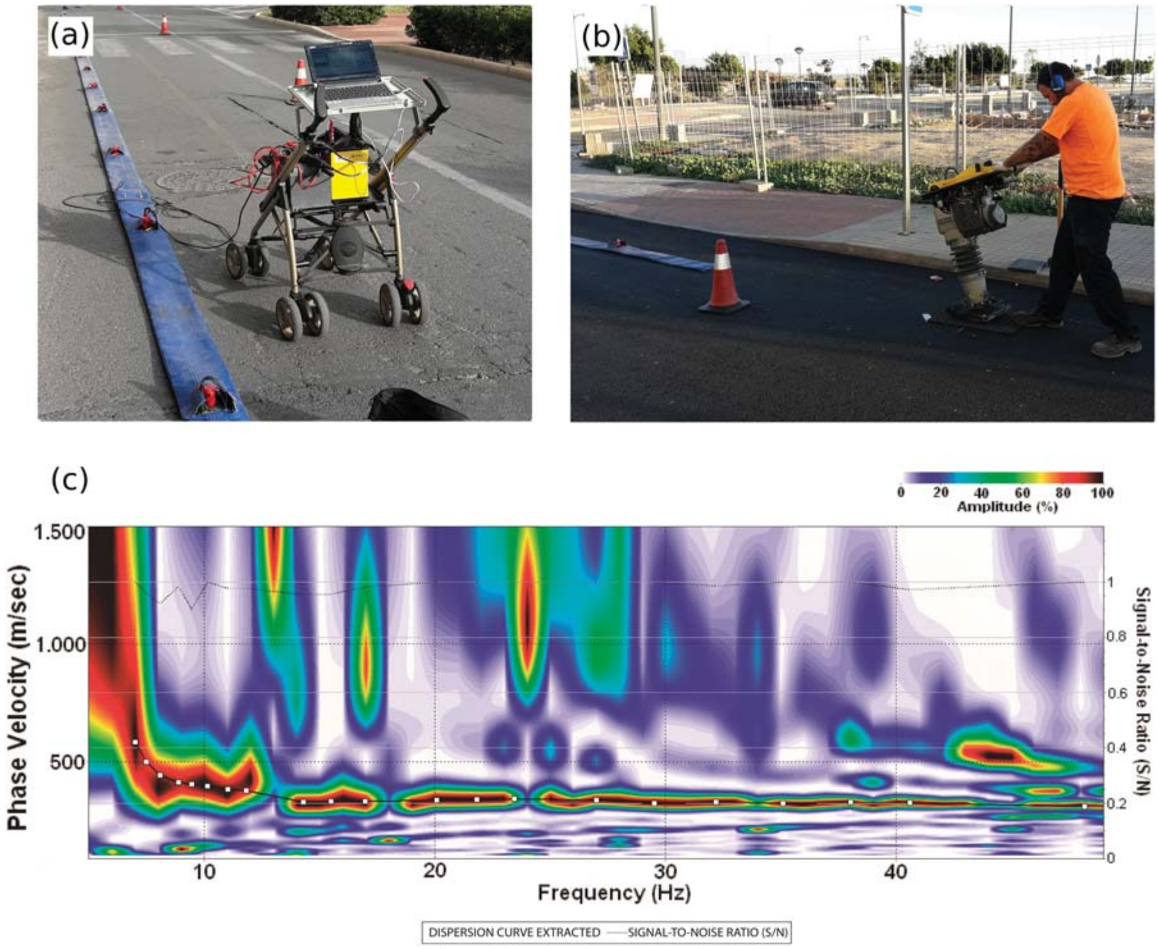

Fig. 5. Experimental setup for data acquisition of MASW data and example of dispersion curve retrieval. (a) Land-streamer of 46 m in length with 4.5 Hz geophones; (b) manual vibratory rammer as seismic source; (c) Dispersion curve picking for a shot gather belonging to profile P 3.3.

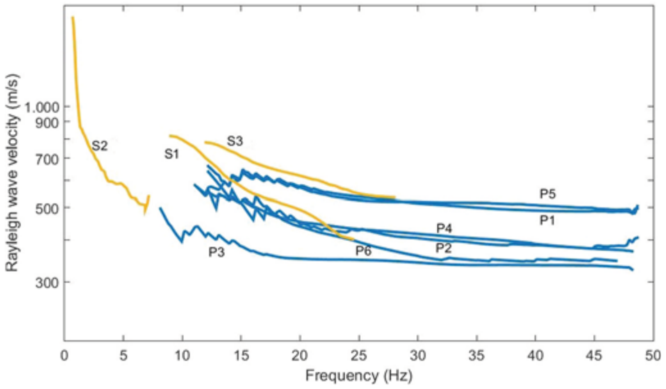

Fig. 6. Mean dispersion curves along the MASW profiles (Pn labels, blue colour). Dispersion curves computed from passive array experiments (Section 3.4) are shown with yellow lines and labelled as Sn. The respective locations can be found in Fig. 4. (For interpretation of the references to color in this figure legend, the reader is referred to the web version of this article.)

experimental setting is about 23 m, V_{S30} estimates involve some extrapolation of the $Vs(z)$ structure, which has been performed assuming continuity of the bottom layer properties down to 30 m.

The highest average V_{S30} values, 738 ± 60 and 725 ± 70 m/s, have been found in zones of marine terraces surveyed by profiles P1 and P5 (eastern hill and northern part of the town, respectively, Fig. 4). Velocities grow towards the north in P1 and they are slightly lower in the eastern part of P5, near a dry watercourse.

Intermediate velocities between 605 ± 40 and 658 ± 70 m/s in V_{S30} have been found in profiles P2, P4 and P6. Even though the shallow geology at P2 and P4 correspond to Quaternary red silts, presence of hard clays, cemented limes and calcareous crusts from 5 to 15 m deep is behind these relatively high velocities. Pliocene calcarenites were reached at depths of 14 and 25 m in the west and east ends of P2, respectively.

The lowest V_{S30} (506 ± 70 m/s) corresponds to profile P3, in the central-southern part of the town, with decreasing values to the south. Nearby geotechnical logs (points 9 and 10 in Fig. 2a) show somewhat softer columns without significant cemented layers or having drilled calcarenites in the upper 19 m.

3.3. HVSR technique

Predominant period of soil was obtained in this work through seismic noise measurements by application of horizontal to vertical spectra ratio method (HVSR, [23]). This method is nowadays used as a standard tool for obtaining resonance frequencies of sediments when a high impedance contrast exists [43]. Over the last years, methods for modelling HVSR(f) were developed to be used in geophysical exploration. A recent review of these techniques has been made by Lunedei an Malischewsky [44].

In view of the relatively high sedimentary thicknesses (Fig. 2) and the expectation of fundamental frequencies distributed in a wide band, especially below 1 Hz, broadband seismometers were chosen to perform the seismic noise observations. Portable Güralp CMG-6TD triaxial seismometers were used to record the three components of ambient

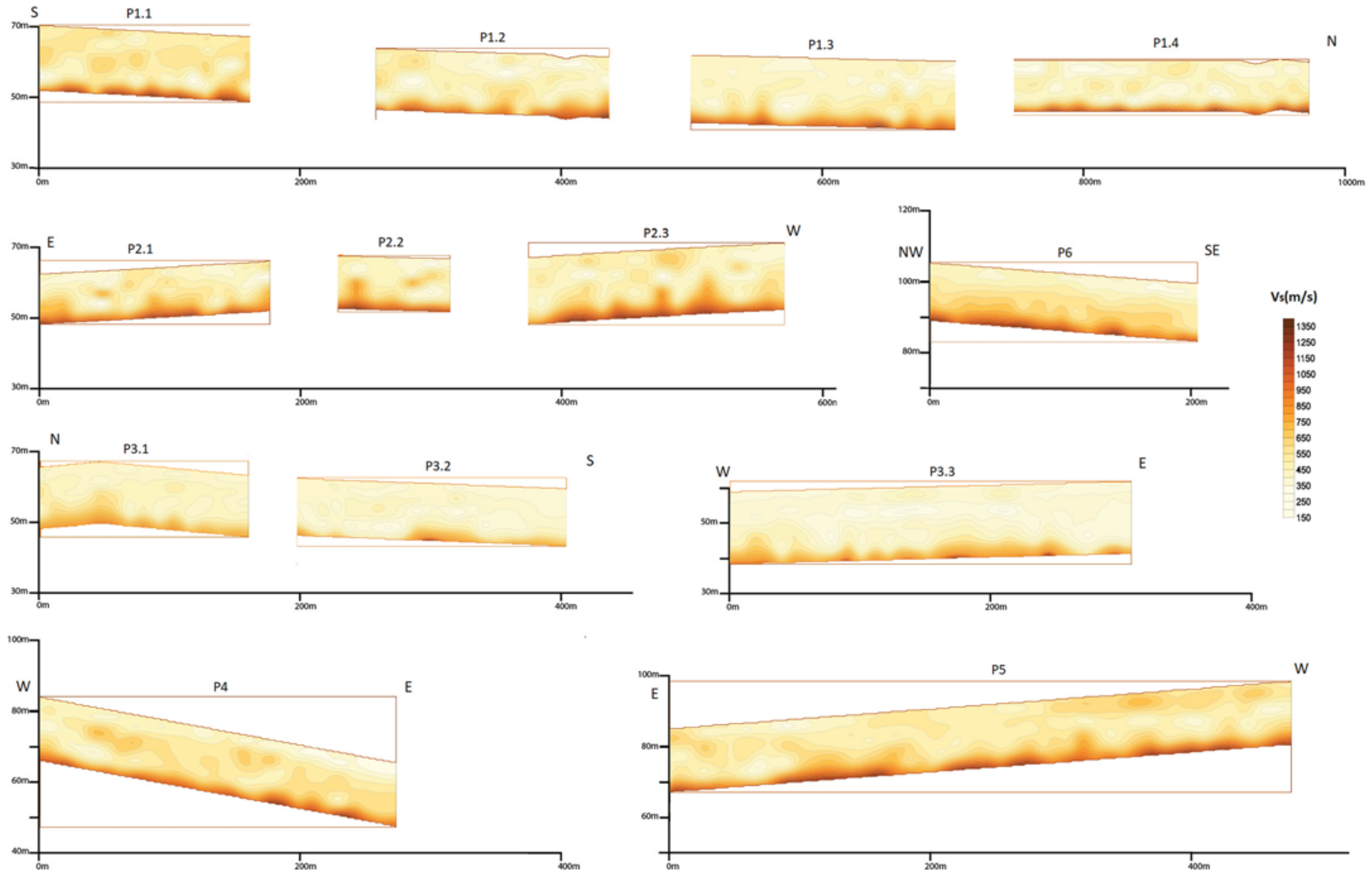

Fig. 7. MASW cross-sections obtained in El Ejido town. Profile locations are shown in Fig. 4.

Table 3
Average V_{S30} values and phase velocities for 40 and 45 m wavelength (c_λ) for each MASW profile. N shows the number of measurements considered.

Profile	N	V_{S30} (m/s)	N	c_{40} (m/s)	N	c_{45} (m/s)
P 1	75	738 ± 60	59	644 ± 60	30	684 ± 50
P 2	44	658 ± 70	15	625 ± 70	8	640 ± 80
P 3	67	506 ± 70	42	465 ± 60	32	494 ± 70
P 4	27	605 ± 40	18	555 ± 40	10	570 ± 40
P 5	47	725 ± 70	34	657 ± 70	21	672 ± 80
P 6	21	606 ± 50	11	583 ± 60	6	612 ± 80

noise vibrations at 94 measurement points in the town (Fig. 4). Flat response in velocity of these seismometers is between 0.03 and 100 Hz. Every single station was equipped with a GPS and the measurements were sampled with a rate of 100 samples per second (sps). For each site, data acquisition lasted between 20 and 30 min depending on the level of local disturbances (pedestrians, nearby traffic, etc.). "Geopsy" software (http://www.geopsy.org; [45]) was used to compute HVSRs in the frequency range 0.25–15 Hz, employing 40 s long time windows overlapped 50%. Removal of those windows clearly contaminated with transients was done manually. Fourier amplitude spectra were smoothed through a Konno & Ohmachi window [46] with a bandwidth coefficient of 40.

Fig. 8 shows the HVSRs obtained at four different sites which exemplify the typologies found: clear peak, broad peak, plateau and double peak. A univocal definition of the fundamental frequency, out of the total number of 94 measurement points, was obtained for 26 points included in the group of clear peaks (Fig. 8a).

Clarity of HVSR peaks obtained in El Ejido was tested following the recommendations proposed in SESAME guidelines, assessing criteria related to amplitude and frequency-dependent thresholds [47]. Only one of the HVSR curves was found with a weak peak, the rest were included in the four groups of typologies defined previously: 40 belong to broad-peak type (42% of our measurements), 27 were classified as clear peaks (28%), 16 double peaks (18%) and 10 plateau (12%). Some trends can be observed in the spatial distribution of HVSR shape (Fig. 9). The northern part of the town is clearly represented by HVSR with broad peaks. In the central part, there is an irregular distribution including all the shape types. A majority of clear peaks are concentrated in the southeast part of the town. This distribution could be interpreted in terms of local complex stratigraphy as well as the effects of dipping interfaces near the basin edge [48–52].

It is remarkable how all HVSRs have their peaks in the frequency band below or close to 1 Hz, independent of its shape. Such low-frequency resonances give information of the deep interfaces between Quaternary-Neogene sediments and soft rocks and Upper Miocene-Triassic stiff rocks. The HVSR curves along sections a-a′ and b-b′ are shown in Fig. 10. The overall trend of frequencies to decrease towards the SE (Figs. 9, 10b) is consistent with the increments in depth shown in the geological cross sections (Fig. 2b) as well as in isopach maps of the basin built from borehole analysis [32].

3.3.1. Inversion of HVSR shape

An innovative interpretation of the HVSR inspired by the possibility of retrieving the 3D elastodynamic Green's tensor between two stations embedded in an elastic medium from cross-correlation of their ambient noise records (ambient noise interferometry) was introduced by Sánchez-Sesma et al. [29]. The theoretical basis of this general hypothesis was developed in several research works [53–55] and confirmed in experiments with ambient noise measurements [56].

In the underlying theoretical approach, a 3D-diffuse equipartitioned displacement vector field is assumed to be established within an elastic

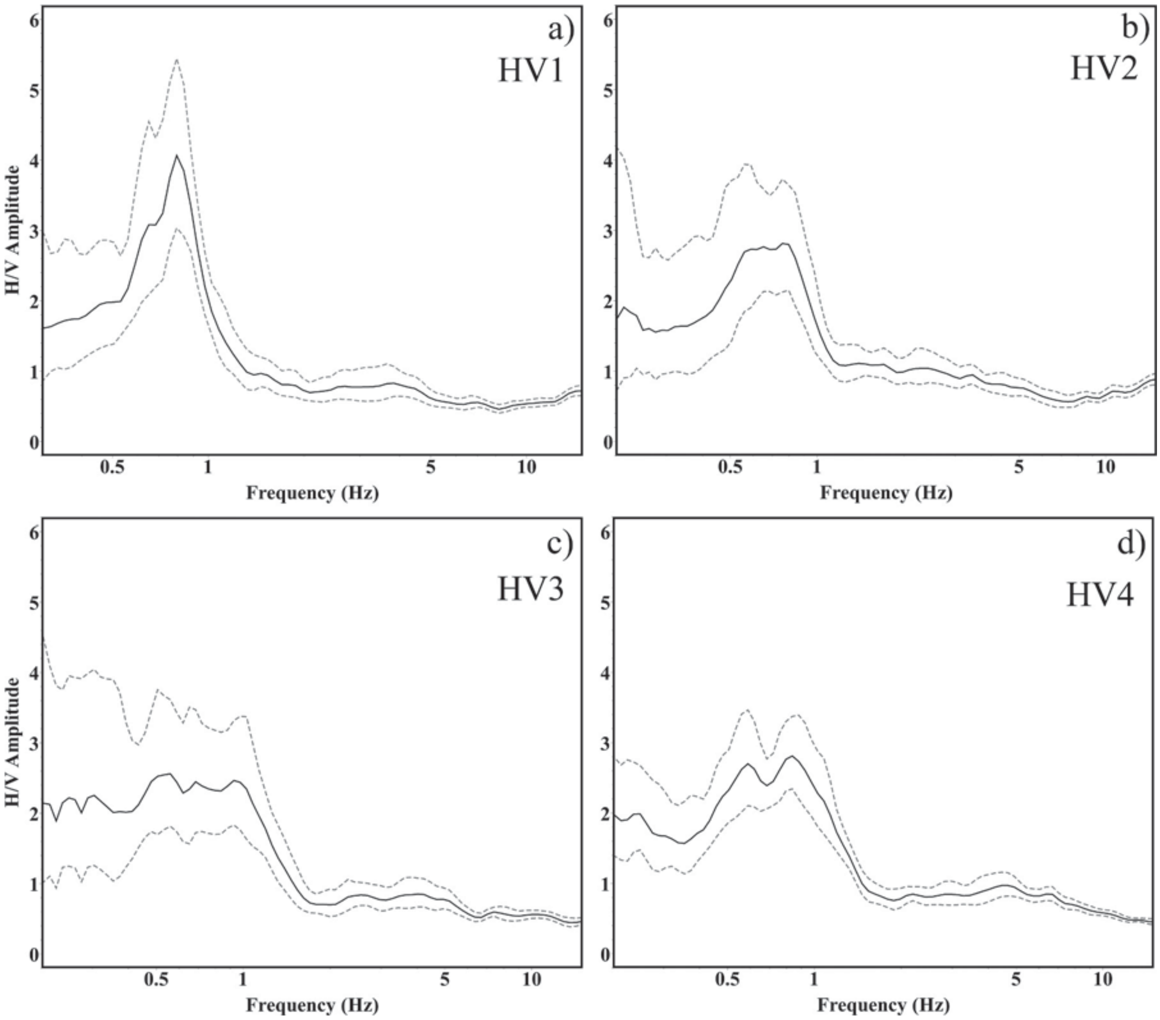

Fig. 8. Four instances of HVSR typologies found in El Ejido: a) curves with a single clear peak b) broad peaks whose widths vary from 0.2 to 0.4 Hz c) plateau-type shape with low amplitude and d) peaks showing narrower peaks on top.

medium with a bounded heterogeneous region. Then, power spectral densities of motion along any Cartesian axis m at an arbitrary point $\mathbf{x}$, $P_m(\mathbf{x};\ \omega)$, are proportional to the imaginary part of the corresponding Green's function at the source $G_{mm}(\mathbf{x};\ \mathbf{x};\ \omega)$, where $\omega = 2\ \pi\ f$ is the circular frequency and $m = 3$ stands for vertical direction [57]. Taking the usual definition, the H/V spectral amplitude ratio under DFA is given by

$$HVSR(x;\omega) \equiv \sqrt{\frac{2P_1(\mathbf{x};\omega)}{P_3(\mathbf{x};\omega)}} = \sqrt{\frac{2Im\left[G_{11}(\mathbf{x};\mathbf{x};\omega)\right]}{Im\left[G_{33}(\mathbf{x};\mathbf{x};\omega)\right]}}. \tag{1}$$

According to this theory, the inversion of seismic velocity models from the experimental HVSRs has been carried out considering a stratified elastic halfspace by using algorithms described in [30] which take advantage of compact expressions of the imaginary part of Green's functions [58] for the special case of coinciding source and receiver at the top of the layered media. “HV-Inv” software (https://w3.ual.es/GruposInv/hv-inv/, [30,59]) was used to obtain seismic velocity profiles for sections a-a′ and b-b′ (Fig. 4). The former profile was chosen according to clarity of the intersected peaks as well for being in the flatland, where shallow exploration methods found softer materials, while the latter by criteria based on the expected trend of sediment thickness growing. In general, the HVSRs were considered between 0.25 Hz and 15 Hz. This frequency range was shortened in cases of unstable behaviour at low frequencies (see e.g. Fig. 8c below 0.4 Hz) and in some cases presenting singular features near this high-frequency limit (e.g. flat HVSR with amplitudes below 1), probably related with very shallow and local ground characteristics. This latter simplification avoids excessive and site-depending model parametrization in the upper 10–15 m.

Attending to the stratigraphic models, where five main geological units are distinguished (Fig. 2b), the inversion procedure began with the establishment of parameters ranges for a general model of four layers over a half-space (Paleozoic-Triassic unit). The limits for the seismic velocities, density, thickness and Poisson's ratio of each layer (Table 4) have been defined on the basis of previous geophysical information (e.g. [33,37]) besides a calibration through 20 HVSR measurements on boreholes, where stratigraphy is known. A combined use of Monte Carlo sampling (in a first stage) and downhill simplex optimization was the strategy followed to adjust the theoretical HVSR curves, resulting from trial models in the parameters space (Table 4), to the experimental ones. Likelihood of the tested models, for both the HVSRs and the dispersion curve inversions (Section 3.4) is based on the definition:

$$misfit(\boldsymbol{m}) = \frac{1}{n}\sum_{i=1}^{n}\frac{(X_{obs}(\omega_i) - X(\omega_i,\ \boldsymbol{m}))^2}{\sigma_X{}^2(\omega_i)}, \tag{2}$$

where X is the inverted observable, σ_X is its standard deviation, and subscripts *obs* and *th* stand for observed and theoretical values.

An example of inversion at a borehole site, using depth constraints based on stratigraphy, is shown in Fig. 11. Conversely, results for sites

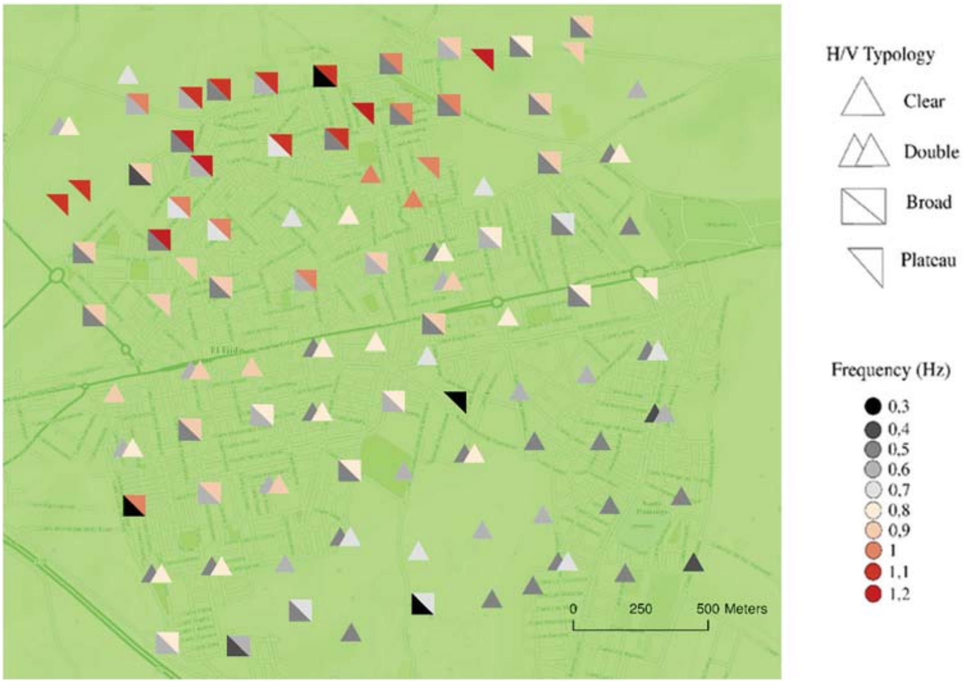

Fig. 9. Spatial distribution of HVSR peak frequencies in El Ejido urban area. Broad peaks are represented by squares, clear peaks by triangles, double peak shapes by twin triangles and plateau shapes by half squares.

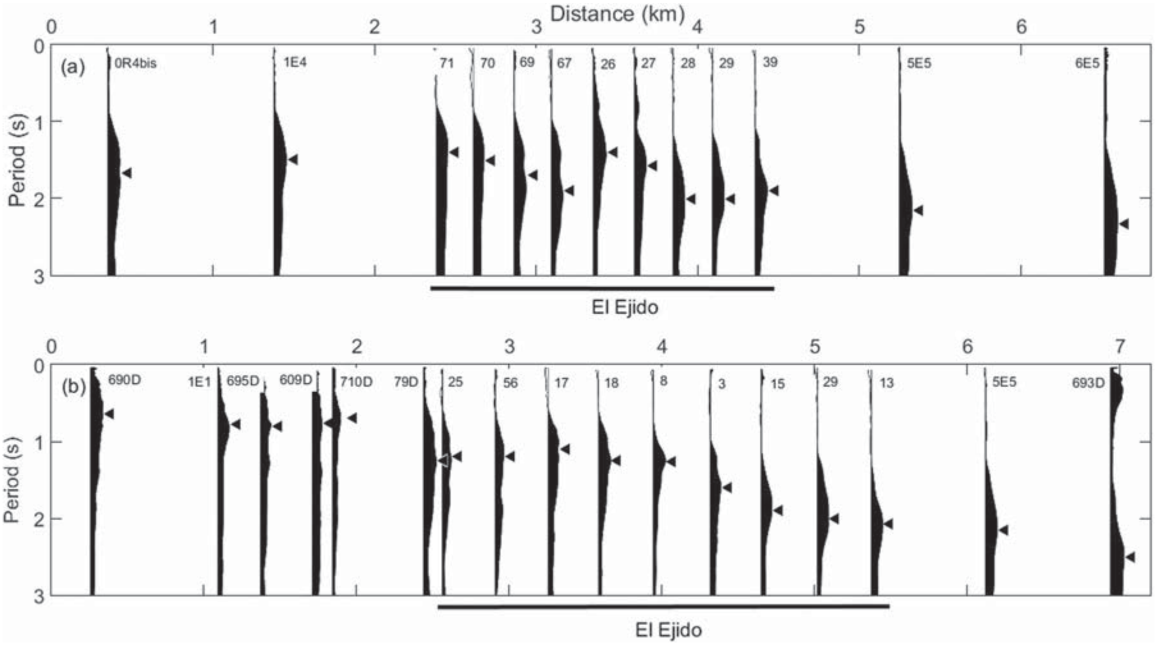

Fig. 10. Representation of HVSRs along sections a-a′ (panel a) and b-b′ (panel b). These profiles have been extended beyond the town limits in order to oversee consistency with the general basin structure. Peak amplitudes have been normalized and their corresponding fundamental periods are highlighted with black triangles.

S1, S2 and S3 (Fig. 4) are shown in Fig. 12 as examples of inversions of HVSR where *a priori* information is lacking, using the general parameter ranges presented in Table 4. These three curves show significant peaks with fundamental frequencies below 0.7 Hz and amplitudes between 4 and 5, reproduced by models with clear velocity contrasts between 400 and 650 m deep. These contrasts can be interpreted as interfaces with hard calcareous rocks. The HVSRs become relatively flat above the main peak except for site S1, where a wide bump in the band 1.2–10 Hz evidences a more complex shallow structure.

The 1-D seismic velocities models obtained along lines a-a′ and b-b′ were assembled into pseudo-2D profiles (Fig. 13) by using a radial-basis function interpolation through “Surfer” software. The a-a′ cross-section (Fig. 4) arises from the best fits of 7 HVSR curves distributed along 1800 m, and the second one (b-b′ Fig. 4) from 9 curves along 2800 m.

In the light of these two profiles, various remarks can be made about the sediments drift and seismic velocity ranges attributed to each geological unit. Firstly, it is observed how the depth down to the halfspace increases from 370 m in the northwest limit to 620 m in the southeast end (b, b′ respectively) while it keeps around 550 m deep along a-a′ profile. Since overlapping between velocity values of different materials

Table 4
Ranges for model space exploration used in the inversion procedure of HVSR curves.

Layer	Thickness (m) min–max	V_P (m/s) min–max	V_S (m/s) min–max	ρ (kg/m^3) min–max	ν min–max
1st	1–70	500–1900	330–900	1950–2050	0.15–0.35
2nd	20–300	800–2100	500–1000	2000–2200	0.21–0.35
3rd	20–300	1400–2500	850–1200	2200–2400	0.21–0.35
4th	30–300	1650–4000	1000–1900	2200–2600	0.21–0.35
Half-space		2450–5100	1500–2800	2700–2750	0.21–0.28

is accepted, an unequivocal and direct identification of each layer from these profiles is not possible. Thus, we prefer to give results in terms of averaged values for each layer of the general model established for inversion (Table 5).

3.4. SPAC technique

The second procedure used here to define the shallow and deep shear-wave velocity structure in El Ejido was based on analysis of dispersion curves of fundamental-mode Rayleigh waves retrieved from the SPAC method [22]. The SPAC coefficient $\rho_{SPAC}(\omega, R)$ was computed as the azimuthally-averaged cross-spectral densities between the records of seismometers evenly spaced on a circumference and a central station, using the power spectral density at the centre for normalization. The SPAC coefficient was separately computed for a set of overlapping time windows, plotted as a function of time and frequency and averaged discarding windows with evident disturbances. Finally, the phase-velocity $c_R(\omega)$ was computed for each frequency from Eq. (3)

$$\rho_{SPAC}(\omega, R) = J_0\left(\frac{\omega}{c_R(\omega)}R\right), \tag{3}$$

where J_0 represents the zero-order Bessel function and R is the array radius.

The next stage is the fitting process of $c_R(\omega)$ by means of an inversion procedure to obtain a 1D layered model profile, in terms of body waves velocities and densities, whose theoretical dispersion curve approximates closely the experimental one.

SPAC observations were carried out in three open spaces inside the urban area (Fig. 14). Pentagonal or triangular arrays with several

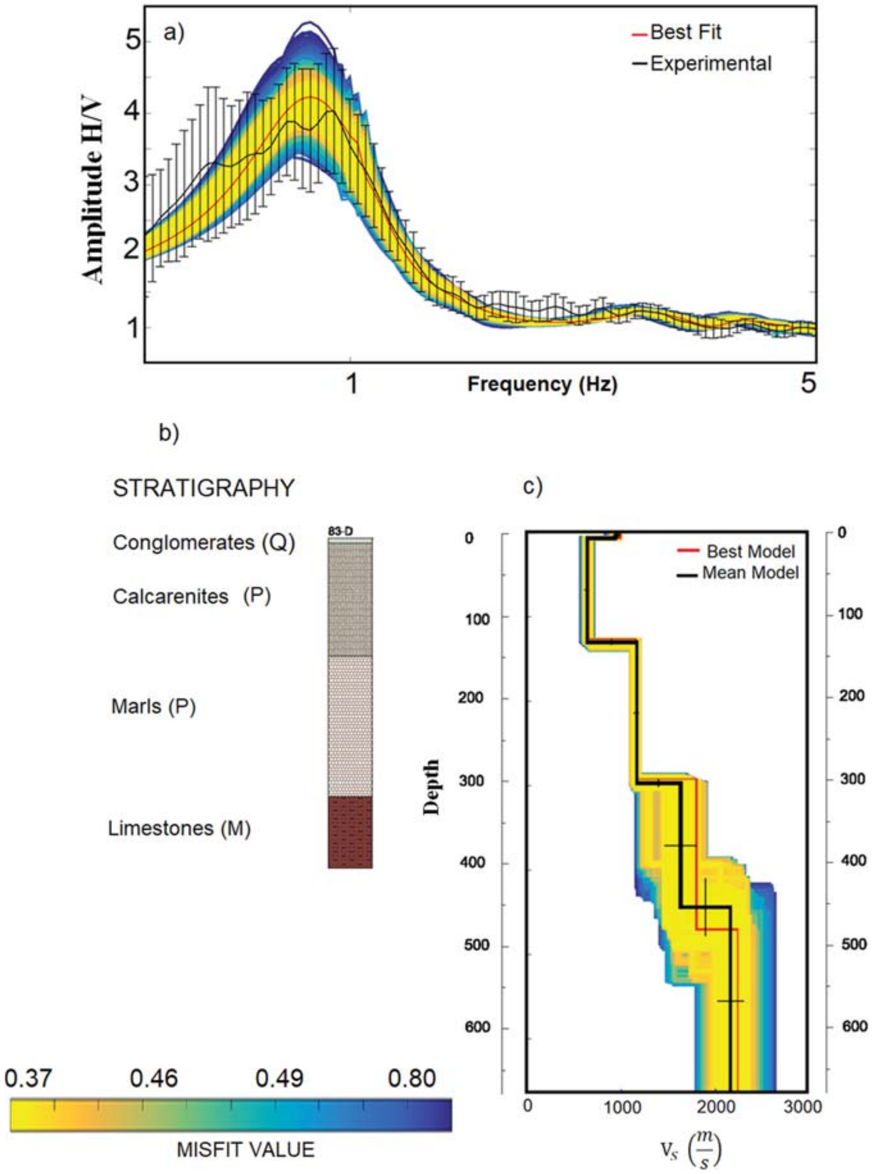

Fig. 11. Example of HVSR inversion on borehole 83-D (see location in Fig. 2a). a) Experimental HVSR curve; b) Stratigraphic column; c) Obtained V_S profile.

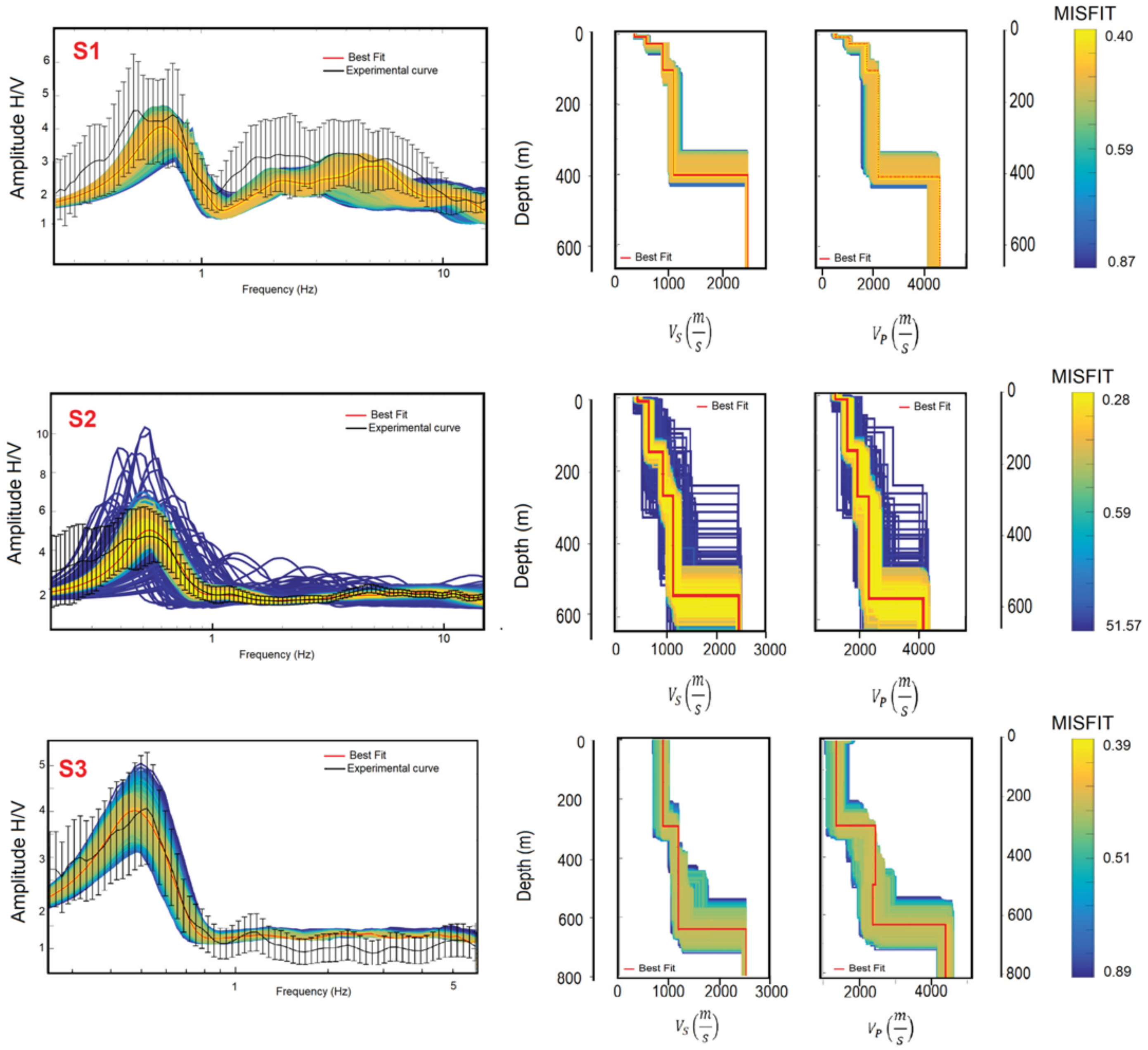

Fig. 12. Inversion of HVSRs (black lines) on sites S1, S2 and S3 (see locations in Figs. 4 and 14). Theoretical curves and their corresponding tested models are coloured according to the misfit bars. The best model achieved and its theoretical HVSR are highlighted in red. (For interpretation of the references to color in this figure legend, the reader is referred to the web version of this article.)

apertures were deployed at each site. The radii ranged from 5 to 40 m for sites S1 and S3 and from 120 to 310 m for S2 (Table 6). Broadband sensors were used as independent stations to record ambient noise in the largest array (site S2) meanwhile VSE-15D sensors all connected to a single SPC-35 digitizer were used for smaller radii (sites S1 and S3). The former setup has the advantage of wireless recording over the latter, being used here in larger arrays. The VSE-15D velocimeters have a flat frequency response from 0.25 to 70 Hz. The records were sampled with a rate of 100 sps, lasting half an hour for the small apertures (sites S1 and S3) and one hour for the larger ones (S2). The window lengths were defined to ensure that they contained each analysed period 50 times at least. Rayleigh wave velocities were retrieved in the range from 9 to 28 Hz for small arrays (S1, S3) and from 0.7 to 7 Hz for the big one (Fig. 6).

Using the assumption of an effective sampling depth between $\lambda/3$ and $\lambda/2$ for fundamental-mode Rayleigh waves of wavelength λ [39,60], the maximum resolved depth would be between a third and a half of maximum wavelength ($\lambda_{\max}$) which can be estimated from the velocity associated to the minimal frequency f_{min} of the dispersion curve as $\lambda_{\max} = c_R(f_{\min})/f_{\min}$. Thus, the maximum estimated depths are between 22 and 33 m for site S3, and from 30 to 45 m for site S1. The big triangle at site S2 would reach maximum depths between 880 and 1320 m.

The results of the inversion procedure are displayed in Fig. 15. Inversion-derived values of V_{S30} can be calculated from thicknesses and V_S values of the best-fit models (Table 6). Due to the limited resolution of the large array (site S2) at short wavelengths, the definition of the upper layers could be fuzzier, even though the computed V_{S30} value remains in a reasonable range in comparison with the smaller arrays. These models are consistent with the results of the MASW, reaffirming the moderate spatial velocity variations in the scale of hundred metres and increasing the exploration depth reached with that active technique

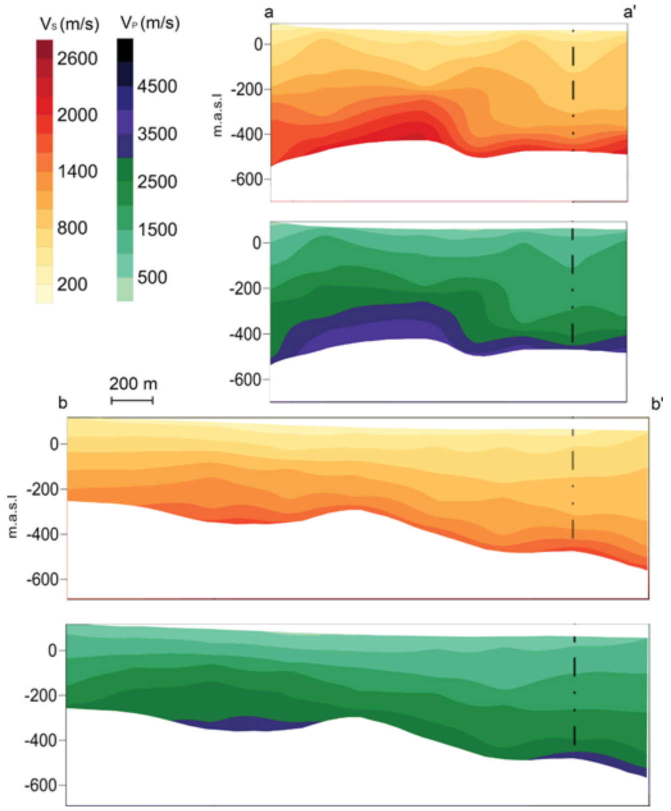

Fig. 13. Interpolated 2-D cross-sections showing the deep structure for El Ejido town in terms of seismic velocities, built from interpolation of 1-D models resulting from HVSR inversion. Models are shown down to the inverted halfspace depth. The vertical black line represents the intersection of profiles a-a′ and b-b′.

Table 5
Mean values and standard deviations obtained from the 16 best fits used for constructing the 2-D profiles shown in Fig. 13.

Layer	Thickness (m)	σ (m)	V_S (m/s)	σ (m/s)	V_P (m/s)	σ (m/s)
1st	14	13	483	70	851	111
2nd	110	57	688	80	1251	164
3rd	144	47	990	100	1936	222
4th	234	112	1381	184	2694	486
Half-space	–	–	2255	329	3950	602

(slightly for S1 and S3 and substantially for S2). However, the inversion of Rayleigh wave dispersion curves is sensitive to an overall or smoothed trend of $Vs(z)$, implying a degree of uncertainty in some characteristics of the velocity structure (e.g. existence of sharp velocity contrasts). The ground model can be more constrained by adding other observations such as the HVSR, which are very sensitive to the existence and depth of such interfaces.

3.5. Joint inversion of HVSR and dispersion curves

Dispersion curves from SPAC and HVSR at the array centres were processed together by a joint inversion scheme (Fig. 16). For site S2, the dispersion curve was extended to high frequencies (48 Hz) including the mean dispersion curve we got from MASW profile P 3.3 (Fig. 6), which go across the largest triangle (Figs. 4 and 14). “HV-Inv” software was also used in this final stage in order to characterize the S-wave velocity structure. Suitable weights for the contributions of HVSRs and dispersion curves were used, defining the misfit of a model **m** as

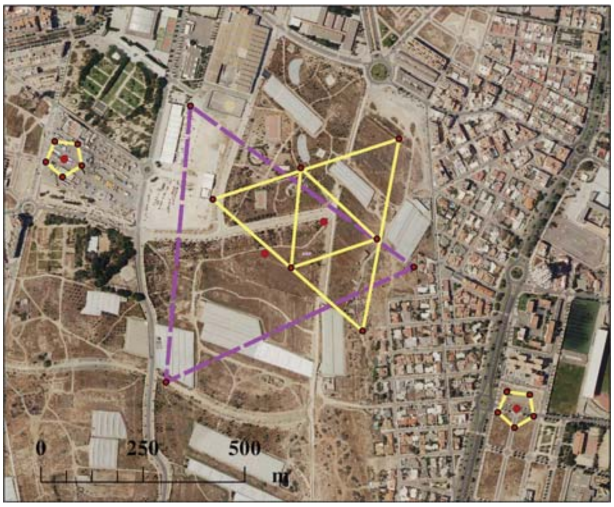

Fig. 14. Array setup for SPAC observations in El Ejido. Red points are the sensor positions on vertexes and centre of each array geometry deployed. In the case of pentagonal arrays, only the largest radius is shown. (For interpretation of the references to color in this figure legend, the reader is referred to the web version of this article.)

Table 6
Summary of array features and ranges of dispersion curves and models retrieved with the SPAC technique.

Site	R (m)	Δf (Hz)	Δc_R (m/s)	ΔV_S (m/s)	Δz (m)	V_{S30} (m/s)
S1	5–10–20–40	9–24	402–816	350–1066	5–45	578
S2	120–220–310	0.7–7	514–1842	592–2300	24–1316	514
S3	6–12–24	12–28	534–788	640–1056	7–33	705

$$misfit\,(\mathbf{m}) = \frac{1}{2n}\sum_{i=1}^{n}\frac{(HVSR_{obs}(\omega_i) - HVSR_{th}(\omega_i,\,\mathbf{m}))^2}{\sigma_{HVSR}{}^2(\omega_i)} + \frac{1}{2m}\sum_{i=1}^{m}\frac{(c_{\mathrm{R}obs}(\omega_i) - c_{\mathrm{R}th}(\omega_i,\,\mathbf{m}))^2}{\sigma_{c_{\mathrm{R}}}{}^2(\omega_i)}, \tag{4}$$

where n and m are the number of samples for the HVSR and the dispersion curve, respectively. This choice equalizes the weight of both observables in the misfit, regardless the respective number of samples (frequencies) and it does not appear to slow down the convergence of the algorithm.

The minimum frequency of the dispersion curve retrieved at site S2 approaches the fundamental frequency given by the HVSR technique, providing additional information about the deep sedimentary structure. On the other hand, the inclusion of the dispersion curve derived from MASW, which provided a theoretical exploration depth of about 23 m, improved the model accuracy in the upper two layers. The major peak in the theoretical HVSR is mainly controlled by the deepest velocity contrast of these inverted models. V_S models obtained by joint inversion of HVSRs and Rayleigh wave dispersion curves have a slightly stiffer half-space in comparison with inversion of HVSR only (Fig. 12). Results for S2 show a somewhat deeper and stiffer basement in comparison with the model derived from dispersion curve fitting (Fig. 15). In general terms, joint inversions provide more constrained models, therefore these halfspace properties should be considered to have been determined in a more reliable procedure. Parametric analysis gives evidences on how cost functions (misfit) display sharper minima for joint inversion [59]. An example of this is shown in Fig. 17a-c, where the misfits for HVSR, c_R (Eq. (2)) and joint inversion (Eq. (4)) are compared for some perturbations in the model for S2 inverted in

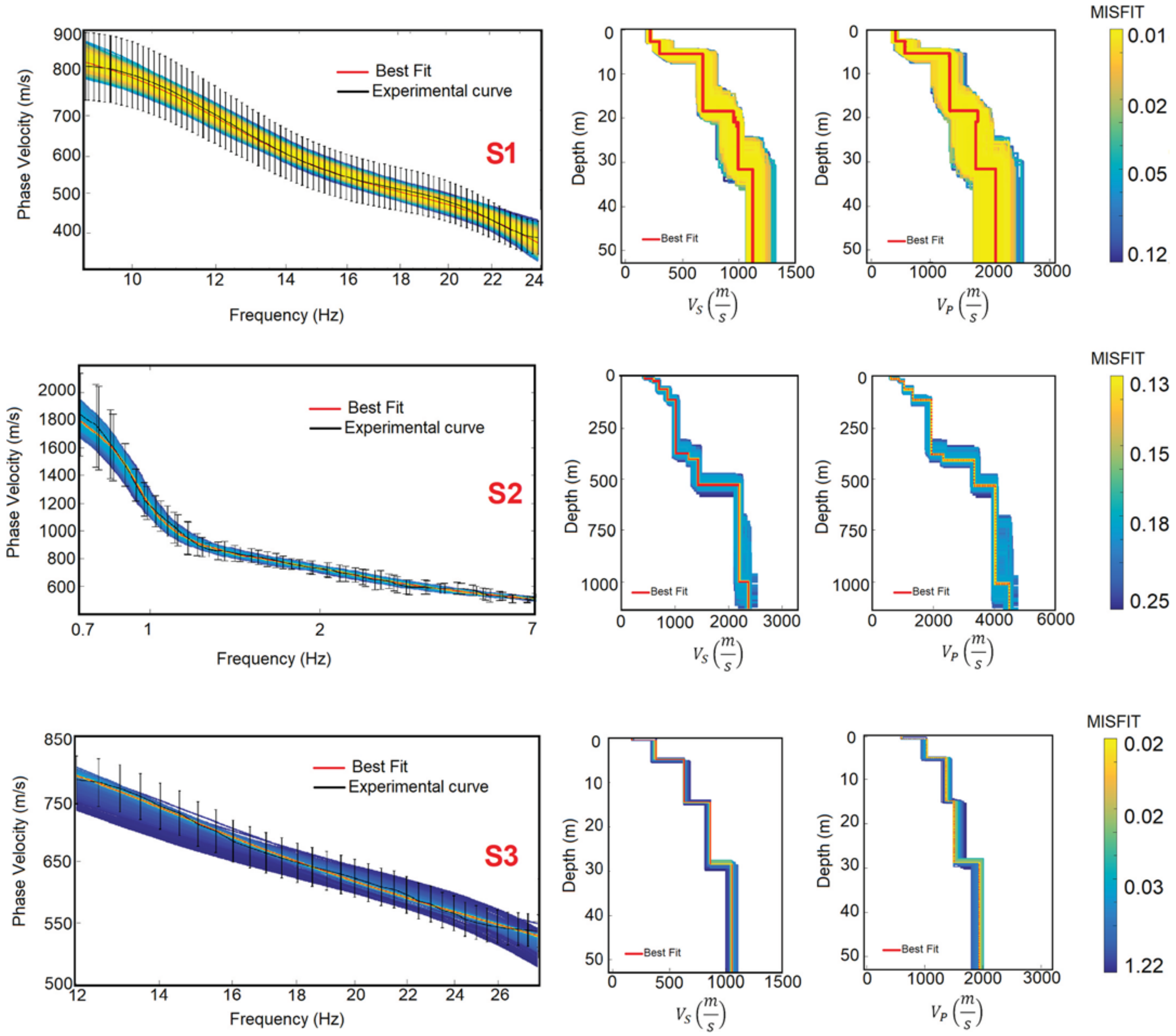

Fig. 15. Empirical dispersion curves (black lines) and theoretical curves corresponding to the tested models (coloured lines). Body wave velocity models for each analysed site. Best model achieved is highlighted in red. (For interpretation of the references to color in this figure legend, the reader is referred to the web version of this article.)

Fig. 16, which is represented by a black dot. Along the horizontal axis, velocities and thickness of the upper four layers of the model are rescaled by the same factor, preserving the travel time of P and S waves through the structure. $c_R(f)$ shows high sensitivity to these perturbations which involve variation of velocities in shallow and intermediate layers. The vertical axis corresponds to variations in P and S velocities for halfspace, preserving the Poisson's ratio. In this case, the HVSR presents greater variations. Joint inversion (Fig. 17c) provided real sensitivity to velocity values and constrained better the existing deep impedance contrasts. It should be noted that the velocity contrast between bedrock and sedimentary fillings is a critical parameter for assessment of strong-motion amplifications. In particular, ground amplifications of 3 times at the fundamental frequency can be estimated at site S2 for vertically incident S-waves (it corresponds to 6 times normalizing by the amplitude of the incident wave, as in Fig. 17e).

The HVSR(f) function depends only on the travel time of P and S waves within the layers and on density contrasts, so that *equivalent* models could be generated if all thicknesses and velocities (or all densities) were rescaled by the same factor. For instance, Sánchez-Sesma et al. [29] interpreted a HVSR curve from Texcoco (Mexico City), similar in shape and predominant frequency (0.47 Hz) to some found in El Ejido, as the resonance of 40 m of very soft clays (*Vs* as low as 70 m/s) overlying a much stiffer substratum (1000 m/s). Thus, constraints to the shallow layer velocities provided by high-frequency segments of the Rayleigh wave dispersion curves, as those retrieved in S1 and S3, still contribute to the non-uniqueness reduction of the resulting models.

4. Discussion and conclusions

Five main types of materials have been identified in El Ejido town from analysis of deep boreholes. Lithologies range from Quaternary deposits on surface, which are mainly composed by sands, silts, gravels and clays to Paleozoic-Triassic dolomites (Fig. 2b). Results of geotechnical tests provided lithological information down to 50 m deep.

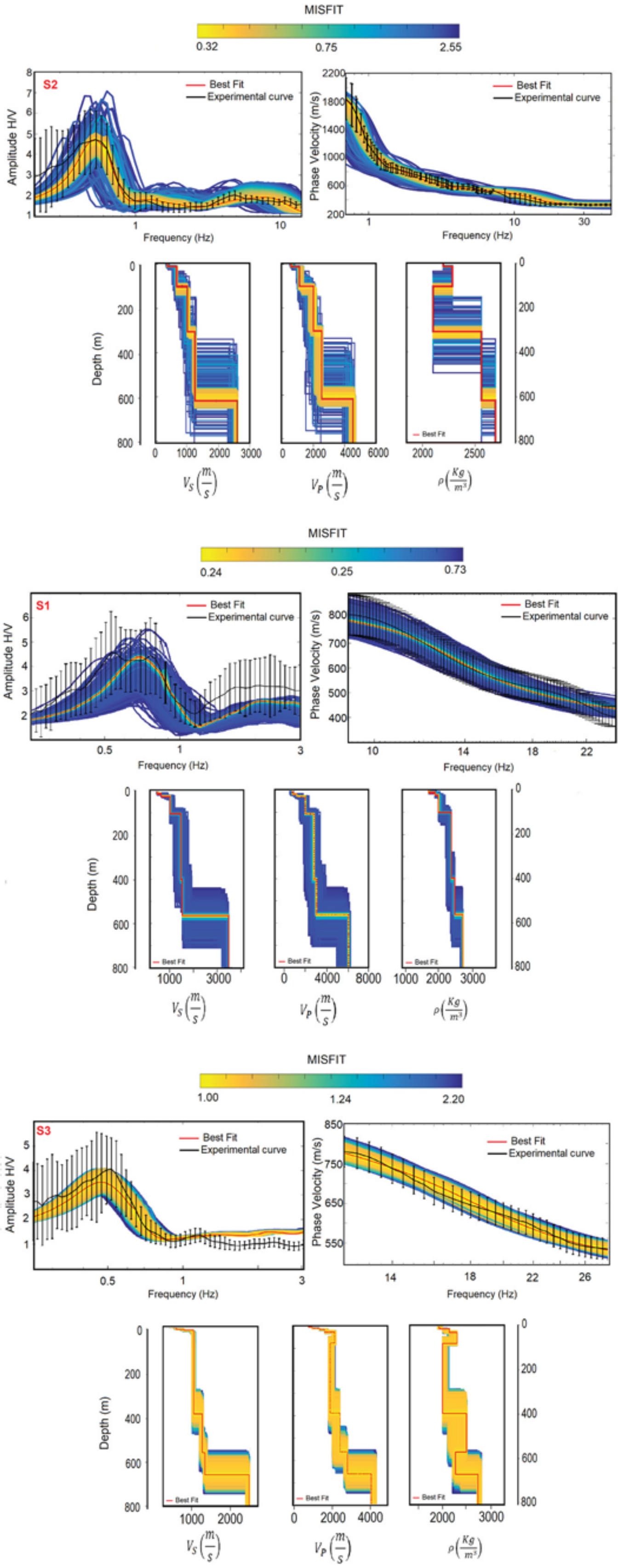

Fig. 16. Results of joint inversions from empirical HVSR and dispersion curves (black lines) for each analysed site (Fig. 14). The theoretical curves are coloured as their corresponding velocity and density models. Best model achieved is highlighted in red. (For interpretation of the references to color in this figure legend, the reader is referred to the web version of this article.)

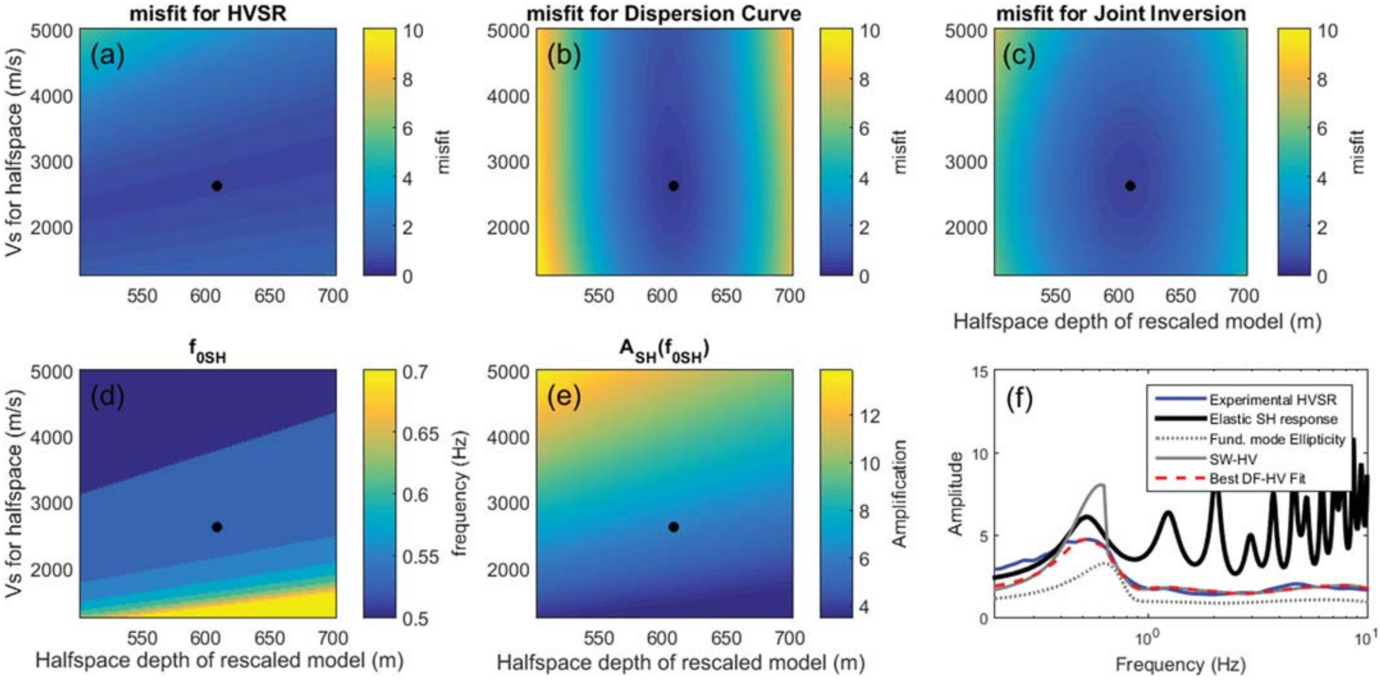

Fig. 17. (a-c) Misfit values considering HVSR, c_R (Eq. (2)) and joint inversion (Eq. (4)), respectively, for perturbations in the model inverted for site S2 in Section 3.5 (Fig. 16). Along the horizontal axis, velocities and thickness of the upper four layers of the model are rescaled by the same factor. Vertical axis corresponds to variations in halfspace velocities, preserving the Poisson's ratio. Black dots represent unperturbed parameters. (d-e) Evolution, under the same model perturbations, of the fundamental frequency for vertically incident S waves (f_{0SH}) and the amplification at f_{0SH} with respect to the amplitude of the incident wave. (f) Experimental HVSR at S2 compared with the transfer function of vertically incident S-waves computed for the inverted model, with the fundamental-mode Rayleigh wave ellipticity and with the theoretical HVSR under the DFA for full-wavefield and for surface waves only.

The Quaternary materials show a relatively high average N_{SPT} value of 32 blow counts. Interleaved in the first metres of Quaternary deposits, calcareous crusts and conglomerates are found, causing refusal in SPT logs. Density of Quaternary materials varies between 1.72 g/cm^3 for gravels and 1.94 g/cm^3 for clays. Pliocene calcarenites show an average N_{SPT} value of 49 blows and a density of 2.15 g/cm^3. Materials such as gravels, conglomerates, calcareous crusts and calcarenites often show similar N_{SPT} values. On the other hand, some materials (mainly clays and silts) presented N_{SPT} varying in wide ranges, so that lithology provides only a rough indication of the physical properties of soils. Empirical relationships (Tables 1 and 2) estimate V_S values for Quaternary materials varying in a range from 205 to 379 m/s, while calcarenites, which only outcrop on southern neighbourhoods (Fig. 2a), would have V_S of 511 ± 150 m/s.

More detailed Vs profiles for the shallow layers have been obtained by using the MASW method. Fig. 18 shows examples of these profiles with superimposed geotechnical information. In terms of Eurocode 8, the ground in El Ejido urban area can be classified as type B, whose V_{S30} values are established to range between 360 and 800 m/s. MASW cross-sections reveal that materials with V_S within this range are predominantly found in the upper 10 – 15 m. Some layers and bodies of softer materials (Vs < 360 m/s) with different sizes and thicknesses appear interleaved or atop these units in the central-southern area (West of MASW profiles P2, line P3 and East of P4) and on the Quaternary alluvial cones of the western zone (P6 line, Fig. 7). The central-southern area presents the softest profiles, being also the only zone of the town where the HVSR show peaks of moderate amplitude (2–3) at intermediate frequencies (6–8 Hz), numerically coinciding with theoretical S-wave resonances in the upper 10–20 m. Velocities above 600 m/s are mainly reached within layers of Pliocene calcarenites (e.g. SPT 8, Fig. 18b) or in levels described as marly or stiff clays (e.g. SPT loggings 9, 10, 12, Fig. 18a, b). As shown in Fig. 18, a good agreement between alternative methods has been reached where comparison was possible.

Seismic methodologies present certain complexity and costs related with the acquisition and deployment of the equipment. It consisted of 50 m long linear array for MASW measurements and, in the case of SPAC measurements, of several bidimensional arrays with different apertures that need to be placed during several hours in a quiet area. With this in mind, the MASW dataset acquired in El Ejido can be used to check and to adjust for this zone a simplified seismic method for estimation of local V_{S30} values using simpler arrays, suitable for active and passive sources. This approach could be useful in the future to characterize this town with higher sampling density or to extend this study to surrounding areas. Konno and Kataoka [61] suggested that the experimental setup used for determination of V_{S30} can be simplified if the array is designed to operate in suitable narrow wavelength ranges. They proved empirically the practical equivalence between V_{S30} and the Rayleigh wave velocity for wavelengths between 35 and 40 m (c_{35}, c_{40}) for a large dataset in Tokyo area.

In the present work, during the checking procedure of the advantages related to this faster approach it has been observed how V_{S30} is better estimated by c_{45} or c_{50} velocities (Fig. 19). This result agrees with those pointed out for places with deep water tables (e.g. [42]) and it can be partially explained by the difference between the characteristic Poison's ratio of soils in these two places (about 0.25 for El Ejido, corresponding to dry and relatively hard materials, and above 0.45 for Tokyo). The much smaller Poisson's ratios reported in our explored area would lead to higher inverted V_{S30} values for a given dispersion curve (up to ~4% increment), as a result, the equivalence with the increasing function $c_R(\lambda)$ would be reached for longer wavelengths.

The HVSR method has been applied in order to obtain a map of predominant frequencies and shape typologies from 94 sites in the town distributed on a 250 × 250 m grid. Robustness of this technique to provide the fundamental frequency when clear HVSR peaks are observed is widely accepted in the literature. That case corresponds to strong contrasts of seismic velocities between soft sediments and bedrock [47,48]. The obtained results show the effectiveness of the HVSR

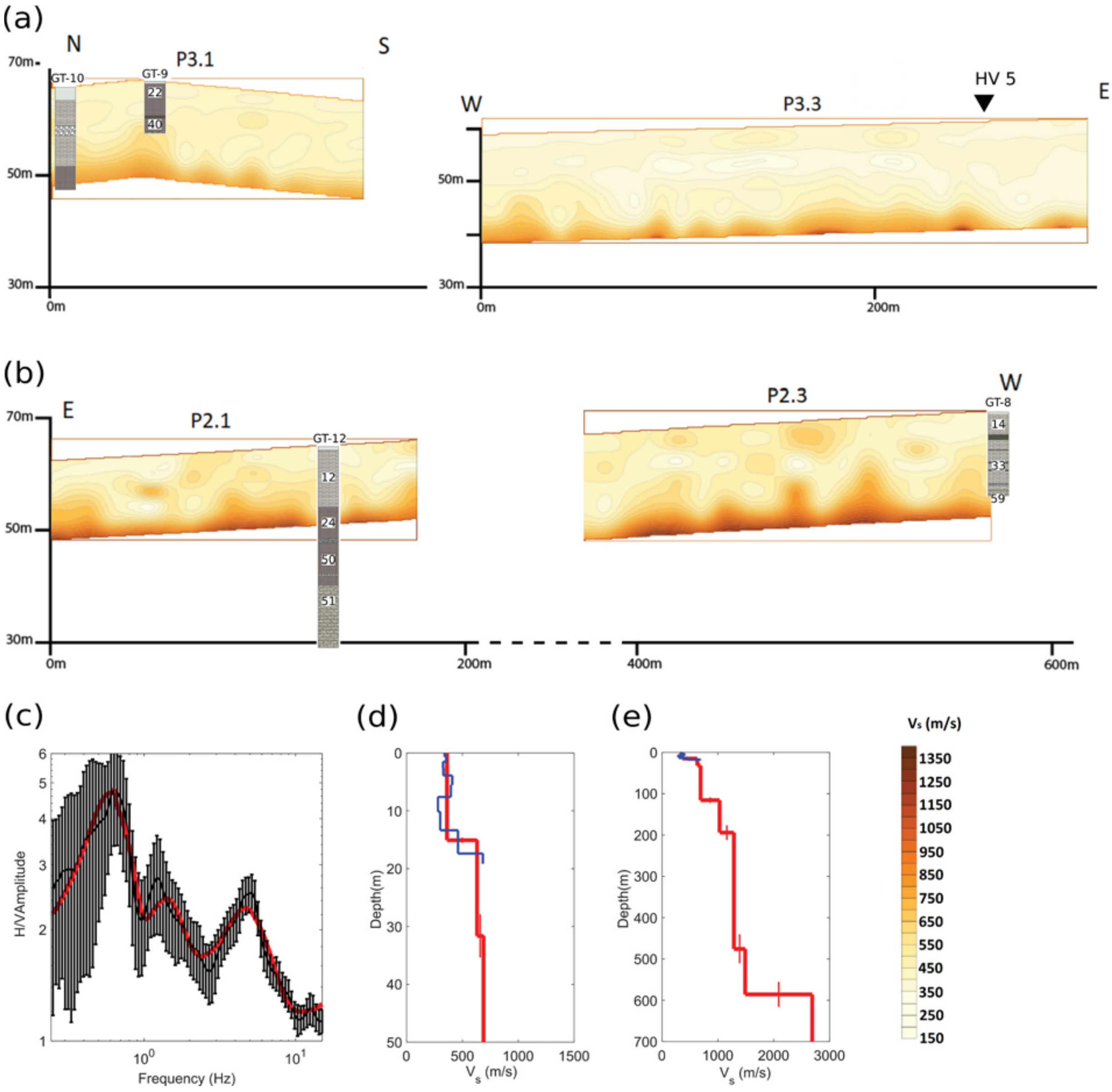

Fig. 18. Examples of *Vs* cross-sections with superimposed stratigraphic columns obtained at nearby geotechnical profiles. (a) Part of profile P3 (b) Part of profile P2. Average N_{SPT} values of the strata are shown. (c) Experimental (black line) and modelled (red line) HVSRs for site HV5, exhibiting a secondary peak at 5 Hz. (d) Upper layers of the *Vs*(*z*) model inverted from HVSR at HV5 (red line), which belongs to section a-a′(Figs. 4 and 13), and shallow profile obtained from MASW at the same point (blue line). Models are shown down to the basement in panel (e). (For interpretation of the references to color in this figure legend, the reader is referred to the web version of this article.)

method even in conditions of relatively high-velocity Pliocene and Miocene rocks keeping an important contrast with the underlying materials. Clear peaks in El Ejido are mainly concentrated in the southeast part, with peak frequencies between 0.5 and 0.7 Hz, although some are scattered between broad- and double-peak neighbours with frequencies from 0.7 to 1 Hz. Broad peaks are the highest percentage of the HVSR dataset, with lower cut-off limits between 0.3 and 0.7 Hz and higher limits from 0.6 to 1.2 Hz. This latter value is specially concentrated in the northern row of the grid. Double-peaked HVSRs are sparsely distributed in the town. In this case, the difference in frequency between the peaks is often moderate so that they appear partially overlapped, with the low frequency subpeak between 0.4 and 0.6 Hz and high frequency one between 0.6 and 0.9 Hz. Plateau-shaped HVSRs [49] are also located in northern rows, with cut-off frequencies ranging from 0.8 to 1.2 Hz. Predominant frequency distribution is not well-linked to shallow soil conditions. On the contrary, a clear dependence on the total thickness of sedimentary materials, estimated from deep borehole and seismic reflection data, is found in the study area. The highest predominant frequencies were found in the NW area of the town, whereas the SE zone shows clear HVSR peaks with lower frequencies. In case of double or broad peaks, the high-frequency value accords better with the nearby clear peaks and with the overall NW-SE trend of the periods to increase.

Since HVSR curves are sensitive to the sediment-bedrock interface, they have been used as a passive technique for approximate subsoil mapping [62–65]. In this work, the inversion of HVSR curves under the DFA provided us with 1-D velocity models where the sediments-bedrock interface is mapped (Fig. 12) as well as other shallow secondary contrasts (e.g. Fig. 18d, e). In this case, the heterogeneity in the upper layers revealed by the geotechnical tests is highly simplified in terms of an equivalent model. In fact, the upper 20 m were described by a maximum of 2 layers out of the 5 defined for the inversion process

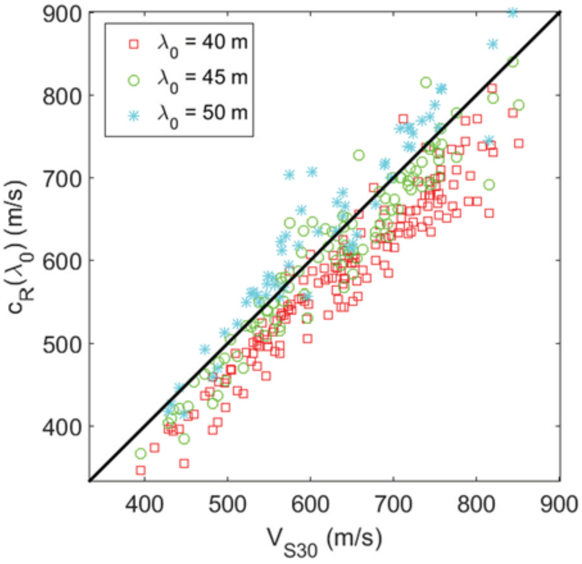

Fig. 19. Phase velocity of Rayleigh waves for fixed wavelengths λ_0 vs. V_{S30} for the individual 1D models which constitute the MASW profiles. All dispersion curves reaching the target wavelength and the corresponding 1D V_S models are considered.

(Table 4). Non-uniqueness of HVSR inversions was diminished providing additional constraints to the model parameters. In particular, an essential part of the procedure was a previous calibration through measurements performed next to deep boreholes, in which the interfaces described in previous geological studies of Campo de Dalías were identified. This processing method based on the DFA is a simple way to achieve reliable 1-D profiles from the fitting of experimental HVSR curves without the need to extract a particular type of waves (see e.g. [66] for an alternative method based on the selection of Rayleigh wave arrivals). Since effects of Love waves, higher modes of Rayleigh waves and body waves in the HVSR are not always negligible (e.g. [67,68]), full-wavefield inversions are definitely more suitable than over-simplified approached based on modelling the HVSR of noise by the Rayleigh wave ellipticity (e.g. [26,69]). For example, the peak frequency for the inverted model S2 shifts from 0.52 Hz to 0.63 Hz if only fundamental-mode Rayleigh waves are considered in the forward modelling (Fig. 17f). Moreover, body waves can be the main contribution to the vertical motion in some frequency bands with low power or high ellipticity of the Rayleigh waves, preserving realistic HVSR amplitudes in the forward modelling (e.g. compare red and solid-grey lines in Fig. 17f).

The assembling of individual velocity profiles (Fig. 13) has confirmed the south-eastward increase of sediment thickness, overcoming the poor information on the deep structure within the urban area. Active-source reflection surveys carried out in Campo de Dalías show that El Ejido lies in the north flank of an asymmetric syncline with ENE-WSW trend. N-S reflection profiles showed a mean apparent dip of about 8° for that flank. Similar behaviour is observed in the two profiles constructed for the urban area by inversion of HVSR curves. The NW-SE section (profile b-b′ Figs. 4 and 13) shows an apparent dip of around 7° with a maximum depth of 620 m down to the half-space, which is close to the 603 m value attributed by P-wave analysis of an active line that passes near b′. Inversion of broad and double peaks in the HVSR often led to models with significant velocity contrasts at intermediate depths and moderate contrasts between the halfspace and the overlaying materials (e.g. points 25 and 56 in the NW side of profile b-b′, Figs. 10 and 13). On the other hand, the E-W section in El Ejido town (profile a-a′ in Figs. 4 and 13) shows variations of the half-space depth between 490 and 630 m. Such geometry also agrees well with a parallel reflection profile conducted 1.8 km northwards (see AL-04 and AL-01 profiles in [70]).

Joint inversions of Rayleigh-wave dispersion curves and HVSR curves were carried out with the aim of enhancing the reliability of the velocity models, reducing the non-uniqueness associated to the independent inversion of any of these curves. An array of larger aperture (site S2, Figs. 4 and 14) was deployed to retrieve Rayleigh wave velocities at low frequencies, close to the HVSR predominant frequency. Even though the resulting ground model has a more constrained deep structure, mainly in *Vs*, the obtained seismic velocities are still within the ranges defined for the models inverted from HVSRs (Table 4). The S-wave velocity of 2.5 km/s found below the main interface is in good accordance with the shallow layers of the general 1D models for Alboran Sea obtained by Grevemeyer et al. [37] and Stich et al. [71] from arrival times of seismic phases of local earthquakes, which are respectively 2.4 and 2.8 km/s for the uppermost 3 km. The V_P/V_S ratio of 1.76 for the halfspace is also consistent with their models which show values in the range 1.65–1.8. Simple 1D analysis predicts S-waves amplifications due to the sedimentary structure of up to 3 times at the resonance frequency (Fig. 17e-f).

As far as the authors' knowledge, our models provide the first bounds for V_S of the whole stratigraphy for the sedimentary fillings in Campo de Dalías basin down to the Triassic basement by means of seismic techniques sensitive to this magnitude. The models coming from inversion of ambient noise measurements at deep boreholes in the outskirts of the town show Quaternary conglomerates with V_S ranging from 820 to 1000 m/s, well above the surface velocity of most of the Quaternary units logged in the urban area. This result highlights the benefits of spending time in techniques capable of resolving weak velocity variations, such as the MASW and the SPAC method (Figs. 7 and 15). Pliocene units are represented in those models by calcarenites varying from 590 to 680 m/s and marls from 990 to 1200 m/s. Despite the aforementioned lack of local relationships between N_{SPT} and *Vs* for Pliocene units, this interval includes the value given from geotechnical analysis, previously considered as a rough approximation. Finally, layers between 1300 and 1600 m/s and those above 1800 m/s are identified as Tortonian calcarenites and Triassic dolomites, respectively. These older units had been only described in terms of V_P and densities. The use of these *Vs* models will help to perform significant simulations of the seismic response of the basin, which is the topic of an ongoing research work.

Acknowledgements

This article is dedicated to the memory of Antonio Sánchez Picón. The authors would like to thank J. Francisco Navarro López, Esther Martín Funes and Marina Arrien for helping in the field measurements. We also thank Luis Molina Sánchez for providing valuable borehole data. The authors gratefully acknowledge the support provided by the staff of the Municipal Archive and Local Police of El Ejido. The constructive comments of the editor and two anonymous referees significantly improved this article.

Funding

This work was supported by the Spanish Ministry of Economy and Competitiveness and the European Regional Development Fund (project number CGL2014–59908).

References

[1] Vidal F. Sismotectónica de las Béticas Centrales y el Mar de Alborán (Ph.D. thesis). University of Granada; 1986.
[2] Medina F, Cherkaoui T-E, et al. The South-Western Alboran Earthquake Sequence of January-March 2016 and Its Associated Coulomb Stress Changes. Open J Earthq Res 2017;6:35.
[3] CEN. Comité Européen de Normalisation, Eurocode 8: Design of structures for earthquake resistance-part 1: general rules, seismic actions and rules for buildings;

2004.

[4] Rodríquez-Marek A, Bray JD, Abrahamson N. An empirical geotechnical seismic site response procedure. Earthq Spectra 2001;17:65–87.

[5] Seed RB, Dickenson SE, Mok CM. Seismic response analysis of soft and deep cohesive sites: a brief summary at recent findings, Sacramento, California; 1991.

[6] Borcherdt RD. Estimates of site-dependent response spectra for design (methodology and justification). Earthq Spectra 1994;10:617–53.

[7] Salameh C, Bard P-Y, Guillier B, Harb J, Cornou C, Gérard J, et al. Using ambient vibration measurements for risk assessment at an urban scale: from numerical proof of concept to Beirut case study (Lebanon). Earth Planets Space 2017;69:60. https://doi.org/10.1186/s40623-017-0641-3.

[8] AS 1170.4. Auatralian Standard: AS 1170.4-2007, structural design actions, Part 4: earthquake actions in Australia. Sydney, Australia; 2007.

[9] E-030. Peruvian earthquake resistant code: earthquake resistant design E-030, Peru; 2016.

[10] Alessandro CD, Bonilla LF, Boore DM, Rovelli A, Scotti O. Predominant-period site classification for response spectra prediction equations in Italy. Bull Seismol Soc Am 2012;102:680–95. https://doi.org/10.1785/0120110084.

[11] Fukushima Y, Bonilla LF, Scotti O, Douglas J. Site classification using horizontal-to-vertical response spectral ratios and its impact when deriving empirical ground-motion prediction equations. J Earthq Eng 2007;11:712–24. https://doi.org/10.1080/13632460701457116.

[12] Anderson JG. Implication of attenuation for studies of the earthquake source. Earthq Source Mech 1986:311–8.

[13] Navarro M, Vidal F, Enomoto T, Alcalá FJ, García-Jerez A, Sánchez FJ, et al. Analysis of the weightiness of site effects on reinforced concrete (RC) building seismic behaviour: the Adra town example (SE Spain). Earthq Eng Struct Dyn 2007;36:1363–83.

[14] Koketsu K, Miyake H. A seismological overview of long-period ground motion. J Seismol 2008;12:133–43. https://doi.org/10.1007/s10950-007-9080-0.

[15] Takai N, Shigefuji M, Rajaure S, Bijukchhen S, Ichiyanagi M, Dhital MR, et al. Strong ground motion in the Kathmandu Valley during the 2015 Gorkha, Nepal, earthquake. Earth Planets Space 2016;68:10. https://doi.org/10.1186/s40623-016-0383-7.

[16] Akin MK, Kramer SL, Topal T. Empirical correlations of shear wave velocity (V s) and penetration resistance (SPT-N) for different soils in an earthquake-prone area (Erbaa-Turkey). Eng Geol 2011;119:1–17.

[17] Ohta Y, Goto N. Empirical shear wave velocity equations in terms of characteristic soil indexes. Earthq Eng Struct Dyn 1978;6:167–87.

[18] Tan CG, Majid TA, Ariffin KS, Bunnori NM. Effects of site classification on empirical correlation between shear wave velocity and standard penetration resistance for soils. Appl. Mech Mater 2013;284–287:1305–10. https://doi.org/10.4028/www.scientific.net/AMM.284-287.1305.

[19] Sairam B, Rastogi BK, Aggarwal S, Chauhan M, Bhonde U. Seismic site characterization using Vs30 and site amplification in Gandhinagar region, Gujarat, India. Curr Sci 2011:754–61.

[20] Park C. MASW for geotechnical site investigation. Lead Edge 2013;32:656–62.

[21] Yilmaz Ö. Engineering seismology with applications to geotechnical engineering. SEG books. 2015.

[22] Aki K. Space and time spectra of stationary stochastic waves, with spectral reference to microtremors. Bull Earthq Res Inst 1957;35:415–56.

[23] Nakamura Y. A method for dynamic characteristics estimation of subsurface using microtremor on the ground surface. Railw Tech Res Inst Q Rep 1989:30.

[24] Claprood M, Asten MW, Kristek J. Combining HVSR microtremor observations with the SPAC method for site resonance study of the Tamar Valley in Launceston (Tasmania, Australia). Geophys J Int 2012;191:765–80.

[25] Claprood M, Asten MW. Combined use of SPAC, FK and HVSR microtremor survey methods for site hazard study over the 2D Tamar Valley, Launceston, Tasmania. ASEG Ext Abstr 2007;2007:1–4. https://doi.org/10.1071/aseg2007ab020.

[26] García-Jerez A, Navarro M, Alcalá FJ, Luzón F, Pérez-Ruiz JA, Enomoto T, et al. Shallow velocity structure using joint inversion of array and h/v spectral ratio of ambient noise: the case of Mula town (SE of Spain). Soil Dyn Earthq Eng 2007;27:907–19. https://doi.org/10.1016/j.soildyn.2007.03.001.

[27] Lontsi AM, Ohrnberger M, Krüger F. Shear wave velocity profile estimation by integrated analysis of active and passive seismic data from small aperture arrays. J Appl Geophys 2016;130:37–52.

[28] Pastén C, Sáez M, Ruiz S, Leyton F, Salomón J, Poli P. Deep characterization of the Santiago Basin using HVSR and cross-correlation of ambient seismic noise. Eng Geol 2016;201:57–66. https://doi.org/10.1016/j.enggeo.2015.12.021.

[29] Sánchez-Sesma FJ, Rodríguez M, Iturrarán-Viveros U, Luzón F, Campillo M, Margerin L, et al. A theory for microtremor H/V spectral ratio: application for a layered medium. Geophys J Int 2011;186:221–5. https://doi.org/10.1111/j.1365-246X.2011.05064.x.

[30] García-Jerez A, Piña-Flores J, Sánchez-Sesma FJ, Luzón F, Perton M. A computer code for forward calculation and inversion of the H/V spectral ratio under the diffuse field assumption. Comput Geosci 2016;97:67–78. https://doi.org/10.1016/j.cageo.2016.06.016.

[31] Rodriguez-Fernandez J, Martin-Penela AJ. Neogene evolution of the Campo de Dalias and the surrounding offshore areas - (Northeastern Alboran Sea). Geodin Acta 1993;6:255–70. https://doi.org/10.1080/09853111.1993.11105253.

[32] Pedrera A, Marín-Lechado C, Galindo-Zaldívar J, Lobo FJ. Smooth folds favoring gypsum precipitation in the Messinian Poniente marginal basin (Western Mediterranean). Tectonophysics 2015;663:48–61. https://doi.org/10.1016/j.tecto.2015.05.019.

[33] Marín-Lechado C. Estructura y evolución tectónica reciente del Campo de Dalías y de Níjar en el contexto del límite meridional de las Cordilleras Béticas orientales (Ph.D. thesis). University of Granada; 2005.

[34] Casado CL, de Galdeano CS, Palacios SM, Romero JH. The structure of the Alboran Sea: an interpretation from seismological and geological data. Tectonophysics 2001;338:79–95.

[35] Aguirre J. El Plioceno del SE de la Península Ibérica (provincia de Almería). Síntesis estratigráfica, sedimentaria, bioestratigráfica y paleogeográfica. Rev Soc Geológica Esp 1998;11:297–315.

[36] Fernández LRR, Zaldívar JG, León AP, Lechado CM. Estructura del Campo de Dalías a partir de datos gravimétricos y sísmicos. Geogaceta 2004:3–6.

[37] Grevemeyer I, Gràcia E, Villaseñor A, Leuchters W, Watts AB. Seismicity and active tectonics in the Alboran Sea, Western Mediterranean: constraints from an offshore-onshore seismological network and swath bathymetry data. J Geophys Res Solid Earth 2015;120:8348–65. https://doi.org/10.1002/2015JB012073.

[38] Toshida Y, Motonori I. Empirical formulas of SPT blow-counts for gravely soils. In: Proceedings of the 1st international symp. on penetration testing. Orlando; 1988.

[39] Park CB, Miller RD, Xia J. Multichannel analysis of surface waves. GEOPHYSICS 1999;64:800–8. https://doi.org/10.1190/1.1444590.

[40] Boiero D, Socco LV, Stocco S, Wisén R. Bedrock mapping in shallow environments using surface-wave analysis. Lead Edge 2013;32:664–72.

[41] Xia J, Miller RD, Park CB. Estimation of near-surface shear-wave velocity by inversion of Rayleigh waves. Geophysics 1999;64:691–700.

[42] Foti S, Hollender F, Garofalo F, Albarello D, Asten M, Bard P-Y, et al. Guidelines for the good practice of surface wave analysis: a product of the InterPACIFIC project. Bull Earthq Eng 2017:1–54. https://doi.org/10.1007/s10518-017-0206-7.

[43] Bard P-Y. Microtremor measurements: a tool for site effect estimation. In: Irikura K, Kudo K, Okada H, Satasini T, editors. Effects surface geology on seismic motion. Rotterdam: Balkema; 1999. p. 1251–79.

[44] Lunedei E, Malischewsky P. A review and some new issues on the theory of the H/V technique for ambient vibrations. In: Ansal A, editor. Perspectives on European earthquake engineering and seismology. Cham: Springer; 2015. p. 371–94.

[45] Wathelet M. An improved neighborhood algorithm: parameter conditions and dynamic scaling. Geophys Res Lett 2008:35.

[46] Konno K, Ohmachi T. Ground-motion characteristics estimated from spectral ratio between horizontal and vertical components of microtremor. Bull Seismol Soc Am 1998;88:228–41.

[47] Bard PY, SESAME-Team. Guidelines for the implementation of the H/V spectral ratio technique on ambient vibrations: measurements, processing, and interpretations. SESAME Eur Res Proj 2005:2005.

[48] Bonnefoy-Claudet S, Baize S, Bonilla LF, Berge-Thierry C, Pasten C, Campos J, et al. Site effect evaluation in the basin of Santiago de Chile using ambient noise measurements. Geophys J Int 2009;176:925–37.

[49] Guillier B, Cornou C, Kristek J, Moczo P, Bonnefoy-Claudet S, Yves-Bard P. et al. Simulation of seismic ambient vibrations: does the H/V provide quantitative information in 2D–3D structure? In: Proceedings of the 3rd international symposium on the effects of surface geology on seismic motion. Grenoble; 2006.

[50] Gosar A. Study on the applicability of the microtremor HVSR method to support seismic microzonation in the town of Idrija (W Slovenia). Nat Hazards Earth Syst Sci 2017;17:925.

[51] Le Roux O, Cornou C, Jongmans D, Schwartz S. 1-D and 2-D resonances in an Alpine valley identified from ambient noise measurements and 3-D modelling. Geophys J Int 2012;191:579–90. https://doi.org/10.1111/j.1365-246X.2012.05635.x.

[52] Maresca R, Berrino G. Investigation of the buried structure of the Volturara Irpina Basin (southern Italy) by microtremor and gravimetric data. J Appl Geophys 2016;128:96–109. https://doi.org/10.1016/j.jappgeo.2016.03.010.

[53] Sánchez-Sesma FJ, Campillo M. Retrieval of the Green's function from cross correlation: the canonical elastic problem. Bull Seismol Soc Am 2006;96:1182–91.

[54] Snieder R. Extracting the Green's function from the correlation of coda waves: a derivation based on stationary phase. Phys Rev E 2004:69. https://doi.org/10.1103/PhysRevE.69.046610.

[55] Wapenaar K, Thorbecke J, Draganov D. Relations between reflection and transmission responses of three-dimensional inhomogeneous media. Geophys J Int 2004;156:179–94.

[56] Shapiro NM, Campillo M. Emergence of broadband Rayleigh waves from correlations of the ambient seismic noise. Geophys Res Lett 2004:31.

[57] Sánchez-Sesma FJ, Pérez-Ruiz JA, Luzón F, Campillo M, Rodríguez-Castellanos A. Diffuse fields in dynamic elasticity. Wave Motion 2008;45:641–54.

[58] García-Jerez A, Luzón F, Sánchez-Sesma FJ, Lunedei E, Albarello D, Santoyo MA, et al. Diffuse elastic wavefield within a simple crustal model. Some consequences for low and high frequencies. J Geophys Res Solid Earth 2013;118:5577–95.

[59] Piña-Flores J, Perton M, García-Jerez A, Carmona E, Luzón F, Molina-Villegas JC, et al. The inversion of spectral ratio H/V in a layered system using the diffuse field assumption (DFA). Geophys J Int 2017;208:577–88. https://doi.org/10.1093/gji/ggw416.

[60] Tokimatsu K. Geotechnical site characterization using surface waves. In: Ishiharaeditor. Earthquake geotechnical engineering, Rótterdam. Balkema; 1997. p. 1333–68.

[61] Konno K, Kataoka S. An estimating method for the average S-wave velocity of ground from the phase velocity of Rayleigh wave. Doboku Gakkai Ronbunshu 2000 2000:415–23.

[62] Gosar A, Lenart A. Mapping the thickness of sediments in the Ljubljana Moor basin (Slovenia) using microtremors. Bull Earthq Eng 2010;8:501–18. https://doi.org/10.1007/s10518-009-9115-8.

[63] Mulargia F, Castellaro S. HVSR deep mapping tested down to ~1.8 km in Po Plane Valley, Italy. Phys Earth Planet Inter 2016;261:17–23. https://doi.org/10.1016/j.pepi.2016.08.002.

[64] Picotti S, Francese R, Giorgi M, Pettenati F, Carcione JM. Estimation of glacier

thicknesses and basal properties using the horizontal-to-vertical component spectral ratio (HVSR) technique from passive seismic data. J Glaciol 2017;63:229–48. https://doi.org/10.1017/jog.2016.135.

[65] Dal Moro G. Surface wave analysis for near surface applications. Amsterdam: Elsevier; 2015.

[66] Poggi V, Fäh D, Burjanek J, Giardini D. The use of Rayleigh-wave ellipticity for site-specific hazard assessment and microzonation: application to the city of Lucerne, Switzerland. Geophys J Int 2012;188:1154–72.

[67] Kawase H, Matsushima S, Satoh T, Sánchez-Sesma FJ. Applicability of theoretical horizontal-to-vertical ratio of microtremors based on the diffuse field concept to previously observed data. Bull Seismol Soc Am 2015;105:3092–103.

[68] Endrun B. Love wave contribution to the ambient vibration H/V amplitude peak observed by array measurements. J Seismol 2010;15:443–72.

[69] Rosa-Cintas S, Clavero D, Delgado J, López-Casado C, Galiana-Merino JJ, Garrido J. Characterization of the shear wave velocity in the metropolitan area of Málaga (S Spain) using the H/V technique. Soil Dyn Earthq Eng 2017;92:433–42.

[70] Plata-Torres T, Lopez-Soseña F, Aracil-Avil E, Lopez-Mendieta F. Estudio estructural del acuífero profundo del Campo Dalías (Almería) mediante sísmica de reflexión Vol. IV. Madrid: Instituto Geológico y Minero de España; 2004.

[71] Stich D, Ammon CJ, Morales J. Moment tensor solutions for small and moderate earthquakes in the Ibero-Maghreb region. J Geophys Res 2003;108:2148.

Journal of Applied Geophysics 177 (2020) 104024

Contents lists available at ScienceDirect

Journal of Applied Geophysics

journal homepage: www.elsevier.com/locate/jappgeo

Use of peaks and troughs in the horizontal-to-vertical spectral ratio of ambient noise for Rayleigh-wave dispersion curve picking

José Piña-Flores [a,b,*], Martín Cárdenas-Soto [a], Antonio García-Jerez [c], Helena Seivane [c], Francisco Luzón [c], Francisco J. Sánchez-Sesma [d]

[a] Facultad de Ingeniería, Universidad Nacional Autónoma de México; CU, Circuito Escolar; Coyoacán 04510, CDMX, Mexico
[b] Posgrado de Ingeniería, Universidad Nacional Autónoma de Mexico, Edificio "S" "Bernardo Quintana Arrioja", Primer Piso, Facultad de Ingeniería, Cd. Universitaria, CDMX C.P. 04510, Mexico
[c] Departamento de Química y Física, Universidad de Almería, 04120 Almería, Spain
[d] Instituto de Ingeniería, Universidad Nacional Autónoma de México, C.U., Coyoacán 04510 D.F., Mexico

ARTICLE INFO

Article history:
Received 22 August 2019
Received in revised form 12 April 2020
Accepted 12 April 2020
Available online 14 April 2020

Keywords:
Ambient seismic noise
Rayleigh waves
Joint inversion
HVSR

ABSTRACT

To assist in the identification of fundamental-mode dispersion curves of Rayleigh waves in dispersion diagrams, we explore the relation between the shape of the horizontal-to-vertical spectral-ratio (HVSR) of ambient seismic noise and the shape of the dispersion curves for phase and group velocities in a stratified medium. We propose to use the information coming from the HVSR to identify the osculation zones and multi-mode effects and to locate inflection points and critical points in the observed phase and group dispersion diagrams of Rayleigh waves. The relationship between these curves has been numerically investigated for some models consisting of one and two homogeneous layers overlying a half-space, with velocities increasing downwards. It is primarily found that the first minimum in the HVSR appears close to the frequency of the inflection point of the fundamental mode of phase velocity. In addition, the osculation and multimode effects occur between frequencies of the fundamental peak and the first minimum of the HVSR. On the other hand, the frequencies of the minima in HVSR closely approximate the critical points of the fundamental-mode group-velocity dispersion curve, even better than the inflection points of the fundamental-mode phase-velocity curve. Finally, we show an example of experimental identification of fundamental-mode phase and group dispersion curves supported by the shape of the HVSR, obtaining a reliable velocity profile through the simultaneous inversion of these three curves.

1. Introduction

In the last two decades, the ambient seismic noise (ASN) has been extensively used to obtain Rayleigh wave dispersion diagrams. The primary objective of these studies is to obtain S-wave velocity profiles and to evaluate site effects (see Xia et al., 1999; Bonnefoy-Claudet et al., 2006; Foti et al., 2011). Different geophysical methods are allowing the retrieval of dispersion curves using ASN signals, among which the most important are the following: 1.- Spatial Autocorrelation (SPAC, Aki, 1957; Köhler et al., 2007; García-Jerez et al., 2008); 2.- Frequency-Wavenumber analysis (FK, Capon, 1969; Ohori et al., 2002); 3.- passive Multichannel Analysis of Surface Waves (MASW, Dai et al., 2019, Coelho et al., 2018, Mi et al., 2017); 4.- Refraction Microtremor (ReMi, Louie, 2001).

Dispersion curves picking in frequency-velocity or equivalent diagrams is generally made manually, identifying high energy bands with segments of dispersion curves of a particular mode. Thus, interpretation errors can be made with some probability. In methods such as the SPAC or with limited array setups, only an effective phase velocity dispersion curve can be usually picked, probably as a combination of several Rayleigh wave modes (Tokimatsu et al., 1992; Zhang, 2011). The transition between different modes can even contain leaky waves which cannot be interpreted in terms of normal Rayleigh-wave modes (Gao et al., 2014; García-Jerez and Sánchez-Sesma, 2015). When the propagation medium has a high impedance contrast or low velocity zones (Mi et al., 2018), the effective phase-velocity dispersion curve of Rayleigh and Love waves often shows jumps due to mode osculation effects and/or significant contributions of higher modes (Tokimatsu et al., 1992; Ikeda et al., 2012; Pan et al., 2013; Gao et al., 2016). This multimode effects can even be due to the directional contribution of noise sources (Ma et al., 2016) or to the presence of surface topography

---

* Corresponding author at: Facultad de Ingeniería, Universidad Nacional Autónoma de México; CU, Circuito Escolar; Coyoacán 04510, CDMX, Mexico.

E-mail addresses: jpf@unam.mx (J. Piña-Flores), martinc@unam.mx (M. Cárdenas-Soto), agarcia-jerez@ual.es (A. García-Jerez), hsr084@ual.es (H. Seivane), fluzon@ual.es (F. Luzón), sesma@unam.mx (F.J. Sánchez-Sesma).

https://doi.org/10.1016/j.jappgeo.2020.104024

which can strongly influence the energy distribution in a dispersion image at high frequency (Zeng et al., 2012; Ning et al., 2018).

When working with a limited number of stations, the lack of resolution in the dispersion diagram can make it difficult to separate the different modes (e.g. Lin et al., 2017), mainly when there are osculation effects. Incorrect identification of the modes will usually lead to an overestimation of S-wave velocities and errors in depths during the inversion (Zhang and Chan, 2009; Gao et al., 2016). Separation of higher-mode dispersion curves from the fundamental-mode group velocity gets even more complicated due to the existence of crossings between different modes at different frequencies (see e.g. Baena-Rivera et al., 2016). However, when a correct identification of fundamental mode and higher modes is made, for phase and group velocities, the incorporation of higher modes in an inversion process allows to get better information about the velocity profile, increasing the depth of investigation and the resolution of the model (Maraschini et al., 2010).

Different studies have tried to mitigate the problem of mode identification. Tokimatsu et al. (1992) discussed the effects of multiple modes on Rayleigh wave dispersion curves to reduce the non-uniqueness of shear wave velocity profiles, proposing the definition of effective dispersion curves that appear as a combination of modal curves. Lunedei and Albarello (2009) found an expression for the effective dispersion curves as a function of the modal phase-velocity dispersion curves. This equation has been used by Farrugia et al. (2016) to obtain velocity profiles with effective dispersion curves. Moreover, Lai et al. (2014) and Astaneh and Guddati (2016) presented explicit mathematical derivations for different definitions of the effective phase velocity of Rayleigh waves in an isotropic elastic horizontally layered medium, based on analytical derivatives. These formulae can lead to the development of a new class of inversion algorithms capable of considering the influence of all modes of Rayleigh wave propagation.

Amplitude ratios, subsoil conditions and analysis of particle motion can help in modal separation. Boaga et al. (2013) examined the subsoil conditions and the common field acquisition procedures that can generate osculation effects in the Rayleigh wave dispersion curves. These osculation effects are linked to the Rayleigh wave ellipticity. These authors show a priori markers of subsoil conditions that can act as warnings against the osculation effects and relate these signs with those frequencies at which dispersion curves can be misidentified. Rivet et al. (2015) proposed to use the horizontal-to-vertical spectral-ratio (HVSR) from records of ASN for the identification of higher modes. They independently inverted the dispersion curves assuming that they corresponded to (1) the fundamental mode and (2) the first higher mode. Afterward, they computed the theoretical HVSR for the obtained models and compared them with the observed HVSR, allowing the identification of the excitation mode.

In contrast, Ma et al. (2016) used the approach proposed by Tokimatsu et al. (1992) to distinguish the fundamental-mode excitation from the higher modes, observing the particle motion for Rayleigh waves in a period range of 1–10 s. Besides, these authors found that the cut-off frequency of the first higher mode is controlled by the depth of the basement and coincides with the rapid decrement of the HVSR of the fundamental mode (ellipticity). Maranò et al. (2017) have succeeded in recovering the ellipticity of Rayleigh waves from records of ASN. They indicated that the phase angle of the ellipticity can be valuable information for mode separation. The ellipticity angle allows to accurately find the frequency of its singularities, which in turn correspond to a change in the direction of the particle motion from retrograde to retrograde or vice versa. Boué et al. (2016) also analyzed the particle motion in cross-correlations (CC) between pairs of stations to distinguish between fundamental- and higher-mode dispersion curves considering these differences in the motion direction.

More recently, Mi et al. (2019) proposed the separation of higher and fundamental modes of Rayleigh waves in the frequency - phase velocity (*f*-*v*) domain through the high-resolution linear Radon transformation. They also calculated the HVSR of Rayleigh waves for the fundamental mode from active seismic records. Finally, Maraschini et al. (2010) proposed a method to invert Rayleigh wave data in which the misfit function is a norm of the Thomson-Haskell matrix determinant evaluated at experimental dispersion data. The main advantage is the possibility of considering several modes simultaneously, without specifying to which mode each velocity belongs.

On the other hand, the HVSR is the simplest and the prevalent method to obtain the dominant frequency of the site by processing ASN recorded by a single station (e.g. Nakamura, 1989; Lermo and Chávez-García, 1993). Theoretical efforts have been carried out to find out the connection between this observable and the vertical distribution of elastic properties (e.g. Arai and Tokimatsu, 2004; Kawase et al., 2011). Modelling ASN as a diffuse field has shown excellent results (e.g. Sánchez-Sesma et al., 2011; Spica et al., 2015; Lontsi et al., 2015). Actually, joint inversion of the HVSR and the fundamental and/or higher modes dispersion curves is a powerful and relatively simple scheme that mitigates trade-off issues between model parameters (e.g. Piña-Flores et al., 2017; Sivaram et al., 2018; García-Jerez et al., 2019).

In this work, we first explore the relationships between the dispersion curves of Rayleigh waves and the HVSR calculated under the diffuse field approach (DFA). Using two simple models with varying parameters, we show that the shape of the observed HVSR allows us to identify the dispersion curves of fundamental-mode Rayleigh waves preventing the contamination by higher modes. An application to array measurements performed at the Andarax river delta (Almeria, Spain) is presented. ASN data recorded by pentagonal arrays were analyzed by using the SPAC, FK and the cross-correlations between pairs of receivers. We took advantage of the characteristics of the HVSR to pick reliable phase and group dispersion curves of fundamental-mode Rayleigh waves. A joint inversion of these curves under the DFA led to an improved velocity profile for this site. Finally, forward computations show that some of the information in the SPAC, FK and CC dispersion diagrams corresponds to higher modes.

2. Theory of the horizontal-to-vertical spectral ratio (HVSR)

It has been established that the HVSR, defined as the square root of the ratio between the horizontal and the vertical power spectral densities in a diffuse field, can be expressed in terms of the imaginary parts of the Fourier-transformed Green functions for coinciding source and receiver (Sánchez-Sesma et al., 2011). In particular, this quantity can be expressed in term of the imaginary part of the Green's function components as:

$$\mathrm{H/V}(\boldsymbol{x},\omega)=\sqrt{\frac{\mathrm{Im}[G_{11}(\boldsymbol{x},\boldsymbol{x};\omega)]+\mathrm{Im}[G_{22}(\boldsymbol{x},\boldsymbol{x};\omega)]}{\mathrm{Im}[G_{33}(\boldsymbol{x},\boldsymbol{x};\omega)]}}. \tag{1}$$

where $\mathrm{Im}[G_{11}(\boldsymbol{x},\boldsymbol{x};\omega)]$ is the imaginary part of the Green function and $G_{11}(\boldsymbol{x},\boldsymbol{x};\omega)$ is the displacement at x in direction 1 produced by a unit harmonic load acting at x in direction 1. The subscripts 1 and 2 refer to horizontal, and 3 to vertical degrees of freedom, and ω stands for circular frequency. Eq. (1) gives the way to compute the HVSR theoretically, assuming that the wavefield can be approached by a diffuse field. In this expression, the Green's function components are associated with the geometry and the elastodynamic properties of the ground. In this work, a layered halfspace with unbounded horizontal interfaces is considered. The top surface is a free surface and the media are assumed homogeneous, isotropic and elastic, with P and S wave velocities α_i and β_i, mass density ρ_i and thickness h_i for layer i. Further details about the efficient computation of HVSR are described in García-Jerez et al. (2016).

3. Relationship between dispersion curves and HVSR

The theoretical relationship between the dispersion curve and the HVSR comes from the calculation of the imaginary part of the main

Table 1
Example models used in this work.

h (m)	α (m/s)	β (m/s)	ρ (kg/m^3)
Model 1			
25	663	200	1700
∞	866	500	2200
Model 2			
15	2000	380	1600
350	2300	850	1800
∞	3500	2000	2500

diagonal of the Green's tensor under a diffuse field approach. These quantities can be expressed, for a given frequency, as integrals on the horizontal (radial) wavenumber k. The kernels in the (k, ω) domain can be extended to the complex k-plane. Since surface waves correspond to simple poles along the real-k axis, their contributions to the integrals can be computed from the Cauchy's residue theorem. As shown in García-Jerez et al. (2016), the expressions for the imaginary part of the Green's function, in the special case of source and receiver coinciding at the top of the layered media, can be written in a very compact form:

$$\mathrm{Im}[G_{11}(0,0;\omega)] = \mathrm{Im}[G_{22}(0,0;\omega)]$$

$$= \underbrace{-\frac{1}{4}\left(\overbrace{\sum_m \chi_m^2 A_{Rm}}^{Rayleigh} + \overbrace{\sum_m A_{Lm}}^{Love}\right)}_{Surface\ waves} + \underbrace{\frac{1}{4\pi}\int_0^{\omega/\beta_N} Re\left[f^H_{PSV}(k) + f_{SH}(k)\right]_{4^{th}} \mathrm{d}k}_{Body\ waves};\ \mathrm{Im}[G_{33}(0,0;\omega)] = \underbrace{-\frac{1}{2}\left(\overbrace{\sum_m A_{Rm}}^{Rayleigh}\right)}_{Surface\ waves} + \underbrace{\frac{1}{2\pi}\int_0^{\omega/\beta_N} Re\left[f^V_{PSV}(k)\right]_{4^{th}} \mathrm{d}k}_{Body\ waves}; \quad (2)$$

where $f^H_{PSV}(k)$, $f^V_{PSV}(k)$ and $f_{SH}(k)$ are the kernels associated to the body waves in 3-D, χ_m is the ellipticity of the m^{th} Rayleigh mode, and A_{Rm} and A_{Lm} correspond to the medium responses for the m^{th} Rayleigh and Love modes, respectively (Harkrider, 1964). The analytical computation of χ_m, A_{Rm} and A_{Lm} requires the precise location of the poles along the real k-axis. These positions can be evaluated rapidly as they correspond to the values of the $k_m(\omega)$ representation of the dispersion curves at a given frequency (see e.g. Piña-Flores et al. 2016). In summary, under the DFA, the HVSR contains implicit information on the fundamental- and higher-modes phase velocity dispersion curves.

The examination of two example models listed in Table 1 will provide insight into the relationship between the Rayleigh wave dispersion curves and the shape of the HVSR. Model 1 consists of a layer overlaying a stiffer half-space, while two layers with two significant impedance contrasts are considered for model 2. Velocity increases downwards and impedance contrasts between the layers are high enough to exemplify the osculation effect between the fundamental mode and the first higher mode. Rayleigh wave dispersion curves for model 1 are shown in Fig. 1 for the fundamental and the first higher mode and for both phase and group velocities, along with the theoretical HVSR computed under the DFA.

Two characteristic frequencies can be identified in the HVSR. The first frequency corresponds to the main peak (approximately coincident with the fundamental resonance frequency of the S waves) and the second one corresponds to the absolute minimum (close to the fundamental resonance frequency of the P waves, see Piña-Flores et al., 2017). These two frequencies are often in the frequency band of interest for geotechnical studies, in particular, the peak frequency. Other important properties are the frequencies of the inflection points in the phase velocity dispersion curves (f_{Inf}, points where the concavity of the dispersion curve changes) and the frequencies of the critical points in the group velocity curves (f_{crit}, points where the first derivative, respect to frequency f vanishes), that is:

$$\frac{d^2c\left(f_{Inf}\right)}{df^2} = 0 \text{ and } \frac{dU\left(f_{crit}\right)}{df} = 0 \quad (3)$$

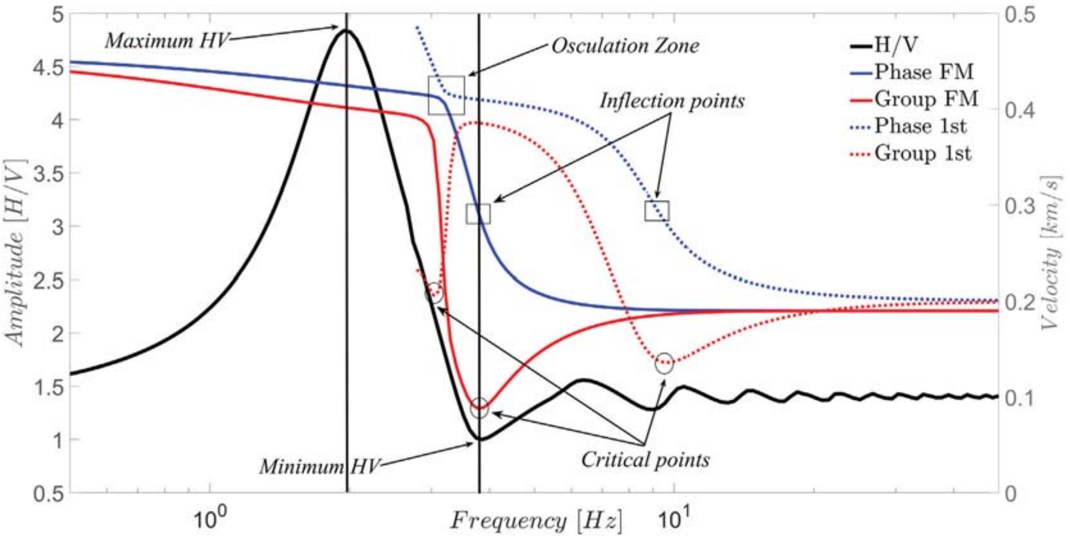

Fig. 1. HVSR (continuous black line) and dispersion curves of Rayleigh waves for group velocity (red lines) and phase velocity (blue lines) computed for model 1. Small circles show the critical points of the group velocity curves while the small squares show the inflection points of the phase velocity curves. The frequency of the inflection point and critical point, for the fundamental mode, are very close to the minimum of the HVSR. The frequencies where possible osculation effects exist are between the first maximum and the first minimum of the HVSR.

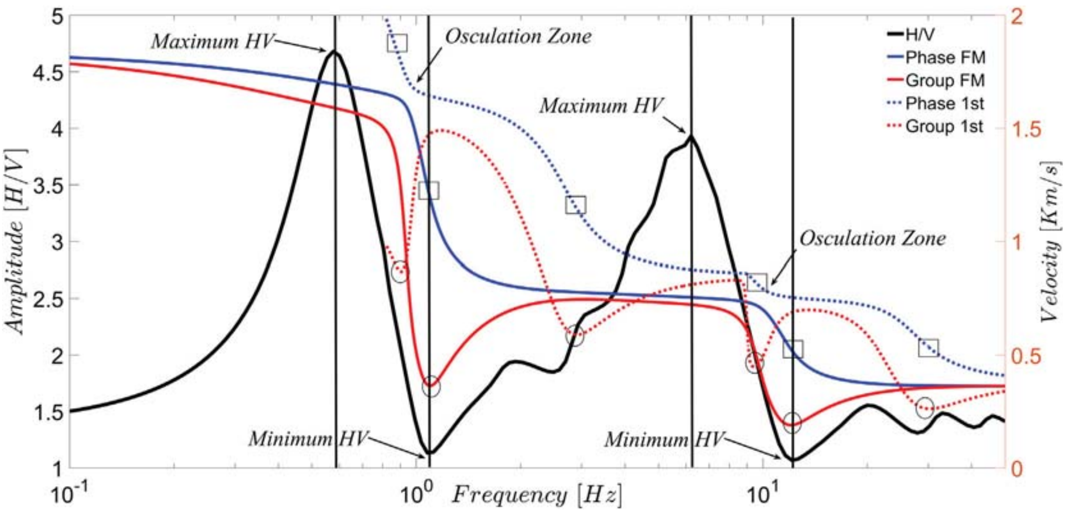

Fig. 2. HVSR (black line) and dispersion curves of Rayleigh waves for group velocity (red lines) and phase velocity (blue lines) computed for model 2. The critical points of the group velocity curves are shown with circles, while the squares show the inflection points for the phase velocity curves. Frequencies of inflection points and critical points in the fundamental mode are next to the troughs of the HVSR. Possible osculation effects appear between the frequencies of the maximum and minimum of the HVSR.

where $\frac{d^2c(f)}{df^2}$ is second derivative of phase velocity dispersion curve and $\frac{dU(f)}{df}$ is the first derivative of the group velocity. $\frac{d^3c(f_{Inf})}{df^3}\neq 0$ has been assumed.

A first relationship between the inflection points of the phase velocity dispersion curves and the shape of the HVSR can be stated considering the frequency of the first minimum of the HVSR. This frequency is next to the frequency of the inflection point of the fundamental-mode dispersion curve. This same pattern can be observed for the first higher mode where the frequency of the inflection point is close to the second minimum of the HVSR. Another characteristic of the phase velocity dispersion curves is that they may have zones of osculation between modes. This osculation between the fundamental mode and the first higher mode is present between the frequencies of the main peak and the first minimum of the HVSR.

The relationship between the HVSR and the group velocity dispersion curve is also evident. The frequency of the minimum in the HVSR is close to the frequency of the critical point of the dispersion

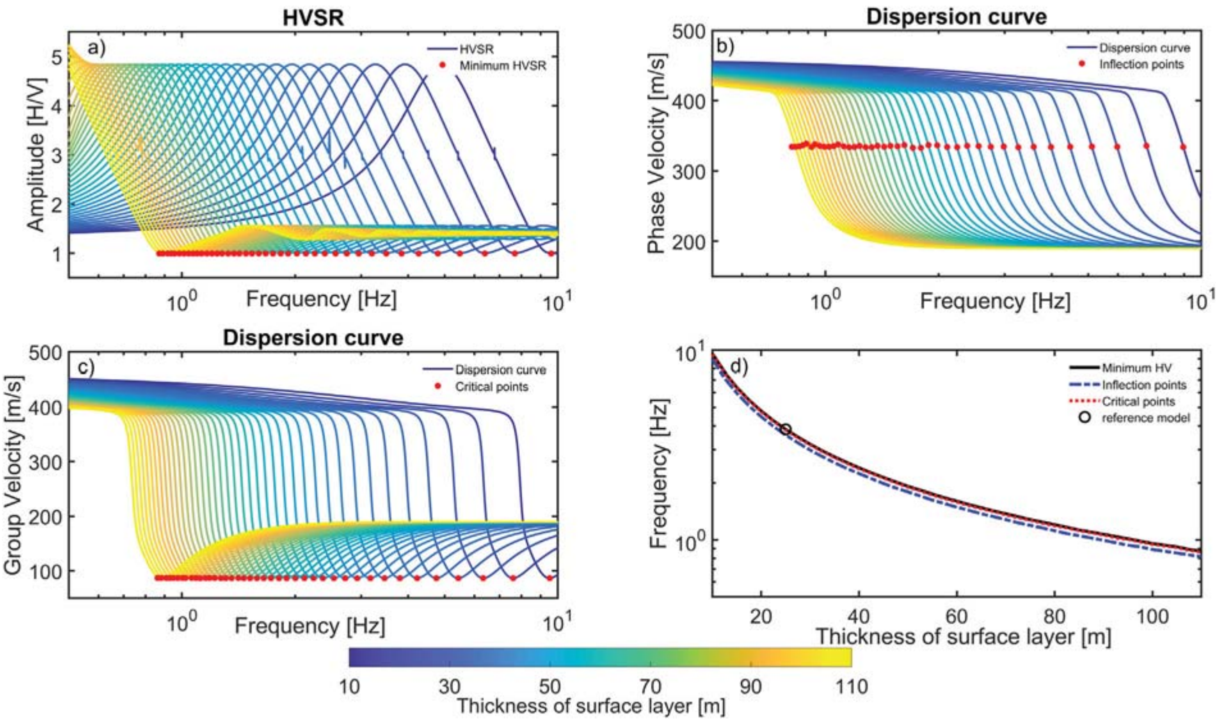

Fig. 3. Fundamental-mode dispersion curve for phase (panel b) and group (panel c) velocities of Rayleigh waves, and HVSR (panel a) obtained from model 1 modifying the thickness of the surface layer (from 10 to 110 m). Red dots represent inflection and critical points of dispersion curves and minima of the HVSR. Panel d shows the frequencies of such points as a function of the layer thickness.

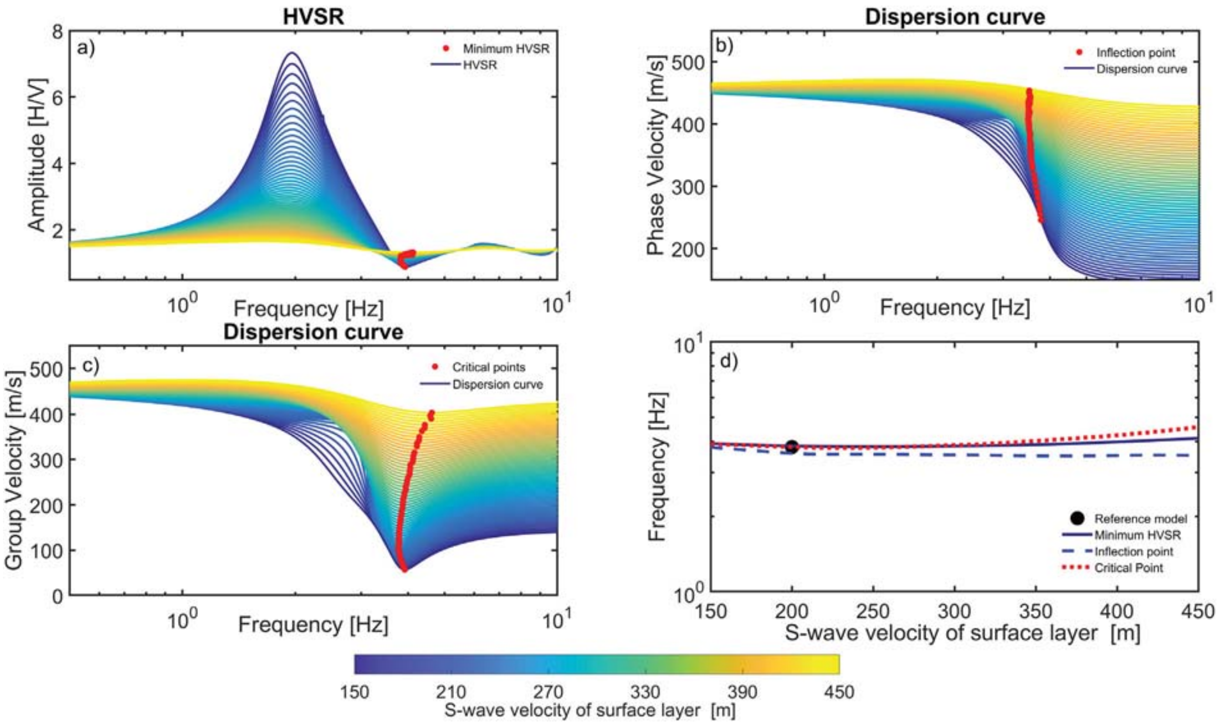

Fig. 4. HVSR (panel a) and fundamental-mode dispersion curves for phase (panel b) and group (panel c) velocities of Rayleigh waves obtained from model 1 modifying the velocities and thickness of the upper layer. β_1 ranged from 150 to 450 m/s; the Poisson ratio of the layer and the β_1/h ratio are preserved. Red points represent inflection points in $c(f)$, critical points in $U(f)$ and minima in the HVSR(f). Panel d shows the variation of the frequencies of the mentioned points as β_1 varies.

curve, even with a higher degree of proximity in comparison with the inflection point. Additionally, the frequency of the first crossing between the fundamental mode and the first higher mode in group velocity is between the main peak and the first minimum. Besides, we can observe a critical point of the group velocity curve for the higher mode in this frequency range.

Fig. 2 shows the calculation of the fundamental mode and the first higher mode for phase and group velocity of Rayleigh waves for model 2, along with the HVSR. For this model, the HVSR shows two prominent peaks and two clear troughs. In the same way as the previous example, we can observe the mentioned behavior of the dispersion curves between the frequencies of the maximum and minimum for the two peak-trough pairs. That is, the frequencies where the HVSR presents these minima approximately correspond to the locations of inflection points in the phase velocity curve and of critical points in the group velocity curve, both for fundamental mode.

The effects of osculation are present between the frequencies of the maximum and minimum of the HVSR. The group velocity dispersion curves present several crossings between the higher modes and the fundamental mode at different frequencies, making it difficult to distinguish the fundamental mode. In the analyzed models, at least a crossing between the fundamental and the first higher mode of group velocity appears between the maximum and minimum of the HVSR.

Fig. 3 shows the dispersion curves of the fundamental mode for phase (panel b) and group (panel c) velocity of Rayleigh waves along with the HVSR (panel a) modifying the thickness of the surface layer in model 1 (from 10 up to 110 m). Fig. 3d shows the frequencies of the critical and inflection points of the dispersion curves (in group and phase velocity, respectively) and the minima in the HVSR as a function of the thickness of the top layer. Note that the variation in thickness in this high-contrast model does

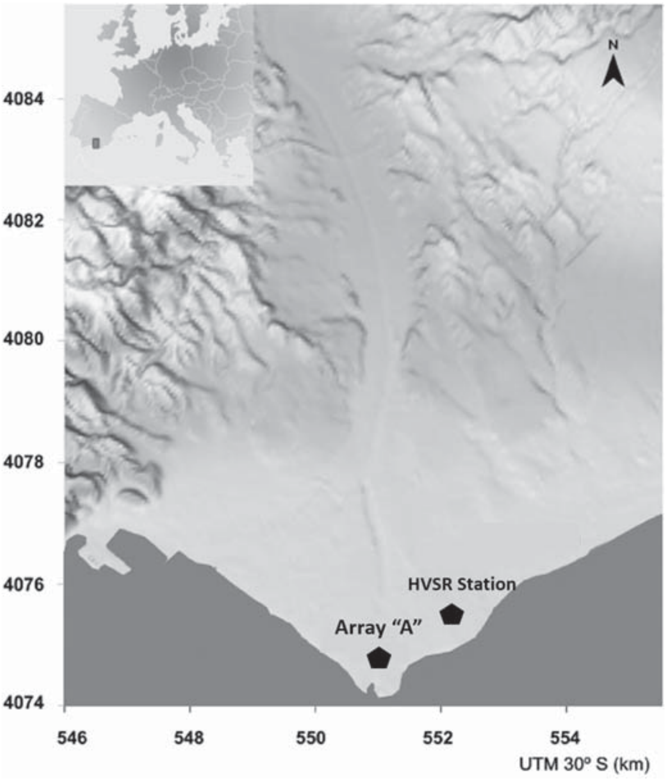

Fig. 5. Location of array "A" measurements and HVSR station (UTM coordinates).

not modify the correspondence among the frequencies of critical, inflection points and troughs.

Following with this parametric analysis, variations in the velocity contrast of model 1 have been also considered (Fig. 4). To do so, several S-wave velocities of the surface layer, β_1, have been taken from 150 to 450 m/s. The thickness has been also modified in order to keep β_1/h constant (it approximately preserves the peak frequency of the HVSR). The Poisson ratio of the layer (0.45) and the properties of the halfspace have been also kept constant. Fig. 4d shows the evolution of the critical and inflection points in the dispersion curves (group and phase velocity, respectively) and of the minima of HVSR as β_1 varies. Note that the approximate coincidence in frequency between the critical point in $U(f)$ and the trough in HVSR(f) persists. The frequencies of the inflection point in $c(f)$ and of the minimum

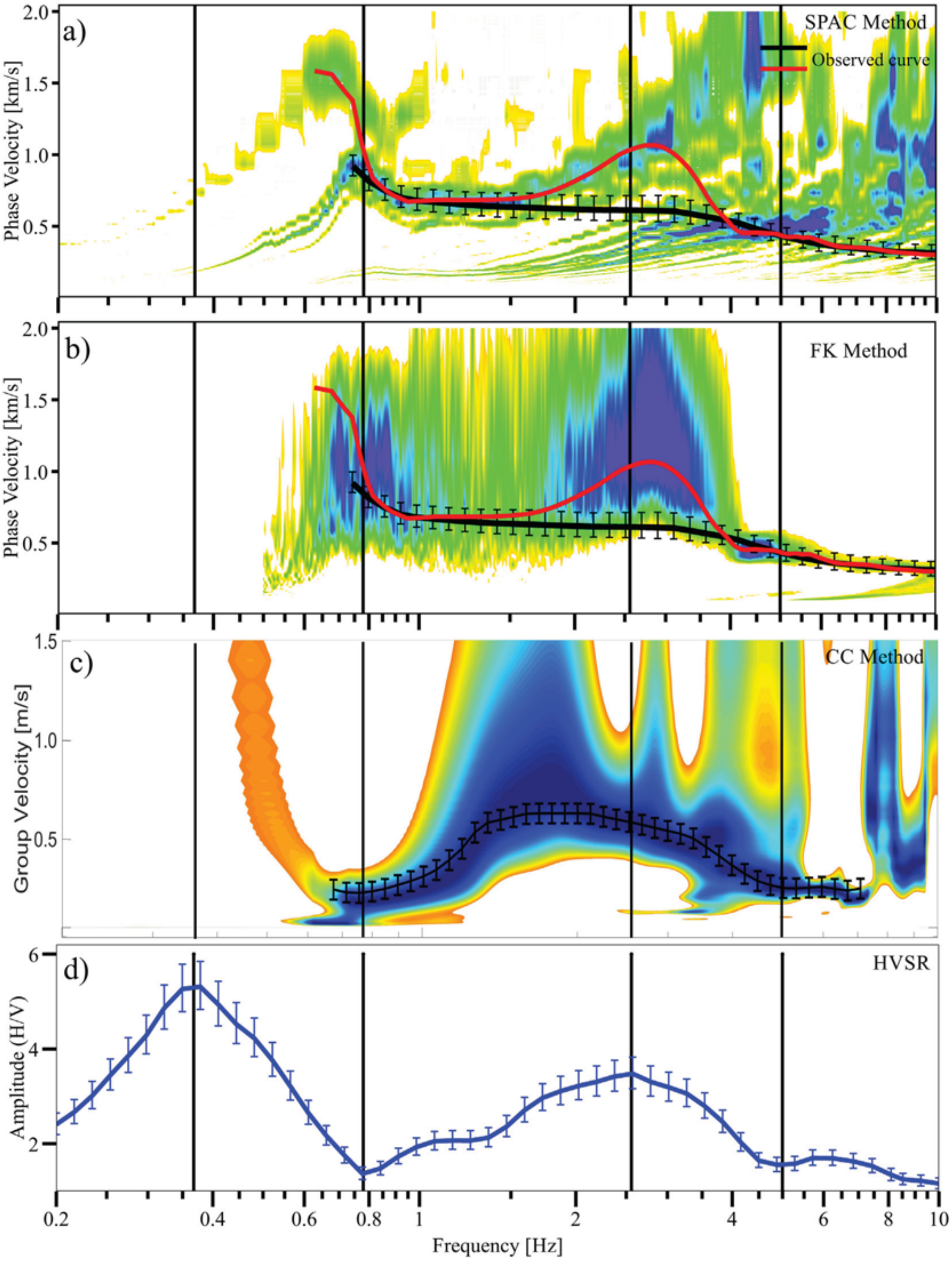

Fig. 6. Dispersion diagrams and HVSR obtained at the Andarax river delta (Fig. 5). a) Dispersion diagram (phase velocity) by applying the SPAC method. b) Dispersion diagram (phase velocity) applying the FK method. c) Dispersion diagram (group velocity) applying the CC method. d) HVSR. The solid black line in the dispersion diagrams shows the fundamental mode dispersion curve, picked considering the shape of the HVSR. The solid red line in the dispersion diagrams shows a possible alternative dispersion curve, picked according to the criteria of maximum energy bands (effective curve). The vertical black lines in all the panels represent the frequencies of the relevant maxima and minima of the HVSR which can be used for identification of possible inflection points, osculation zones and multimode effects in the dispersion diagrams.

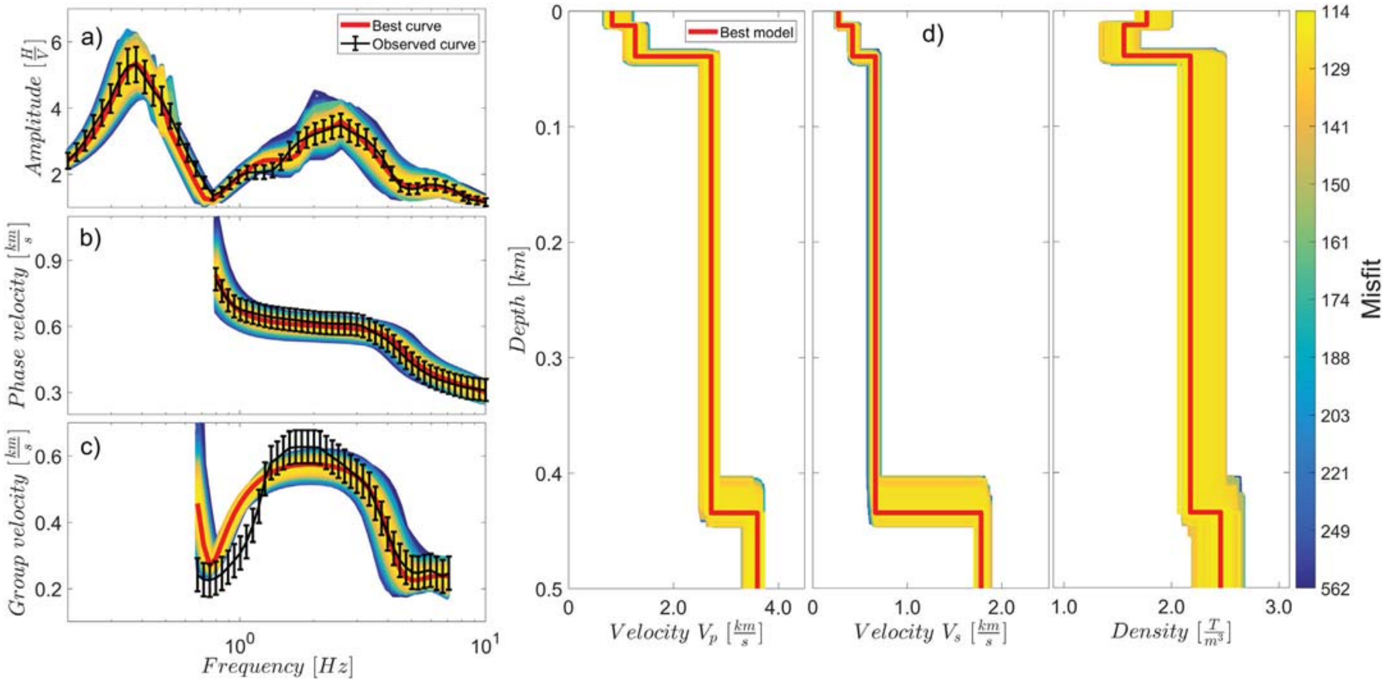

Fig. 7. Results from joint inversion at the test site in the mouth of the Andarax river. a) Target HVSR (black line) and theoretical HVSR for the best-fitting model (red line). b) Experimental phase-velocity dispersion curve (black line) and theoretical dispersion curve for the best fitting model (red line). c) Experimental group velocity dispersion curve (black line) and theoretical dispersion curve for the best fitting model (red line). d) Velocity and density profiles results from simultaneous inversion. The colored curves are associated with the trial models generated by the iterative inversion method. The bedrock depth is estimated from the best fitting model at 0.43 Km and agrees well with geophysical prospecting carried out by the Spanish Geological Survey (IGME, 1983).

in HVSR(f) exhibit better correspondence for those models with high impedance contrast producing amplitudes higher than two at the main HVSR peak.

4. Application to experimental data in the Andarax river delta (Almería, Spain)

In order to obtain a representative velocity profile for the Andarax river delta, ASN data were recorded using five sensors in pentagonal array configurations with radii of 12, 25, 50, 94 and 420 m. Identification of dispersion curves for the fundamental mode of Rayleigh waves was done by using the SPAC, FK and HVSR techniques using the Geopsy software (Wathelet et al., 2008, Köhler et al., 2007, http://www.geopsy.org/, last accessed February 2017). The time windowing used for processing ranged from 40 s to 120 s long with a 50% overlapping between consecutive windows. Rayleigh-wave group-velocity dispersion diagrams were also obtained from the CC between pairs of receivers using frequency-time analysis (FTAN, e.g. Bensen et al., 2007). The application of the SPAC, FK and CC techniques was carried out using ~2 h of ASN records at array “A” site (Fig. 5). Since wind, poor thermal isolation, etc. can generate instability in the HVSR at low frequencies, an 8 h record from a nearby permanent broadband station properly installed in the campus of the University of Almería was used to calculate the HVSR. In this way, the curve was be safely extended below 0.2 Hz to better show the shape of the main peak. For frequencies around and above the main peak, this spectral ratio does not differ significantly from those taken at the array site with portable seismometers.

Fig. 6 shows the dispersion diagrams obtained and the HVSR for the study area. From the dispersion diagram derived from the SPAC technique (Fig. 6a) it is possible to observe a possible discontinuity or jump from the fundamental mode to the higher mode in the range from 0.6 to 0.8 Hz. In the range between 0.8 and 2 Hz the fundamental mode dispersion curve emerges clearly. In the frequency band between 1.72 and 4 Hz the phase velocity seems to increase as the frequency increases. This type of phenomenon can occur in two cases where: 1.- the medium has a low velocity zone (LVZ); 2.- higher modes are present (Tokimatsu et al., 1992). For the first case, the existence of an LVZ can be ruled out because the amplitude of curve of HVSR is not less than the unit in the entire range of observation frequencies (Castellaro and Mulargia, 2006) and, consequently, we associate this effect to higher modes. Finally, in the range from 4 to 8 Hz, the dispersion diagram shows a part of the fundamental mode dispersion curve with severe contamination by higher modes that makes picking difficult.

From another perspective, the dispersion diagram obtained from the FK technique (Fig. 6b) clearly shows the fundamental mode dispersion curve in the frequency range from 4 to 10 Hz (where its identification from SPAC technique was unclear). The bump in the frequency band from 1.5 to 3.8 Hz can be associated with the presence of higher modes, as in the case of the dispersion diagram derived from SPAC. In the band between 0.5 and 1 Hz, this method provided poor resolution and the trend of the dispersion curve is unclear. On the other hand, in the dispersion diagram obtained from the CC technique (Fig. 6c) it is possible to observe the group-velocity dispersion curve in the frequency range between 0.7 and 7 Hz. In this case, the wide range of observation frequencies for the dispersion curve may be associated to a softer transition

Table 2
Best model inverted at the Andarax river test site.

h (m)	α (m/s)	β (m/s)	ρ (kg/m^3)
Proposed velocity profile			
12	828	270	1749
26	1269	420	1538
395	2705	662	2165
∞	3538	1810	2500

between different modes, which may show very close group velocities. Note that higher mode group velocity curves might cross each other, and even the fundamental mode. Finally, the HVSR (Fig. 6d) presents two main peaks at 0.38 and 2.5 Hz and two minima at 0.79 and 5 Hz, respectively. Small oscillations that do not represent main peaks are observed in the frequency range between 0.8 and 2.5 Hz.

As mentioned in the previous section, observation of the shape of the HVSR curve is handy for identifying the fundamental mode and those bands with possible osculation and multimode effects in the dispersion diagrams, which correspond to the frequencies between and around the main maxima and minima of the HVSR. The frequencies of the troughs in the HVSR (0.8 and 5 Hz in this case) indicate the proximity of inflection points in the phase dispersion curve. As mentioned above, the dispersion diagrams derived from FK and SPAC techniques exhibit well defined velocities in the range from 2.5 to 4 Hz which corresponds to energy of higher modes. In many cases, this effect causes an erroneous identification of the dispersion curve. However, the HVSR indicates that a multimode or osculation effect is expected in the frequency range between 0.38 (first peak) and 0.8 Hz (first trough) and between 2.5 (second peak) and 5 Hz (second trough). In the dispersion diagram computed from the CC technique, two critical points are observed at 0.8 and 5 Hz, corresponding with the minima of the HVSR. Instead, if only the criterion of maximum energy is taken, we can obtain an effective dispersion curve from the dispersion diagrams. An example of a possible effective curve is shown in figure 6ab (solid red line), presenting an inversion of phase velocities. The inversion of that curve as the fundamental mode would lead to an unreliable model with significant intermediate low-velocity layers.

Besides, the amplitude of the peaks in the HVSR is an indicator of the impedance contrasts between the corresponding layers of the medium, and hence of the expected trend of the dispersion curves. That is, the amplitude of the peaks in the HVSR increases as the slope of the fundamental-mode phase-velocity curve increases (in absolute value). As shown in Fig. 6d, the main peak at high frequencies (5 Hz) has an amplitude of 3.5 while the main peak at low frequencies (0.79 Hz) exhibits an amplitude of 5.5. Therefore, we can expect a sharper variation in phase velocity around 0.79 Hz. Once the dispersion curve was picked, a joint inversion of HVSR and dispersion curve was performed using the

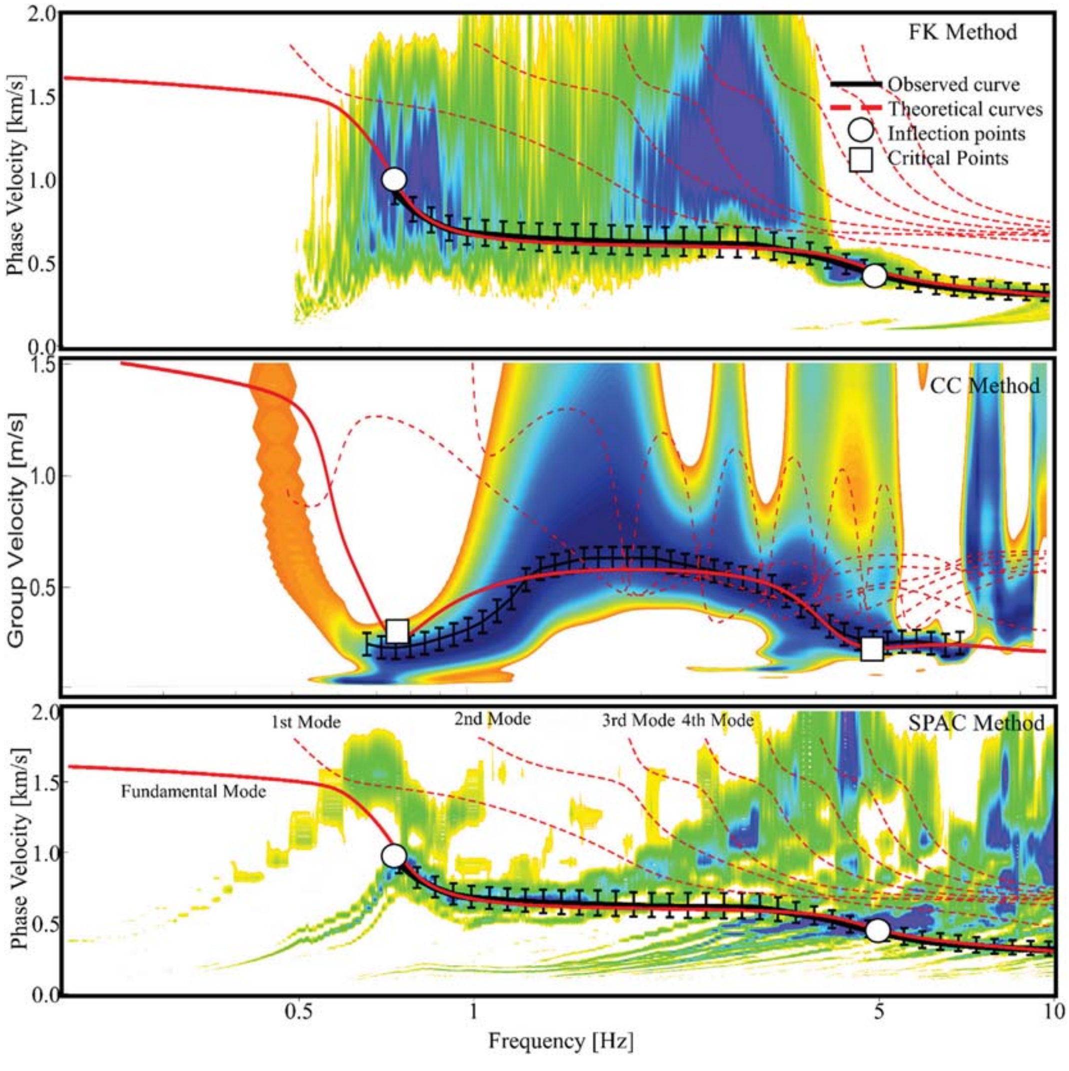

Fig. 8. Dispersion diagrams shown in Fig. 6, including theoretical dispersion curves of several modes (solid and dashed red lines) calculated from the velocity profile obtained from joint inversion of the observed dispersion curves and the HVSR (solid black lines). The squares show the critical points of the fundamental-mode group-velocity dispersion curve, while the circles show the inflection points of the fundamental-mode phase-velocity dispersion curve.

HV-Inv free software (https://w3.ual.es/GruposInv/hv-inv/, last accessed June 2018) to obtain a representative estimation of the velocity profile of the zone. Fig. 7 shows the result of the inversion which exhibits an excellent agreement between the observed HVSR, phase-velocity and group-velocity dispersion curves and the theoretical counterparts in the whole frequency range. The joint inversion of these curves allowed to estimate the velocity structure at the test site in the mouth of Andarax river, defined by α and β velocity structures and ρ structure. Piña-Flores et al. (2017) suggested that the minimum number of layers to consider for an HVSR inversion should be equal to the number of main peaks. Since three main peaks are visible on the HVSR here, a profile with three layers on top on a half-space has been considered. Table 2 lists the parameters of the model which best fitted the observations, which shows an estimated bedrock depth of 0.43 km with β of 1810 m/s. The depth of the basement agrees well with the results of independent geophysical studies carried out in the '80 s by the Spanish Geological Survey (IGME, 1983). The theoretical dispersion curves for phase and group velocities of higher modes were calculated for the inverted model and incorporated in the experimental dispersion diagrams (see Fig. 8). This figure evidences that some high energy zones in dispersion diagrams correspond to higher modes.

5. Conclusions

In this work, we explore the relationship between the behavior of the group and phase velocity dispersion curves for the fundamental and first higher mode of Rayleigh waves and the HVSR interpreted under the diffuse field theory. The relationship between these two curves can be summarized in the following five points.

1. The inflection and critical points in the dispersion curves can be used as control points to distinguish the fundamental mode from the higher ones. This knowledge is of great help for the correct picking of phase and group Rayleigh-wave modes from the dispersion diagrams.
2. For the fundamental mode, the frequencies of the inflection points in the phase-velocity dispersion curve and of the critical points in the group-velocity curve are very close to the frequencies of the main troughs of the HVSR.
3. The osculation effect between the fundamental mode and the first higher mode is located between the frequencies of the main peaks and the following minima of the HVSR.
4. The band with possible effect of multiple modes is located between the frequencies of the main peak and the subsequent minimum of the HVSR.
5 The amplitude of the main peaks of the HVSR increases as the slope (in absolute value) of the phase-velocity dispersion curve increases

As an example, we used the HVSR to assist in the identification of fundamental mode phase and group velocity dispersion curves from dispersion diagrams in the Andarax river delta (SE Spain). A reliable velocity profile for the zone was obtained from joint inversion of these three curves. We propose to use information in the HVSR of ASN to identify the osculation zones, multi-mode effect, inflection points and critical points of the fundamental mode from the dispersion diagrams. This way of proceeding can be a very useful complementary tool along with other ways of mode identification. It allowed to obtain a representative velocity profile of the zone using joint inversion, aimed at obtaining a more accurate assessment of local site effects in the event of an earthquake.

CRediT authorship contribution statement

José Piña-Flores: Conceptualization, Methodology, Software, Investigation, Writing - original draft. **Martín Cárdenas-Soto**: Methodology, Investigation, Writing - review & editing. **Antonio García-Jerez**: Resources, Validation, Formal analysis, Writing - review & editing. **Helena Seivane**: Validation, Formal analysis, Writing - review & editing. **Francisco Luzón**: Resources, Validation, Formal analysis, Writing - review & editing. **Francisco J. Sánchez-Sesma**: Writing - review & editing.

Acknowledgements

We thank Professor Jianghai Xia and two anonymous reviewers for their constructive comments and keen remarks. This work has been partially supported by UNAM-DGAPA projects: PAPIIT (IN117217, IN100917) and PAPIME (PE103918), by Ministerio de Economía y Competitividad of Spain and (ERDF) European Regional Development Fund under Project CGL2014-59908/JIN and by the Consejo Nacional de Ciencia y Tecnología, Mexico (CONACYT) through the National Scholarship CONACYT number 449268.

Declaration of Competing Interest

The authors declare that they have no known competing financial interests or personal relationships that could have appeared to influence the work reported in this paper.

References

Aki, K., 1957. Space and time spectra of stationary stochastic waves, with special reference to microtremors. *Bulletin of the Earthquake Research Institute*, University of Tokyo 35, 415–457.

Arai, H., Tokimatsu, K., 2004. S-wave velocity profiling by inversion of microtremor H/V spectrum. Bull. Seismol. Soc. Am. 94 (1), 53–63.

Astaneh, A.V., Guddati, M.N., 2016. Improved inversion algorithms for near-surface characterization. Geophys. J. Int. 206, 1410–1423. https://doi.org/10.1093/gji/ggw192.

Baena-Rivera, M., Perton, M., Sánchez-Sesma, F.J., 2016. Surface-Wave Retrieval from Generalized Diffuse Fields in 2D Synthetic Models of Alluvial Valleys. Bull. Seismol. Soc. Am. Vol. **106** (6). https://doi.org/10.1785/0120160084.

Bensen, G.D., Ritzwoller, M.H., Barmin, M.P., Levshin, A.L., Lin, F., Moschetti, M.P., Shapiro, N.M., Yang, Y., 2007. Processing seismic ambient noise data to obtain reliable broad-band surface wave dispersion measurements. Geophys. J. Int. 169, 1239–1260. https://doi.org/10.1111/j.1365-246X.2007.03374.x.

Boaga, J., Cassiani, G., Strobbia, C.L., Vignoli, G., 2013. Mode misidentification in Rayleigh waves: Ellipticity as a cause and a cure. Geophysics **78** (4), EN17–EN28. https://doi.org/10.1190/geo2012-0194.1.

Bonnefoy-Claudet, S., Cotton, F., Bard, Pierre-Yves, 2006. The nature of noise wavefield and its applications for site effects studies: a literature review. Earth Sci. Rev. 79, 205–227. https://doi.org/10.1016/j.earscirev.2006.07.004.

Boué, P., Denolle, M., Hirata, N., Nakagawa, S., Beroza, G.C., 2016. Beyond basin resonance: characterizing wave propagation using a dense array and the ambient seismic field. Geophys. J. Int. 206, 1261–1272. https://doi.org/10.1093/gji/ggw205.

Capon, J., 1969. High-resolution frequency-wavenumber spectrum analysis. Geophysics. 34 (1), 21–38.

Castellaro, S., Mulargia, F., 2006. The effect of Velocity Inversions on H/V. Pure Appl. Geophys. 166, 567–592. https://doi.org/10.1007/s00024-009-0474-5.

Coelho, M.J., Santos, J., Pereira, M., 2018. Stacking of multilayout and multichannel surface-wave data on the f-k domain. J. Appl. Geophys. 159, 93–107. https://doi.org/10.1016/j.jappgeo.2018.08.006.

Dai, K., Liu, K., Li, X., You, Q., Tang, H., Xu, Q., 2019. Application of passive multichannel analysis of surface waves method at sites close to underground railways-Problems and a case study. J. Appl. Geophys. 164, 191–199. https://doi.org/10.1016/j.jappgeo.2019.03.009.

Farrugia, D., Paolucci, E., D'Amico, S., Galea, P., 2016. Inversion of surface wave data for subsurface shear wave velocity profiles characterized by a thick buried low-velocity layer. Geophys. J. Int. 206 (2), 1221–1231. https://doi.org/10.1093/gji/ggw204.

Foti, S., Parolai, S., Albarello, D., Picozzi, M., 2011. Application of Surface-Wave Methods for Seismic Site Characterization. Surv. Geophys. 32 (6), 777–825. https://doi.org/10.1007/s10712-011-9134-2.

Gao, L., Xia, J., Pan, Y., 2014. Misidentification caused by leaky surface wave in high-frequency surface wave method. Geophys. J. Int. 199 (3), 1452–1462. https://doi.org/10.1093/gji/ggu337.

Gao, L., Xia, J., Pan, Y., Xu, Y., 2016. Reason and Condition for Mode kissing in MASW Method. Pure Appl. Geophys. 173 (5), 1627–1638. https://doi.org/10.1007/s00024-015-1208-5.

García-Jerez, A., Sánchez-Sesma, F.J., 2015. Slowly-attenuating P-SV Leaky Waves in a Layered Elastic Halfspace. Effects on the Coherences of Diffuse Wavefields. Wave Motion **54**, 43–57. https://doi.org/10.1016/j.wavemoti.2014.11.010.

García-Jerez, A., Luzón, F., Navarro, M., Pérez-Ruiz, J.A., 2008. Determination of elastic properties of shallow sedimentary deposits applying a spatial autocorrelation method. Geomorphology. 93, 74–88. https://doi.org/10.1016/j.geomorph.2006.12.018.

García-Jerez, A., Piña-Flores, J., Sánchez-Sesma, F.J., Luzón, F., Perton, M., 2016. A computer code for forward computation and inversion of the H/V spectral ratio under the diffuse field assumption. Comput. Geosci. 97, 67–78. https://doi.org/10.1016/j.cageo.2016.06.016.

García-Jerez, A., Seivane, H., Navarro, M., Martínez-Segura, M., Piña-Flores, J., 2019. Joint analysis of Rayleigh-wave dispersion curves and diffuse-field HVSR for site characterization: the case of El Ejido town (SE Spain). Soil Dyn. Earthq. Eng. 121, 102–120. https://doi.org/10.1016/j.soildyn.2019.02.023.

Harkrider, D.G., 1964. Surface waves in multilayered elastic media I. Rayleigh and love waves from buried sources in a multilayered elastic half-space. Bull. Seismol. Soc. Am. 54 (2), 627–679.

IGME, 1983. Prospección geotérmica en la depresión de Almería. vol. V. Spain, Madrid In Spanish. Available at:. http://info.igme.es/ConsultaSID/presentacion.asp?Id=800 (last accessed 12 January 2020).

Ikeda, T., Matsuoka, T., Tsuji, T., Hayashi, K., 2012. Multimode inversion with amplitude response of surface waves in the spatial autocorrelation method. Geophys. J. Int. 190, 541–552. https://doi.org/10.1111/j.1365-246X.2012.05496.x.

Kawase, H., Sánchez-Sesma, F.J., Matsushima, S., 2011. The optimal use of horizontal-to-vertical spectral ratios of earthquake motions for velocity inversions based on diffuse-field theory for plane waves. Bull. Seismol. Soc. Am. 101 (5), 2001–2014. https://doi.org/10.1785/0120100263.

Köhler, A., Ohrnberger, M., Scherbaum, F., Wathelet, M., Cornou, C., 2007. Assessing the reliability of the modified three-component spatial autocorrelation technique. Geophys. J. Int. 168, 779–796. https://doi.org/10.1111/j.1365-246X.2006.03253.x.

Lai, C.G., Mangriotis, M.-D., Rix, G.J., 2014. An explicit relation for the apparent phase velocity of Rayleigh waves in a vertically heterogeneous elastic half-space. Geophys. J. Int. 199, 673–687. https://doi.org/10.1093/gji/ggu283.

Lermo, J., Chávez-García, F.J., 1993. Site effect evaluation using spectral ratios with only one station. Bull. Seismol. Soc. Am. 83 (5), 1574–1594.

Lin, C.P., Lin, C.H., Chien, C.J., 2017. Dispersion analysis of surface wave testing–SASW vs. MASW. J. Appl. Geophys. **143**, 223–230. https://doi.org/10.1016/j.jappgeo.2017.05.0080926–9851.

Lontsi, A.M., Sánchez-Sesma, F.J., Molina-Villegas, J.C., Ohrnberger, M., Krüger, F., 2015. Full microtremor H/V (z, f) inversion for shallow subsurface Characterization. Geophys. J. Int. 202, 298–312. https://doi.org/10.1093/gji/ggv132.

Louie, J.N., 2001. Faster, Better Shear wave velocity to 100m depth from ReMi arrays. Bull. Seismol. Soc. Am. 91 (2), 347–364.

Lunedei, E., Albarello, D., 2009. On the seismic noise wavefield in a weakly dissipative layered Earth. Geophys. J. Int. 177, 1001–1014. https://doi.org/10.1111/j.1365-246X.2008.04062.x.

Ma, Y., Clayton, R.W., Li, D., 2016. Higher-mode ambient-noise Rayleigh waves in sedimentary basins. Geophys. J. Int. 206, 1634–1644. https://doi.org/10.1093/gji/ggw235.

Maranò, S., Hobiger, M., Fäh, D., 2017. Retrieval of Rayleigh wave ellipticity from ambient vibration recordings. Geophys. J. Int. 209, 334–352. https://doi.org/10.1093/gji/ggx014.

Maraschini, M., Ernst, F., Foti, S., Socco, L.V., 2010. A new misfit functions for multimodal inversion of surface waves. Geophysics 75 (4), G31–G43. https://doi.org/10.1190/1.3436539.

Mi, B., Xia, J., Shen, C., Wang, L., Hu, Y., Cheng, F., 2017. Horizontal resolution of multichannel analysis of surface waves. Geophysics 82 (3), EN51–EN66. https://doi.org/10.1190/geo2016-0202.1.

Mi, B., Xia, J., Shen, C., Wang, L., 2018. Dispersion energy analysis of Rayleigh and love waves in the presence of low-velocity layers in near-surface seismic surveys. Surv. Geophys. **39**, 271–288 (2018). https://doi.org/10.1007/s10712-017-9440-4.

Mi, B., Hu, Y., Xia, J., Socco, L.V., 2019. Estimation of horizontal to vertical spectral ratios (HVSR, ellipticity) of Rayleigh waves from multi-station active-seismic records. Geophysics 84 (6), EN81–EN92. https://doi.org/10.1190/geo2018-0651.1.

Nakamura, Y., 1989. A method for dynamic characteristics estimation of subsurface using microtremor on ground surface. QR of RTRI 30 (1), 25–33.

Ning, L., Dai, T., Wang, L., Yuan, S., Pang, J., 2018. Numerical investigation of Rayleigh-wave propagation on canyon topography using finite-difference method. J. Appl. Geophys. 159, 350–361. https://doi.org/10.1016/j.jappgeo.2018.09.0070926-9851.

Ohori, M., Mobata, A., Wakamatsu, K., 2002. A comparison of ESAC and FK methods of estimating phase velocity using arbitrarily shaped microtremor arrays. Bull. Seismol. Soc. Am. 92 (6), 2323–2332.

Pan, Y., Xia, J., Gao, L., Shen, C., Zeng, C., 2013. Calculation of Rayleigh-wave phase velocities due to models with a high-velocity surface layer. J. Appl. Geophys. 96, 1–6. https://doi.org/10.1016/j.jappgeo.2013.06.005.

Piña-Flores, J., Perton, M., García-Jerez, A., Carmona, E., Luzón, F., Molina-Villegas, J.C., Sánchez-Sesma, F.J., 2017. The inversion of spectral ratio H/V in a layered system using the diffuse field assumption (DFA). Geophys. J. Int. 208, 577–588. https://doi.org/10.1093/gji/ggw416.

Rivet, D., Campillo, M., Sanchez-Sesma, F., Shapiro, N.M., Singh, S.K., 2015. Identification of surface wave higher modes using a methodology based on seismic noise and coda waves. Geophys. J. Int. 203, 856–868. https://doi.org/10.1093/gji/ggv339.

Sánchez-Sesma, F.J., Rodríguez, M., Iturrarán-Viveros, U., Luzón, F., Campillo, M., Margerin, L., García-Jerez, A., Suarez, M., Santoyo, M.A., Rodríguez-Castellanos, A., 2011. A theory for microtremor H/V spectral ratio: application for a layered medium. Geophys. J. Int. 186 (1), 221–225. https://doi.org/10.1111/j.1365-246X.2011.05064.x.

Sivaram, K., Gupta, S., Kumar, S., Prasad, B.N.V., 2018. Shear velocity structural characterization around the Lonar crater using joint inversion of ambient noise HVSR and Rayleigh wave dispersion. J. Appl. Geophys. 159, 773–784. https://doi.org/10.1016/j.jappgeo.2019.06.0220926-9851.

Spica, Z., Caudron, C., Perton, M., Lecocq, T., Camelbeeck, T., Legrand, D., Piña-Flores, J., Iglesias, A., Syahbana, D.K., 2015. Velocity models and site effects at Kawah Ijen volcano and Ijen caldera (Indonesia) determined from ambient noise cross-correlations and directional energy density spectral ratios. J. Volcanol. Geotherm. Res. 302, 173–189. https://doi.org/10.1016/j.jvolgeores.2015.06.016.

Tokimatsu, K., Tamura, S., Kojima, H., 1992. Effects of multiple modes on Rayleigh wave dispersion characteristics. J. Geotech. Eng. 118 (10), 1529–1543.

Wathelet, M., Jongmans, D., Ohrnberger, M., Bonnefoy-Claudet, S., 2008. Array performances for ambient vibrations on a shallow structure and consequences over Vs inversion. J. Seismol. 12, 1–19. https://doi.org/10.1007/s10950-007-9067-x.

Xia, J., Miller, R.D., Park, C.B., 1999. Estimation of near-surface shear-wave velocity by inversion of Rayleigh waves. Geophysics. 64 (3), 691–700. https://doi.org/10.1190/1.1444578.

Zeng, C., Xia, J., Miller, R.D., Tsoflias, G.P., Wang, Z., 2012. Numerical investigation of MASW applications in presence of surface topography. J. Appl. Geophys. 84, 52–60. https://doi.org/10.1016/j.jappgeo.2012.06.004.

Zhang, S., 2011. Effective Dispersion Curve and Pseudo Multimode Dispersion Curves for Rayleigh Wave. J. Earth Sci. 22 (2), 226–230. https://doi.org/10.1007/s12583-011-0175-8.

Zhang, S.X., Chan, L.S., 2009. Possible effects of misidentified mode number on Rayleigh wave inversion. J. Appl. Geophys. 53, 17–29. https://doi.org/10.1016/S0926-9851(03)00014-4.

Bulletin of the Seismological Society of America

The Search of Diffusive Properties in Ambient Seismic Noise

--Manuscript Draft--

Manuscript Number:	BSSA-D-20-00189R1
Article Type:	Reply
Section/Category:	Regular Issue
Full Title:	The Search of Diffusive Properties in Ambient Seismic Noise
Corresponding Author:	José Piña-Flores Facultad de Ingeniería, UNAM Coyoacan, CDMX MEXICO
Corresponding Author's Institution:	Facultad de Ingeniería, UNAM
Corresponding Author E-Mail:	jpf@unam.mx
Order of Authors:	José Piña-Flores
	Martín Cárdenas-Soto
	Antonio García-Jerez
	Michel Campillo
	Francisco J Sánchez-Sesma
Abstract:	Ambient seismic noise (ASN) is becoming of interest for geophysical exploration and engineering seismology as it is possible to exploit its imaging characteristics. Theory asserts that the Green's function can be retrieved from correlations within a diffuse field. Surface waves are the most conspicuous part of Green's function in layered media. Thus, the velocities of surface waves can be obtained from ASN if the wavefield is diffuse. There is widespread interest in the conditions of emergence and properties of diffuse fields. In the applications, useful approximations of the Green's function can be obtained from cross-correlations of recorded motions of ASN. An elastic field is diffuse if the illumination is azimuthally uniform and equipartitioned. This happens with the coda waves in earthquakes and has been verified in carefully planned experiments. For one of these data sets, those from the 1999 Chilpancingo (Mexico) experiment, there are some records of earthquake pre-events that undoubtedly are composed of ASN, so that the processing for coda can be tested on them. We decompose the ASN energies and study their equilibration. The scheme is inspired in the original experiment and uses the ASN recorded in a L-shaped array that allows computing spatial derivatives. This implies care in establishing the appropriate ranges for measuring parameters. In this search for robust indicators of diffusivity we are led to establish that, under certain circumstances, the S and P energy equilibration is a process which anticipates the diffusion regime (no necessarily isotropy) which justifies the use of horizontal-to-vertical spectral ratio in the theoretical context of diffusion.
Author Comments:	Dear Editor Enclosed please find our revised manuscript by José Piña-Flores et. al. on " The Search of Diffusive Properties in Ambient Seismic Noise " that we submit to your kind consideration for possible publication in the Bulletin of the Seismological Society of America. Our manuscript presents a study that describes the Search of Diffusive Properties in Ambient Seismic Noise. We hope that this work could become a valuable addition to the Bulletin of the Seismological Society of America. Sincerely yours José Piña-Flores Doctoral Student UNAM México

Response to Reviewers:	The response to the reviewers and editor comments is included in one of the uploaded files.
Additional Information:	
Question	**Response**
Key Point #1: <i>Three key points will be printed at the front of your manuscript so readers can get a quick overview. Please provide three COMPLETE sentences addressing the following: 1) state the problem you are addressing in a FULL sentence; 2) state your main conclusion(s) in a FULL sentence; and 3) state the broader implications of your findings in a FULL sentence. Each point must be 110 characters or less (including spaces).	We explore the stabilization of Ws/Wp energy in the pre-event and the seismic coda of the earthquake records
Key Point #2:	We show clear evidence that seismic energy equipartition is present in the ambient seismic noise records
Key Point #3:	The stabilization of the Ws/Wp energy ratio is a process which anticipates the diffusion regime

The Search of Diffusive Properties in Ambient Seismic Noise

By

José Piña-Flores (1-2), Martín Cárdenas-Soto (2),

Antonio García-Jerez (3), Michel Campillo (4) and Francisco J Sánchez-Sesma (5)

(1) Facultad de Ingeniería, Universidad Nacional Autónoma de México; CU, Circuito Escolar; Coyoacán 04510 CDMX, Mexico. Email: jpf@unam.mx and martinc@unam.mx
(2) Posgrado de Ingeniería, Universidad Nacional Autónoma de México; Edificio "S" "Bernardo Quintana Arrioja", Primer Piso, Facultad de Ingeniería, CU, Coyoacán 04510 CDMX, Mexico.
(3) Grupo de Investigación en Geofísica Aplicada, Universidad de Almería; La Cañada de San Urbano, s/n, 04120 Almería, Spain. Email: agj574@ual.es
(4) Institut des Sciences de la Terre, Universite Grenoble Alpes, Grenoble, F-38401, France. E-mail: michel.campillo@univ-grenoble-alpes.fr
(5) Instituto de Ingeniería, Universidad Nacional Autónoma de México, CU, Coyoacán 04510 CDMX, Mexico. E-mail: sesma@unam.mx

Accepted date: xx/xx/xxxx. Received date: xx/xx/xxxx.

Corresponding author: José Piña-Flores. jpf@unam.mx

Key Points:

- We explore the stabilization of W_S/W_P energy in the pre-event and the seismic coda of the earthquake records.
- We show clear evidence that seismic energy equipartition is present in the ambient seismic noise records.
- The stabilization of the W_s/W_p energy ratio is a process which anticipates the diffusion regime.

Keywords:

Ambient seismic noise, Energy equipartition, Earthquake

Abstract

Ambient seismic noise (ASN) is becoming of interest for geophysical exploration and engineering seismology as it is possible to exploit its imaging characteristics. Theory asserts that the Green's function can be retrieved from correlations within a diffuse field. Surface waves are the most conspicuous part of Green's function in layered media. Thus, the velocities of surface waves can be obtained from ASN if the wavefield is diffuse. There is widespread interest in the conditions of emergence and properties of diffuse fields. In the applications, useful approximations of the Green's function can be obtained from cross-correlations of recorded motions of ASN. An elastic field is diffuse if the illumination is azimuthally uniform and equipartitioned. This happens with the coda waves in earthquakes and has been verified in carefully planned experiments. For one of these data sets, those from the 1999 Chilpancingo (Mexico) experiment, there are some records of earthquake pre-events that undoubtedly are composed of ASN, so that the processing for coda can be tested on them. We decompose the ASN energies and study their equilibration. The scheme is inspired in the original experiment and uses the ASN recorded in a L-shaped array that allows computing spatial derivatives. This implies care in establishing the appropriate ranges for measuring parameters. In this search for robust indicators of diffusivity we are led to establish that, under certain circumstances, the S and P energy equilibration is a process which anticipates the diffusion regime (no necessarily isotropy) which justifies the use of horizontal-to-vertical spectral ratio in the theoretical context of diffusion.

Introduction

In recent years, the ambient seismic noise (ASN) has been widely used in geophysical exploration and engineering seismology. This ubiquitous excitation is a combination of oceanic, atmospheric, seismic and human contributions (see *e.g.* Asten & Henstridge, 1984; Ardhuin *et al*., 2011). Although the sources of noise associated with different frequency bands are not known precisely, it has been found that for low-frequency ($f < 0.3\ Hz$), the ASN may be dominated by interactions of the ocean with solid earth (Friederich *et al*., 1998; Rhie & Romanowicz, 2004; Ardhuin *et al*., 2011). On the other hand, at higher frequency ($f > 0.3\ Hz$), the ASN is produced locally by human activity and wind. Due to the attenuation in subsoil materials, this high-frequency noise cannot be propagated at great distances. In any case, the ASN comes from shallow sources that largely generate surface waves (Campillo, 2006).

The first systematic works with ASN at the beginning of the last century are due to Kanai (see Kanai *et al.*, 1954). Later, in a pioneering study, Aki (1957) computed spatial autocorrelation of ASN denominated SPAC (Spatial Autocorrelation). In this technique, the azimuthal average of the correlation coefficient of vertical motion of ASN allows evaluating the phase velocity of Rayleigh surface waves. The treatment of horizontal components allows the retrieval of Love waves. Note that this approach takes advantage of the natural illumination of seismic noise. Also, it has been shown that with ASN it is possible to obtain the most conspicuous part of Green function in a layered system by cross-correlation between two receivers. Shapiro and Campillo (2004), Sabra *et al.* (2005) and Shapiro *et al*. (2005) used long-range cross-correlations for practical applications in seismology.

Since then, numerous studies around the world have used this technique to retrieve empirical Green functions and extract the dispersion curves of Rayleigh and Love surface waves, which are propagation velocities as functions of frequency. For example, there are tomography maps of phase and group velocities for different parts of the world. These maps correlate well with the geology and tectonics of the region and, in some cases, they revealed new features. Let us mention the work by Shapiro & Campillo (2004); Shapiro *et al.* (2005) and Ritzwoller *et al.* (2011) for North America, the research by Ward *et al.* (2013) in South America, of Yang & Ritzwoller (2008) for Europe, the study by Zheng *et al.* (2008) for Asia, Saygin & Kennett (2010) considered New Zealand and Australia, and Gudmundsson *et al.* (2007) dealt with New Zealand and Australia.

Likewise, since Sánchez-Sesma *et al.* (2011a) established the relationship between the horizontal-to-vertical spectral ratio (HVSR), proposed by Nakamura (1989, 2000), with the imaginary parts of the Green function, several studies (Spica *et al.,* 2015; García-Jerez *et al.,* 2016 and Piña-Flores *et al.,* 2017, García-Jerez *et al.,* 2019) have been carried out in order to obtain velocity profiles as a function of depth through inversion. Matsushima *et al.* (2017) and Perton *et al.* (2018) considered the lateral irregularity as well. The success of these studies can be explained because they relate the observed HVSR with its model counterpart in terms of the Green functions which are intrinsic properties of layered systems. This relationship implies the assumption that the ASN is a diffuse field and therefore it can be regarded as the by-product of isotropic illumination of random waves. From this perspective, the sources of ambient noise are random and the generated seismic waves in their propagation suffer multiple diffractions due to the medium heterogeneities (Campillo, 2006). According to Shapiro *et al.* (2000) a diffusive regime is reached when the distribution of seismic energy (sources and secondary sources) is almost isotropic and the phase is random as a result of multiple scattering. If the medium does not have significant lateral irregularity the ideal illumination conditions can be checked in reality. In the presence of irregularities, the field isotropy cannot be verified but the field could still be diffusive. In Sánchez-Sesma *et al.* (2006) and Pérez-Ruiz *et al.* (2008) one sees that uniform illumination in the system's envelope produces a diffuse field that near the scatters it is not isotropic.

According to Weaver (1982; 1985), two simple definitions of a diffusive regime can be conceived. The first considers a diffuse field at a given frequency as a state of vibration for which the normal modes of the system are in statistical equilibrium. In this definition, seismic energy is distributed among all normal modes according to the Principle of Equipartition. This principle states that all modes (which together constitute a diffuse field), appropriately normalized, contribute the same energy to construct the Green function if they are summed up. In fact, some relevant connections between analytic and deterministic solutions arise from diffuse field theory (see Sánchez-Sesma *et al.,* 2011b, Pérez-Ruiz *et al.,* 2008; Perton and Sánchez-Sesma, 2016). The second and most popular definition asserts that for each point of the medium in vibration, the diffuse field can be represented as an isotropic and random superposition of plane waves. Each one has amplitude that varies slowly over time and with a random phase (Shapiro *et al.,* 2000). This view implicitly assumes isotropy and neglects irregularity but can be regarded as the concept that applies to the illumination itself.

The first observation of energy equipartition in seismic records was the result of a carefully planned experiment in which the codas of 13 earthquakes recorded in a very small square array (c. 50m) in Guerrero (Mexico) were analyzed (Shapiro *et al*., 2000; Hennino *et al*., 2001). The seismic energies could be separated in terms of the squared curl modulus and the divergence of the field obtained numerically from spatial derivatives. The energy ratio could be computed, and they suggest that the stability of this ratio is a strong indicator that the wave field has a diffusive regime, in this case for the seismic coda. They pointed out multiple diffraction in the coda of seismograms recorded in Guerrero, Mexico and, following Aki and Chouet (1975), excluded single scattering as an alternative explanation of the coda. In other experiment Margerin *et al.* (2009) study the potential and kinetic energies of the shear waves in the ten-earthquake codas recorded at Pinyon Flats Observatory, California. They demonstrated a clear stabilization of the relationship between P wave and S wave (W_S/W_P) energies in the coda, with similar values for the ten earthquakes studied, interpreting these observations as an energy equipartition signature. On the other hand, complete wave simulations both in acoustics (Wegler *et al.,* 2006) and in dynamic elasticity (Papanicolaou *et al.,* 1996; Przybilla *et al.,* 2006) demonstrated that in a diffusive regime, the ratio of the energy densities of the P and S waves stabilizes to a constant.

In the literature, various works which found that find the ambient field is not fully diffuse (Weaver *et al.*, 2009; Mulargia (2012), Sens-Schonfelder *et al.,* 2015; Liu and Ben-Zion, 2016). For example, Mulargia (2012) developed a procedure to establish the applicability of the diffuse field paradigm to ambient seismic noise. His method is based on azimuthal isotropy and spatial homogeneity and was applied to ASN recorded in 65 sites covering a wide variety of environmental and subsurface conditions. Mulargia asserts that seismic noise is not diffuse and that basic physical arguments suggest that diffuse field theory may not be applicable to seismic noise. However, he notes that such a conclusion has no practical inhibitory effect on passive imaging. We think he overlooked the roles of multiple scattering and the field stabilization towards a state, non-necessarily an isotropic one.

In this work, we explore the stabilization of the W_S/W_P energy ratio of the recorded ASN at different locations in Mexico by means of small sensor arrays, following the approaches of Shapiro *et al.* (2000), Hennino *et al*. (2001) and Margerin (2009). Three sites were studied:

1. UNAM's main campus South of Mexico City. Ambient seismic noise, ASN, was recorded at two nearby sites (the School of Engineering and the Sport Field) using L-shaped arrays of three sensors each recording during two hours. We found that W_S/W_P energy ratio in the ASN records is stable (7.28 ± 0.88) for long recording times.
2. La Primavera park in Zapopan, Jalisco, Mexico. ASN was recorded during three hours in a L-shaped array of three sensors. The M 7.1 earthquake of September 19, 2017 (SSN, 2017)

was recorded as well. For this site, we found that W_S/W_P energy ratio for the pre-event (noise), post-event (coda) and the daily ASN are stable (7.1 ± 0.5). Moreover, for this site, the stability of HVSR for the three array stations is observed along with the equilibrium of W_S/W_P energy ratio as a function of time.

3. Chilpancingo, Guerrero, Mexico. Part of the data from a well-known experiment regarding the coda of 11 events in 1999 (see Shapiro *et al.*, 2000 and Hennino *et al.*, 2001) was re-analyzed for one of the earthquakes recorded there. It was the only one that has a good quality pre-event. We study W_S/W_P energy ratio both in the pre-event ASN and the coda and found the ratio is stable in both regimes.

These results, which correspond to sundry geological settings, display the energy ratio stabilization in the ASN regime. This anticipates a diffusion regime, no necessarily isotropic.

Equipartition Theory.

Following Shapiro *et al.* (2000), the energies of compression and shear deformations are:

$$W_P = \frac{1}{2}\rho\alpha^2(\nabla \cdot \vec{u})^2 \tag{1}$$

$$W_S = \frac{1}{2}\rho\beta^2|\nabla \times \vec{u}|^2 \tag{2}$$

where α, β and ρ denote the compressional and shear wave velocities and mass density at the receiver and $\vec{u}$ is the displacement vector. Therefore, the ratio of the energy densities, W_S and W_P associated with the deformation in a solid medium at the surface is given by:

$$\frac{W_S}{W_P} = \frac{\left(\frac{\mu}{2}\right)|\nabla \times \vec{u}|^2}{\left(\frac{\lambda}{2}+\mu\right)(\nabla \cdot \vec{u})^2} \tag{3}$$

where λ and μ are the Lamé constants.

For an array of seismometers installed on the free surface of a half-space the *z*-derivatives can be obtained from the stress free boundary condition. In fact, if stresses $\sigma_{zz}, \sigma_{zx},$ and σ_{zy} are null at z=0, we found that $\frac{\partial u_z}{\partial z} = \frac{2\beta^2-\alpha^2}{\alpha^2}\left(\frac{\partial u_x}{\partial x} + \frac{\partial u_y}{\partial y}\right)$, $\frac{\partial u_x}{\partial z} = -\frac{\partial u_z}{\partial x}$ and $\frac{\partial u_y}{\partial z} = -\frac{\partial u_z}{\partial y}$. Therefore, this energy ratio can be written in terms of derivatives with respect to the horizontal Cartesian coordinate system as

$$\frac{W_S}{W_P} = \frac{1}{4}\left(\frac{\alpha}{\beta}\right)^2 \frac{4\left(\frac{\partial u_z}{\partial x}\right)^2 + 4\left(\frac{\partial u_z}{\partial y}\right)^2 + \left(\frac{\partial u_x}{\partial y} - \frac{\partial u_y}{\partial x}\right)^2}{\left(\frac{\partial u_x}{\partial x} + \frac{\partial u_y}{\partial y}\right)^2} \qquad (4)$$

The ratio of equation 4 allowed to assess the partitioned energy in the seismic coda (Shapiro *et al.,* 2000; Hennino *et al.,* 2001; Margerin, 2009). However, we apply this ratio for the analysis of ASN records. For ASN in a full-space, composed only of body waves, Weaver (1982) obtained for that ratio $2(\alpha/\beta)^3$, which for a Poisson solid is 10.4. On the other hand, for ASN consisting only of surface waves, the figure is close to 6.5 (Hennino *et al.*, 2001).

Arrays at the Engineering School and the Sport Field of the UNAM and La Primavera park.

To estimate the strain energies W_S and W_P in the ASN data, two arrays of three Guralp 6TD sensors each were deployed at the yard of the Engineering School and the Sport Field (UNAM). At each site, the sensors were installed in a L-shaped array with a spacing of 12 and 15 m, respectively, from the vertex station. Figure 1 shows the configuration of the arrays. The duration of the records, with common time, was approximately two hours and the absolute time was encoded in the radio signals of the GPS satellites. With this type of array, we can estimate the spatial derivatives of the displacement field in two linearly independent horizontal directions.

The ASN data of the La Primavera experiment were obtained from a spatial arrangement of Guralp 6TD sensors located at La Primavera park in Zapopan, Jalisco, Mexico. The sensors were installed in a L-shaped array with a spacing of 1.5 km from the vertex station (See Figure 1). During the experiment, the M7.1 September 19, 2017 earthquake was recorded. The epicenter was located between Puebla and Morelos Mexican states, 12 km southeast of Axochiapan, Morelos (SSN, 2017) with an epicentral distance of approximately 500 km.

Before applying Equation 4 in the ASN data, we have preprocessed the signals removing the instrumental response and integrating the velocity records to obtain displacements. The orientation of the sensors in the array was verified at the time of installation, so no rotation procedure was required. Then, we estimate the spatial derivatives of the displacements at each time sample through the following equations:

$$\frac{\partial u_i}{\partial x} = \frac{u_i^2 - u_i^1}{d}$$

$$\frac{\partial u_i}{\partial y} = \frac{u_i^3 - u_i^2}{d}; \;\; i = x, y, z \tag{5}$$

Where u_i^n is the displacement in the i direction at station n. d is the distance between receivers.

Shapiro *et al.* (2000) indicate that the derivative estimated with finite difference differs from the exact value according to the following equation (Bodin *et al.,* 1997; Lomnitz, 1997):

$$\frac{\left[\frac{\partial u_i}{\partial x_j}\right]_{array}}{\left[\frac{\partial u_i}{\partial x_j}\right]_{exact}} = \frac{\sin(\pi L/\lambda)}{\pi L/\lambda} \tag{6}$$

Where L is the distance between receivers and λ is the wavelength. If $L/\lambda \leq 0.1$ the error of the calculation of the derivatives is less than 2%.

Therefore, the available range of frequencies to estimate the derivatives of displacements, according to the separation of stations is between 2 and 4 Hz for the Engineering School array, from 2.5 to 4.5 Hz for the Sport Field array and between 0.25 and 0.45 Hz for La Primavera array. These values of frequencies were obtained by applying the relationship $f = V_s/\lambda$, where f is the value of the frequency, Vs is the velocity of the S waves and λ is the wavelength. To obtain the values of Vs and λ, we use the same "L" arrangement (see figure 1) to obtain the phase velocity of the Rayleigh waves using SPAC (Aki, 1957). For example, assuming that the material has a Poisson coefficient of 0.25, we can estimate the velocity of the S waves as a function of the phase velocity $V_s = V_R/0.92 = 600\ \frac{m}{s}$. In our case we chose the range a $0.05 \leq L/\lambda \leq 0.07$ for our treatment in order to equation

(6).

Chilpancingo Experiment

The ASN data used in this study were gathered at a temporary array located near Chilpancingo, Guerrero (Mexico) during June - August 1997. The array consisted of four stations installed in the corners of a square with sides of 50 m. During the experiment, 13 seismic events were well recorded. The results of the energy partition of the coda has been reported elsewhere (Shapiro *et al.,* 2000 & Hennino *et al*., 2001). However, only the event 12 has pre-event data long enough (an ASN record) to perform our analysis. We estimate the strain energies W_P and W_S for these data using the same pre-processing and methods described in Shapiro *et al.* (2000).

Experimental results

After data processing, we estimate the W_S/W_P energy ratio using equation 4. Energy equipartition among the various modes is a property of the average wavefield if the modes can be distinguished and numbered. To approximately compute the average energy ratio for each record, different moving-average windows length (MAWL) are used. Margerin, (2001) and Shapiro *et al.* (2000) selected these window widths close to the "mean free-time". Nevertheless, this last parameter is very difficult to estimate with traditional techniques based on attenuation studies because the effects of energy absorption and those of multiple scattering are related (Larose *et al.,* 2004). The mean-free-time can be related to the medium diffusivity that can be estimated by direct measurements of energy density in terms of the diffusive acoustic model and/or the radiation transfer equations (Wegler, 2005). In practice, we regard the time-width of the MAWL for which stabilization is reached as an estimate of the mean free-time.

Figure 2 depicts the results for the Chilpancingo array. As shown by Shapiro *et al.* (2000) and Hennino *et al.* (2001), the W_S/W_P in the coda stabilizes at very different levels from the noise in the pre-event and in the direct arrivals (see figure 2-b). However, sometimes (*e.g.* 0 to 200s) the W_S/W_P of ASN is reasonably stable with average values of 7.47 ± 0.83 while W_S/W_P of the coda is stable with average values of 7.29 ± 0.42. The fluctuations are likely due to multiple scattering of waves in the random medium and the available energy amount. Note that the W_S/W_P of ASN stabilizes for 55s MAWL while the W_S/W_P of coda only needed a 16s MAWL (Shapiro *et al.,* (2000) and Hennino *et al.,* 2001). Moreover, the W_S/W_P of ASN does not exhibit fluctuations larger than ten per cent of the average value in the seismic coda.

For the UNAM-ES array, the W_S/W_P is stabilized in some time intervals with an average value of 7.28 (for example, see the interval 2,000-5,000 s), this W_S/W_P energy ratio stabilizes for a MAWL of 35 s. However, the W_S/W_P value shows fluctuations in the range from 5 to 10 to different measure of the ASN. Table 1 shows the theoretical and observed values of stabilization of the energies and the MAWL on the free surface of a half-space with $\lambda = \mu$. The results for the Engineering School array are displayed in figure 3.

For the UNAM-SF array, the W_S/W_P energy ratio stabilizes at an average of 2.9 ± 0.47 with a MAWL of 45 s. This average is very far from the expected theoretical value of 7.19 for equipartitioned elastic waves at the surface of a homogeneous Poissonian half-space. In fact, Margerin *et al*., (2009) found similar energy values, W_S/W_P =2.8, for 10 earthquakes recorded on a dense array, located at Pinyon Flats Observatory, California. In order to explain these values, they developed a theory of equipartition in a layered elastic-space using a rigorous spectral decomposition of the elastic wave equation. They observed that, close to the resonance frequency, a decrease of the W_S/W_P takes place.

The experiment at La Primavera site is described in figure 4. We find that, after the seismic event (0.3 to 0.5 hrs.), the W_S/W_P is unstable and well below the expected theoretical value of equipartition ($<$ 6.5). However, as time progresses, the W_S/W_P oscillates between 6 and 10. These values are within the ratio expected for a purely Rayleigh wave field and the ratio for a purely body-wave field. Finally, it tends to stabilize at 7.1 ± 0.5 (see, for example, the interval from 1.5 to 3 hrs. in figure 3c). This stabilization occurs for a MAWL of 150s used in this figure. The partitioning regime is reached for long windows. It indicates that the typical dimension of heterogeneity is about the size of the wavelength (Shapiro *et al*. 2000). Besides, the required long MAWL is a consequence of the narrow band width of 0.2 Hz at low frequencies.

In order to explore some consequences of the stabilization of the W_S/W_P energy ratio, we used the

HVSR for the dataset of the Primavera experiment. A 150s window length was used (the estimated MAWL) with an overlap of 99% to obtain the HVSR as a function of time. The HVSR in a frequency range between 0.2-20 Hz is shown in figure 4 d-f as a function of time, together with their corresponding average HVSR curves. From these results, we observe that during the seismic pre-event, the HVSR is stable in their shape and amplitude (0-0.1 hrs.). However, when the seismic event begins, the HVSR becomes unstable and does not reach the average amplitude during the first arrivals. After the first arrivals, there is a time interval (surface waves arrivals) where the amplitude stabilizes. On the other hand, in the time interval 0.2 - 0.4 hrs. we find that the HVSR is unstable and its shape differs from that found in windows dominated by ASN. While both the seismic coda and the ASN are presented, the HVSR gradually converges in shape and amplitude towards the level found in the pre-event (ASN). For a distant earthquake like this and at the frequencies that remain the equilibration takes time. Certainly, the subject requires attention but now it is beyond the focus of this research. These long period fluctuations may imply large scale structures. Careful analysis is required to understand their origin. An extreme case is the breakdown of equipartition for large period (10 to 40 s) coda waves (Sens‐Schönfelder, *et al.* 2015).

Based on these results, we observe a relationship between the stabilizations of the W_S/W_P energy ratio and the HVSR. If the W_S/W_P does not stabilize to the expected theoretical values (between values of 6 and 10) then, the HVSR does not recover its average amplitude and shape. This behavior is observed in figure 4 for the time interval between 0.2 to 0.4 hrs. On the other hand, the oscillations in the W_S/W_P are reflected in the amplitude of the HVSR, that is, while the W_S/W_P exceeds the average value, the amplitude of the HVSR increases and vice versa. An example of this is observed for the time intervals of 0.8-1 hrs. and 1.3-1.4 hrs. (figure 4). This confirms that, in absence of energy equipartition in ASN or earthquake data, the shape and amplitude of the HVSR are disturbed and, consequently, Green's functions cannot be recovered.

The conspicuous fluctuations of the W_S/W_P energy ratio in some time windows reflect the variability of different mode contents in the wavefield. The energy stabilization of the seismic coda represents a genuine process of multiple scattering and diffraction (Hennino *et al*., 2001). Moreover, the ASN can be interpreted, based on the clear stabilization of the W_S/W_P, as a diffusive regime as well. Summing up the observations, we find that W_S/W_P for ASN is stable. The equilibration between the different modes of vibration occurs faster in the seismic coda as compared to the ASN. The W_S/W_P stabilization within the ASN is a process which anticipates the diffusion regime. Moreover, Margerin *et al.* (2000) pointed out that the time evolution of the W_S/W_P could be used as a marker for the different scattering mechanisms. Figure 5 shows the stabilization of the W_S/W_P for the arrays as the MAWL increases.

Conclusions

By means of the W_S/W_P energy ratio we studied the stabilization of energies carried by ambient seismic noise (ASN) in different settings:

(1) The Chilapancingo (Guerrero, Mexico) Array at a relatively firm site using the ASN in the pre-event of an earthquake that allowed the first experimental evidence of equipartition in the coda (Shapiro *et al.,* 2000 and Hennino *et al*., 2001);

(2) The UNAM's Engineering School experiment for ASN. The site is a weathered basalt in the yard of the school building;

(3) The UNAM's Sport field experiment for ASN. The site is characterized by a very soft soil layer on weathered basalt at some meters deep.

(4) The La Primavera experiment for ASN. This site is within the Mexican Transverse Neo Volcanic Belt and it is characterized by intercalations of lava and pyroclastic materials of andesitic-basaltic composition.

We applied the procedure described by Shapiro *et al.* (2000) in order to approximately separate the energies and follow their time evolution. For the UNAM's Engineering School and La Primavera experiments, we observed that the ratio remains stable for long time lapses. However, it occasionally exhibits fluctuations between the expected theoretical values for body waves (W_S/W_P=9.76) and for Rayleigh waves (W_S/W_P=6.46). The results for the UNAM's Sports field show that the W_S/W_P stabilizes at an average of 2.9 ± 0.47, very far from the expected theoretical value of 7.19 for equipartitioned elastic waves at the surface of a homogeneous Poissonian half-space. Even though this result deserves further scrutiny, it is very likely that the soft and thin sediments of that site played a role for that low average.

For the Chilpancingo array, we find that the W_S/W_P energy ratio of pre-seismic event stabilizes for windows longer than those of seismic coda. While the W_S/W_P for the seismic coda is 7.29±0.42, the W_S/W_P of the pre-event stabilizes in values of 7.47±0.83. In addition, the energy partition in the coda is reached quickly, after a few seconds of MAWL. The stabilization of the W_S/W_P energy ratio in the ASN is a process which anticipates that the wave field has reached a diffusion regime. This exploration into the noise in various settings strongly supports the idea that ambient seismic noise, like the coda, is a genuine multiple scattering process. In contrast to Mulargia (2012) remark that ASN is not diffuse, we show that approximate equipartition, implicit in the S and P energy ratio (W_S/W_P), clearly emerges and suggests that the ASN could be diffuse. Recently, a time windowing scheme has been proposed to enhance diffuse properties of the fields (Weaver & Yoritomo, 2018). Therefore, the corresponding processing must be the same to exploit its diffuse field nature and justifies the use of HVSR in the theoretical context of diffusion.

Data and Resources

The Chilpancingo data that support the findings of this study are available on request from the author Campillo, M. (michel.campillo@univ-grenoble-alpes.fr). The Engineering School and Sport Field and La Primavera data that support the findings of this study are available on request from the corresponding author Piña-Flores, J. (jpf@unam.mx). The seismic data were preprocessed with MATLAB Version: 9.8.0.1359463 (R2020a) Update 1 (License Number 40816183).

Acknowledgements

Thanks are given to Dr. Adrien Oth and two anonymous reviewer. We also thank to L. Margerin and N. M. Shapiro for providing us with the Chilpancingo Array data and their keen, constructive and insightful remarks, to Javier Lermo and his working group for providing us with the data seismic of the La Primavera park. This work has been partially supported by the Mexican National Council of Science and Technology (CONACYT) through the National Scholarship CONACYT number

449268, and by UNAM-DGAPA projects: PAPIIT (IN117119, IN107720) and PAPIME (PE103918), by Ministerio de Economía y Competitividad de España and ERDF under Project CGL2014-59908/JIN

References

Aki, K., 1957. Space and time spectra of stationary stochastic waves, with special reference to microtremores, *Bull. Earth. Res. Inst.,* **35,** 415–456.

Aki, K. & Chouet, B., 1975. Origin of coda waves: source, attenuation, and scattering effects, *J. Geophys. Res.,* **80**(23), 3322–3342. doi:10.1029/JB080i023p03322

Ardhuin, F., Stutzmann, E., Schimmel, M. & Mangeney, A., 2011, Ocean wave sources of seismic noise, *J. Geophys. Res.- Oceans*, **116**, C09004.

Asten, M.W. & Henstridge, J.D., 1984. Arrays estimators and the use of microseisms for reconnaissance of sedimentary basins, *Geophysics* **49**(11), 1828–1837. doi: 10.1071/EG984263

Bodin, P., Gomberg J., Singh S. K., & Santoyo, M., 1997. Dynamic deformations of shallow sediments in the Valley of Mexico, Part I: three dimensional strains and rotations recorded on a seismic array, *Bull. seism. Soc. Am.*, **87,** 528–539.

Campillo, M., 2006. Phase and Correlation in ‘Random’ Seismic Fields and the Reconstruction of the Green Function, *Pure appl. Geophys.,* **163** (2-3), 475-502. doi: 10.1007/s00024-005-0032-8

Friederich, A., Kruger F. & Klinge, K., 1998. Ocean-generated microseismic noise located with the GRFO array, *J. Seismol.,* **2**, 47–64. doi: 10.1023/A:1009788904007

García-Jerez, A., Piña-Flores, J., Sánchez-Sesma, F. J., Luzón, F., & Perton, M., 2016. A computer code for forward calculation and inversion of the H/V spectral ratio under the diffuse field assumption, *Comput. Geosci*., **97**, 67-78. doi:10.1016/j.cageo.2016.06.016

Garcia-Jerez, A., Seivane, H., Navarro, M., Martínez-Segura, M and Piña-Flores, J. 2019. Joint analysis of Rayleigh-wave dispersion curves and diffuse-field HVSR for site characterization: The case of El Ejido town (SE Spain). *Soil Dynamics and Earthquake Engineering.* **121.** 102-120. doi:10.1016/j.soildyn.2019.02.023.

Gudmundsson, O., Khan, A., & Voss, P., 2007. Rayleigh□wave group□velocity of the Icelandic crust from correlation of ambient seismic noise, *Geophys. Res. Lett.,* **34**(14), L14314. doi:10.1029/2007GL030215

Hennino, R., Tregoures, N., Shapiro, N.M., Margerin, L., Campillo, M., Van Tiggelen B.A. & Weaver, R. L., 2001. Observation of equipartition of seismic waves, *Phys. Rev. Lett.,* **86**, 3447–3450. doi: 10.1103/PhysRevLett.86.3447

Kanai, K., Tanaka, T. & Okada, K., 1954. Measurement of the microtremor, *Bull. Earthquake Res. Inst. Tokio Univ.* **32,** 199–210.

Larose, E., Margerin, L., Campillo, M. & Van Tiggelen, B.A., 2004. Weak localization of seismic waves, *Phys. Rev. Lett*., **93**, 048501. doi: 10.1103/PhysRevLett.93.048501.

Liu, X., & Ben-Zion, Y. (2016) Estimating correlations of neighbouring frequencies in ambient seismic noise, *Geophys. J. Intl*. **206**, 1065-1075, doi:10.1093/gji/ggw196

Lomnitz, C., 1997. Frequency response of a strainmeter, *Bull. Seism. Soc. Am.*, **87,** 1078–1080.

Margerin, L., Van Tiggelen, B. A. & Campillo, M., 2001. Effect of absorption on energy partition of elastic waves in the seismic coda, *Bull. Seism. Soc. Am.*, **91**(3), 624-627. doi: 10.1785/0120000228

Margerin, L., Campillo, M., Van Tiggelen, B. A., & Hennino, R., 2009. Energy partition of seismic coda waves in layered media: Theory and application to Pinyon Flats Observatory, *Geophys. J. Int.*, **177**(2), 571-585. doi: 10.1111/j.1365-246X.2008.04068.x

Margerin, L., Campillo, M. and Van Tiggelen, B., 2000 Monte Carlo simulation of multiple scattering of elastic waves. *Journal of Geophysical Research: Solid Earth* **105**.B4 7873-7892. doi: 10.1029/1999JB900359

Matsushima, S., Kosaka, H. & Kawase, H., 2017. Directionally dependent horizontal‐to‐vertical spectral ratios of microtremors at Onahama, Fukushima, Japan, *Earth, Planets and Space*. **69**(1), 96. doi: 10.1186/s40623-017-0680-9

Mulargia, F., 2012. The seismic noise wavefield is not diffuse. *J. Acoust. Soc. Am.*, **131**, 2853–2858. doi: 10.1121/1.3689551

Nakamura, Y., 1989. A method for dynamic characteristics estimation of subsurface using microtremor on ground surface, *QR of RTRI* **30**(1), 25-33

Nakamura, Y., 2000, Clear identification of fundamental idea of Nakamura's technique and its applications, *in* 'Proceedings of the 12th World Conference on Earthquake Engineering', Auckland New Zealand.

Papanicolaou, G. C., Ryzhik, L. V. & Keller. J. B., 1996. Stability of the P- to S-energy ratio in the diffusive regime. *Bull. Seism. Soc. Am.*, **86,** 1107–1115.

Pérez-Ruiz, J. A., Luzón, F. & Sánchez-Sesma, F. J., 2008. Retrieval of elastic Green's tensor near a cylindrical inhomogeneity from vector correlations, *Commun. Comput. Phys.*, **3**(1), 250-270. doi:10.1029/. 2006GL026454

Perton, M. & Sánchez-Sesma, F.J., 2016. Green's function calculation from equipartition theorem, *J. acoust. Soc. Am.*, **140**(2), 1309-1318. doi: 10.1121/1.4961208

Perton, M., Spica, Z., & Caudron, C., 2018. Inversion of the horizontal-to-vertical spectral ratio in presence of strong lateral heterogeneity, *Geophys. J. Int.*, **212**, 930-941. doi: 10.1093/gji/ggx458

Piña-Flores, J., Perton, M., García-Jerez, A., Carmona, E., Luzón, F., Molina-Villegas, J. C., & Sánchez-Sesma, F. J. (2017). The inversion of spectral ratio H/V in a layered system using the Diffuse Field Assumption (DFA), *Geophys. J. Int.*, **208**(1), 577-588. doi: 10.1093/gji/ggw416

Przybilla, J., Korn, M. & Wegler, U., 2006. Radiative transfer of elastic waves versus finite difference simulations in two-dimensional random media, *J. Geophys. Res.*, **111**, B04305. doi:

10.1029/2005JB003952

Rhie, J. & Romanowicz, B., 2004. Excitation of Earth's continuous free oscillations by atmosphere–ocean–seafloor coupling. Nature, **431**(7008), p.552. doi: 10.1038/nature02942

Ritzwoller, M. H., Lin, F. C., & Shen, W., 2011. Ambient noise tomography with a large seismic array, *C. R. Geosci.*, **343**(8), 558-570. doi: 10.1016/j.crte.2011.03.007

Sabra, K.G., Gerstoft, P., Roux, P., Kuperman, W.A., & Fehler, M.C., 2005. Extracting timedomain Green's function estimates from ambient seismic noise, *Geophys. Res. Lett.,* **32**, L03310, doi: 10.1029/2004GL021862

Sánchez-Sesma, F. J., Pérez-Ruiz, J. A., Campillo, M. and Luzón, F., 2006. Elastodynamic 2D Green function retrieval from cross-correlation: Canonical inclusion problem', *Geophys. Res. Lett.,* **33**, L13305. doi:10.1029/2006GL026454

Sánchez-Sesma, F. J., Rodríguez, M., Iturrarán-Viveros, U., Luzón, F., Campillo, M., Margerin, L., García-Jerez, A., Suárez, M., Santoyo, M. A. & Rodríguez-Castellanos, A., 2011a, A theory for microtremor H/V spectral ratio: application for a layered médium, *Geophys. J. Int*., **186**, 221–225. doi: 10.1111/j.1365-246X.2011.05064.x

Sánchez-Sesma, F. J., Weaver, R. L., Kawase, H., Matsushima, S., Luzón, F. & Campillo, M., 2011b. Energy partitions among elastic waves for dynamic surface loads in a semi-infinite solid, *Bull. Seism. Soc. Am.*, **101**(4), 1704–1709. doi: 10.1785/0120100196

Saygin, E., & Kennett, B. L. 2010. Ambient seismic noise tomography of Australian continent, *Tectonophysics*, **481**(1), 116-125. doi: 10.1016/j.tecto.2008.11.013

Sens‐Schönfelder, C., Snieder, R., and Stähler, S. C. (2015), The lack of equipartitioning in global body wave coda, *Geophys. Res. Lett*. 42, 7483- 7489, doi:10.1002/2015GL065108

Shapiro, N.M., Campillo, M., Margerin, L., Singh, S.K., Kostoglodov, V., & Pacheco, J., 2000. The energy partitioning and the diffusive character of the seismic coda, *Bull. Seism. Soc. Am.*, **90**, 655–

665. doi: 10.1785/0119990021

Shapiro, N.M. and Campillo, M., 2004, Emergence of broadband Rayleigh waves from correlations of the ambient seismic noise, *Geophys. Res. Lett.,* **31**, L07614. doi: 10.1029/2004GL019491

Shapiro, N.M., Campillo, M., Stehly, L., and Ritzwoller, M., 2005. High resolution surface wave tomography from ambient seismic noise, *Science.,* **307**, 1615–1618. doi: 10.1126/science.1108339

Spica, Z., Caudron, C., Perton, M., Lecocq, T., Camelbeeck, T., Legrand, D., Piña-Flores, J., Iglesias, A. & Syahbana, D. K. 2015, Velocity models and site effects at Kawah Ijen volcano and Ijen caldera (Indonesia) determined from ambient noise cross-correlations and directional energy density spectral ratios, *J. Volcanol. Geoth. Res*., **302**, 173–189. doi: 10.1016/j.jvolgeores.2015.06.016

SSN (2017): Universidad Nacional Autónoma de México, Instituto de Geofísica, Servicio Sismológico Nacional, México. Dirección electrónica: http://www.ssn.unam.mx

Ward, K. M., Porter, R. C., Zandt, G., Beck, S. L., Wagner, L. S., Minaya, E., & Tavera, H., 2013. Ambient noise tomography across the Central Andes, *Geophys. J. Int.*, **196** (2), 1264-1265. doi: 10.1093/gji/ggt166

Weaver, R. L., 1982. On diffuse waves in solid media, *J. Acoust. Soc. Am*., **71**(6), 1608-1609. doi: 10.1121/1.387816

Weaver, R. L., 1985. Diffuse elastic waves at a free surface, *J. Acoust. Soc. Am*., **78**(1), 131-136. doi: 10.1121/1.392576

Weaver, R., Froment, B., & Campillo, M. (2009). On the correlation of non-isotropically distributed ballistic scalar diffuse waves. *J. Acoust. Soc. Am*, **126**(4), 1817-1826.

Weaver, R. L., & Yoritomo, J.Y., 2018. Temporally weighting a time varying noise field to improve Green function retrieval. *J. Acoust. Soc. Am*. **143**(6), 3706–3719. doi: 10.1121/1.5043406

Wegler, U. (2005). Diffusion of seismic waves in layered media: boundary conditions and analytical solutions, *Geophys. J. Int.* 163, 1123–1135. doi: 10.1111/j.1365-246X.2005.02798.x

Wegler, U., Korn, M. & Przybilla, J., 2006. Modeling full seismogram envelopes using radiative transfer theory with born scattering coefficients, *Pure appl. Geophys*., **163,** 503–531. doi: 10.1007/s00024-005-0027-5

Yang, Y., & Ritzwoller, M. H., 2008. Characteristics of ambient seismic noise as a source for surface wave tomography, *Geochem. Geophys. Geosyst.,* **9** (2), Q02008. doi:10.1029/2007GC001814.

Zheng, S., Sun, X., Song, X., Yang, Y., & Ritzwoller, M. H., 2008. Surface wave tomography of China from ambient seismic noise correlation, *Geochem. Geophys. Geosyst.,* **9** (5). doi:10.1029/2008GC001981

Table 1 Comparison between the W_S/W_P of the data and theoretical values on free surface z=0.

	Data Z=0	**Theory z=0**	**Theory z=∞**	**Theory Rayleigh Only z=0**	**Theory Bulk Only z=0**	**MAWL (s)**
Seismic Coda	7.29±0.42	7.19	10.39	6.46	9.76	16
Pre event Noise	7.47±0.83	7.19	10.39	6.46	9.76	55
Engineering School	7.28±0.88	7.19	10.39	6.46	9.76	32
Sport Field	2.9±0.47	7.19	10.39	6.46	9.76	45
La Primavera	7.1±0.5	7.19	10.39	6.46	9.76	150

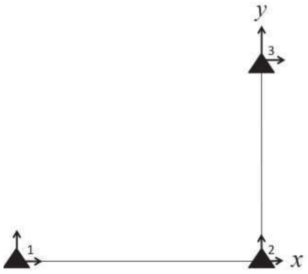

Figure 1.- L-shape array configuration used in the Engineering School, the Sports Field (UNAM) and La Primavera park. The arrows on the triangles indicate the orientation of each sensor.

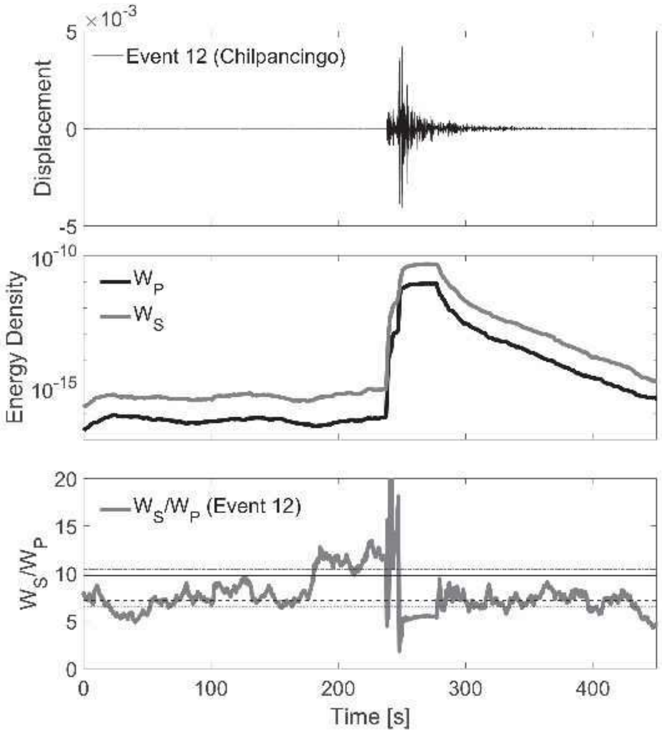

Figure 2.- Measurements of the W_P and W_S energies and their W_S/W_P energy ratio for the 1999 Chilpancingo array. The upper panel shows the record of the vertical component filtered between 1 and 3 Hz. In the middle panel, the W_P and W_S energies depicted correspond to MAWL of 16s for coda (Shapiro *et al.,* 2000; Hennino *et al.,* 2001) and of 55s for the pre-event noise. Even with this averaging difference, the energy densities of coda range from four to five orders of magnitude of the of pre-event (noise) levels. The lower panel displays the W_S/W_P energy ratio for data; the dotted line represent the theoretical values of W_S/W_P Bulk only at z=0; the dashed line represent the theoretical values of W_S/W_P at z=0 (for a Poisson solid and all the wave modes); the solid line represent the theoretical values of W_S/W_P Rayleigh only z=0; the dotted-dashed line represent the theoretical values of W_S/W_P at $z=\infty$. These variations are well within expected variations due to transients but, giving the huge difference in energy levels, the stability of ratios is remarkable.

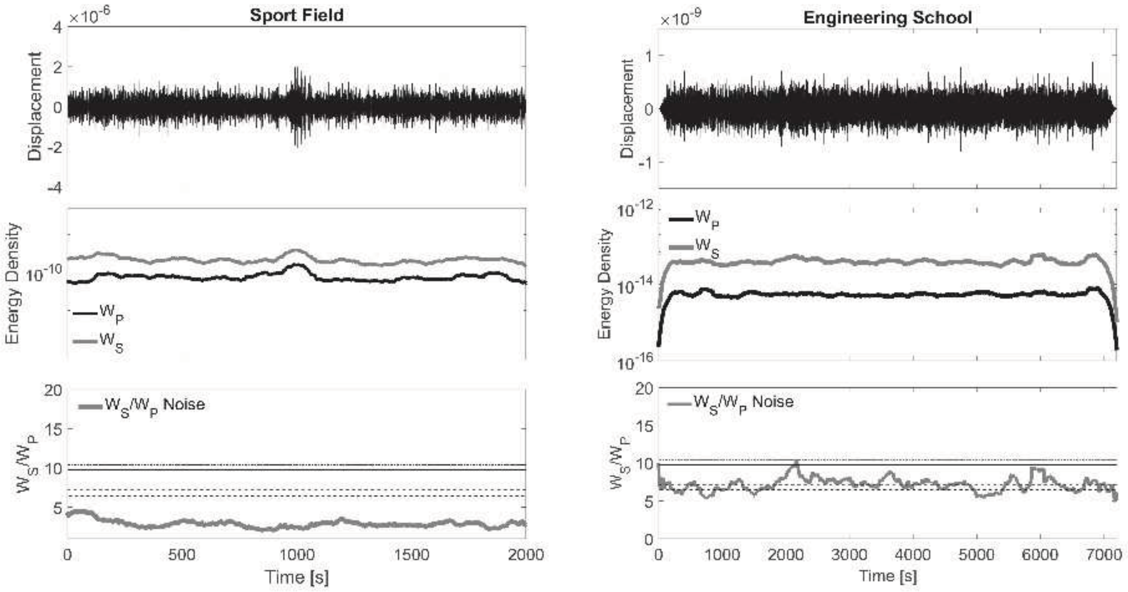

Figure 3.- Measurements of the W_P and W_S energies and their ratio W_S/W_P at both the Engineering School and the Sports field (UNAM's main campus). The left-upper panel shows the vertical component, filtered between 2 and 4 Hz, recorded at the Sport field. The left-middle panel depicts the W_P and W_S energies with a 32s MAWL and the left-lower panel displays the W_S/W_P. The right-upper panel shows the vertical component, filtered between 2.5 and 4.5 Hz, recorded at the Engineering School. In the right-middle panel, the W_P and W_S energies are shown with a 45s MAWL, and the left-lower panel shows the W_S/W_P ratio for ASN data; the dash lines represent mean values of W_S/W_P for data. The dotted line represent the theoretical values of W_S/W_P Bulk only at $z=0$; the dashed line represent the theoretical values of W_S/W_P at $z=0$ (for a Poisson solid and all the wave modes); the solid line represent the theoretical values of W_S/W_P Rayleigh only $z=0$; the dotted-dashed line represent the theoretical values of W_S/W_P at $z=\infty$

435

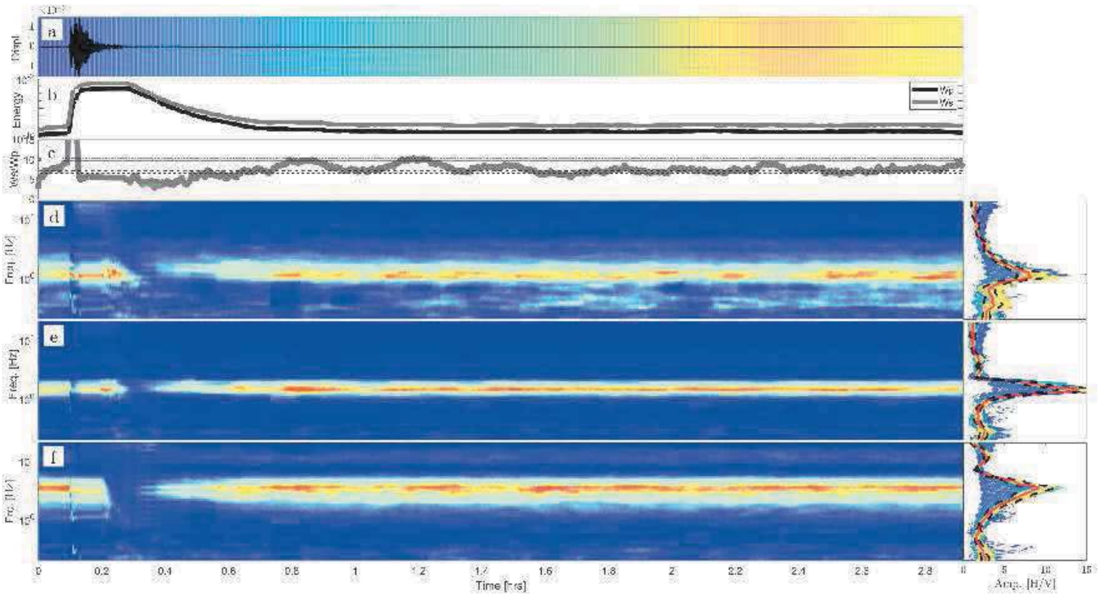

Figure 4.- Measurements of the W_P and W_S energies and their ratio W_S/W_P at the La Primavera (Zapopan, Jalisco) Array. Panel a) shows the vertical component, filtered between 0.2 and 0.4 Hz. The vertical striations represent the time windows associated to compute the HVSR for the unfiltered records. Panel b) depicts the W_P and W_S energies with a 150s MAWL and panel c) displays the W_S/W_P ratio for seismic data; the dotted line represent the theoretical values of W_S/W_P Bulk only at $z=0$; the dashed line represent the theoretical values of W_S/W_P at $z=0$ (for a Poisson solid and all the wave modes); the solid line represent the theoretical values of W_S/W_P Rayleigh only $z=0$; the dotted-dashed line represent the theoretical values of W_S/W_P at $z=\infty$. Panels d), e) and f) show, for each station of the array, the evolution of the HVSR as a function of time. Note that the HVSR for each station clearly reflects important site effect.

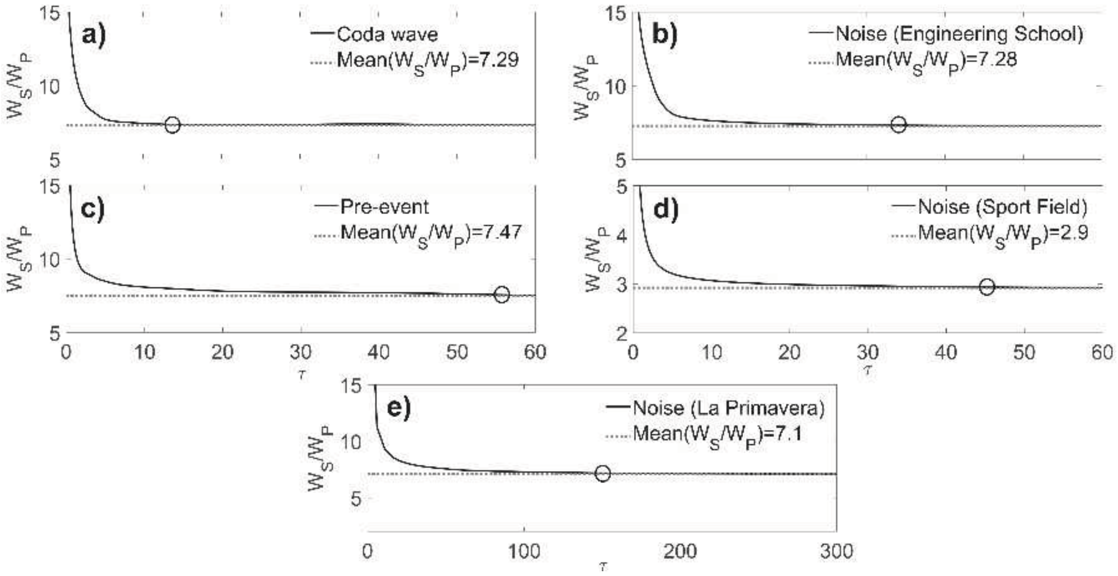

Figure 5.- Measurements of the W_S/W_P versus the MAWL (τ) for the analyzed experiments. The solid lines represent de average W_S/W_P. The dotted lines represent the stabilization mean values of W_S/W_P. The open circles mark the MAWL from which the W_S/W_P stabilizes (i.e. our estimate of the mean free time). a) The W_S/W_P for coda wave for the Chilpancingo experiments, requiring 16 s MAWL. b) The stabilization of W_S/W_P for ASN at the Engineering School (MAWL of ~32s). c) The stabilization of W_S/W_P in the pre-event of the same record needed 55 s. d) The stabilization of W_S/W_P for ASN at UNAM-SF (MAWL of ~45s). e) The stabilization of W_S/W_P for ASN at La Primavera park, where 150 s of MAWL were required to reach equipartition.

Manuscript Details

Manuscript number	ENGEO_2020_493
Title	IMAGING THE STRUCTURE OF THE SUN PYRAMID (TEOTIHUACÁN, MEXICO) FROM PASSIVE SEISMIC METHODS
Article type	Research Paper

Abstract

We present a three-dimensional model of shear wave velocity for the Sun Pyramid in Teotihuacán using the cross-correlation of seismic ambient noise recorded at 15 temporally broadband stations distributed on different levels of the structure. To invert the travel time of Rayleigh waves between stations, we used the Fast Marching Method (FMM) with an azimuthal projection that considers the station distribution at different heights. Our wave-velocity model reproduce three main features of the Sun Pyramid: i) it describes low-velocity anomalies related to the natural flow of water that has a preferential northwest-southeast direction; ii) it shows low-velocity anomalies which correlate well with the staggered walls or stirrups of stone and mud on the surface that were part of the constructive process to extend the structure and provide support to weak parts of the Sun Pyramid (high-velocity zones lack these staggered walls); and iii) it images the dome-like structure of the Pyramid, pointing to the susceptibility of the walls to landslides. These results will be useful for the structural diagnosis and assessment of seismic vulnerability of this emblematic pre-Hispanic monument.

Keywords	Ambient noise tomography, H/V spectral ratio, Structure imaging, Sun Pyramid, Seismic vulnerability
Corresponding Author	Antonio Garcia-Jerez
Corresponding Author's Institution	Universidad de Almería
Order of Authors	José Piña-Flores, Martin Cardenas-Soto, Alejandro Sarabia-González, Antonio Garcia-Jerez, Cesar Augusto Sierra Alvarez, Mario A. Sáenz-Castillo, Francisco Luzon, francisco sanchez
Suggested reviewers	Gerardo Alguacil, Alessandro Giocoli, Yoshiya Oda, Shinichi Matsushima

Submission Files Included in this PDF

File Name [File Type]

Cover_Letter.pdf [Cover Letter]

Highlights.pdf [Highlights]

Sun_Pyramid_resubmitted.pdf [Manuscript File]

declaration-of-competing-interests.pdf [Conflict of Interest]

Supplementary_Material.pptx [Supplementary Material]

To view all the submission files, including those not included in the PDF, click on the manuscript title on your EVISE Homepage, then click 'Download zip file'.

Research Data Related to this Submission

Data set	https://data.mendeley.com/datasets/zbxvkfcdpb/draft?a=311fbcdb-519f-4b21-b97e-5af0bcfc534e

Data for: IMAGING THE STRUCTURE OF THE SUN PYRAMID (TEOTIHUACÁN, MEXICO) FROM PASSIVE SEISMIC METHODS

Simultaneous seismic records of ambient noise on Sun Pyramid, obtained with Güralp 6TD seismometers.

- Cross correlation of ambient seismic noise is applied to a structure with topography
- A projection scheme is used to correct the wave propagation velocities
- Joint inversion of dispersion curves and H/V spectral ratio improves resolution
- The model for the Sun Pyramid shows a dome structure with some low-velocity anomalies

IMAGING THE STRUCTURE OF THE SUN PYRAMID (TEOTIHUACÁN, MEXICO) FROM PASSIVE SEISMIC METHODS

by

José Piña-Flores[ab], Martín Cárdenas-Soto[a], Alejandro Sarabia-González[c], Antonio García-Jerez[d], César A. Sierra-Álvarez[e], Mario A. Sáenz-Castillo[e], Francisco Luzón[d], and Francisco J. Sánchez-Sesma[f]

[a]Facultad de Ingeniería, Universidad Nacional Autónoma de México. Circuito Escolar, Ciudad Universitaria, Coyoacán 04510 México DF, Mexico. jpf@unam.mx, martinc@unam.mx

[b]Posgrado de Ingeniería, Universidad Nacional Autónoma de México. Edificio S, 1er piso, Facultad de Ingeniería, CU, 04510 México DF, Mexico.

[c]Zona Arqueológica de Teotihuacán, Instituto Nacional de Antropología e Historia (INAH). Autopista Ecatepec-Pirámides Km 22.6, Teotihuacán 55800, Mexico. alejandro_sarabia@inah.gob.mx

[d]Departamento de Química y Física, Universidad de Almería. Edificio CITE IIA, 04120 Almería, Spain. agarcia-jerez@ual.es, fluzon@ual.es

[e]Universidad EAFIT. Carrera 49, nº 7 sur-50, 050022 Medellín, Colombia. csierraa@eafit.edu.co, msaenzc@eafit.edu.co

[f]Instituto de Ingeniería, Universidad Nacional Autónoma de México. Circuito Escolar, Ciudad Universitaria, Coyoacán 04510 México DF, Mexico. sesma@unam.mx

Corresponding author:

Antonio García Jerez, agarcia-jerez@ual.es

Submitted to Engineering Geology

April, 2020

IMAGING THE STRUCTURE OF THE SUN PYRAMID (TEOTIHUACÁN, MEXICO) FROM PASSIVE SEISMIC METHODS

José Piña-Flores, Martín Cárdenas-Soto, Alejandro Sarabia-González, Antonio García-Jerez, César A. Sierra-Álvarez, Mario A. Sáenz-Castillo, Francisco Luzón, and Francisco J. Sánchez-Sesma

ABSTRACT

We present a three-dimensional model of shear wave velocity for the Sun Pyramid in Teotihuacán using the cross-correlation of seismic ambient noise recorded at 15 temporally broadband stations distributed on different levels of the structure. To invert the travel time of Rayleigh waves between stations, we used the Fast Marching Method (FMM) with an azimuthal projection that considers the station distribution at different heights. Our wave-velocity model reproduce three main features of the Sun Pyramid: i) it describes low-velocity anomalies related to the natural flow of water that has a preferential northwest-southeast direction; ii) it shows low-velocity anomalies which correlate well with the staggered walls or stirrups of stone and mud on the surface that were part of the constructive process to extend the structure and provide support to weak parts of the Sun Pyramid (high-velocity zones lack these staggered walls); and iii) it images the dome-like structure of the pyramid, pointing to the susceptibility of the walls to landslides. These results will be useful for the structural diagnosis and assessment of seismic vulnerability of this emblematic pre-Hispanic monument.

KEYWORDS

Ambient noise tomography, H/V spectral ratio, Structure imaging, Sun Pyramid, Seismic vulnerability

1. INTRODUCTION

The ancient city of Teotihuacán flourished in the highlands of Central Mexico between 150 BC and 550/650 AD. At its peak, the city had a population of more than one hundred thousand inhabitants and was the largest one in the western hemisphere, with an extension larger than 20 square kilometers

(Cowgill, 2015). The center of the city had a group of large integrated buildings displaying, in a very particular order, the vast spaces and platforms that formed the most monumental architectural ensembles of Ancient America. The Sun Pyramid is one of the largest buildings made by men in ancient times. Currently, the Sun Pyramid is 64 m high with 215 m on each side of the square base. This structure was built on four levels or architectural bodies, somehow different from what it is seen today. Besides, in the western part of the pyramid, there is a terraced platform that was built after its completion (Millon and Drewitt, 1961). The pyramid was built in a single operation, with landfills and stones from the region achieving a solid volume of more than a million cubic meters. It was built between the first and the second century of our era during the First Stage of the city of Teotihuacán (Sarabia and Núñez, 2017).

The Teotihuacán archaeological site, and especially the Sun Pyramid, is one of the most visited ceremonial centers in Mexico. The number of people visiting the pyramid can reach 20,000 in the spring equinox. Another threat to this monument is the seismic activity in central Mexico, regularly affected by subduction earthquakes, by normal fault intraplate shakings ($M > 6$) and, although less frequent, by shallow cortical earthquakes. Therefore, it is necessary to know the mechanical properties of the materials and of the subsoil below the pyramid and to assess the seismic response of the structure for restoration and preservation purposes. A success history is the Pyramid of Zoser in Egypt, which did not collapse during some local earthquakes because it was previously restored (Khalil *et al.,* 2017).

Non-invasive seismic methods based on ambient noise are suitable techniques to estimate the physical and geotechnical properties of this monumental building. Since the pioneering work of Aki (1957), several signal processing techniques have been developed and applied at different scales to retrieve seismic wave velocities from this natural wavefield. In particular, it has been demonstrated that Rayleigh waves arrivals of the Green's functions between pairs of station can be recovered from cross-correlations of ambient seismic noise (or seismic coda) records (Shapiro *et al.,* 2005).

Using this result, surface-wave tomography based on ambient seismic noise has been successfully applied to large-scale geophysical studies (e.g. Ritzwoller *et al.,* 2011 in North America), providing significant data on the regional geology and tectonics. Since this method can be extended to the short-period vibrations (Chávez-García and Luzón, 2005; Nunziata et al., 2009), it is also useful for geotechnical-scale studies. For example, array records of seismic noise have been used to image complex 3D bodies such as magmatic chambers (e.g. Spica *et al.,* 2017) and to perform geotechnical surveys in laterally varying structures (e.g. Pilz et al., 2012). On the other hand, simpler one-station methods based on the analysis of the spectra or the horizontal-to-vertical spectral ratio (H/V) of ambient noise are often applied to the characterization of resonance frequencies of soils and buildings (e.g. Navarro *et al*., 2007, Gallipoli *et al*., 2009, Giocoli *et al*., 2019). A modern interpretation of the H/V ratio as a limit case of the cross-correlation method (Sánchez-Sesma *et al.*, 2011) increases the potential of this technique for subsoil exploration, providing independent constraints to ground models. This idea has been applied to obtaining images of different geological structures, such as regolith sites in Australia (Setiawan *et al*., 2018ab), a sedimentary coastal plain in Spain (García-Jerez *et al*., 2019) or an inter-mountain Quaternary basin in the Apennines (Famiani *et al*., 2020), among many others.

A 3D model for the shear wave velocity (Vs) within the Sun Pyramid, suitable for structural diagnosis, has been obtained in this work from an adaptation of the cross-correlation method of ambient noise. Correlations between pairs of stations are computed to retrieve and identify group velocity dispersion curves from prominent Rayleigh-wave trains in the Green's functions, from which dispersion curves are calculated. Using the recovered dispersion curves, a 2D surface wave tomography has been performed for different frequencies. Finally, the distribution of Rayleigh waves velocities has been used together with the H/V spectral ratios of seismic noise to obtain the 3D model of the Vs structure by means of a suitable inversion procedure.

2. DATA PROCESSING

For the assessment of the shear wave velocity (Vs) model of the Sun Pyramid, we used 15 triaxial seismic broadband (30 s) sensors 6TD, manufactured by Güralp Systems. The sensor distribution was carried out at different levels of the Sun Pyramid to approximately cover the whole surface of the structure (see figure 1a).

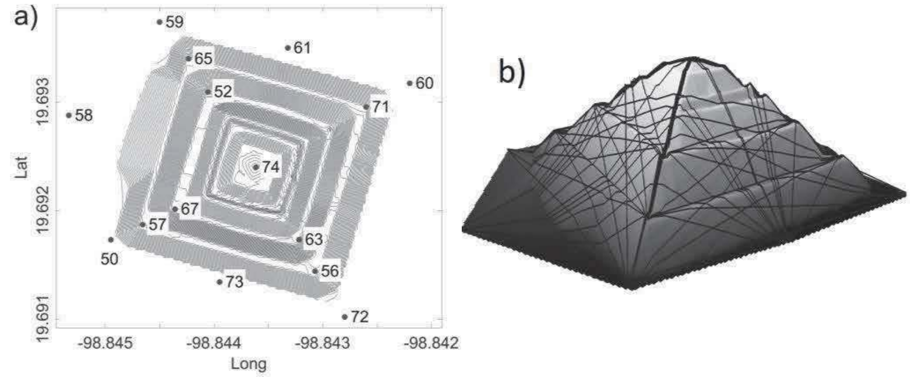

Figure 1. (a) Diagram of the sensors distribution on the surface of the Sun Pyramid. (b) Outline of shortest surface paths between pairs of stations for which the distances along the slopes were calculated.

Ambient seismic noise measurements were taken during ~ 4hrs in continuous mode, using GPS for synchronization. The records were corrected from instrumental response, base line and linear trend. Subsequently, the cross-correlation of vertical displacement between station pairs (see figure 1b) was carried out following the proposal of Bensen *et al.,* (2007). Examples of these cross-correlations are depicted in figures 2a and 2b. The time-frequency analysis (FTAN) was used (e.g. Ritzwoller and Levshin, 1998, Bensen *et al,* 2007) to extract group velocity curves from each cross correlation, one for each pair of stations. We obtained 105 reliable dispersion diagrams to extract dispersion curves in a frequency range between 3 and 10 Hz. At a frequency of 3 Hz, we find velocities around 750 m/s while at higher frequencies (10 Hz) the velocity is ~100 m/s on average for all dispersion curves (see figure 2e). The picking of dispersion curves was performed manually, and it was assumed that they correspond to the fundamental mode of Rayleigh waves. Figures 2c and 2d show the dispersion diagrams, for different wave paths, obtained from the correlation between the peak station (#74) and the base (#73) or the first level (#57) stations (figures 2a and 2b).

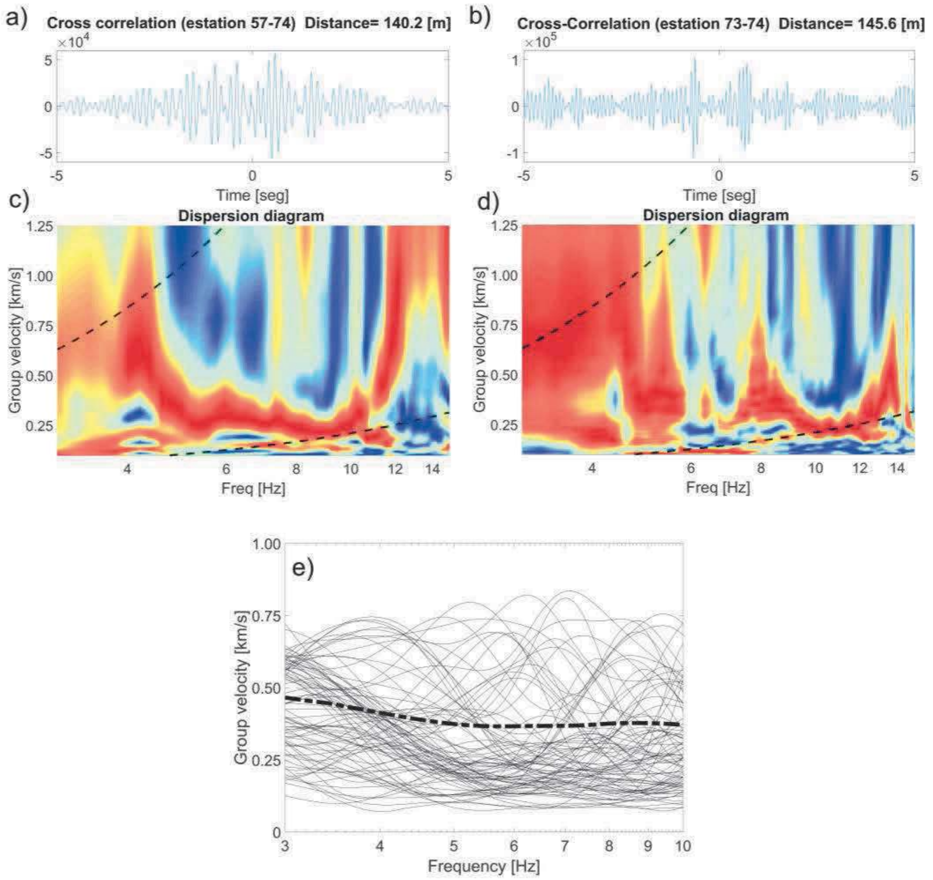

Figure 2. (a) and (b) Cross-correlation for seismic noise (causal and anticausal parts) between stations 57-74 and 73-74, respectively. (c) and (d) Rayleigh wave dispersion diagrams for 57-74 and 73-74 pairs, respectively. Dashed lines represent the upper and lower wavelength limits as a function of the distance between receivers. (e) Dispersion curves for the 105 pairs of stations (black lines) and average curve (dashed line)

We simulated the 2D propagation of elastic waves considering that the Sun Pyramid is a solid structure with irregular topography overlying a half-space, built and mainly filled of clays and rocks from the surroundings. Vertical displacements caused by a vertical unit source were computed by using the Boundary Element Method (BEM, Manolis and Beskos, 1988) in a triangular profile comparable with cross-sections of the pyramid, and with properties similar to those of earth dams (see appendix A). From the simulation we noted that, up to a certain degree of approximation, Rayleigh travel on the pyramid surface. In addition, we computed the cross-correlations of the synthetic seismograms and verify that the group velocity dispersion curves can be obtained from cross-correlation of vertical displacements. From the dispersion diagram, we observed that the dispersion curve fragment which could be retrieved was limited by maximum and minimum wavelengths of the order of 1.2 and 0.2 times the distance between the receivers, respectively (see appendix A). Based on these observations, the information on the topography of the Sun Pyramid has been included to calculate the distances on the pyramid faces to obtain correct propagation distances which prevent from overestimation of Rayleigh's group velocities. To model the structure of the Sun Pyramid, 657 differential GPS points at different levels were obtained. Figure 1b shows a diagram of the trajectories on the surface of the pyramid from which the distances on the faces were calculated.

3. SURFACE-WAVE TOMOGRAPHY

The Rayleigh-wave tomography was performed from the travel times, taken from the measurements of group velocities at each frequency, using the Fast Marching Method (FMM) as inversion scheme. The FMM is a solver of the eikonal equation based on 2-D meshes, currently used in seismology to predict the travel time between source and receiver (forward problem). Detailed descriptions of the FMM can be found in Rawlinson and Sambridge (2004, 2005). Since the FMM tomography works in 2-D and the structure is 3-D, a correction has been carried out by applying a suitable projection scheme (Gómez-Moreno, 2004) to the structure that minimizes the distortion in distances and azimuth for the pairs of stations and thus avoids overestimation of the velocity values. To carry out this projection, an indeterminate system of nonlinear equations (eq. 1-2) was solved by an iterative process to find the new coordinates of the 2-D array of receivers that preserves, as best as possible, the original distances (computed along the slopes) and azimuths. This is:

$$D_m^n = \sqrt{(X_n - X_m)^2 + (Y_n - Y_m)^2} \qquad (1)$$

$$\alpha_m^n = \tan^{-1}\left[\frac{Y_n - Y_m}{X_n - X_m}\right] \qquad (2)$$

where D^n_m are defined as real distances (i.e. computed from the 3D coordinates), α^n_m is the true azimuth, n and m identify the stations, and X and Y are the new coordinates. The (X, Y) coordinates of the central station (located at the top of the structure) were fixed. However, this projection does not preserve distances and azimuths for all the points in the plane; the farther away are the points from the center, which in our case is the apex of the pyramid, the error increases (Gómez-Moreno, 2004). Figure 3c shows the errors in the distances between pairs of projected stations depending on the real distances measured on the faces. The maximum error found was 16%. If only distances in the horizontal plane were considered (i.e. ignoring the height z), errors of up to 110% would be found. Therefore, we consider that the new coordinate system is good enough to perform a tomography with the FMM scheme.

Using the transformed coordinates of the receivers, a chessboard test was carried out to determine the optimum resolution of the grid, verifying that the density of rays between pairs of stations is enough. After some trials, a spatial resolution ~40 meters (square cell) was selected to be used in the model. Figures 3a and 3b show the chessboard's test and its reconstruction by the inversion procedure for that cell size, respectively.

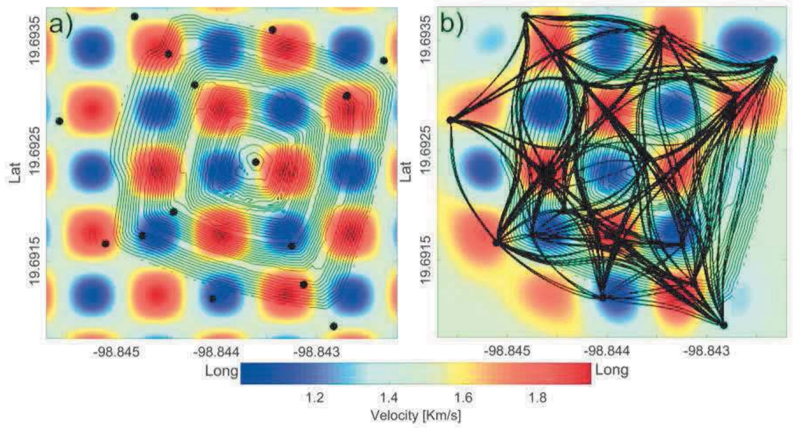

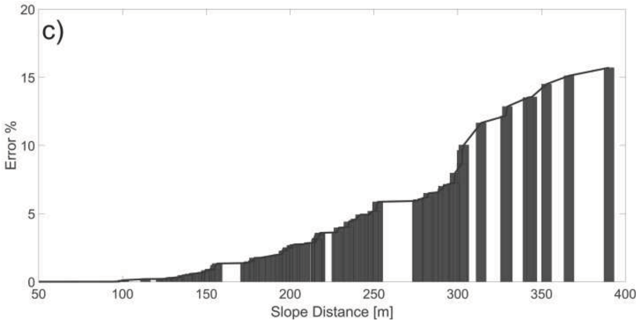

Figure 3. Checkerboard and tests of the projection scheme. (a) Synthetic velocity model for the chessboard test, with cell velocities between 1 and 2 km/s. Black lines represent the level curves of the structure, and points represent the stations. (b) Result of the inversion using synthetic data. Thick black lines represent the ray paths between stations. (c) Error (expressed as a percentage) between real station distances (measured on the lateral faces) and the distances between projected points)

The initial velocity model for the tomographic inversion was the average of the group velocity measurements for each frequency (see figure 2e). Because of the good coverage of rays and the moderate spatial resolution, we choose to apply smoothing during the inversion. Theoretical travel time values for the resulting model show RMS deviations from the observed data ranging between 140 ms and 280 ms, depending on the analyzed frequency.

The spatial distribution of group velocities of Rayleigh waves for 3, 5, 7 and 9 Hz are shown in figures 4a-d, respectively. Figure 4e depicts the RMS value of the tomographic inversion for each frequency. The tomography at 3 Hz shows two low-velocity anomalies (with values of ~500 m/s), one in the northwest and the other in the southeastern part of the pyramid. The image at 5 Hz clearly shows that the northwest anomaly decreases its velocity down to ~100 m/s, while the southeast anomaly is extending to the southwest. At 7 Hz, low-velocity anomalies remain in the southern part of the Sun Pyramid as well as in the northwestern part. However, there is a new isolated low-velocity anomaly in the northeastern part. Finally, the distribution at 9 Hz shows that low-velocity anomalies predominate in the center and southeast parts of the Sun Pyramid. Possible causes of these patterns will be discussed in the next section.

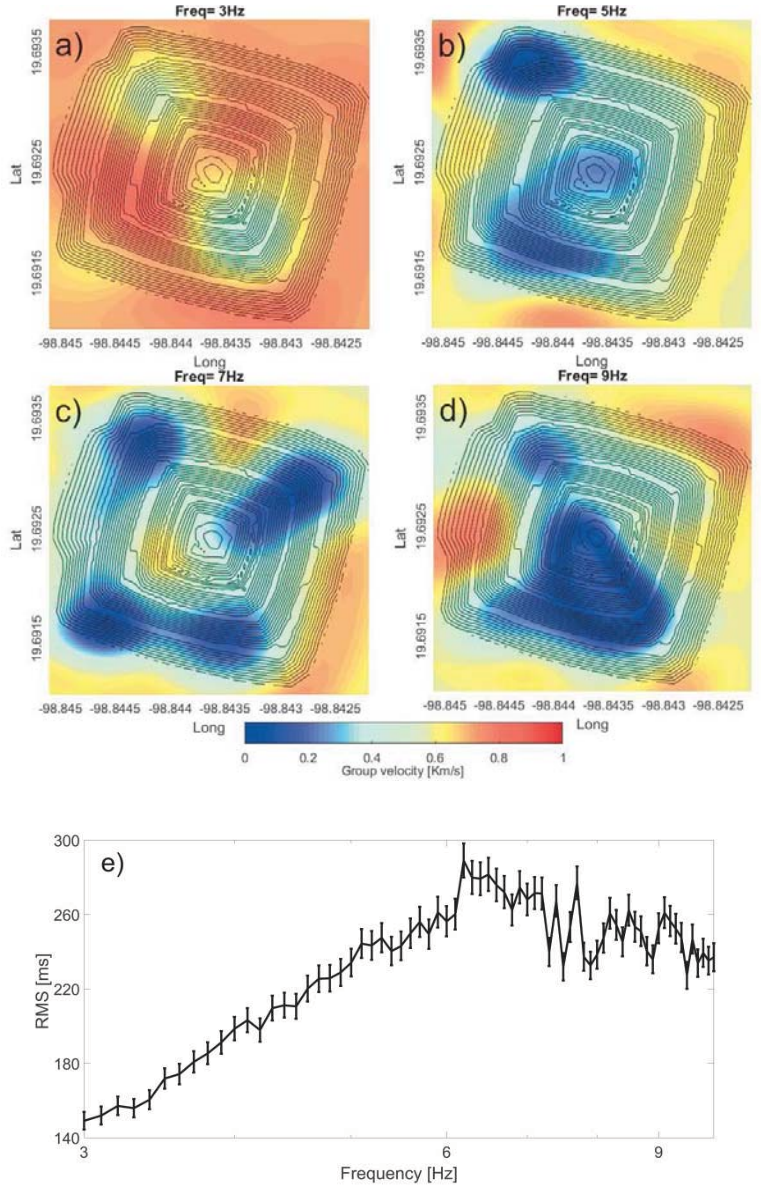

Figure 4. (a-d) 2D seismic tomography for frequencies of 3, 5, 7 and 9 Hz, respectively. Black lines represent the level curves of the structure. (e) RMS time residual for each frequency.

4. INVERSION OF THE V$_S$ STRUCTURE

From the seismic tomography maps corresponding to each analyzed frequency (3-10 Hz), a dispersion curve was built for each cell and inverted using the HV-Inv software (García-Jerez *et al.,* 2016). To mitigate the non-uniqueness problem in dispersion curve inversions (e.g. Piña-Flores *et al.,* 2017), we obtained the H/V spectral ratio for the station at the top of the Sun Pyramid and performed a joint inversion of these two observations for the cells placed around to the apex. This H/V spectral ratio shows a single peak with amplitude ~2.8 located at 1.75 Hz. For frequencies from 5 to 10 Hz the amplitude is less than the unit (see figure 5a). We can interpret this fact as the effect of an inversion in velocity as depth increases (Castelaro and Mulargia, 2009). It is assumed that the H/V spectral ratio, which has been modelled under the theory of diffuse fields (Sánchez-Sesma *et al.,* 2011), is a point measurement not very sensitive to the lateral irregularity (Perton *et al.,* 2018).

Figures 5 a-c show the results of the joint inversion of the H/V spectral ratio and the group velocity dispersion curve assigned to the top of the pyramid. The Vs velocity profile resulting from the joint inversion (figure 5c) shows the mentioned velocity inversion, with a stiff ~10 m thick surface layer of ~1800 m/s in Vs which seems to correspond to the coating of the Sun Pyramid composed of concrete and basalt fragments (Batres, 1993). The second layer has a thickness of 15 m and Vs = 250 m/s and the third one has a thickness of 25 m and Vs ~450 m/s. Finally, the inverted Vs profile was used as the initial model for dispersion curve inversions in the neighboring cells. This procedure was iterated until all curves were inverted.

In order to explore the investigation depth reached from the dispersion curves in the band 3 - 10 Hz, a sensitivity analysis of the group velocity was performed, in terms of frequency, under variations in Vs at different depths around the values obtained for the apex model. In particular, we computed the sensitivity matrix (f, h) defined as

$$S(f,h) = \frac{dU(f)}{d\,Vs(h)} \tag{3}$$

where $U\ (f)$ is the group velocity at frequency f and Vs(h) is the S-wave velocity as a function of the depth h. In this analysis (Figure 5 d-f), we show that the fragments of dispersion curves are sensitive ($S(f,h) > 0.01$) to variations in the Vs profile in the range from 7 m to 100 m deep.

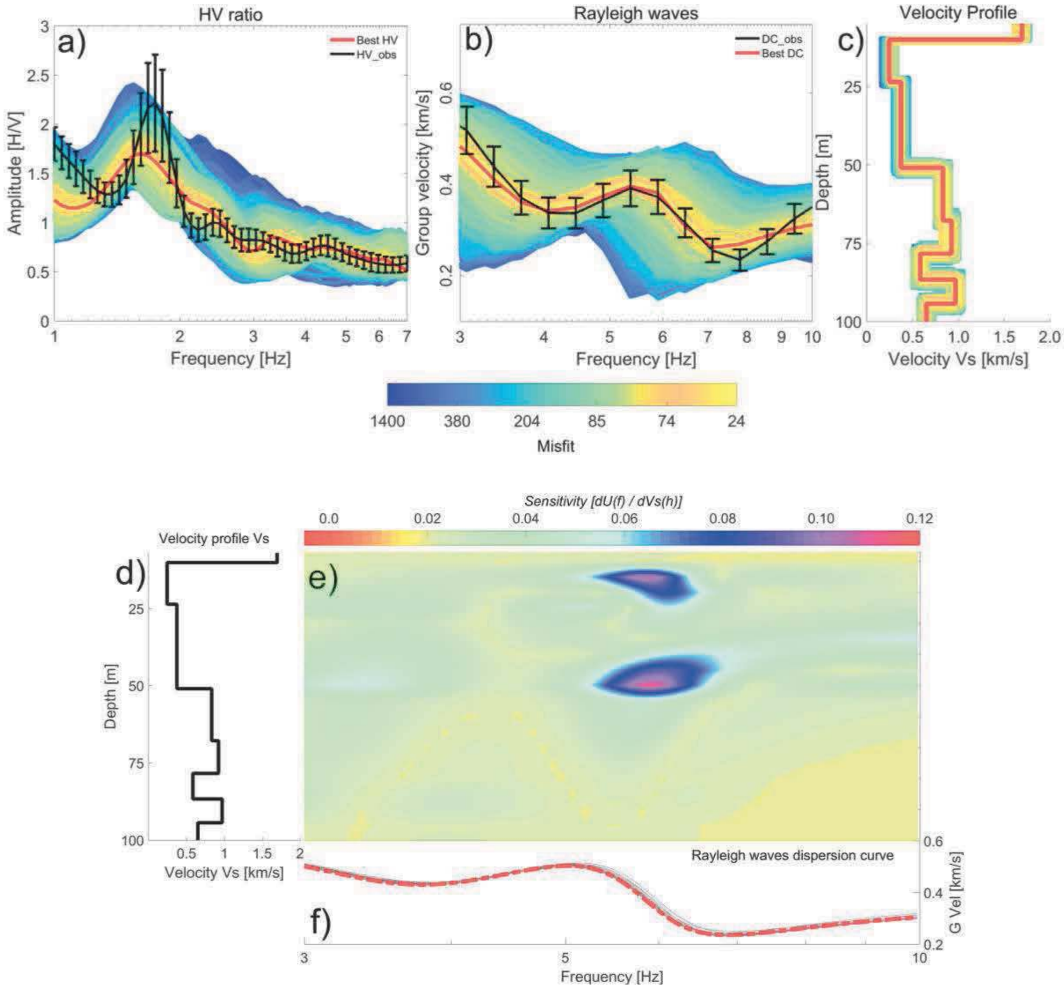

Figure 5. Joint inversion results from (a) the H/V spectral ratio and (b) the group velocity dispersion curve for Rayleigh waves. Black lines represent the curves observed with their standard deviation, and red lines represent the best fit. (c) Vs profile obtained from joint inversion. Red line represents the best profile. Panels d-f show the results of the sensitivity analysis of the dispersion curve. (d) Velocity profile obtained from the dispersion curve (dash line in panel f). (e) Sensitivity *S* to variations in Vs as a function of the layer depth and the frequency.

Once the Vs velocity profiles were inverted for each cell, an interpolation of them with moderate smoothing was performed. Then, each velocity profile was moved back to the 3D space on the basis of the (projected) coordinates of the corresponding cell center. To do so, we interpolated from the inverse transformation described above (i.e. from 2D to 3D station coordinates) and assigned the local elevation of the pyramid surface to the model free surface. Some features of the inverted 3D Vs model have been presented in figure 6. Figure 6a shows two low velocity (~150 m/s) anomalies; one of them is located in the northwest area and the second one in the southeast part of the pyramid. These anomalies (which were already detectable in the Rayleigh velocity maps) can be associated to water saturation of the materials and/or the differential weathering due to rainwater that is captured inside the pyramid in specific areas. This would be congruent with the natural water flow in the zone, with predominant northwest-southeast direction.

These results can be also compared with the surficial features of the Pyramid. Figures 6a and 6b show that these low-velocity areas correspond to some staggered walls, which provide stability to the structure (Batres, 1993). In contrast, high-velocity zones (~1800 m/s) lack these walls. It should be noted that the staggered walls are part of a series of structures that were attached to the slopes of the first two levels in order to widen the base of the pyramid. Initially, many more were built as part of the constructive system to stabilize the enlargement of just over 6 m wide of the Sun Pyramid. Unlike the original construction, which is made up of clays, the staggered walls consist of *tezontle* (light and porous volcanic rock) and basalt rocks cemented with mud. Most of these staggered walls disappeared and only 64 are currently preserved.

A vertical section of the 3D Vs model passing through the center of the pyramid in east-west direction is shown in figure 6c. It shows that the interior consists of different layers forming a dome-like structure, with a softer material (~450 m/s) surrounding a high-velocity core (~1200 m/s). This structure is consistent with the data gathered by Millon *et al.* (1965) from the excavations of the Gamio and Noguera's tunnels (Gamio, 1922; Noguera, 1935) which cross the entire Pyramid (see figure 7). The reader is referred to the supplementary material for more sections of the model.

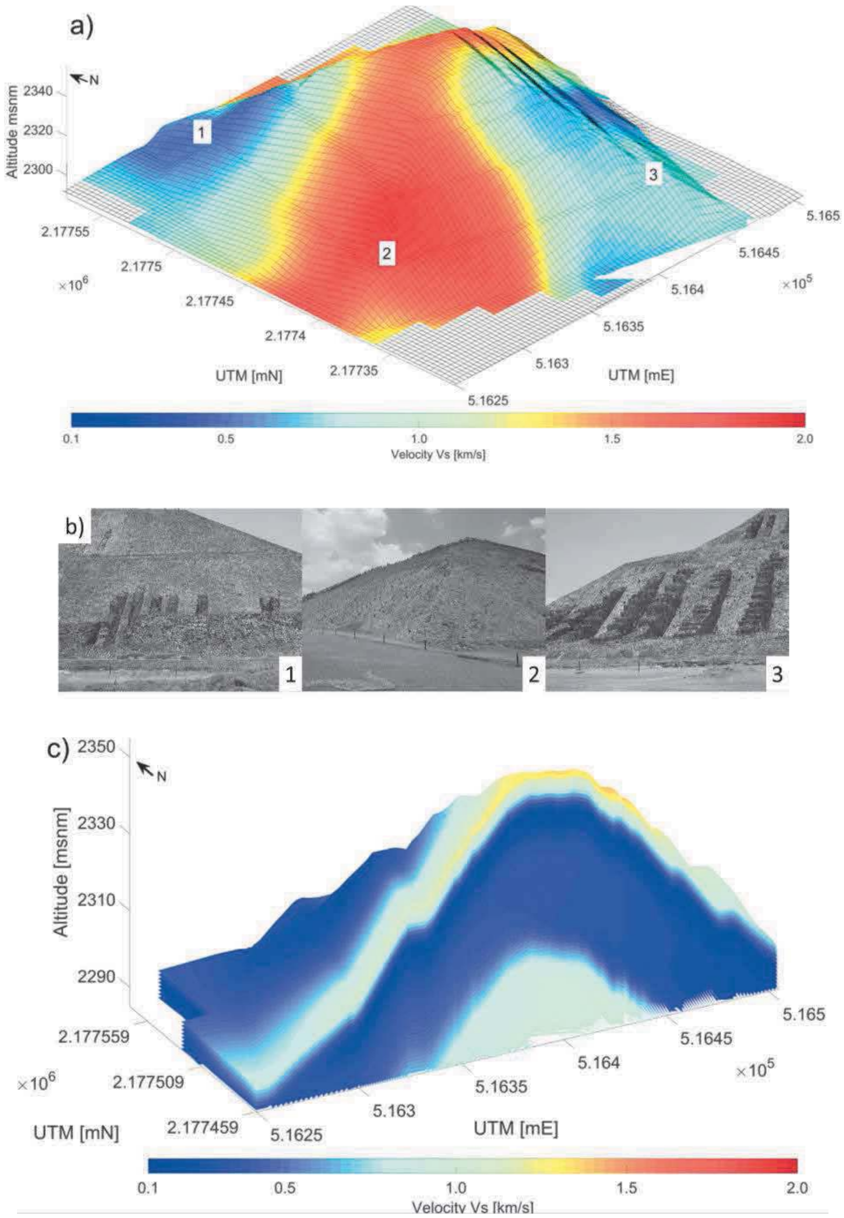

Figure 6. Some views of the 3D Vs model of the Sun Pyramid (more sections are available as supplementary material). (a) Velocity at 7 m below the topography. For the low velocity zones (zones 1 and 3) high staggered walls are present, whereas the zone of high velocity (zone 2) does not have these structures, (b) Photographs of the structural features of the Sun Pyramid (taken in July 2016), corresponding to zones of low (1, 3) and high velocities (2), (c) Cross-section of the velocity model in east-west direction (the upper 7 m below the topography, at which the sensitivity decreases, are not shown).

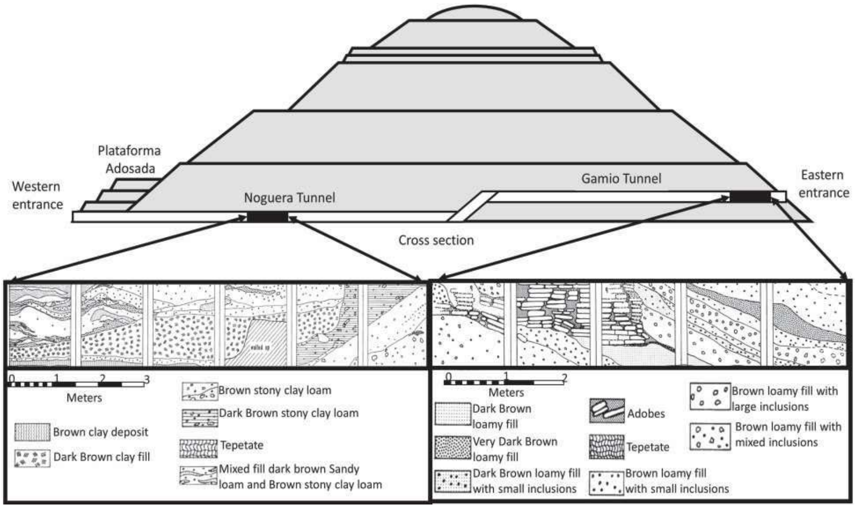

Figure 7. Lithological description of the interior of the Sun Pyramid from the excavations carried out by Gamio and Noguera. Modified from Millon *et al.* (1965) pp. 86, 88 and 90.

5. DISCUSSION Y CONCLUSIONS

Valuable structural information on the mechanical properties of the materials that make up the Sun Pyramid (Teotihuacán, Mexico) has been obtained from a passive seismic method. In the experiment, 15 triaxial sensors were deployed on the surface of the pyramid to record approximately 4 h of ambient seismic noise. We first obtained the average cross-correlations between stations from this dataset and used them to retrieve Rayleigh wave dispersion curves and to obtain a tomography. The joint inversion of the local Rayleigh velocities and the H/V spectral ratio allowed to obtain a 3D Vs model of the Sun Pyramid. A 2D test, modeling the propagation of surface waves in the pyramid using the boundary element method (BEM) let us verify that Rayleigh-wave components of the Green function can be safely recovered in an elastic medium with this geometry.

This work was carried out with strict quality control of the data and of the dispersion curves picking. As the Sun Pyramid is a structure with irregular topography, we have successfully applied a projection method to correctly evaluate the propagation velocities of Rayleigh waves. In addition, a simultaneous inversion of the local dispersion curves, obtained from the group velocity tomography, and the H/V spectral ratio was applied to mitigate non-uniqueness issues in the retrieved Vs model. This combination let us improve the vertical resolution of the model, revealing some features such as the stiff coating of the pyramid (that was outside the range of depths to which our dispersion curves are sensitive) and the precise depth and magnitude of the main velocity contrasts.

Our results reproduce three main features of the Sun Pyramid. Firstly, the model describes low-velocity anomalies related to the natural flow of water that has a preferential northwest-southeast direction. The second characteristic is of structural type: presence of low-velocity anomalies (~150 m/s) which correlates with staggered walls or stirrups of stone and mud on the surface (Batres, 1993). In high-velocity zones (~1800 m/s), the structure lacks these staggered walls. No doubt, these structures were part of a constructive process to extend the structure and provide support to weak parts of the Sun Pyramid. The last feature is that materials inside the Pyramid form a dome-like structure. These features are consistent with the observations conducted by Millon *et al*., (1965) based on the excavations of Gamio and Noguera (Gamio, 1922; Noguera, 1935) that cross the entire Pyramid. The nucleus of the Pyramid consists of several layers of silty sands, ground *tepetate* (a whitish-yellow calcareous hardpan which, when cut into blocks, is used in construction) mixed with stones and a high quantity of ceramic fragments and charcoal. No large rock or adobes were used (Sugiyama *et al*., 2014). The structure of the Sun Pyramid, with large zones of very soft material subjected to the action of infiltrated water, is susceptible to landslides. This problem is evidenced by the existing damage to the coating, mainly in the SE and NW areas. For example, cracks and landslides of several cm were detected after the Puebla - Morelos earthquake (Mw 7.1) that occurred on September 19, 2017, 130 km from the pyramid. The data provided by our work will be useful for the structural diagnosis of the Sun Pyramid in Teotihuacán aimed at preserving this monument, declared World Heritage by UNESCO.

ACKNOWLEDGEMENTS

We would like to express our thanks to Dr. Jorge Aguirre-Gonzalez and Eng. Horacio Mijares, and the staff and students of the Institute and the School of Engineering of UNAM who participated in the ambient seismic noise measurement campaigns. We also thank Jesús Sánchez-González and his working group for providing us with the GPS points of the pyramid structure, the Archaeology Council for its continued support of the research on the Sun Pyramid, and MSc. David Escobedo-Zenil for his comments and keen suggestions. This work has been partially supported by the Mexican National Council of Science and Technology (CONACYT) through the National Scholarship CONACYT number 449268 and DGAPA-UNAM Projects PAPIIT IN100917 and PAPIME PE103918.

REFERENCES

Aki, K., 1957. Space and time spectra of stationary stochastic waves, with special reference to microtremors. Bulletin of the Earthquake Research Institute 35, 415– 457.

Batres, L., 1993. El “descubrimiento” de la Pirámide del Sol. Arqueología Mexicana 1, 45-48.

Bensen, G.D., Ritzwoller, M.H., Barmin, M.P., Levshin, A.L., Lin, F., Moschetti, M.P., Shapiro, N.M., Yang, Y., 2007. Processing seismic ambient noise data to obtain reliable broad-band surface wave dispersion measurements. Geophys. J. Int. 169, 1239–1260. doi: 10.1111/j.1365-246X.2007.03374.x.

Castelaro, S., Mulargia, F., 2006. The Effect of Velocity Inversions on H/V. Pure Appl. Geophys 166, 567–592. doi: 10.1007/s00024-009-0474-5.

Chávez-García, F.J., Luzón, F., 2005. On the correlation of seismic microtremors. Journal of Geophysical Research: Solid Earth 110(B11). doi: 10.1029/2005JB003671.

Cowgill, G.L., 2015. Ancient Teotihuacan. Early Urbanism in Central México, Cambridge University Press, New York, USA.

Gallipoli, M.R., Mucciarelli, M., Vona, M., 2009. Empirical estimate of fundamental frequencies and damping for Italian buildings. Earthquake Engineering & Structural Dynamics 38(8), 973-988.

Gamio, M., 1922. La población del valle de Teotihuacán, Secretaría de Educación Pública, Dirección de Talleres Gráficos, Mexico.

Famiani, D., Brunori, C.A., Pizzimenti, L., Cara, F., Caciagli, M., Melelli, L., Mirabella, F., Barchi, M.R., 2020. Geophysical reconstruction of buried geological features and site effects estimation of the Middle Valle Umbra basin (central Italy). Engineering Geology 269, 105543. doi:10.1016/j.enggeo.2020.105543.

García-Jerez, A., Piña-Flores, J., Sánchez-Sesma, F.J., Luzón, F., Perton, M., 2016. A computer code for forward computation and inversion of the H/V spectral ratio under the diffuse field assumption. Comput. Geosci. 97, 67–78. doi: 10.1016/j.cageo.2016.06.016.

García-Jerez, A., Seivane, H., Navarro, M., Martínez, M., Piña-Flores, J., 2019. Joint analysis of Rayleigh-wave dispersion curves and diffuse-field HVSR for site characterization: The case of El Ejido town (SE Spain). Soil Dynamics and Earthquake Engineering 121, 102-120. doi:10.1016/j.soildyn.2019.02.023.

Giocoli, A., Hailemikael, S., Bellanova, J., Calamita, G., Perrone, A., Piscitelli, S., 2019. Site and building characterization of the Orvieto Cathedral (Umbria, Central Italy) by electrical resistivity tomography and single-station ambient vibration measurements. Engineering Geology 260, 105195.

Gómez-Moreno, R.A., 2004. Guía de proyecciones cartográficas (No. IN 526.8 G654G.), Instituto Nacional de Estadística, Geografía e Informática (INEGI), CDMX, Mexico.

Khalil, A.E., Abdel Hafi, H.E., Girgis, M., Taha, M.A., 2017. Earthquake ground motion simulation at Zoser pyramid using the stochastic method: A step toward the preservation of an ancient Egyptian heritage. NRIAG Journal of Astronomy and Geophysics 6(1), 52-59. doi: 10.1016/j.nrjag.2016.11.003.

Manolis, G.D., Beskos, D.E., 1988. Boundary Element Methods in Elastodynamics, Unwin Hyman Ltd., London, UK.

Millon, R., Drewitt, B., 1961. Earlier Structures within the Pyramid of the Sun at Teotihuacan. American Antiquity 26(3), 371-380. doi:10.2307/277403

Millon, R., Drewitt, B., Bennyhoff, J., 1965. The Pyramid of the Sun at Teotihuacán: 1959 Investigations. Transactions of the American Philosophical Society 55(6), 1-93. doi:10.2307/1005892.

Navarro, M., Vidal, F., Enomoto, T., Alcalá, F., García-Jerez, A., Sánchez, F.J., Abeki, N., 2007. Analysis of the weightiness of site effects on reinforced concrete (RC) building seismic behaviour: The Adra town example (SE Spain). *Earthquake Engineering and Structural Dynamics* 36, 1363-1383. doi: 10.1002/eqe.685

Noguera, E., 1935. Antecedentes y relaciones de la cultura teotihuacana. El México Antiguo. Ediciones Mexicanas. Mexico.

Nunziata, C., De Nisco, G., Panza, G.F., 2009. S-waves profiles from noise cross correlation at small scale. Engineering Geology 105, 161–170.

Perton, M., Spica, Z., Caudron, C., 2018. Inversion of the horizontal-to-vertical spectral ratio in presence of strong lateral heterogeneity. Geophys. J. Int. 212(2), 930–941. doi: 10.1093/gji/ggx458.

Pilz, M., Parolai, S., Picozzi, M., Bindi, D., 2012. Three-dimensional shear wave velocity imaging by ambient seismic noise tomography. Geophys. J. Int. 189, 501–512. doi: 10.1111/j.1365-246X.2011.05340.x.

Piña-Flores, J., Perton, M., García-Jerez, A., Carmona, E., Luzón, F., Molina-Villegas, J.C., Sánchez-Sesma, F.J., 2017. The inversion of spectral ratio H/V in a layered system using the diffuse field assumption (DFA). Geophys. J. Int. 208, 577–588. doi: 10.1093/gji/ggw416.

Rawlinson, N., Sambridge, M., 2004. Wave front evolution in strongly heterogeneous layered media using the fast marching method. Geophys. J. Int. 156, 631–647. doi: 10.1111/j.1365-246X.2004.02153.x.

Rawlinson, N., Sambridge, M., 2005. The fast marching method: an effective tool for tomographic imaging and tracking multiple phases in complex layered media. Exploration Geophysics 36(4), 341-350. doi: 10.1071/EG05341.

Ritzwoller, M.H., Levshin, A.L., 1998. Eurasian surface wave tomography: group velocities. J. geophys. Res. 103, 4839–4878. doi: 10.1029/97JB02622.

Ritzwoller, M.H., Lin, F.C., Shen, W., 2011. Ambient noise tomography with a large seismic array. C. R. Geosci. 343(8), 558-570. doi: 10.1016/j.crte.2011.03.007.

Sarabia, A., Núñez, N., 2017. The Sun Pyramid architectural complex in Teotihuacan: vestiges of worship and veneration. in: Robb, M. (Eds.), Teotihuacan City of Water, City of Fire. Fine Arts Museums of San Francisco, California.

Setiawan, B., Jaksa, M., Griffith, M., Love, D., 2018a. Estimating bedrock depth in the case of regolith sites using ambient noise analysis. Engineering Geology 243(4), 145-159.

Setiawan, B., Jaksa, M., Griffith, M., Love, D., 2018b. Seismic site classification based on constrained modeling of measured HVSR curve in regolith sites. Soil Dynamics and Earthquake Engineering 110, 244–261.

Sánchez-Sesma, F.J., Rodríguez, M., Iturrarán-Viveros, U., Luzón, F., Campillo, M., Margerin, L., García-Jerez, A., Suarez, M., Santoyo, M.A., Rodríguez-Castellanos, A., 2011. A theory for microtremor H/V spectral ratio: application for a layered medium. Geophys. J. Int. 186(1), 221–225. doi: 10.1111/j.1365-246X.2011.05064.x.

Shapiro, N.M., Campillo, M., Stehly, L., Ritzwoller, M., 2005. High resolution surface wave tomography from ambient seismic noise. Science 307, 1615–1618. doi: 10.1126/science.1108339.

Spica, Z., Caudron, C., Perton, M., Lecocq, T., Camelbeeck, T., Legrand, D., Piña-Flores, J., Iglesias, A., Syahbana, D.K., 2015. Velocity models and site effects at Kawah Ijen volcano and Ijen caldera (Indonesia) determined from ambient noise cross-correlations and directional energy density spectral ratios. J. Volc. Geotherm. Res. 302, 173–189. doi: 10.1016/j.jvolgeores.2015.06.016.

Sugiyama, S., Sugiyama, N., Sarabia-Gonzalez, A., 2014. El interior de la Pirámide del Sol en Teotihuacán. Arqueología Mexicana 125, 24-29.

APPENDIX

The boundary element method (BEM) is a numerical method that has produced satisfactory results in many problems of dynamic elasticity. From the theorems of reciprocal integral representation and through the discretization of the boundaries between homogeneous subdomains, the displacements and tractions can be worked out by an iterative process. Among the advantages of the method, it should be emphasized that it requires only the discretization of the boundaries and satisfies automatically the radiation condition without using special no reflective boundaries, as required by other methods (finite-difference methods). Detailed descriptions of the usage of the BEM in Elastodynamics can be found in Manolis and Beskos (1988).

To observe the propagation of the surface waves in a 2D medium with irregular topographical surface (i.e. a cross-section of the Sun Pyramid) a numerical simulation based on the BEM was performed. The model used consisted of an almost-triangular body partly buried on a half-space, both homogeneous and isotropic. Figure A1 shows the dimensions of the model and the properties assigned to each region. In this first simulation, a concentrated force was applied in the vertical direction at the top of the model to obtain the displacement in a dense array of vertical receivers placed on the surface and inside the model.

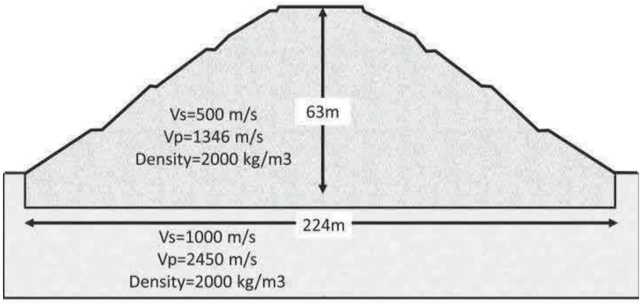

Figure A1. Outline of the model of the Sun Pyramid used in the BEM test. The model consists of two media with different dynamic properties.

Figure A2 shows some snapshots of the simulation results (more details can be found in the supplementary material). We observed first the propagation of compression waves with velocity Vp, sometime later (0.2 s) we can see the propagation of shear waves and finally, Rayleigh surface waves emerge. These surface waves have significant energy at depth and displacements are be nearly perpendicular to the surface. The parallel component is usually smaller. When the surface waves reach one half of the pyramid height the motion involves the half-space.

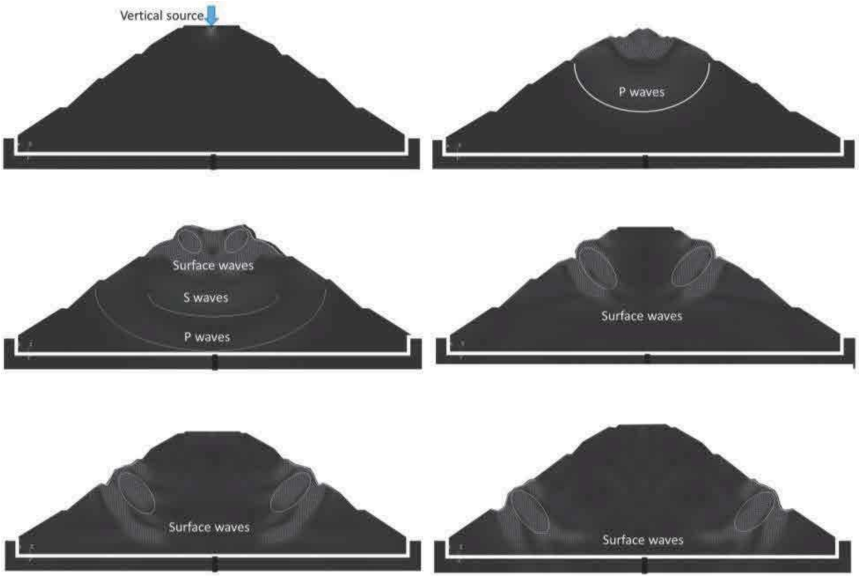

Figure A2. Snapshots of vertical displacement due to a vertical source using the BEM method.

On the other hand, in order to check the cross-correlation and dispersion curve calculation from cross correlation of vertical records, we computed synthetic seismograms along the surface of the irregular medium (the pyramid) (see Figure A3a) for a vertical source applied on the flat halfspace, outside the pyramid. That source location would be closer to the typical ambient noise sources. From these results we estimated cross-correlation of two synthetic records (Fig. A3b) following the methodology described by Bensen *et al*., (2017). The time-frequency analysis (FTAN) (e.g. Ritzwoller and Levshin 1998, Bensen *et al*., 2007) was used to compute the dispersion diagram from the cross correlation. It shows the group velocity dispersion curve of Rayleigh waves in a frequency range between 5 and 15

Hz with velocities between 250 m/s and 750 m/s (Figure A3c). For reference, we show the theoretical dispersion curve for a 1D model consisting of a 30 m thick flat layer, which corresponds to the mean value of the receivers height, over a half space, using the same dynamic properties of the materials of our 2-D model. This theoretical dispersion curve resembles the dispersion diagram (better for low frequencies).

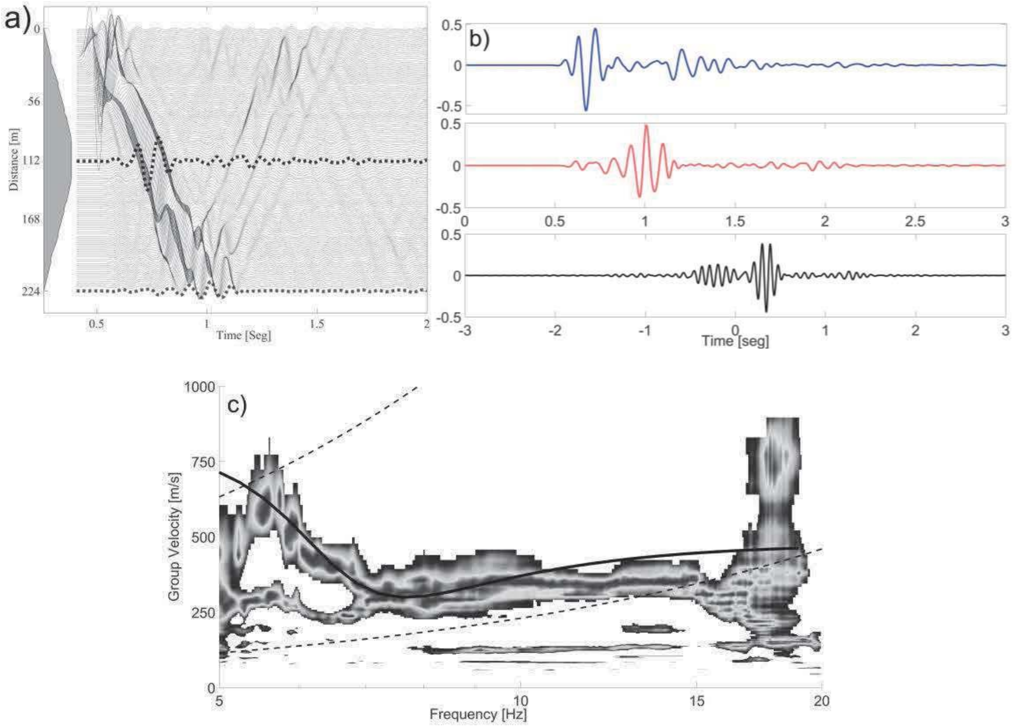

Figure A3. (a) synthetic seismograms obtained from the numerical simulation with BEM. (b) Cross-correlation (black line) obtained from the synthetic seismograms of the base (red line) and of the apex (blue line). (c) Dispersion curve obtained from the cross correlation. The solid line represents the theoretical dispersion curve for a 30 m thick horizontal layer with the properties given to the pyramid overlying a half-space with the ground properties. Dashed lines correspond to wavelength limits of 1.2 and 0.2 times the interstation distance.

Declaration of interests

☒ The authors declare that they have no known competing financial interests or personal relationships that could have appeared to influence the work reported in this paper.

☐The authors declare the following financial interests/personal relationships which may be considered as potential competing interests: